



SAIMM

THE SOUTHERN AFRICAN INSTITUTE
OF MINING AND METALLURGY

VOLUME 120 NO. 2 FEBRUARY 2020



HOT DIP GALVANIZING

THE PROVEN CORROSION CONTROL TECHNOLOGY FOR STEEL AND IRON



HOT DIP GALVANIZERS ASSOCIATION
SOUTHERN AFRICA

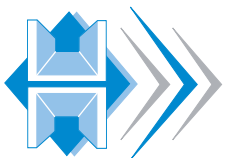
www.hdgasa.org.za

The Hot Dip Galvanizers Association Southern Africa is a not-for-profit trade association dedicated to serving the needs of end-users, specifiers, architects, engineers, contractors, fabricators and hot dip galvanizers throughout Southern Africa.



COMMITTED TO
DELIVERING EXCELLENCE

Hot dip galvanizing – the proven corrosion control technology for steel and iron



HOT DIP GALVANIZERS ASSOCIATION
SOUTHERN AFRICA

Developing and expanding the market for hot dip galvanizing and duplex systems as cost effective corrosion control systems.

Western Cape: Advanced Galvanising (Pty) Ltd | South Cape Galvanizing (Pty) Ltd |

Eastern Cape: Galvanising Techniques (Pty) Ltd | Morhot Galvanisers |

KwaZulu Natal: A & A Galvanising cc | Bay Galvanizers | Durban Galvanizing (Pty) Ltd | Phoenix Galvanizing (Pty) Ltd | Pinetown Galvanizing | Voigt & Willecke (Pty) Ltd |

Gauteng: ArcelorMittal South Africa | Armco Galvanizers - Isando | Armco Galvanizers - Randfontein | Galferro Galvanisers | Lianru Galvanisers (Pty) Ltd | Monoweld Galvanizers | Pro-Tech Galvanizers (Pty) Ltd | Silverton Engineering | SMT Galvanizers | Transvaal Galvanisers |

Telephone: +27 11 456 7960 **Email:** hdgasa@icon.co.za

www.hdgasa.org.za

OFFICE BEARERS AND COUNCIL FOR THE 2019/2020 SESSION

Honorary President

Mxolisi Mgojo
President, Minerals Council South Africa

Honorary Vice Presidents

Gwede Mantashe
Minister of Mineral Resources, South Africa

Ebrahim Patel
Minister of Trade and Industry, South Africa

Blade Nzimande
Minister of Science and Technology, South Africa

President

M.I. Mthenjane

President Elect

V.G. Duke

Senior Vice President

I.J. Geldenhuys

Junior Vice President

Z. Botha

Incoming Junior Vice President

W.C. Joughin

Immediate Past President

A.S. Macfarlane

Co-opted to Office Bearers

S. Ndlovu

Honorary Treasurer

V.G. Duke

Ordinary Members on Council

B. Genc	S.M Rupprecht
W.C. Joughin	N. Singh
G.R. Lane	A.G. Smith
E. Matinde	M.H. Solomon
G. Njowa	A.T. van Zyl
B. Ntsoelengoe	E.J. Walls

Co-opted Members

T. Makgala R.C.W. Webber-Youngman

Past Presidents Serving on Council

N.A. Barcza	J.L. Porter
R.D. Beck	S.J. Ramokgopa
J.R. Dixon	M.H. Rogers
H.E. James	D.A.J. Ross-Watt
R.T. Jones	G.L. Smith
C. Musingwini	W.H. van Niekerk
S. Ndlovu	

G.R. Lane-TPC Mining Chairperson
Z. Botha-TPC Metallurgy Chairperson

G. Dabula-YPC Chairperson
S. Manjengwa-YPC Vice Chairperson

Branch Chairpersons

Botswana	Vacant
DRC	S. Maleba
Johannesburg	D.F. Jensen
Namibia	N.M. Namate
Northern Cape	F.C. Nieuwenhuys
Pretoria	S. Uludag
Western Cape	A.B. Nesbitt
Zambia	D. Muma
Zimbabwe	C.P. Sadomba
Zululand	C.W. Mienie

PAST PRESIDENTS

*Deceased

* W. Bettel (1894-1895)	* M. Barcza (1958-1959)
* A.F. Crosse (1895-1896)	* R.J. Adamson (1959-1960)
* W.R. Feldtmann (1896-1897)	* W.S. Findlay (1960-1961)
* C. Butters (1897-1898)	* D.G. Maxwell (1961-1962)
* J. Loevy (1898-1899)	* J. de V. Lambrechts (1962-1963)
* J.R. Williams (1899-1903)	* J.F. Reid (1963-1964)
* S.H. Pearce (1903-1904)	* D.M. Jamieson (1964-1965)
* W.A. Caldecott (1904-1905)	* H.E. Cross (1965-1966)
* W. Cullen (1905-1906)	* D. Gordon Jones (1966-1967)
* E.H. Johnson (1906-1907)	* P. Lambooy (1967-1968)
* J. Yates (1907-1908)	* R.C.J. Goode (1968-1969)
* R.G. Bevington (1908-1909)	* J.K.E. Douglas (1969-1970)
* A. McA. Johnston (1909-1910)	* V.C. Robinson (1970-1971)
* J. Moir (1910-1911)	* D.D. Howat (1971-1972)
* C.B. Saner (1911-1912)	* J.P. Hugo (1972-1973)
* W.R. Dowling (1912-1913)	* P.W.J. van Rensburg (1973-1974)
* A. Richardson (1913-1914)	* R.P. Plewman (1974-1975)
* G.H. Stanley (1914-1915)	* R.E. Robinson (1975-1976)
* J.E. Thomas (1915-1916)	* M.D.G. Salamon (1976-1977)
* J.A. Wilkinson (1916-1917)	* P.A. Von Wielligh (1977-1978)
* G. Hildick-Smith (1917-1918)	* M.G. Atmore (1978-1979)
* H.S. Meyer (1918-1919)	* D.A. Viljoen (1979-1980)
* J. Gray (1919-1920)	* P.R. Jochens (1980-1981)
* J. Chilton (1920-1921)	* G.Y. Nisbet (1981-1982)
* F. Wartenweiler (1921-1922)	* A.N. Brown (1982-1983)
* G.A. Watermeyer (1922-1923)	* R.P. King (1983-1984)
* F.W. Watson (1923-1924)	* J.D. Austin (1984-1985)
* C.J. Gray (1924-1925)	* H.E. James (1985-1986)
* H.A. White (1925-1926)	* H. Wagner (1986-1987)
* H.R. Adam (1926-1927)	* B.C. Alberts (1987-1988)
* Sir Robert Kotze (1927-1928)	* C.E. Fivaz (1988-1989)
* J.A. Woodburn (1928-1929)	* O.K.H. Steffen (1989-1990)
* H. Pirow (1929-1930)	* H.G. Mosenthal (1990-1991)
* J. Henderson (1930-1931)	* R.D. Beck (1991-1992)
* A. King (1931-1932)	* J.P. Hoffman (1992-1993)
* V. Nimmo-Dewar (1932-1933)	* H. Scott-Russell (1993-1994)
* P.N. Lategan (1933-1934)	* J.A. Cruise (1994-1995)
* E.C. Ranson (1934-1935)	* D.A.J. Ross-Watt (1995-1996)
* R.A. Flugge-De-Smidt (1935-1936)	* N.A. Barcza (1996-1997)
* T.K. Prentice (1936-1937)	* R.P. Mohring (1997-1998)
* R.S.G. Stokes (1937-1938)	* J.R. Dixon (1998-1999)
* P.E. Hall (1938-1939)	* M.H. Rogers (1999-2000)
* E.H.A. Joseph (1939-1940)	* L.A. Cramer (2000-2001)
* J.H. Dobson (1940-1941)	* A.A.B. Douglas (2001-2002)
* Theo Meyer (1941-1942)	* S.J. Ramokgopa (2002-2003)
* John V. Muller (1942-1943)	* T.R. Stacey (2003-2004)
* C. Biccard Jeppe (1943-1944)	* F.M.G. Egerton (2004-2005)
* P.J. Louis Bok (1944-1945)	* W.H. van Niekerk (2005-2006)
* J.T. McIntyre (1945-1946)	* R.P.H. Willis (2006-2007)
* M. Falcon (1946-1947)	* R.G.B. Pickering (2007-2008)
* A. Clemens (1947-1948)	* A.M. Garbers-Craig (2008-2009)
* F.G. Hill (1948-1949)	* J.C. Ngoma (2009-2010)
* O.A.E. Jackson (1949-1950)	* G.V.R. Landman (2010-2011)
* W.E. Gooday (1950-1951)	* J.N. van der Merwe (2011-2012)
* C.J. Irving (1951-1952)	* G.L. Smith (2012-2013)
* D.D. Stitt (1952-1953)	* M. Dworzanowski (2013-2014)
* M.C.G. Meyer (1953-1954)	* J.L. Porter (2014-2015)
* L.A. Bushell (1954-1955)	* R.T. Jones (2015-2016)
* H. Britten (1955-1956)	* C. Musingwini (2016-2017)
* Wm. Bleloch (1956-1957)	* S. Ndlovu (2017-2018)
* H. Simon (1957-1958)	* A.S. Macfarlane (2018-2019)

Honorary Legal Advisers

Scop Incorporated

Auditors

Genesis Chartered Accountants

Secretaries

The Southern African Institute of Mining and Metallurgy

Fifth Floor, Minerals Council South Africa

5 Holland Street, Johannesburg 2001 • P.O. Box 61127, Marshalltown 2107

Telephone (011) 834-1273/7 • Fax (011) 838-5925 or (011) 833-8156

E-mail: journal@saimm.co.za

Editorial Board

R.D. Beck
P. den Hoed
L.M. Falcon
B. Genc
R.T. Jones
W.C. Joughin
D.E.P. Klenam
H. Lodewijks
R. Mitra
C. Musingwini
S. Ndlovu
P. Neingo
N. Rampersad
T.R. Stacey
M. Tlala
F.D.L. Uahengo

Editorial Consultant

R.M.S. Falcon

Typeset and Published by

The Southern African Institute of Mining and Metallurgy
P.O. Box 61127
Marshalltown 2107
Telephone (011) 834-1273/7
Fax (011) 838-5923
E-mail: journal@saimm.co.za

Printed by

Camera Press, Johannesburg

Advertising Representative

Barbara Spence
Avenue Advertising
Telephone (011) 463-7940
E-mail: barbara@avenue.co.za

ISSN 2225-6253 (print)
ISSN 2411-9717 (online)



Directory of Open Access Journals



THE INSTITUTE, AS A BODY, IS NOT RESPONSIBLE FOR THE STATEMENTS AND OPINIONS ADVANCED IN ANY OF ITS PUBLICATIONS.

Copyright© 2020 by The Southern African Institute of Mining and Metallurgy. All rights reserved. Multiple copying of the contents of this publication or parts thereof without permission is in breach of copyright, but permission is hereby given for the copying of titles and abstracts of papers and names of authors. Permission to copy illustrations and short extracts from the text of individual contributions is usually given upon written application to the Institute, provided that the source (and where appropriate, the copyright) is acknowledged. Apart from any fair dealing for the purposes of review or criticism under **The Copyright Act no. 98, 1978, Section 12**, of the Republic of South Africa, a single copy of an article may be supplied by a library for the purposes of research or private study. No part of this publication may be reproduced, stored in a retrieval system, or transmitted in any form or by any means without the prior permission of the publishers. **Multiple copying of the contents of the publication without permission is always illegal.**

U.S. Copyright Law applicable to users in the U.S.A.

The appearance of the statement of copyright at the bottom of the first page of an article appearing in this journal indicates that the copyright holder consents to the making of copies of the article for personal or internal use. This consent is given on condition that the copier pays the stated fee for each copy of a paper beyond that permitted by Section 107 or 108 of the U.S. Copyright Law. The fee is to be paid through the Copyright Clearance Center, Inc., Operations Center, P.O. Box 765, Schenectady, New York 12301, U.S.A. This consent does not extend to other kinds of copying, such as copying for general distribution, for advertising or promotional purposes, for creating new collective works, or for resale.



SAIMM

THE SOUTHERN AFRICAN INSTITUTE OF MINING AND METALLURGY



VOLUME 120 NO. 2 FEBRUARY 2020

Contents

Journal Comment

by J.H. Selby iv

President's Corner

by M.I. Mthenjane v

SAMCODES: Sign-off on Public Documents using SAIMM/GSSA membership ... vi

HEAVY MINERALS PAPERS

Design of sidewall lining/cooling systems for AC or DC ilmenite smelting furnaces

H. Joubert and H. Kotzé 97

In ilmenite smelting, the slag produced is aggressive towards the furnace sidewall lining. The formation of a stable slag freeze lining is essential as the sidewall lining can be severely damaged within a short period of time. The effectiveness of high-intensity copper coolers combined with an externally cooled furnace shell is explored.

Technological developments in processing Australian mineral sand deposits

M.I. Pownceby, W.J. Bruckard, and G.J. Sparrow 105

Almost all Australian mineral sand deposits are placer deposits. The development of new technology for mineral separation and its adaption to changes in the composition of the minerals in the deposits are discussed. Also, novel processing conditions to lower the levels of impurity elements and to remove gangue minerals are summarized.

Online spiral grade control

A.M. Russell 113

Online control of gravity spiral concentrators has not been widely implemented. A new technique making use of process water jets for the control of spiral product quality is proposed, and which is suitable for retrofitting to existing spiral circuits. Tests carried out at a chromite plant processing UG2 flotation tailing have shown that online control of the spiral plant concentrate grade using this technique is feasible.

International Advisory Board

R. Dimitrakopoulos, McGill University, Canada
D. Dreisinger, University of British Columbia, Canada
M. Dworzanowski, Consulting Metallurgical Engineer, France
E. Esterhuizen, NIOSH Research Organization, USA
H. Mitri, McGill University, Canada
M.J. Nicol, Murdoch University, Australia
E. Topal, Curtin University, Australia
D. Vogt, University of Exeter, United Kingdom



A literature review and interpretation of the properties of high-TiO₂ slags	
H. Kotzé	121
<i>The properties of high TiO₂ slags are markedly different from those of slags encountered in many other metallurgical processes. The objectives of this paper are firstly to review TiO₂ slag properties, and secondly, to attempt to correlate published experimentally measured data with theoretically based parameters, which will enable the application of the measured properties to a wider range of slag compositions within the pseudobrookite-TiO₂ slag system.</i>	

A geometallurgical approach to enhance the gravity beneficiation of a strontium deposit	
A. Perroton, T. Wallmach, S.B. Blancher, and G. Rameau	131
<i>QEMSCAN® analyses and the QEMSCAN® integrated process simulation software were used to characterize a heavy mineral concentrate of celestine originating from the Beni Mansour deposit in Algeria. The objective was to propose physical methods to improve the quality of the concentrate by maximizing the strontium (Sr) grade and minimizing the barium (Ba) content. Density modelling by QEMSCAN® software showed the potential to improve the quality of the celestine concentrate.</i>	

PAPERS OF GENERAL INTEREST

Assessment of errors in the transmission of the orientation and cartographic system from the surface to an underground mine	
L. Sanmiquel, M. Bascompta, and J.M. Rossell	139
<i>The accuracy of the transmission of orientation between the surface and underground workings was assessed using the two-shafts plumbing and gyroscope methods. The different sources of error that affect the measurements are thoroughly analysed. Mine ventilation was found to be one of the most important sources of error in the plumbing method. The paper outlines some measures to reduce the influence of ventilation and details a compensation method.</i>	

Identifying barriers to growth in mineral value chains	
H.J. Van Zyl, W.G. Bam, and J.D. Steenkamp	149
<i>This article describes the development of a framework that supports the identification of barriers to growth in mineral value chains. The resultant process was applied to the manganese value chain in South African, and 31 barriers to growth in this sector were identified. The results were validated by a panel of experts, and the feedback was used to improve the framework.</i>	

Kinetics of advanced oxidative leaching of pyrite in a potassium peroxy-disulphate solution	
J. Ma, Y. Tang, D.Q. Yang, and P. Pei	165
<i>This study investigates the leaching kinetics of gold-bearing pyrite in the potassium peroxydisulphate system and the potassium peroxydisulphate-ferrous sulphate combined system. The results provide a basis for effective leaching of gold from gold-bearing pyritic ores using advanced oxidative leaching.</i>	



Hheavy minerals is a small and often neglected field of mining and metallurgy. However, this industry produces some of the most important minerals and metals of the modern world. Where would we be without titanium for its multitude of uses, zirconium for its ultra-hard properties in zirconia, or the rare earth elements for their plethora of uses in modern technology?

The mining challenges of this industry are somewhat different to traditional hard-rock mining as the mines are almost exclusively surface operations. However, because of that, the environmental, social, and resource challenges of this type of mining have a character of their own. The economics of the industry can be rewarding, but because of the relatively low price of the intermediates the industry has to move large tonnages of material. The processing of mined minerals, although seemingly simple, has many nasty 'hookers' such as the effect of the surface properties of the minerals. The effect of atmospheric conditions on surface properties can have significant consequences regarding the recovery and grade of concentrates. In addition to the metallurgical challenges, the issue of radioactivity requires management. Although not at a level to cause any health issues, the levels are significant enough to attract attention from health and safety regulators. The challenges of the industry do not stop there as the end products of this sector often require high-cost and high-technology solutions. In no way can high-temperature chlorination in a gaseous atmosphere be considered straightforward. Similarly, the production of neodymium or samarium for high-powered magnets is not simple, a fact illustrated by the small number of facilities that operate this technology.

The International Heavy Minerals Conference series hosted by the SAIMM is an industry-driven initiative to allow sharing of ideas, technologies, and methods of handling the various challenges. The first conference was in 1997 and was held in Durban, South Africa. At this conference, which was organized by the Zululand and Western Cape branches of the SAIMM, there were 38 papers and over a 100 delegates. This was followed every second year by further conferences in the HMC series. The committees of the Institute encouraged sister organizations in other heavy-minerals-producing countries to participate, resulting conferences being held in Australia (2001), South Africa (2003), the USA (2005), South Africa (2007 and 2009), Australia (2011), India (2013), South Africa (2016), and finally this conference in South Africa in 2019.

At the most recent conference, held in Cape Town, there were 19 papers presented covering a wide range of topics including ore reserve evaluation, mining, minerals processing, pyrometallurgy, and mine closure. There were three keynote presentations given at the conference: *Learning from Kwale to build Toliara* by Colin Bwye, Executive Director at Base Resources; *Tronox - to infinity and beyond* by Willem van Niekerk, Senior Vice President at Tronox; and *Do heuristics influence the mineral sands mining landscape?* by Rob Hattingh, CEO at Sierra Rutile. The two-day conference was followed by a site visit to the Tronox Namakwa Sands Plant at Saldanha Bay.

The International Heavy Minerals series of conferences has become established as one of the main sources of collaboration for those in this industry. While not as large as some other mineral resource sectors, the diversity and complexity found in the heavy minerals industry stands on a par with any of the other resource sectors.

J.H. Selby

Chairman: 2019 HMC Organizing Committee

The beginning of February marks the annual Investing in African Mining Indaba Conference, which takes place in our beautiful Cape Town. This was the 26th event and remains Africa's largest mining investment event. It brings together investors, government, junior miners, mid-caps, and the world's largest companies – all under one roof.

I was privileged to attend the event this year, which was aptly themed 'growth and investment in the digitized mining economy'. The conference had a positive vibe given the number of attendees, estimated at over 7000. However, the theme did not capture another topic that was high on the agenda of many presentations and panel discussions to promote the growth of investment in mining, viz., sustainability and the topic of ESG (Environment, Social and Governance).

There was a heightened attention to ESG during 2019 and specifically the topic of climate change, owing to some severe weather conditions and natural disasters, such as the fires in Australia and floods in various parts of the world. ESG has shifted from periphery to the mainstream among the investment community. It is a primary filter for investment decision-making and selection of shares on the stock market. This is a significant shift in the mindset of investors and will result in material changes to the conduct of mining companies (and other industries) and allocation of capital investment.

It is therefore pleasing for me to highlight and compliment the SAMESG Committee for receiving the United Nations Intergovernmental Working Group of Experts on International Standards of Accounting and Reporting (ISAR) Honours Award on 30 October 2019. ISAR reviews developments in the field of international reporting and promotes best practices for corporate governance. Within the context of Agenda 2030, ISAR contributes to the realization of the Sustainable Development Goals through enhanced transparency and sustainability standards for companies. Now in its second year, the ISAR Honours 2019 attracted 33 entrants from around the world and SAMESG received the Award for an Outstanding National Initiative to Advance the Sustainable Development Goals. The SAMESG Committee, who were present to receive the award said: 'The development of the SAMESG guideline was seen as an imperative considering that resources companies listed on the Johannesburg Stock Exchange, at that time, were not subjected to a formalized standard for reporting on ESG matters and determining their impact on mineral project reserves, resources and valuations ... 'We believe that this guideline, when applied diligently, has the potential to significantly improve the quality of information made available to investors in and shareholders of mineral resources companies in respect of environmental, social and governance considerations.'¹

Hence, ESG is providing an opportunity for deeper alignment between shareholders and corporate leadership to share both on the upside and downside performance of the company arising from capital allocation decisions. Mining is a long-term investment with positively transformative qualities in terms of its impact on society, therefore the focus on the long term that is emerging through ESG is absolutely welcome. The individual ESG elements are integrated and represent an aggregate of the several individual and material indicators of a company's performance.

Consequently, the future of mining, not only coal mining, was topical (and frankly looks promising given this changing perspective). Given the emphasis on digitalization and ESG, with a focus on climate change, mining and its role in society was extensively discussed at the Indaba. Amazingly, the discussions were not all on the technical merits of the future of mining. The most spoken about issues included the 'future of work' in terms of the future profile of a 'mining employee' and the related skills, how mining will take place in terms of automation and remote mining, as well as the accountability to society that mining will conduct itself with². This latter issue is already evident in terms of the EY's top ten business risks facing mining and metals in 2020 (www.ey.com), where License to Operate (LTO) is the no. 1 risk for the second year in a row. The publication is an interesting read for emerging risk trends in the mining sector and I recommend it.

A high-level assessment of the top ten risks for 2020, compared to the previous year, is a clear indication of the changing nature of mining. Sustainability is the prevailing theme in terms of license to operate, employee wellbeing (future of workforce), productivity in terms of cost performance, technology and innovation, and return on investment. As the industry evolves, and it is doing so in a big way, so should we as the Institute in order to remain relevant and worthy to our members. Are we sufficiently grappling with these issues and evolving as an institution? Please share with me your thoughts at president@saimm.co.za



¹www.saimm.co.za

² I was a on an EY panel discussion on the topic of 'The Future of Mining'.

M.I. Mthenjane
President, SAIMM

Sign-off on Public Documents using SAIMM/GSSA membership

One of the requirements for Competent Persons is that they need to be registered with or be a member of one of a specified list of statutory or professional bodies (or RPOs). The following note is of specific interest for members of the GSSA and/or SAIMM who wish to use such membership to sign off on Public Documents (Competent/Qualified Persons Reports, Competent/Qualified Persons Valuation Reports, Annual Integrated Reports, etc). *Please note that this does not apply if you are also registered with one of the statutory bodies (SACNASP, ECSA or SAGC) or IMSSA and are using that registration.*

No member of the GSSA or SAIMM may be signing off on a publicly released Competent Person Report or Competent Valuators Report using their GSSA/SAIMM membership as the accreditation body, without first going through the peer review process.

Since 2017, the by-laws of both the GSSA and SAIMM require peer review of Competent Persons/Valuators (who are **using their GSSA/SAIMM membership as the accreditation body**). This process is to be followed for each public, newly released Public Report.

Members of the GSSA or SAIMM, who wish to sign off on a specific public report must submit themselves to this peer review process. The purpose of the process is to confirm that a person wishing to sign off as a Competent/Qualified Person/Valuator satisfies all the requirements of a Competent/Qualified Person/Valuator, and that his/her professional status has been validated by his/her Professional Association – it does not imply competence or proficiency and the professional bodies do not take responsibility for the quality of reporting by such persons.

Please note that this “peer review process” is not specific to the SAMCODES, the SSC or the JSE, or in fact, to any other Code or Stock Exchange. It is a requirement from both the SAIMM and the GSSA (the professional bodies) that all CP’s using their professional membership to sign-off public reports go through this peer review process. In the first instance, this is specifically applicable to authors signing off on SAMCODES documents to the JSE. However, by extension, this is applicable to all publicly released documents. It has nothing to do with the Code or the reporting jurisdiction. If you are using the name of the SAIMM or the GSSA to sign off on a public report, then you need to have “clearance” from that body to do so. This process is primarily to protect the professional bodies from abuse, but it also serves to assure other jurisdictions that membership with one of these professional bodies is as valuable as registration with a statutory body. The process is standardised for all reporting codes/jurisdictions.

The peer review “process” is not a big deal – the applicant simply fills out the form and sends it to Sam at the SAIMM. The members of the subcommittee (all Fellows of SAIMM and GSSA) look at whether the academic qualifications and experience of the applicant would qualify him/her as a CP and then approve the members request. The whole process takes 3-5 working days. There is no review of any documents/CPR, etc involved. No-one declares another to be competent (or not); no one goes onto any “List” of Competent Persons – it is simply an acknowledgement by the professional body that, based on the applicants declared qualifications, he/she should be sufficiently knowledgeable and experienced to report on the mineralization type referred to in the specified Public Report.

Two different application documents are available on the website:

SAIMM-GSSA-Application for peer review_SAMCODES

SAIMM-GSSA-Application for peer review_OTHER CODES

Click to download the applicable form (or see the Registrations page) and submit it to sam@saimm.co.za timeously (the process usually takes five (5) working days from receipt of application).

The forms may also be requested directly from sam@saimm.co.za



SAIMM
THE SOUTHERN AFRICAN INSTITUTE
OF MINING AND METALLURGY
www.saimm.co.za



GSSA
Geological Society of South Africa
www.gssa.org.za



Design of sidewall lining/cooling systems for AC or DC ilmenite smelting furnaces

H. Joubert¹ and H. Kotzé²

Affiliation:

¹Tenova Pyromet, Midrand, South Africa.

²Consensi Consulting, Mtunzini, South Africa.

Correspondence to:

H. Joubert

Email:

hugo.joubert@tenova.com

Dates:

Received: 13 Aug. 2019

Revised: 13 Dec 2019

Accepted: 18 Dec. 2019

Published: February 2020

How to cite:

Joubert, H. and Kotzé, H.
Design of sidewall lining/cooling systems for AC or DC ilmenite smelting furnaces.
The Southern African Institute of Mining and Metallurgy

DOI ID:
<http://dx.doi.org/10.17159/2411-9717/878/2020>

This paper was first presented at *The Eleventh International Heavy Minerals Conference*, 5–6 August 2019, The Vineyard, Cape Town, South Africa.

Synopsis

Ilmenite smelting is well established using both direct current and alternating current furnaces. Regardless of the furnace type, the slag produced is aggressive towards the sidewall lining. The formation of a stable slag freeze lining is essential to arrest lining wear and ensure an acceptable furnace campaign life. The sidewall lining can be severely damaged within a short period of time under upset conditions and without a stable freeze lining in place. The sidewall lining/cooling system adjacent to the furnace slag bath must be designed to ensure a stable freeze lining and prevent lining wear under normal as well as upset conditions. In this paper we explore the effectiveness of high-intensity copper coolers compared to the more traditional magnesia working lining combined with an externally cooled furnace shell. An increase in furnace heat losses has been raised as a concern for intensively cooled sidewalls. The estimated furnace heat losses are compared for the different lining/cooling system designs.

Keywords

ilmenite smelting, AC furnace, DC furnace, sidewall cooling, freeze lining.

Introduction

Ilmenite is smelted in both direct current (DC) and alternating current (AC) furnaces to produce titania-rich slag and pig iron (Kotzé, Bessinger, and Beukes, 2006; Gous, 2006; Williams and Steenkamp, 2006). The slag is the main product and is primarily used as a feedstock for the production of TiO₂ pigment (Kahn, 1984).

As described by MacPherson (1982), the slag produced in ilmenite smelting is extremely aggressive towards the furnace lining and no known refractory material can withstand the slag attack. The formation of a frozen slag layer or freeze lining is essential to protect the furnace lining and maintain sidewall integrity. The slag superheat must be controlled to prevent the rapid destruction of the freeze lining, and subsequently the refractory lining. Pistorius (2004) estimated that a 130 mm thick freeze lining can be worn away within 15 minutes if the feed to the furnace is terminated while the power input is maintained. In contrast, it will take much longer to re-form the freeze lining. Part of the reason for the aggressive nature of ilmenite smelting slag is its low viscosity at temperatures above its liquidus temperature, resulting in a remarkably fluid slag with a high convective power (Handfield and Charette, 1971).

A typical ilmenite smelting furnace working lining consists of high-quality magnesia refractory bricks. Magnesia bricks are used owing to their resistance at high operating temperatures and relatively high thermal conductivity (assumed 5.9 W/mK), which helps establish a freeze lining. Another reason for maintaining the freeze lining is to avoid potential slag contamination by magnesia (MgO) due to refractory wear (Kotzé, Bessinger, and Beukes, 2006).

In this paper, we explore the use of an alternative lining/cooling system which will maintain a competent freeze lining in ilmenite smelting furnaces. A freeze lining is considered competent when it is thick enough to maintain structural stability, typically at least 20 mm thick, and this thickness is maintained across all operating conditions. Key criteria considered in evaluating the furnace lining/cooling system include its ability to form and maintain a competent freeze lining under normal as well as upset operating conditions, prevent slag contamination, reduce metal penetration and wear in the critical slag-metal tidal zone, improve monitoring of the freeze lining and slag bath conditions, and limit heat losses from the furnace. Coetzee *et al.* (2007) proposed the use of a carbon-based lining to achieve a more stable freeze lining in an ilmenite smelting furnace. We propose the use of intensive

Design of sidewall lining/cooling systems for AC or DC ilmenite smelting furnaces

sidewall copper cooling as an alternative. The proposed lining/cooling system design is evaluated considering the key criteria listed above. A comparison is made with a typical lining design consisting of high-quality magnesia bricks in the working lining.

Proposed sidewall lining/cooling system design

The proposed lining/cooling system design consists of high-intensity copper coolers installed in the sidewall adjacent to the slag bath. The proposed arrangement is shown in Figure 1. It includes Tenova's high-intensity MAXICOOL® sidewall cooler designed to operate at hot face fluxes of up to 500 kW/m². The height and location of the high-intensity cooler are determined by evaluating the expected maximum metal and slag bath levels in the furnace. Safety margins for both maximum slag bath level and metal bath level are considered. For the safety margin between the metal bath level and the bottom of the cooler, a safety margin equal to at least 24 hours of production without tapping above the normal maximum metal level is considered appropriate. This is to prevent superheated molten metal from contacting and damaging the copper cooling element. It is important to note that ilmenite smelting furnaces, and in particular the furnace arrangement considered, are stationary and do not tilt.

The MAXICOOL® cooler's cast copper body consists of a hot face star pattern to retain frozen slag more securely and cast-in Monel piping for the cooling water. Two cast-in cooling circuits run in parallel throughout the cooler. The cooler is designed to operate safely with only one circuit in the event that cooling water supply is lost to one of the circuits. All cooling water connections remain external to the furnace shell. A steel frame incorporating special friction joints, and a single hold-down spring mechanism per cooler connects the cooler to the furnace shell through four locating bolts. The hold-down mechanism ensures sufficient pressure is maintained on the lower sidewall lining to prevent metal penetration through horizontal joints, even during furnace cool-down periods. Each cooler is fitted with cast-in thermocouples extending past the hot face of the cast-in cooling pipes. For furnace start-up a sacrificial monolithic refractory lining is cast on the hot face of each cooler. Vertical lap joints between adjacent coolers ensure that there is no through path for superheated slag.

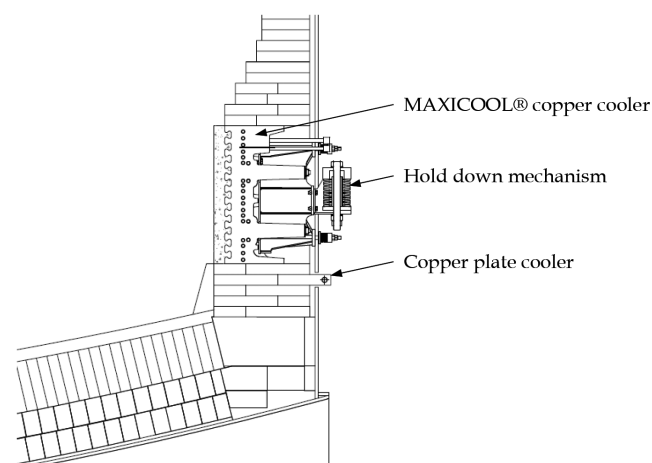


Figure 1 – Typical high-intensity sidewall cooling arrangement proposed for an ilmenite smelting furnace

As shown in Figure 1, a single row of copper plate coolers with cooling water channels external to the furnace shell is incorporated in the lining below the high-intensity cooler. This is to provide deep cooling in the critical metal-slag tidal zone while eliminating the risk of metal making contact with cooling water. The copper plate coolers are fitted with thermocouples extending close to the cooler hot face.

Sidewall heat load and evaluation

The evaluation of the lining/cooling system design, with and without intensive sidewall cooling, depends primarily on the slag bath superheat and the convective heat transfer between the slag bath and the sidewall. In turn, both parameters depend on the operating conditions and the slag composition. The operating conditions, in particular the ilmenite feed to input power ratio (IPR), determine the bulk slag temperature that influences the slag superheat. The slag composition affects the slag properties that determine the bath to sidewall heat transfer coefficient, including the molten slag thermal conductivity, viscosity, expansion coefficient, liquidus and solidus temperatures, and in turn the slag freezing temperature. The slag properties, in particular the slag viscosity, are a function of the IPR as well as the selected feeding regime. The feeding regime is primarily determined by the reductant (normally anthracite) to ilmenite feed ratio (AIR) (Pistorius, 1999). Depending on the furnace design, size, and operating mode, the bath to sidewall heat transfer coefficient can be affected by forced convection due to phenomena such as arc thrust, as is likely the case for AC furnaces (Timm, 2006; Stenkvist, 1984). In addition, the slag composition affects the thermal conductivity of the frozen slag.

In this paper, natural convection next to the sidewall is considered for the calculation of the heat transfer coefficient between the bath and the sidewall hot face. The Nusselt number used in the calculation of the heat transfer coefficient is based on an empirical relationship developed for slag bath furnaces (Kang, 1991; Joubert, 2000). The effect of arc thrust on the bath flow patterns and the convective heat transfer adjacent to the furnace sidewall is not considered in this paper. If arc thrust is present, it is expected to enhance the convective heat transfer adjacent to the sidewall.

Operating conditions and slag properties

Table I lists the slag bath operating conditions and slag properties considered in the calculation of the bath to sidewall convective heat transfer coefficient. A slag with an equivalent FeO content of 12% by mass is considered. The slag liquidus temperature is calculated based on work done separately by Kotzé (2019) considering equivalent FeO content. The slag bath temperature is considered to be 60°C above the slag liquidus temperature. The slag solidus temperature is calculated using an empirical relationship considering equivalent FeO content (Kotzé and Pistorius, 2010). Typically, the slag freezing temperature is calculated as the average between the liquidus and solidus slag temperatures (Joubert and McDougall, 2019). Considering that the viscosity increases rapidly around the liquidus temperature for ilmenite furnace slags (Handfield and Charette, 1971; Hu *et al.*, 2018), the freezing temperature is assumed to be closer to the liquidus temperature and is calculated as the solidus temperature plus 80% of the difference between the liquidus and solidus temperatures. The slag superheat is calculated as the difference between the slag bath and the slag freezing temperatures.

Design of sidewall lining/cooling systems for AC or DC ilmenite smelting furnaces

The dynamic viscosity for typical ilmenite smelting slags has been measured and is reported to be 0.03 kg/ms (Handsfield and Charette, 1971) and 0.06 kg/ms (Hu *et al.*, 2018). In both studies, the viscosity was found to remain remarkably constant at temperatures above the liquidus temperature. However, both studies considered a fully molten slag without any iron droplets, crystallization, or other solid inclusions. The presence of these solid inclusions is what gives rise to the slag foaming typically encountered in ilmenite smelters and it is therefore considered that the effective viscosity will be higher than for fully molten slag (Pistorius and Coetzee, 2003; Roscoe, 1952). Viscosity measurements of slag with inclusions are not possible using the typical measurement equipment, and no such data could be found. Considering this, a range of viscosities is used in the calculations with an effective viscosity of 0.7 kg/ms assumed for the typical case (see Table I).

Dingwell (1991) reported the density of pure liquid TiO_2 to range between 3270 and 3300 kg/m^3 for the range of slag bath temperatures considered. Based on separate work by Kotzé (2019) on TiO_2 - Ti_2O_3 -FeO melts, it was decided to use a density of 3850 kg/m^3 for the purpose of calculating the heat transfer coefficient.

The thermal conductivity of the molten slag affects the slag to sidewall heat transfer coefficient through the Prandtl number as well as directly in the calculation of the coefficient from the Nusselt number. A thermal conductivity value of 1 W/mK was proposed by Pistorius (2004) for frozen slag and by Zietsman and Pistorius (2004) for molten slag. As the thermal conductivity of the molten slag has a significant influence on the calculated heat transfer coefficient, a range is proposed in Table I with the typical value equal to 1 W/mK. The maximum value of 5 W/mK is based on the measured thermal conductivity of frozen slag at 1400°C by Heimo (2018). This value is considered as an extreme.

A molten slag volumetric expansion coefficient of $1 \times 10^{-4} \text{ m}^3/\text{m}^3\text{K}$ is used to calculate the Grashof number (Kang, 1991). The specific heat of the slag bath is calculated using an empirical relationship based on equivalent FeO (Kotzé and Pistorius, 2010). Finally, the thermal conductivity of the frozen slag layer is assumed to be 3 W/mK. The effect of the frozen slag conductivity is limited to determining the slag freeze lining thickness, if formed, and the conductivity has little influence on the sidewall hot face temperature and heat flux (Joubert and Mc Dougall, 2019).

The slag bath temperature, freezing temperature, and slag superheat for the base case are used in the heat transfer calculations. The heat transfer coefficient is calculated across the range of slag viscosities and molten slag thermal conductivities to evaluate its sensitivity.

Calculation results

The results of the calculations are shown in Figure 2. The calculations and results are limited to the sidewall slag bath zone. The results include the calculated heat transfer coefficient, the equilibrium working lining thickness for a lining based on a typical magnesia refractory lining design with external shell cooling, and the freeze lining thickness if intensive sidewall cooling is employed. For the typical refractory lining design, the equilibrium working lining thickness represents the worn lining thickness at which the hot face temperature will be equal to the slag freezing temperature. Further wear of the lining will occur only if the bath operating conditions or slag properties change for the worse.

In Figure 2a the results are plotted against the range of slag bath dynamic viscosity values listed in Table I. The thermal conductivity of the molten slag bath is maintained at the base case value of 1 W/mK. The bath to sidewall heat transfer coefficient decreases with increasing viscosity, while the equilibrium working lining thickness for the typical lining design, as well as the freeze lining thickness for the intensive sidewall cooling design, increase. The base case values are labelled on the graph in Figure 2a for reference.

In Figure 2b the results are plotted against the range of molten slag thermal conductivity values listed in Table I. The slag bath viscosity is kept constant at the base case value of 0.7 kg/ms. The bath to sidewall heat transfer coefficient increases with increasing bath thermal conductivity. The equilibrium working lining thickness for the typical lining design, as well as the freeze lining thickness for the intensively cooled design, decrease with increasing bath thermal conductivity. The base case values are labelled on the graph in Figure 2b for reference.

The first observation from the results is that for the base case, 0.7 kg/ms viscosity and 1 W/mK molten slag thermal conductivity, the equilibrium working lining thickness for the typical refractory lining design is calculated to be 319 mm. This is at the limit of maintaining a stable working lining and any adverse deviations in operating conditions and slag properties

Table I

Slag bath operating conditions and slag properties used in heat transfer coefficient calculations

Temperatures:	Units	12% equivalent FeO (by mass)		
		Min.	Base case	Max.
Liquidus temperature	°C		1610	
Bath temperature	°C		1670	
Solidus temperature	°C		1450	
Freezing temperature	°C		1563	
Superheat	°C		107	
Slag properties:	Units	Min.	Base case	Max.
Dynamic viscosity	kg/ms	0.03	0.7	1
Density	kg/m^3	3850	3850	3850
Thermal conductivity (molten)	W/mK	0.5	1	5
Expansion coefficient	1/K	0.0001	0.0001	0.0001
Specific heat	J/kgK	1012	1012	1012
Thermal conductivity (frozen)	W/mK	3	3	3

Design of sidewall lining/cooling systems for AC or DC ilmenite smelting furnaces

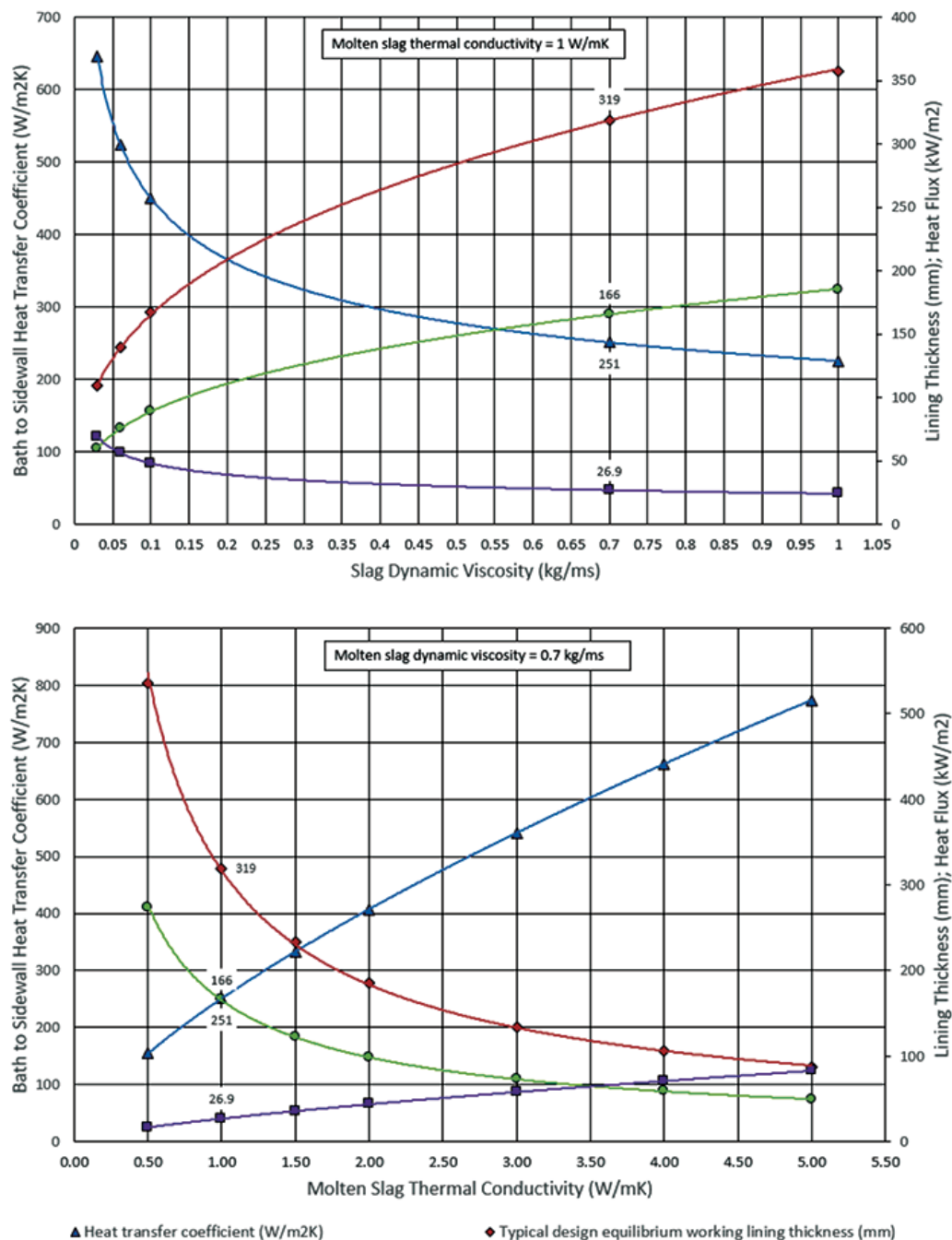


Figure 2—Heat transfer coefficient, working lining equilibrium thickness (typical lining design with external shell cooling), freeze lining thickness (intensive sidewall cooling), and sidewall hot face heat flux plotted against (a) bath dynamic viscosity and (b) thermal conductivity

could result in lining failure. For the same base case the freeze lining thickness on the hot face of the intensive sidewall cooling system is calculated to be 166 mm. This is considered a very competent freeze lining thickness.

The second observation is that for the minimum viscosity of 0.03 kg/ms, as measured for fully liquid slag by Handsfield and Charette (1971), the equilibrium lining thickness is calculated to be 109 mm (Figure 2a), which is considered unsustainable. For the same load case the freeze lining thickness developed on the hot face of the intensive sidewall cooling will reach equilibrium at 60 mm, which is a competent freeze lining thickness. As noted previously, freeze lining thickness is directly proportional to the thermal conductivity of the frozen slag (Joubert and Mc Dougall,

2019). If the thermal conductivity is assumed to increase from 3 W/mK to 5 W/mK considering the operating temperatures (Heimo, 2018), the freeze lining thickness will increase to approximately 101 mm.

A parameter that has not been varied in the calculations is the slag superheat. As noted by MacPherson (1982), the slag cannot be allowed to attain significant superheat as this will result in the rapid destruction of the freeze lining and subsequent wear of the refractory lining. Considering the base case viscosity and thermal conductivity, and lowering the superheat from 60°C to 30°C above the slag liquidus, the equilibrium lining thickness for the typical refractory design will increase from 319 mm to 507 mm. Increasing the superheat to 90°C results in a

Design of sidewall lining/cooling systems for AC or DC ilmenite smelting furnaces

reduced equilibrium lining thickness of 224 mm. The calculation results confirm that the equilibrium lining thickness of a typical refractory lining design is sensitive to the slag bath superheat, assuming all other parameters remain unchanged. If the same changes in the slag superheat are applied to the calculations for the intensively cooled sidewall design, the calculated equilibrium freeze lining thickness varies between 260 mm and 119 mm compared to the base case 166 mm. In all cases a competent freeze lining is maintained on the hot face of the lining/cooling system.

As noted, the calculations are based on natural convection between the bath and the sidewall hot face. For AC furnaces the heat transfer coefficient may be higher considering the forced convection effect that is likely to be induced by the arc thrust. This differentiates AC from DC furnaces, where arc thrust is not a significant contributor.

Lining/cooling system integrity

The campaign life of a furnace lining is determined by extreme or upset conditions, and not by the normal operating conditions (Joubert, 1997). Severe lining wear can occur during a short period of upset conditions. This is true for all furnace operations, and in particular for ilmenite smelting where the typical refractory lining is subjected to high bath temperatures and aggressive chemical attack (Garbers-Craig and Pistorius, 2006).

The extreme case listed in Table II is used to evaluate the lining/cooling system integrity. The extreme case considers the base case slag composition combined with the minimum slag viscosity and the maximum molten slag thermal conductivity. The bath operating temperature is increased to 1750°C, resulting in a bath to freezing temperature superheat of 187°C.

Applying the extreme condition to the typical refractory lining design for ilmenite furnaces, it is calculated that the working lining will be worn away completely. In fact, equilibrium is calculated to be achieved halfway through the expansion layer typically installed between the refractory lining and the externally cooled furnace steel shell.

For the intensively cooled sidewall design, the extreme condition results in an average equilibrium freeze lining thickness of 4 mm on the hot face of the copper cooler. The

equilibrium heat flux under extreme conditions is calculated to be 441 kW/m². The extreme case is not considered a viable long-term operating condition as the heat losses will be too high. The purpose of considering the extreme case is to evaluate the lining integrity under extreme conditions that may occur for short periods during the furnace campaign. It is calculated that the typical refractory lining design will not withstand such extreme conditions, and exposure for only short periods of time will severely damage the lining.

To evaluate the integrity of the intensive sidewall cooler considering the extreme case, a more detailed 3D FEA model is used. The model is shown in Figure 3. The model represents a symmetrical MAXICOOL® cooler section. The extreme case bath temperature of 1750°C is applied to the model hot face through the calculated bath to sidewall heat transfer coefficient of 2356 W/m²K. A transient thermal analysis is performed with nonlinear properties for the slag bath to calculate the freeze lining formation on the hot face. The results are presented in Figure 4.

The freeze lining thickness stabilizes at approximately 8 mm in front of the slag-retaining copper stars' hot face, and at a thickness less than or behind the hot face of the copper stars in the pockets between the copper stars. This result compares well with the calculated average equilibrium freeze lining thickness of 4 mm. Under these extreme conditions, the maximum copper temperature is calculated to be 353°C, which is below the 400°C limit Tenova Pyromet aims for during the design of copper sidewall coolers to ensure structural integrity of the cooler is maintained.

The main observation from these results is that the intensively cooled sidewall design will maintain its integrity under these extreme operating conditions. A thin freeze layer will be maintained on the copper cooler hot face and the maximum copper temperatures are below the design limit to ensure structural integrity is maintained. The typical refractory lining design used for ilmenite furnaces will not be able to maintain its integrity under these extreme conditions.

Slag-metal tidal zone

For any furnace the sidewall slag-metal tidal zone is one of the most important and difficult areas to design. The lining/cooling system hot face is exposed to both metal and slag. As such the lining is exposed to the more aggressive wear mechanisms associated with the slag, while the use of intensive sidewall cooling is not advised as it may come in contact with molten metal, which can lead to failure.

For the purpose of evaluating the slag-metal tidal zone the base case slag composition, slag viscosity (0.7 kg/ms), and

Temperatures:	Units	12% equivalent FeO (By mass)
Liquidus temperature	°C	1610
Bath temperature	°C	1750
Solidus temperature	°C	1450
Freezing temperature	°C	1563
Superheat	°C	187
Slag properties:	Units	Extreme case
Dynamic viscosity	kg/ms	0.03
Density	kg/m ³	3850
Thermal conductivity (molten)	W/mK	5
Expansion coefficient	1/K	0.0001
Specific heat	J/kgK	1012
Thermal conductivity (frozen)	W/mK	3
Calculated bath to sidewall heat transfer coefficient	W/m ² K	2356

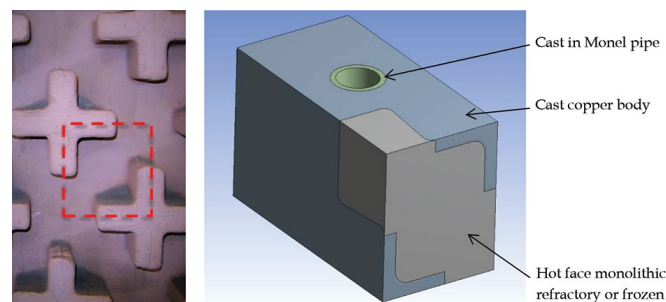


Figure 3—MAXICOOL® high-intensity sidewall cooler model

Design of sidewall lining/cooling systems for AC or DC ilmenite smelting furnaces

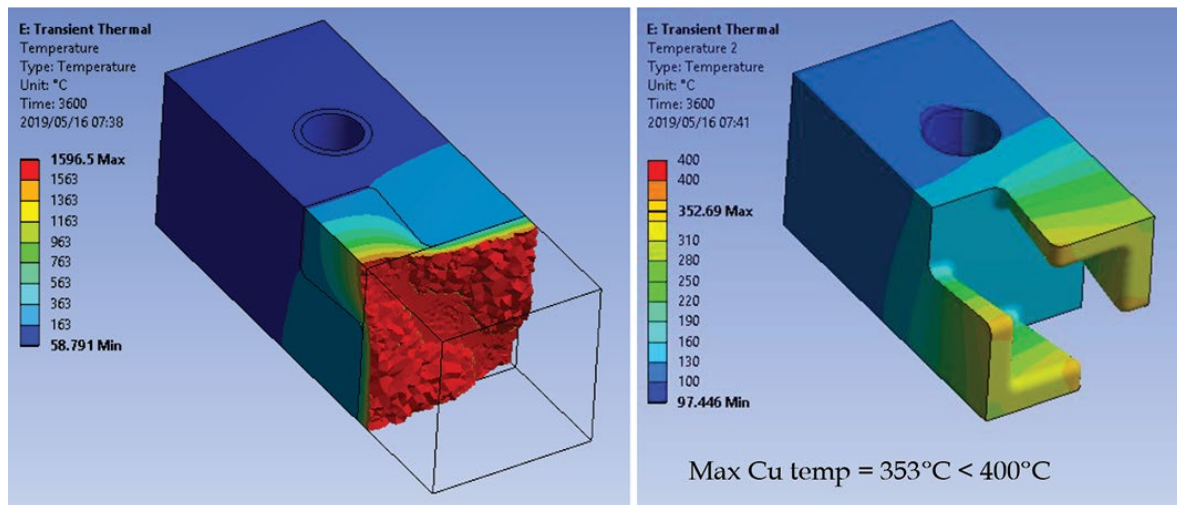


Figure 4—MAXICOOL® cooler FEA modelling results under extreme conditions, showing equilibrium freeze lining thickness (left) and resulting copper temperatures (right)

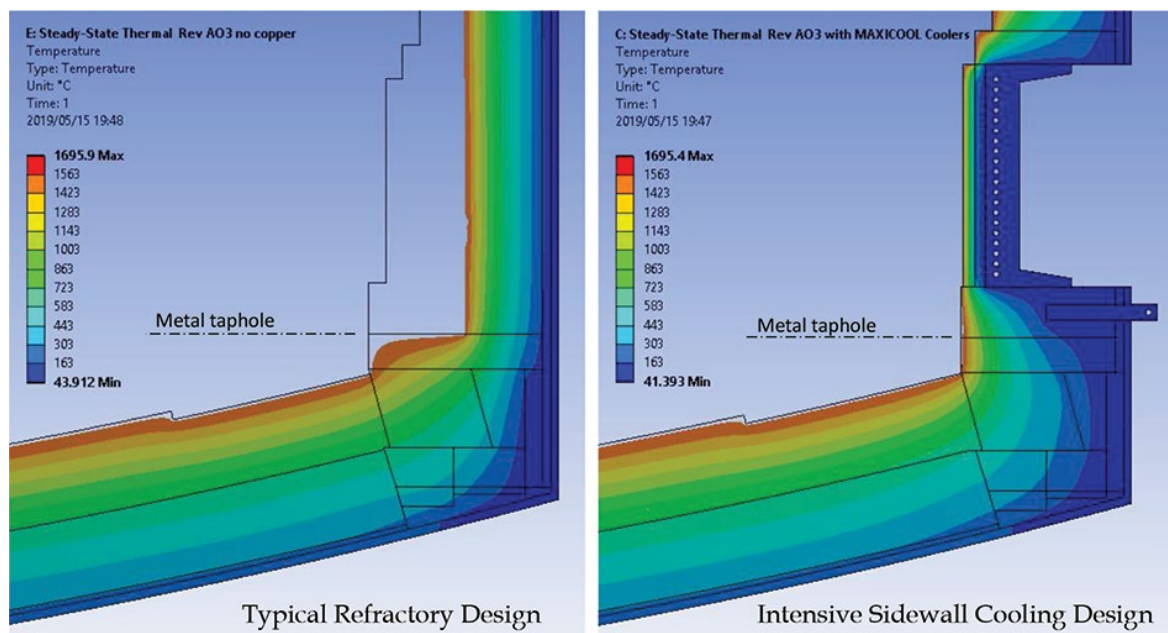


Figure 5—Lining wear in the slag-metal tidal zone for typical refractory design and intensive sidewall cooling design

molten slag thermal conductivity (1 W/mK) are considered. As for the extreme case, a bath operating temperature of 1750°C is considered, resulting in a bath to freezing temperature superheat of 187°C. A 2D axisymmetric, thermal steady-state FEA model with nonlinear material properties is employed. For the working lining the equilibrium lining thickness is calculated considering a slag freezing temperature of 1563°C as for the base case slag composition in Table I. For the purpose of the evaluation it is assumed that all metal is tapped until slag appears. In other words, the lower sidewall hot face is exposed to the slag bath from the metal tap-hole level upwards. The results for the typical refractory lining design and the high-intensity sidewall cooling design are shown in Figure 5.

For the typical refractory lining design, the extensive working lining wear profile will extend down to the metal tap-hole level. For the intensive sidewall cooling design, the working lining wear

below the MAXICOOL® cooler will be minimal, with only slight wear shown on the hot face directly above the metal tap-hole. This is due to the cooling effect from the MAXICOOL® cooler above and the copper plate cooler behind the slag-metal tidal zone, ensuring the equilibrium lining thickness is close to the original lining thickness.

The main observation is that the intensive sidewall cooling design will better maintain the sidewall integrity adjacent to the slag bath, as well as the working lining integrity in the critical slag-metal tidal zone. In addition, the spring-loaded hold-down mechanism will help prevent metal penetration into the lower sidewall lining. By maintaining pressure on the lower sidewall, it prevents horizontal gaps from opening up due to contraction of the refractory bricks during cool-down periods. This will further enhance the working lining integrity in the slag-metal tidal zone. Even though the modelled area does not include the actual

Design of sidewall lining/cooling systems for AC or DC ilmenite smelting furnaces

metal tap-hole, the intensive sidewall cooling design will be advantageous in maintaining the integrity of the metal tap-hole area in the long run.

Heat losses

Under steady-state conditions the heat flux, and therefore the heat loss, through the slag sidewall working lining will be the same for the typical refractory lining design and the proposed high-intensity sidewall cooling design. As per Equation [1], once steady state is reached, either due to refractory wear up to the point where the hot face temperature is equal to the slag freezing temperature or when a stable freeze lining is formed, the heat flux is a function of the bath temperature, the slag freezing temperature, and the heat transfer coefficient between the bath and the sidewall hot face. As such, under steady-state conditions, the slag sidewall heat losses will be a function of the operating conditions and slag chemistry, or physicochemical properties, and not a function of the lining/cooling system design.

$$q_{\text{sidewall}} = h_{\text{bath}}(T_{\text{bath}} - T_{\text{freeze}}) \quad [1]$$

Overall heat losses will, however, be higher for the high-intensity sidewall cooling design due to the exposed cooler area above the slag bath. The height of this area depends on the safety margin allowed for and the actual operating bath level. Typically, a design safety margin of approximately 300 mm is included above the maximum expected bath level. The additional heat losses are limited and expected to be in the order of 5% of the overall furnace heat losses.

The initial heat losses until equilibrium is reached will be higher for the intensively cooled sidewall design. However, the heat losses will change less over the campaign life of the furnace as there is no significant lining wear adjacent to the slag bath.

Under extreme conditions the heat losses will increase more rapidly for the intensively cooled sidewall design. This is desirable for two reasons. Firstly, the higher heat removal rate is required to re-establish steady state, maintain the freeze lining, and ensure the sidewall integrity under extreme conditions. Secondly, the rapid increase in heat losses will assist in the more

responsive monitoring of the bath conditions under extreme conditions, as described in the next section.

Monitoring

Apart from protecting the furnace lining, it is important to maintain a stable freeze lining on the sidewall of ilmenite furnaces as it forms a critical part of the overall bath smelting process as well as the process control (Pistorius, 1999, 2004). Monitoring of the freeze lining condition and any upset bath conditions are therefore critical in ilmenite smelting. The most obvious and widely used monitoring method is by thermocouples installed in the sidewall refractory lining. The depth of installation is limited by the maximum allowable operating temperature of approximately 1200°C for the typically used Type K thermocouples. As a consequence, the thermocouples are not responsive to changes in bath conditions and freeze lining thickness due to the thermal inertia or specific heat of the refractory lining between the thermocouple and the lining hot face (Zietsman, 2004).

The intensively cooled sidewall design and the use of copper coolers allow more rapid monitoring of changes in bath conditions and the freeze lining thickness. Thermocouples are installed close to the hot face of the copper cooling elements, reducing the distance to the freeze lining. In addition, the copper between the thermocouple and the freeze lining has a lower specific heat and a significantly higher thermal conductivity compared to magnesia refractory material. As a result, thermocouple temperature measurements will respond more rapidly to changes in the bath conditions and freeze lining thickness.

As an example, on a slag cleaning furnace operating at bath temperatures in excess of 1600°C and equipped with high-intensity MAXICOOL® sidewall coolers, an upset condition was experienced adjacent to the sidewall (Joubert *et al.*, 2005). During the event, a sudden rise or jump in the copper cooler temperatures occurred on one of the coolers, eventually triggering the high-level alarms (see Figure 6). The cooling water outlet temperatures increased as well. On inspection it was noticed that the freeze layer that formed on the hot face of the cooler had

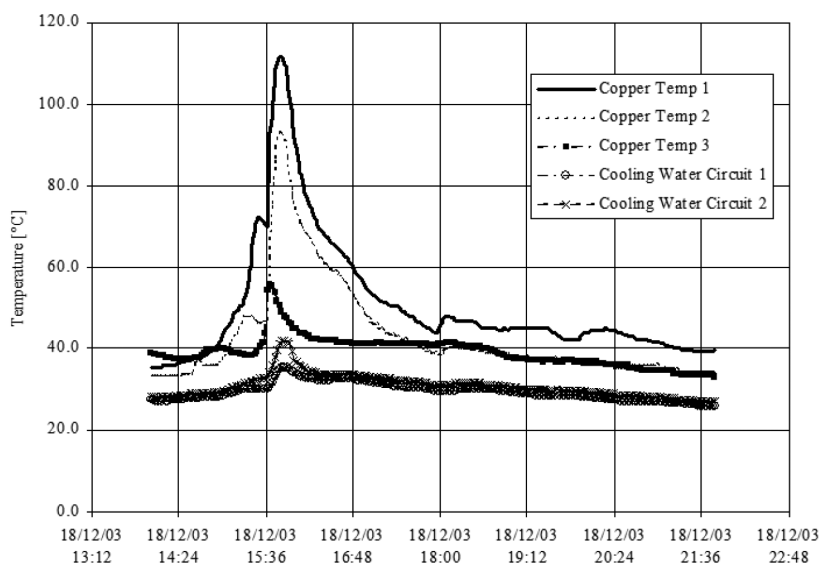


Figure 6—MAXICOOL® sidewall cooler temperature trends during freeze lining loss (Joubert *et al.*, 2005)

Design of sidewall lining/cooling systems for AC or DC ilmenite smelting furnaces

collapsed. The copper star pattern on the hot face of the cooler was visible through an inspection port. Thermocouples were installed on three levels inside the cooler body. The thermocouple that responded first and showed the highest increase in temperature was the closest to the location of the collapsed freeze layer. The other thermocouples responded as well, but slower and with a lower temperature increase. The furnace was kept operating and within approximately 3 hours the freeze layer re-formed and full equilibrium was re-established.

The main observation here is that the number and location of thermocouples in the copper coolers can be selected based on the expected operating bath levels to monitor local conditions and detect events.

Conclusions

The campaign life of an ilmenite smelting furnace lining, and consequently the furnace campaign life, is not determined by the normal operating conditions, but by the extreme operating conditions. For this reason, among others, the aim is to form and maintain a slag freeze lining on the sidewall hot face. An intensively cooled sidewall design will help to form and maintain a freeze lining, ensuring sidewall and furnace integrity even under extreme operating conditions. In addition, the high-intensity cooling system hold-down mechanism will help to prevent metal penetration in the lower sidewall working lining.

Once equilibrium is reached and a freeze lining is formed on the lining hot face, the heat losses are a function of process parameters such as slag superheat, viscosity, and conductivity, and not of the cooling system design or cooling medium temperature.

A high-intensity cooling system will allow more responsive monitoring of the freeze lining condition and thickness. Upset conditions and bath events will be more rapidly detected.

An intensively cooled sidewall design will reduce the sensitivity of the freeze lining and sidewall integrity to changing operating and process conditions. This will allow operators to focus more on optimizing the process to achieve the required throughput and product quality.

References

- COETZEE, C., LAMONT, P.H., BESSINGER, D., RABE, J., ZIETSMAN, J., and MULLER, J. 2007. Application of UCAR® Chill Kote™ lining to ilmenite smelting. *Proceedings of the Eleventh International Ferroalloys Conference (Infacon XI)*, New Delhi, India. Indian Ferro Alloy Producers Association. pp. 837–846.
- GARBERS-CRAIG, A.M. and PISTORIUS, P.C. 2006. Slag-refractory interactions during the smelting of ilmenite. *South African Journal of Science*, vol. 102, no. 11. pp. 575–580.
- GOUS, M. 2006. An overview of the Namakwa Sands ilmenite smelting operations. *Journal of the Southern African Institute of Mining and Metallurgy*, vol. 106, no. 6. pp. 379–384.
- HANDFIELD, G. and CHARETTE, G.G. 1971. Viscosity and structure of industrial high TiO₂ slags. *Canadian Metallurgical Quarterly*, vol. 10, no. 3. pp. 235–243.
- HEIMO, J. 2018. Thermal conductivity of titanium slags. Master's thesis, Aalto University, Helsinki.
- HU, K., LV, X., LI, S., LV, W., SONG, B., and HAN, K. 2018. Viscosity of TiO₂-FeO-Ti₂O₃-SiO₂-MgO-CaO-Al₂O₃ for high-titania slag smelting process. *Metallurgical and Materials Transactions B*, vol. 49, no. 4. pp. 1963–1973.
- JOUBERT, H. 1997. Analysis of blast furnace lining/cooling systems using computational fluid dynamics. Master's thesis, University of Johannesburg.
- JOUBERT, H. 2000. Designing for slag freeze linings on furnace sidewalls—an engineering perspective. *Proceedings of the Sixth International Conference on Molten Slags, Fluxes and Salts*, Stockholm, Sweden and Helsinki, Finland. Royal Institute of Technology, Stockholm. pp. 1–11.
- JOUBERT, H., NOURSE, R.B., MASTERS, B., and HUNDERMARK, R. 2005. Copper cooling design, installation and operational results for the slag cleaning furnace at Waterval Smelter, Rustenburg Platinum, South Africa. *COM2005, Proceedings of the 44th Conference of Metallurgists, International Symposium on Nickel and Cobalt Production*. Canadian Institute of Mining, Metallurgy and Petroleum, Montreal. pp. 19–35.
- JOUBERT, H. and Mc DOUGALL, I. 2019. Designing furnace lining/cooling systems to operate with a competent freeze lining. *Proceedings of the 148th Annual Meeting & Exhibition of TMS: Supplemental Proceedings*. Springer, Cham. pp. 1181–1195.
- KAHN, J.A. 1984. Non-rutile feedstocks for the production of titanium. *Journal of Metals*, vol. 36, no. 7. pp. 33–38.
- KANG, S. 1991. A model study of heat transfer and fluid flow in slag-cleaning furnaces. PhD thesis, University of Missouri-Rolla, MO.
- KOTZÉ, H. 2019. Literature review on the physiochemical properties of high TiO₂ slags. *Proceedings of Heavy Minerals 2019*, Cape Town, 5–7 August. Southern African Institute of Mining and Metallurgy, Johannesburg [in press].
- KOTZÉ, H., BESSINGER, D., and BEUKES, J. 2006. Ilmenite smelting at Ticon SA. *Journal of the Southern African Institute of Mining and Metallurgy*, vol. 106, no. 3. pp. 165–170.
- KOTZÉ, H. and PISTORIUS, P.C. 2010. A heat transfer model for high titania slag blocks. *Journal of the Southern African Institute of Mining and Metallurgy*, vol. 110, no. 2. pp. 57–66.
- MACPHERSON, R.D. 1982. Mineral processing at Richards Bay Minerals. *Proceedings of the 12th CMMI Congress*, vol. 2. Southern African Institute of Mining and Metallurgy, Johannesburg. pp. 835–840.
- PISTORIUS, P.C. 1999. Limits on energy and reductant inputs in the control of ilmenite smelters. *Proceedings of Heavy Minerals 1999*. Southern African Institute of Mining and Metallurgy, Johannesburg. pp. 183–188.
- PISTORIUS, P.C. 2004. Equilibrium interactions between freeze lining and slag in ilmenite smelting. *Journal of the Southern African Institute of Mining and Metallurgy*, vol. 104, no. 7. pp. 417–422.
- PISTORIUS, P.C., and COETZEE, C. 2003. Physicochemical aspects of titanium slag production and solidification. *Metallurgical and Materials Transactions B*, vol. 34, no. 5. pp. 581–588.
- ROSCOE, R. 1952. The viscosity of suspensions of rigid spheres. *British Journal of Applied Physics*, vol. 3, no. 8. pp. 267–269.
- STENKVIST, S.E. 1984. The properties and practical applications of the high-power graphite-cathode D.C. arc plasma. (Retroactive coverage). *Proceedings of MINTEK 50: International Conference on Mineral Science and Technology*, vol. 2. Mintek, Randburg, South Africa. pp. 769–775.
- TIMM, K. 2006. Principles of AC-arcs. *Proceedings of the International Symposium: Electrical Engineering of Arc Furnaces*, Braunschweig, Germany, 23–26 October. Verlag Stahleisen GmbH, Düsseldorf.
- WILLIAMS, G.E. and STEENKAMP, J.D. 2006. Heavy mineral processing at Richards Bay Minerals. *Proceedings of Southern African Pyrometallurgy 2006*. Southern African Institute of Mining and Metallurgy, Johannesburg. pp. 181–188.
- ZIETSMAN, J.H. 2004. Interactions between freeze lining and slag bath in ilmenite smelting. PhD thesis, University of Pretoria.
- ZIETSMAN, J.H. and PISTORIUS, P.C. 2004. Process mechanisms in ilmenite smelting. *Journal of the Southern African Institute of Mining and Metallurgy*, vol. 104, no. 11. pp. 653–660. ◆



Technological developments in processing Australian mineral sand deposits

M.I. Pownceby¹, W.J. Bruckard¹, and G.J. Sparrow¹

Affiliation:

¹CSIRO Mineral Resources,
Clayton South, Australia.

Correspondence to:

M.I. Pownceby

Email:

Mark.Pownceby@csiro.au

Dates:

Received: 15 Aug. 2019

Revised: 21 Nov. 2019

Accepted: 29 Nov. 2019

Published: February 2020

How to cite:

Pownceby, M.I., Bruckard, W.J.,
and Sparrow, G.J.

Technological developments in
processing Australian mineral
sand deposits.

The Southern African Institute of
Mining and Metallurgy

DOI ID:

<http://dx.doi.org/10.17159/2411-9717/881/2020>

This paper was first presented at
*The Eleventh International Heavy
Minerals Conference*, 5–6 August
2019, The Vineyard, Cape Town,
South Africa.

Synopsis

Almost all Australian mineral sand deposits are placer deposits, with the major commercial deposits located in four provinces along the east, west, and south coasts and in ancient basins in the southeast of the country. The development of new technology for mineral separation and its adaption to changes in the mineralogy of the deposits are discussed. Also, a summary is given of novel processing conditions developed to lower the levels of impurity elements (in particular manganese and radionuclides) in the heavy minerals, and to remove gangue minerals to obtain the maximum value from the deposits. The extensive, but still undeveloped, fine-grained Murray Basin deposits will require unique flotation conditions and roasting processes to produce marketable heavy mineral concentrates. The numerous potential novel processes that have been proposed for these deposits are discussed.

Keywords

mineral sands, mineral processing, technological developments, Australia.

Introduction

Australia is a major world producer of titanium and zirconium minerals from mineral sand deposits. The principal heavy minerals of commercial value recovered from these deposits are ilmenite (FeTiO_3), rutile (TiO_2), and zircon (ZrSiO_4). According to Geoscience Australia, Australia has the world's largest economic resources of rutile and zircon, and the second largest share of the world's ilmenite resources after China (Britt *et al.*, 2019). Commercial concentrations of titanium and zirconium minerals are found around the world in hard rock deposits, or in placer (alluvial) deposits resulting from the weathering of a hard rock deposit and the concentration of the heavy minerals by wave action on modern or ancient beaches, or by deposition in fluvial (river) systems. Almost all Australian mineral sand deposits are placer deposits, but although alluvial mineral sands occur in many places, commercial concentrations are found in only a small number of locations. The major commercial deposits in Australia are found along the east and west coasts and in ancient basins in the south (Eucla Basin) and southeast (Murray Basin) of the country.

In addition to ilmenite, and its alteration products (including pseudorutile, hydroxylated pseudorutile, and leucosene, as discussed below), rutile, and zircon, there are usually small amounts of anatase (TiO_2), monazite ($[\text{Ce}, \text{La}, \text{Th}] \text{PO}_4$), xenotime (YPO_4), cassiterite (SnO_2), and other lower-value heavy minerals also present in the deposits (Popp, 2005). Major gangue minerals in Australian deposits that can affect processing conditions are aluminium silicates, in particular clay minerals, and oxides such as spinels (*e.g.*, chromite, FeCr_2O_4). Gangue minerals can form significant proportions (>20%) of the heavy mineral assemblage and the specific mineral suite can vary significantly.

While ilmenite has a nominal chemical formula of FeTiO_3 ($\text{FeO} \cdot \text{TiO}_2$), assaying 52.7 wt% TiO_2 and 47.3 wt% FeO (52.6 wt% Fe_2O_3), this ideal composition seldom occurs in nature due to substitution of impurity elements (*e.g.*, Mg, Mn, V, Nb, Fe^{3+}) for Fe^{2+} in the crystal lattice, the presence of Fe^{3+} in Fe_2O_3 in solid solution in ilmenite, and incorporation of elements such as Al, Si, U, Th, P and Cr in the pores of grains during weathering of the ilmenite. Weathering is also associated with removal of iron and an increase in TiO_2 levels. As a result, in a commercial mineral concentrate, the individual titanium-containing grains may have a range of compositions.

- **Primary or unaltered ilmenite** contains 48–55 wt% TiO_2 with a composition close to the theoretical formula and a $\text{Ti}/[\text{Ti}+\text{Fe}]$ ratio of 0.5. It may contain some Fe^{3+} as a haematite-ilmenite solid solution (Fe_2O_3 - FeTiO_3) or as exsolution lamellae of ilmenite-haematite, and appreciable amounts of impurities give rise to the formula $\text{Fe}^{3+}_{2-2x}(\text{Fe}^{2+}, \text{Mg}, \text{Mn})_x \text{Ti}_x \text{O}_3$.

Technological developments in processing Australian mineral sand deposits

- **Secondary or weathered ilmenite** has 55–65 wt% TiO_2 and a $\text{Ti}/[\text{Ti}+\text{Fe}]$ ratio between 0.5 and 0.6. It has a variable composition consisting of a mixture of ilmenite and pseudorutile.
- **Pseudorutile** is formed on further weathering and has a composition of 60–71 wt% TiO_2 and a $\text{Ti}/[\text{Ti}+\text{Fe}]$ ratio of 0.6–0.7. This is an iron titanium oxyhydroxide solid solution with one end-member close to $\text{Fe}^{3+}_2\text{Ti}_3\text{O}_9$ and an extended range of homogeneity towards $\text{Fe}^{3+}_{1.5}\text{Ti}_3\text{O}_{7.5}(\text{OH})_{1.5}$ (Grey and Reid, 1975).
- **Hydroxylated pseudorutile**, with a composition of around 70 wt% TiO_2 and a $\text{Ti}/[\text{Ti}+\text{Fe}]$ ratio of 0.85–0.9, is a porous hydrated iron titanate that can contain more than 10 wt% water. This mineral is present in the Murray Basin deposits. It has recently been accepted as a new mineral by the International Mineralogical Association and has been given the name kleberite (Grey and Li, 2003; Grey, Steinike, and MacRae 2013).
- **Leucoxene** is an inhomogeneous, cryptocrystalline, high- TiO_2 (>70 wt% TiO_2) product of ilmenite weathering with a $\text{Ti}/[\text{Ti}+\text{Fe}]$ ratio of 0.7–0.9. Further weathering can proceed to form microcrystalline phases similar in composition to rutile.
- **Rutile** (and its low-temperature polymorph, anatase) is a titanate mineral that usually contains over 95 wt% TiO_2 . In natural systems V, Fe, Cr, Sn, Mo, Mn, Bi, Nb, Ta, and Sb may substitute into the rutile lattice (Bramdeo and Dunlevey, 1999).

As a result of the wide range of heavy minerals with similar physical properties, and the variable compositions and particle sizes of some, the concentration and separation of the minerals of value in alluvial mineral sand deposits is often not totally efficient and the final mineral products usually contain small amounts of gangue minerals (*e.g.*, quartz and aluminium silicate minerals). A commercial ilmenite concentrate may contain 45–65 wt% TiO_2 , the value depending on the composition of the individual mineral ilmenite grains.

Most of the heavy minerals in Australian mineral sand deposits are coarse-grained, such as in the deposits in Western Australia, where the ilmenite has a particle size of nominally 90–300 μm . In the Murray Basin deposits, the mineralization is generally finer with deposits in the north of the basin containing ilmenite with a particle size in the range 75–180 μm , while the further south in the basin that the deposits are located, the finer the particle size of the mineralization. There are major heavy mineral resources in the southeast of the Murray Basin that contain very fine-grained WIM-type mineralization with a particle size of 40–80 μm (Pownceby, 2010).

In this paper the properties of the Australian heavy mineral deposits are discussed, along with the development and advances made in equipment used to produce individual heavy mineral concentrates. Processing conditions developed and modified to treat the changing impurities in these deposits are reviewed.

Australian mineral sand deposits

Areas in Australia containing the major commercial deposits of mineral sands are shown in Figure 1. Mining of these alluvial mineral sand deposits is done either dry, with earthmoving equipment to excavate and transport the sand, or wet, using dredging techniques when the ground conditions are suitable and access to water is not a problem. The heavy minerals in the

mined sand are processed by gravity separation processes or flotation to yield a heavy mineral concentrate (HMC), and then the valuable minerals are separated in a mineral separation plant (MSP) into individual mineral concentrates using a combination of gravity, magnetic, and electrostatic separations or flotation. The commercial development of the Australian mineral sand provinces is discussed in chronological order here.

East coast deposits

Sediments weathered and eroded from the Lachlan fold belt of eastern Australia were captured by high-energy fluvial systems and transported to the east, where they were deposited to form the eastern Australian heavy mineral deposits along the coast of New South Wales and Queensland. Morley (1981) has presented a detailed review of the people and companies involved in the development and processing of these east coast deposits and the following summary is taken from his publication.

Concentrations of heavy minerals were identified along the east coast of Australia in the 1870s but these 'sniggers' were initially mined for their gold, tin, and platinum content. The first commercial production of zircon, rutile, and ilmenite commenced in 1934 at Byron Bay and expanded to various sites along the New South Wales and Queensland coastlines such that in the 1950s there were up to 33 operations in production. Production from eastern Australia reached its peak in the 1970s but has since decreased and only the mining operations on North Stradbroke Island by Sibelco Australia remain. These are the longest continuously operating sand mining operations in Queensland, but are expected to cease production before 2025 (fact sheet by Wort in Rankin, 2013). Final separation of the minerals is done at the MSP at Pinkenba on the mainland near Brisbane.

The first three companies to commercially produce heavy minerals from the beach sands were Zircon-Rutile Ltd, Metal Recoveries Ltd, and the Titanium Alloy Manufacturing Company. Dry mining with shovels and scoops was used to collect the black beach sand and the heavy minerals were initially recovered as a mixed zircon-rutile-ilmenite concentrate by passing the sand over sluice boxes lined with carpet material and using tables. Zircon-Rutile Ltd discovered (accidentally) that when the beach sand was added to hot water in the presence of kerosene and soap, on stirring the heavy minerals floated to the surface. Today this 'hot

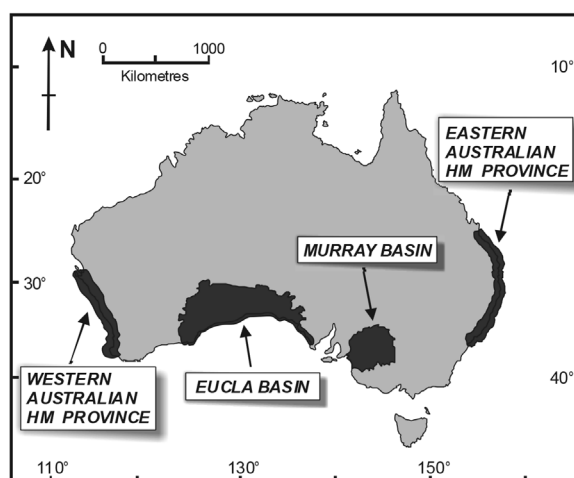


Figure 1—Location of the major mineral sand provinces in Australia (modified from Pownceby, Sparrow, and Fisher-White, 2008)

Technological developments in processing Australian mineral sand deposits

soap' flotation process is used to recover many oxide minerals. Moreover, it also was found that the addition of sulphuric acid to the heavy mineral concentrate depressed the rutile and ilmenite, leaving a froth of white zircon. Using this technology, Zircon-Rutile Ltd focused on producing a zircon concentrate (96–98% zircon) and a rutile-ilmenite mixture from the beaches around Byron Bay.

After 1945, mining of the sand was carried out with bulldozers and front-end loaders. A dragline was used to strip overburden and a bucket wheel excavator was used to mine hard indurated deposits. Later, when areas were re-worked, the lower grades resulted in the introduction of the floating dredge-concentrator arrangement. Gravity concentration was with pinched sluices and trays, spirals, and cones. The introduction of magnetic and electrostatic separators allowed the production of individual zircon, rutile, and ilmenite concentrates rather than a combined concentrate.

Mineral Deposits Pty Ltd (now Mineral Technologies, based at Carrara south of Brisbane) was formed at this time, and became a major developer and supplier of gravity, magnetic, and electrostatic separation equipment, and a construction company for the mineral sand industry. Early equipment developed by the company included the Reichert spiral and cone concentrators and electrostatic separators. Also during the same period, H.T. Readings at Lismore commenced the development and manufacturing of electromagnetic separators. Readings is now part of Mineral Technologies.

In the 1930s, the Commonwealth Council for Scientific and Industrial Research (CSIR) established an Ore Dressing Section at Melbourne University. This group worked with the fledgling mineral sands industry to assist in improving processing conditions and the development of downstream products. This government-industry collaboration has continued to the present day through the Commonwealth Scientific and Industrial Research Organisation (CSIRO), with research scientists located at several laboratories around the country.

While the zircon and rutile separated from the east coast deposits were easily marketed, the ilmenite was not suited to the production of white titania pigment by either the sulphate or chloride process due to its high chromium content. It was usually stockpiled or buried. However, with an increased demand for rutile as a feedstock for the new chloride process, Murphyores Inc. Pty Ltd, working with CSIRO from 1963 to 1977, developed the Murso process to upgrade ilmenite (and lower its chromium content) to a synthetic rutile that was a suitable feedstock for the chloride process. The ilmenite was oxidized in air at 1000°C to convert Fe²⁺ to Fe³⁺ and form micro-cracks in the ilmenite grains. The oxidized product was then reduced at 850–900°C in a reducing gas mixture of H₂-CO-CO₂-H₂O under conditions that minimized the formation of metallic iron. The highly reactive reduced product was dissolved in 20% HCl at 105–110°C under reflux and from the acid a high-grade synthetic rutile product containing 96 wt% TiO₂ precipitated. Although a pilot plant was run successfully in Japan, the process was never implemented in practice (Sinha, 1973).

In 1985, in response to a shortfall in world ilmenite production, Consolidated Rutile commenced upgrading stockpiled high-chrome ilmenite at its Pinkenba (Brisbane) MSP using dry magnetic separation to produce a product with a minimum of 50 wt% TiO₂ and a maximum of 0.40 wt% Cr₂O₃ for pigment production (Woodcock and Hamilton, 1993).

The Goondicum mine in central Queensland, owned by Melior Resources Inc. (Melior), is a weathered residual hard-rock deposit. Material in the Goondicum crater is mined, crushed, screened and sized, and gravity (spirals) and magnetic separations are used to produce primary ilmenite and apatite concentrates.

West coast deposits

Mineral sand deposits, many of a commercial size, have been formed by wave action along the coast of Western Australia in the Swan Coastal Plain, which stretches over 600 km from Jangardup south of Perth to Eneabba in the north. Many of these mineral-bearing strandlines are now located as much as 50 km inland from the current coastline. The degree of weathering of ilmenite in Western Australian deposits generally increases from south to north. Manganese is a major impurity element in west coast ilmenites. Also, the levels of uranium, thorium, and their radionuclide daughters tend to increase the further north the deposit is located, in association with the increased degree of weathering of the ilmenite.

Numerous companies have been established over the years to recover heavy minerals from these west coast deposits. However, few have been able to ride out the cyclical nature of market conditions (demand and price) and overcome difficult mining and processing conditions.

Commercial production of heavy minerals commenced in 1956 in the Capel region, south of Perth, with the operations of Cable Sands Pty Ltd (Cable Sands) and Western Titanium NL (which became Associated Minerals Consolidated Ltd, and then Renison Goldfields Consolidated Mineral Sands Ltd, RGC). In 1959 Westralian Sands Ltd (Westralian Sands) began mining near Capel. Initial operations in the Capel area generally used dry mining with scrapers and dozers to mine the sand and wet gravity concentration with spirals and cones to produce a heavy mineral concentrate (HMC). Mineral separation was carried out in plants at Capel (RGC), Bunbury (Cable Sands), and in the North Capel and Capel plants of Westralian Sands using spirals, cones, and magnetic and electrostatic separators.

Currently the major operators in Western Australia are Iluka Resources Ltd (Iluka, a merger of Westralian Sands and RGC in 1998) and Tronox Management Pty Ltd (Tronox, formerly TiWest Joint Venture). In April 2019, Tronox acquired Cristal Mining Australia Ltd (Cristal) and with it the Cable Sands operations that Cristal had acquired previously. Tronox has the only integrated operation, with ilmenite from its Cooljarloo mine being fed to its pigment plant at Kwinana. Through the acquisition of Cristal it also has pigment plants near Bunbury. Individual mineral concentrates and upgraded products are exported to overseas customers.

Initially, Western Titanium NL produced a primary ilmenite concentrate (approx. 54 wt% TiO₂) as a feedstock for production of titania pigment by the sulphate process. With the supply of rutile (>95 wt% TiO₂), the preferred feedstock for the chloride process, diminishing, the Becher process was developed by the Western Australian Government Research Laboratory (Becher *et al.*, 1965) to upgrade the primary ilmenite from 54 wt% TiO₂ to a synthetic rutile containing over 90 wt% TiO₂. Large-scale commercial production of synthetic rutile commenced from 'B plant' at Capel in 1974.

In the Becher process, iron in the ilmenite is reduced at 1100–1180°C in a rotary kiln (5.1 m diameter and 62 m in length) for 10 hours to form metallic iron dispersed in a titania

Technological developments in processing Australian mineral sand deposits

matrix (reduced ilmenite, RI). The locally available reactive Collie coal (and char) is used as the reductant. After magnetic separation to remove residual char, aeration of the reduced ilmenite in an ammonium chloride solution results in oxidation of the metallic iron and precipitation of finely divided iron oxides in the suspension that can be separated easily from the coarser titania grains, typically with a hydrocyclone. The iron oxide is discharged to a storage area from which an iron-rich concentrate is recovered for sale. A leach with dilute sulphuric acid is used to remove residual iron and other impurities from the aeration product to produce a premium-grade synthetic rutile (SR) product containing around 92.5 wt% TiO₂. To increase the reactivity of the primary Capel ilmenite for the Becher process, initially it was necessary to pre-oxidize the mineral at around 1000°C in air. When, subsequently, the ilmenite mined at Capel, and from the Eneabba deposits discovered north of Perth in the early 1970s, became progressively more oxidized (58–62 wt% TiO₂), the pre-oxidation step was no longer necessary.

Work commenced in the late 1960s at CSIRO, in collaboration with Western Titanium NL, to identify the phase changes occurring in the reduction step of the Becher process in order to optimize the process. Subsequent work targeted the removal of specific impurities by modifications to the Becher processing conditions. To lower the manganese levels, elemental sulphur is added to the reduction kiln to form a manganese sulphide phase (Rolfe, 1973; Li and Merritt, 1990) that dissolves in the acid leach after the aeration step. In another modification, the Synthetic Rutile Enhancement Process (SREP), a borate flux is added during the reduction step to collect uranium and thorium and their radionuclide daughters into an acid-soluble glassy phase that can be leached out after the aeration step to lower uranium and thorium levels in the synthetic rutile to <100 ppm U+Th (Ellis, Harris, and Hudson, 1994; Aral *et al.*, 1997).

RGC (later Iluka) processed the large Eneabba strandline deposits north of Perth until 2015. Dry and wet mining operations were used, with MSPs at Eneabba and at Narngulu near Geraldton. Two reduction kilns (the C and D plants) were commissioned at Narngulu to upgrade ilmenite to synthetic rutile (92–95 wt% TiO₂). Over the years Iluka (and its predecessors) processed numerous deposits south of Perth, but in 2018 their operations at the Tutunup South deposit were completed. Production from the Cataby deposit north of Perth commenced in 2019, with an estimated mine life of around 8.5 years. The HMC is separated on site into a nonmagnetic fraction that is transported to the Narngulu MSP for separation of zircon and rutile and a magnetic fraction that is feed for SR production at Capel.

The Tiwest Joint Venture commenced operations at Cooljarloo north of Perth in 1989 using a dredge and floating concentrator to mine and concentrate the heavy minerals. The HMC was transported to a MSP at Chandala. A Becher plant was also built at Chandala to produce SR as a feedstock for the company's chloride pigment plant at Kwinana. Now known as Tronox, the company continues to source its ilmenite from deposits in the Lancelin to Gingin area north of Perth. Image Resources NL recently commenced production of HMC from its Boonanarring deposit near Gingin. The HMC is exported to China for separation.

Several other operations are currently producing ilmenite in the southwest of Western Australia. Tronox (previously Cristal) is producing HMC from its Wonnerup mine, with separation of the minerals at the Cable Sands MSP at Bunbury. The company has

five other mines scheduled to come into production and expects to continue mining in the southwest for the next two decades. Doral Mineral Sands Pty Ltd (Doral) is mining deposits in the Jangardup area, also in the southwest of Western Australia, with treatment of the HMC at its MSP at Picton. The current operation is in the western extension to the original project (Burekup), which has a mine life of 3.5–5 years.

Details of the processing conditions for the major operations in Western Australia have been presented in the Maurice Mawby memorial volumes produced by the Australasian Institute of Mining and Metallurgy (Woodcock, 1980; Woodcock and Hamilton, 1993; Rankin, 2013).

Over the years there have been significant developments in concentration and separation equipment used in the Western Australian operations. More efficient gravity concentration has been achieved with banks of spirals of improved design and materials of construction and improved flow sheets (Palmer and Vadeikis, 2010). Kelsey centrifugal jigs have been used to separate zircon from gangue minerals such as kyanite (Jones and Foster, 2010). The development of higher strength rare earth permanent magnets has resulted in advances in magnetic separators. Several types of rare earth magnetic separators, including rare earth roll (RERMS) and rare earth drum magnetic separators (REDMS) for both wet and dry separations, and matrix-type separators such as wet high-intensity magnetic separators (WHIMS) are used to concentrate and separate heavy minerals in different parts of the processing circuit. Traditional electrostatic separation equipment for nonmagnetic minerals have used combinations of high-tension roll (HTR) and electrostatic plate (ESP) separators. Germain *et al.* (2003) summarized novel technology that gave better separation efficiency by reducing the effects of particle size. The Julius Kruttschnitt Mineral Research Centre (JKMRC), through the industry-funded Australian Minerals Industry Research Association (AMIRA) P255 project, has developed a range of instruments and process models for improved optimization and control in separation plants (Kojovic, Pax, and Holtham, 1999). Pax (2011) has used finite element modelling of the equipment to improve mineral separation.

Significant developments have also occurred in the characterization of heavy mineral ores, concentrates, and processed products through the commercial availability of instruments such as scanning electron microscopes (SEMs) and electron probe microanalysers (EPMAs) in the 1950s and 1960s. The value of these systems in process mineralogy was quickly established (Jones, 1987; Sutherland and Gottlieb, 1991), although it was not until the late 1990s, when computing hardware and speed were sufficiently advanced, that automated SEMs (Reid *et al.*, 1984; Gu, 2003; Fandrich *et al.*, 2007), and more recently EPMAs (Pownceby and MacRae, 2011, 2016) became commercially available and were routinely applied to mineral sands characterization.

Automated SEM-based systems such as the original QEMSCAN and MLA systems (now owned by Thermo Fisher Scientific) and the more recent TIMA (Tescan), Mineralogic (Carl Zeiss NV), INCAMineral (Oxford Instruments), and AMICS (Hitachi/Bruker) systems have found the greatest use in heavy mineral characterization by providing information such as quantitative modal analysis, mineral grain size, liberation, and textural analysis. The advantage of automated SEM-based mineralogy systems is their ability to rapidly collect quantitative data for many thousands of particle sections, with

Technological developments in processing Australian mineral sand deposits

minimal operator intervention (Baum, 2014), and automated mineralogical methods are now widely used in heavy mineral mines and MSPs for ore characterization, grade control, and process design optimization. EPMA, being of higher cost and usually requiring specialist operators, have largely been limited to generating quantitative chemical information on individual valuable minerals to assess potential marketability and to guide and improve process parameters (*e.g.* in MSP plants or after upgrading to a high-TiO₂ product). More recent EPMA advances have seen the development of integrated X-ray and cathodoluminescence mapping systems (MacRae *et al.*, 2005; Wilson and MacRae, 2005) to illustrate mineral phase distributions (particularly useful for determining particle coatings), impurity mineral/element distributions (Pownceby, 2005; Pownceby, MacRae, and Wilson, 2007), and textural information (Pownceby, 2010), thereby providing a powerful technique for characterizing heavy mineral deposits and process products.

Murray Basin deposits

Detritus from the weathering and erosion of sediments from the Lachlan fold belt of eastern Australia that was shed to the west was reworked in the palaeo-Darling, Lachlan, Murrumbidgee, and Murray River systems and subsequently deposited in the Murray Basin, the remains of a shallow inland sea (Roy *et al.*, 2000). The basin extends over an area of 320,000 km² across Victoria, New South Wales and South Australia. In Pliocene times (approx. 5.3–1.8 Ma), economic heavy mineral concentrations formed within the Loxton-Parilla sands unit. These were first reported in the late 1960s and extensive exploration commenced in 1970, leading to the discovery of over a hundred areas of mineralization. However, few of the occurrences contain economic quantities of heavy minerals. Locations of the more important deposits are shown in Figure 2.

The first major discovery in the Murray Basin, in 1982, was the fine-grained WIM 150 deposit near Horsham in the southeast of the basin. Subsequently, four similar deposits (WIM 050, WIM 100, WIM 200, and WIM 250) were discovered nearby. The discovery of the WIM 150 deposit led to increased exploration across the basin and between 1989 and 1999 coarser strandline deposits were discovered and subsequently brought into production. These included Mindarie in the west, Wemen, Kulwin,

Woorack, and Rownack in the centre, Douglas in the south, and Ginkgo and Snapper in the north of the basin (Figure 2).

Murray Basin Titanium Joint Venture (MBTJV) commenced the first operation in the basin at their Wemen deposit in 2001. It was a relatively small resource and mining was completed in 2004. Bemax Resources NL (Bemax) acquired MBTJV, and Cable Sands in Western Australia, in 2004. Iluka commenced their operations in the basin with the Douglas and nearby Echo deposits in 2004, with mining of these two deposits completed in 2012. The Kulwin deposit was mined between 2009 and 2012 and production from the Woorack, Rownack and Pirro (KWP) deposits commenced in 2012 and finished in 2015. Iluka is currently undertaking the development of a large deposit in the Balranald area of New South Wales.

Iluka used wet gravity concentration equipment to produce a HMC. WHIMS was used to separate part of the ilmenite (the most magnetic fraction) which was retained on-site due to its high chromium levels (1–2 wt% Cr₂O₃). The rest of the HMC was sent to the MSP at Hamilton where zircon, rutile, and weathered ilmenite products were produced. Since completing the treatment of stockpiled HMC, the MSP at Hamilton has closed. Processing conditions used by Iluka are summarized by Hugo and Jones in Rankin (2013).

Bemax commenced production from its Pooncarie deposits in the north of the Murray Basin in New South Wales in 2005. Initial production was from the Ginkgo deposit with the HMC sent to the MSP at Broken Hill that was commissioned in 2006. In 2010 production commenced from the Snapper deposit, and from the nearby Crayfish deposit in 2017. In 2008 Cristal acquired Bemax, and in 2019 Tronox procured Cristal. The HMC produced at the Ginkgo, Snapper, and Crayfish mines is trucked to the recently expanded MSP at Broken Hill, where magnetic leucoxene and secondary ilmenite products are produced and railed to Port Adelaide in South Australia for export. The nonmagnetic fraction is shipped to the Bunbury dry plant for separation of rutile and zircon products that are exported through the port of Bunbury. Little of the ilmenite concentrate was sold initially because of its high chromium content of over 1 wt% Cr₂O₃.

The Mindarie deposit in the west of the basin consists of numerous strandlines between Mindarie and Karoonda in South Australia. Mineralogical data for the deposit reports a grain size of between 45 µm and 63 µm, suggesting that the mineralization

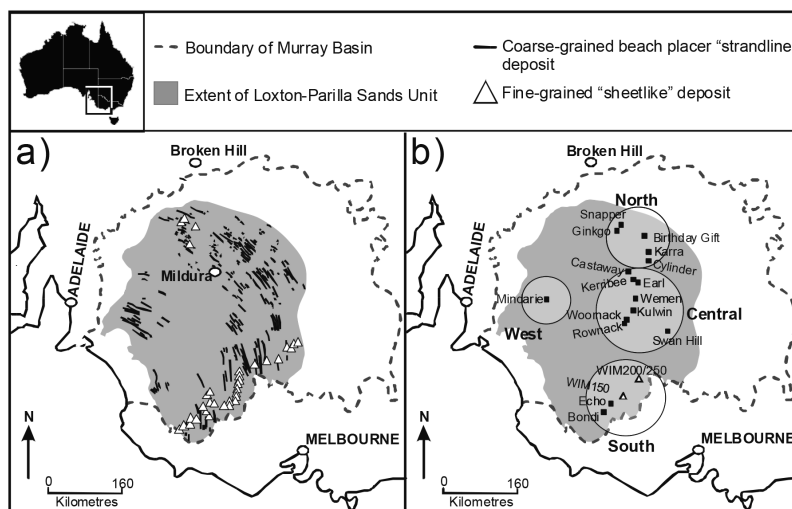


Figure 2—Location map of Murray Basin mineral sand deposits (modified from Pownceby, 2010)

Technological developments in processing Australian mineral sand deposits

is finer than that in other strandline deposits in the Murray Basin. The deposit was developed by Australian Zircon NL (Australian Zircon) with production commencing in 2007. The HMC was exported to China. After several changes in ownership, the project was put on care and maintenance in 2015.

Ilmenite concentrates produced from the Murray Basin deposits contain high levels of chromium due to the presence of chrome spinel minerals. The wide range in the composition of these spinels makes it hard to remove them during processing. Extensive experimental work has been done to characterize the compositional variations (Pownceby, 2010), and Bruckard *et al.* (2015) summarized the various treatment conditions evaluated to remove the chrome spinels to obtain products with chromium levels low enough for pigment production. A magnetizing roast to increase the magnetic susceptibility of the titanate grains relative to that of the chrome spinels has been shown to yield a titanate product with a lower chromia content after magnetic separation. For a primary ilmenite fraction, a low-temperature magnetizing roast around 600°C, which limits the amount of rutile produced in the roast, is successful. (Rutile does not dissolve well in concentrated sulphuric acid.) A higher roasting temperature may be used with weathered ilmenite since the formation of rutile during the roast is not a problem in the subsequent chlorination process. Bemax has proposed constructing a multi-hearth fluid bed roaster at its Broken Hill MSP to roast high-chromium ilmenite at around 620°C under reducing conditions to yield a magnetic product suitable as a chlorinatable feedstock in which the chromium content has been lowered from >1.5 wt% to <0.3 wt% Cr₂O₃ (Everett *et al.*, 2003).

Under reducing conditions, such as in a Becher reduction kiln, chromium is chalcophilic and has a strong affinity for sulphur. The possibility of modifying the chemical and physical properties of the chrome spinels in a Murray Basin ilmenite concentrate was investigated by adding elemental sulphur to the Becher reduction step. Examination of the reduced ilmenite product revealed the presence of small amounts of bronze-coloured grains indicating chrome spinels coated with rims of sulphur-rich phases (*i.e.*, selective chromite sulphidization). After de-metallization of the reduced ilmenite, removal of the sulphur-coated chrome spinel grains may be possible by flotation using reagents typically used to float base metal sulphides. Initial results were promising, and further work is in progress to optimize the treatment conditions (Ahmad *et al.*, 2014, 2016; Rhamdhani *et al.*, 2018). In Western Australian Becher plants, chromite is removed in the nonmagnetic fraction from the magnetic separation after reduction of the ilmenite.

Weathered ilmenites are usually upgraded to over 90 wt% TiO₂ to serve as feedstock for a chloride pigment plant. Processes that may be used for Murray Basin weathered ilmenites include kiln-based or fluidized bed processes. Magnesium and manganese are major impurities in Murray Basin ilmenites, and while manganese levels can be lowered by addition of elemental sulphur in the reduction step of the Becher process, magnesium is not removed in a standard Becher treatment. Consequently, modifications to the Becher processing conditions have been proposed to produce satisfactory sulphate and chloride pigment feedstocks from weathered Murray Basin ilmenites. Kiln-based processes that have been evaluated for Murray Basin weathered ilmenite concentrates include the Hybrid, Acid Soluble Synthetic Rutile (ASSR) and the Recovery of Upgraded Titania by Impurity Liquefaction and Extraction (RUTILE) processes. While these

processes have been tested at pilot plant scale, the use of a modified Becher process is likely to require demonstration of the technology at a larger scale. The Murso, Auspac ERMS and NewGenSR processes use fluidized bed reactors to oxidize and reduce iron in the ilmenite at temperatures between 750 and 1000°C. All these processes have been demonstrated at pilot plant scale, but no commercial operation has been established as yet. A summary of the application of these processes to weathered Murray Basin ilmenites has been given by Bruckard *et al.* (2015).

Eucla Basin deposits

Another major heavy mineral province in Australia is the Eucla Basin, an approximately 2000 km wide marginal marine basin spanning the border between South Australia and Western Australia (Hou, Keeling, and Hocking, 2011). Exploration since 2004 has led to the discovery of numerous major heavy-mineral deposits in Tertiary shorelines along the east of the basin (Jacinth, Ambrosia, Atacama, Typhoon, and Cyclone). Other prospects (Cyclone Extended, Balladonia, and Plumridge) are around the western edge of the basin (Hou, Keeling, and Hocking, 2011; Pownceby, Sparrow, and Fisher-White, 2008). Iluka commenced production from the Jacinth deposit in October 2009, primarily for production of zircon. After a short suspension in production in April 2016, production recommenced in December 2017 with the HMC being transported to the Narngulu MSP in Western Australia. Mining of the Ambrosia deposit is expected to commence in 2019. At Narngulu, a hot acid leach is used to clean the surfaces of the final zircon product to lower iron contamination levels.

Future developments

New deposits

In addition to the commercial operations noted above, several companies are actively evaluating other resources in Western Australia. Sheffield Resources Limited is evaluating several prospects in the Eneabba area. North of Geraldton, Strandline Resources Limited has the Coburn heavy mineral sands project just south of Shark Bay, and even further north is the flagship Thunderbird mineral sands deposit of Sheffield Resources Limited. This project is in the Canning Basin, on the Dampier Peninsula west of Derby, and is the first major mineral sand deposit discovered in the Canning Basin. A prefeasibility study indicated that an ilmenite product with 56.1% TiO₂ and low levels of alkalis and chromium could be produced from the deposit following a low-temperature roast.

In Victoria, future developments are expected to occur in the north of the Murray Basin. Iluka is developing a large deposit in the Balranald area. This deposit is under 60 m of overburden and underground mining and backfilling techniques are being evaluated to recover the heavy minerals. Cristal Mining is developing the Atlas/Campaspe Project north of Balranald with a planned mine life of 11–20 years.

Also in Victoria, there are many occurrences of mineral sands around the eastern edge of the Murray Basin. Over the years numerous companies have evaluated them but no development has occurred. The Gippsland Basin in the southern part of Victoria also is host to extensive late Miocene–Pliocene strandline deposits and exploration and drilling have shown that these have similar properties to the Murray Basin strandline deposits. The Glenaladale deposit was discovered by Rio Tinto Exploration in 2004, and in 2013, Kalbar Resources Ltd (Kalbar) acquired the

Technological developments in processing Australian mineral sand deposits

resource and has started developing the higher grade areas as its Fingerboards Mineral Sands Project.

Developments for fine-grained mineralization

The five WIM-type deposits located in the south of the Murray Basin around Horsham are fine-grained, sheet-like heavy mineral deposits. The WIM 150 deposit was discovered by CRA Limited, now Rio Tinto Pty Ltd, with initial development carried out through its subsidiary company, Wimmera Industrial Minerals Pty Ltd (WIM). An intensive effort was made to develop processing options for the WIM 150 deposit, including pilot plant test work, but no commercial operation resulted and WIM relinquished its leases on the deposits. They were subsequently taken up by other companies (*e.g.*, Australian Zircon and Murray Zircon – now a joint venture between OZC and Million Up Ltd) but despite a significant amount of further development work the deposits still have not come into production.

Astron Ltd (Astron) is evaluating two WIM-type deposits; WIM 200 (the Jackson deposit) and WIM 250 (the Donald deposit). Astron is concentrating on production from the Donald deposit first, and proposes to produce a HMC for export to China for further processing.

While the extensive WIM-type deposits located in the south of the Murray Basin contain more heavy minerals than there are in the strandline deposits in the basin, they remain undeveloped. Although they are low grade, the fine particle size has been the major issue preventing them from being developed to date. A significant amount of research has been undertaken to design equipment and identify processing options to concentrate and separate these fine minerals.

Continuing developments are being made with the design of spirals to increase the recovery of the finer mineralization from the WIM-type deposits (Richards *et al.*, 2000). Higher mineral recoveries of fines down to around 6 µm, with better concentrate grades, and separation of minerals with small specific gravity differences are claimed with a Kelsey jig compared with other gravity separation techniques (Jones and Foster, 2010). Kelsey jigs, along with spirals and flotation, are proposed to be used in processing the WIM 150 deposit. Capps and Waldram (1986) have reported the recovery of fine-grained (32–75 µm) heavy minerals from a mineral sand deposit using Kelsey jigs. Wet magnetic separators are usually considered to be efficient for minerals with particle sizes above 75 µm. Consequently, it is likely that magnetic separation efficiencies for fine-grained deposits may not be satisfactory.

Flotation has been used to concentrate and separate heavy minerals, and since it operates efficiently with fine (<100 µm) particle sizes, it can be expected to be applicable to the concentration and separation of heavy minerals in the fine-grained deposits (Bruckard *et al.*, 1999). A strategy of producing a bulk float of the valuable minerals, depression of the titanium minerals, and a float to separate the rutile and ilmenite using modern collectors (*e.g.*, sulphasuccinamates, phosphonic acids, amines) is expected to be able to yield individual concentrates of the fine-grained minerals. Pownceby *et al.* (2015) have summarized some of the reported flotation work with WIM 150 samples.

Removal of chrome spinels from the ilmenite concentrate will also be an issue with the fine-grained deposits. Flotation and roasting conditions discussed above for the coarser-grain deposits should also be applicable to the finer mineralization. However, there are expected to be problems in treating the fine-

grained mineralization with a fluidized bed or kiln-based process as the particles may be blown out of the fluidized bed, or from a rotary kiln in the high exhaust gas flows from the kiln. Research is required to design a circulating fluidized bed reactor capable of treating fine-grained mineralization, or to determine whether agglomeration of fine-grained ilmenite can successfully be used in existing reactor designs.

The final zircon concentrate, as well as requiring attritioning in water and acid or alkaline solutions to remove surface contaminants, is also likely to require further treatment to lower radionuclide (uranium, thorium, and their daughter products) levels in the grains. Heat and leach treatments that involve decomposition of zircon either through the addition of a flux, or through the application of temperatures above the temperature at which zircon breaks down to zirconia and quartz, and other flux-based treatments that retain the integrity of the zircon crystalline lattice have been used to significantly lower the U+Th levels in the fine-grained zircon. Pownceby *et al.* (2015) have summarized this work.

Summary

Australia has four major mineral sands provinces. Since 1934, when the commercial mining of mineral sands commenced in eastern Australia, there has been continuous mining and processing of heavy minerals from these deposits. This has been associated with significant advances in equipment design to recover the heavy minerals and in processing conditions to remove impurity elements from the heavy minerals to produce marketable products for further local processing or for export. New deposits currently being characterized and developed will ensure continuing production of heavy minerals in Australia.

Acknowledgements

Some information and details of current operations were taken from company web sites. Alex de Andrade is acknowledged for information on recent developments in separation equipment by Minerals Technologies. The external reviewers are thanked for their valuable comments.

References

- AHMAD, S., RHAMDHANI, M.A., POWNCEBY, M.I., and BRUCKARD, W.J. 2014. Thermodynamic assessment and experimental study of sulphidation of ilmenite and chromite. *Transactions of the Institution of Mining and Metallurgy C: Mineral Processing and Extractive Metallurgy*, vol. 123, no. 3. pp. 165–177.
- AHMAD, S., RHAMDHANI, M.A., POWNCEBY, M.I., and BRUCKARD, W.J. 2016. Selective sulphidising roasting for the removal of chrome spinel impurities from weathered ilmenite ore. *International Journal of Mineral Processing*, vol. 146. pp. 29–37.
- ARAL, H., BRUCKARD, W.J., FREEMAN, D.E., GREY, I.E., HARRIS, H.R., HOUCHEIN, M.R., McDONALD, K.J., and SPARROW, G.J. 1997. Radionuclide removal from Eneabba North ilmenite. *Proceedings of Heavy Minerals 1997*. Robinson R.E. (ed.). South African Institute of Mining and Metallurgy, Johannesburg. pp. 137–142.
- BAUM, W. 2014. Ore characterization, process mineralogy and lab automation a roadmap for future mining. *Minerals Engineering*, vol. 60. pp. 69–73.
- BECHER, R.G., CANNING, R.G., GOODHEART, B.A., and UUSNA, S. 1965. A new process for upgrading ilmenitic mineral sands. *Proceedings of the Australasian Institute of Mining and Metallurgy*, no. 214, June. pp. 21–43.
- BRAMDEO, S. AND DUNLEVEY, J.N. 1999. Mineral chemistry of rutile. *Proceedings of Heavy Minerals 1999*. Stimson R.G. (ed.). South African Institute of Mining and Metallurgy, Johannesburg. pp. 63–65.
- BRITT, A., SENIOR, A., SUMMERFIELD, D., HUGHES, A., HITCHMAN, A., CHAMPION, D., HUSTON, D., SIMPSON, R., KAY, P., SEXTON, M., and SCHOFIELD, A. 2019. Australia's identified mineral resources 2018, Geoscience Australia, Canberra. doi: <http://dx.doi.org/10.11636/1327-1466.2018> [accessed 19 March 2019].

Technological developments in processing Australian mineral sand deposits

- BRUCKARD, W.J., CREED, M.D., GUY, P.J., and HEYES, G.W. 1999. Beneficiation of Australian mineral sands deposits using flotation. *Extended abstracts: Murray Basin Mineral Sands Conference*. Stewart, R. (ed.). *Australian Institute of Geoscientists Bulletin*, no. 26. pp 111–115.
- BRUCKARD, W.J., POWNCEBY, M.I., SMITH, L.K., and SPARROW, G.J. 2015. Review of processing conditions for Murray Basin ilmenite concentrates. *Transactions of the Institution of Mining and Metallurgy C: Mineral Processing and Extractive Metallurgy*, vol. 124, no. 1. pp. 47–63.
- CAPPS, P.G. and WALDRAM, J.T. 1986. Concentration of fine grained heavy minerals using the Kelsey centrifugal jig. *Proceedings of Australia: A World Source of Ilmenite, Rutile, Monazite and Zircon*. Australasian Institute of Mining and Metallurgy, Melbourne. pp. 99–106.
- ELLIS, B.A., HARRIS, H.R., and HUDSON, R.L. 1994. The reduction of radionuclides in titaniferous feedstocks. *Proceedings of the 11th Industrial Minerals International Congress*. Griffiths J.B. (ed.). Industrial Minerals Division of Metal Bulletin plc, Surrey, UK. pp. 102–108.
- EVERETT, S.C., SCHACHE, I.S., BALDERSON, G.F., and BANNISTER, P.A. 2003. Pooncarie Project — The technical challenges. *Proceedings of Heavy Minerals 2003*. South African Institute of Mining and Metallurgy, Johannesburg. pp. 81–93.
- FANDRICH, R., GU, Y., BURROWS, D., and MOELLER, K. 2007. Modern SEM-based mineral liberation analysis. *International Journal of Mineral Processing*, vol. 84. pp. 310–320.
- GERMAIN, M., LAWSON, T., HENDERSON, D.K., and MACHUNTER, D.M. 2003. The application of new design concepts in high tension electrostatic separation to the processing of mineral sands concentrates. *Proceedings of Heavy Minerals 2003*. South African Institute of Mining and Metallurgy, Johannesburg. pp. 101–107.
- GREY, I.E. and REID, A.F. 1975. The structure of pseudorutile and its role in the natural alteration of ilmenite. *American Mineralogist*, vol. 60. pp. 898–906.
- GREY, I.E. and LI, C. 2003. Hydroxylated pseudorutile derived from microilmenite in the Murray Basin, southeastern Australia. *Mineralogical Magazine*, vol. 67, no. 4. pp. 733–747.
- GREY, I.E., STEINKE, K., and MACRAE, C.M. 2013. Kleberite, $\text{Fe}^{3+}\text{Ti}_6\text{O}_{11}(\text{OH})_5$, a new ilmenite alteration product, from Königshain, northeast Germany. *Mineralogical Magazine*, vol. 77, no. 1. pp. 45–55.
- GU, Y. 2003. Automated scanning electron microscopy based mineral liberation analysis. An introduction to JKMR/FEI Mineral Liberation Analyser. *Journal of Minerals and Materials Characterization and Engineering*, vol. 2. pp. 33–41.
- HOU, B., KEELING, J.L., and HOCKING, R.M. 2011. Heavy mineral prospectivity in the Eucla Basin. *Proceedings of Eighth International Heavy Minerals Conference*. Australasian Institute of Mining and Metallurgy, Melbourne. pp. 135–145.
- JONES, M.P. 1987. *Applied Mineralogy: A Quantitative Approach*. Graham and Trotman, London.
- JONES, T. and FOSTER, A. 2010. Smarter gravity separation using the Kelsey centrifugal jig. *Proceedings of the XXV International Mineral Processing Congress (IMPC) 2010*. Australasian Institute of Mining and Metallurgy, Melbourne. pp. 859–869.
- KOJOVIC, T., PAX, R., and HOLTHAM, P. 1999. Developments in titanium minerals processing technology. *Extended abstracts: Murray Basin Mineral Sands Conference*. Stewart, R. (ed.). *Australian Institute of Geoscientists. Bulletin* No. 26. pp 139–144.
- LI, C. and MERRITT, R.R. 1990. Reduction of ilmenite in the presence of sulphur. *Australian Journal of Chemistry*, vol. 43, no. 1. pp. 1–9.
- MACRAE, C.M., WILSON, N.C., JOHNSON, S.A., PHILLIPS, P.L., and OTSUKI, M. 2005. Hyperspectral mapping – combining cathodoluminescence and X-ray collection in an electron microprobe. *Microscopy Research and Technique*, vol. 67. pp. 271–277.
- MORLEY, I.W. 1981. *Black Sands. A History of the Mineral Sand Mining Industry in Eastern Australia*. University of Queensland Press, St Lucia. 278 pp.
- PALMER, M. and VADEIKIS, C. 2010. New developments in spirals and spiral plant operations. *Proceedings of the XXV International Mineral Processing Congress (IMPC) 2010*. Australasian Institute of Mining and Metallurgy, Melbourne. pp. 1099–1108.
- PAX, R.A. 2011. The use of finite element modelling to better understand electrostatic separation. *Proceedings of the Eighth International Heavy Minerals Conference*. Australasian Institute of Mining and Metallurgy, Melbourne. pp. 239–249.
- POPP, A.W. 2005. Murray Basin heavy mineral strandline deposit mineralogy. *Proceedings of Heavy Minerals 2005*. Asker M. and Elder J. (eds). Society for Mining, Metallurgy and Exploration, Inc., Littleton, CO. pp. 91–102.
- POWNCBEY, M.I. 2005. Compositional and textural variation in detrital chrome spinels from the Murray Basin, southeastern Australia. *Mineralogical Magazine*, vol. 69. pp. 191–204.
- POWNCBEY, M.I. 2010. Alteration and associated impurity element enrichment in detrital ilmenites from the Murray Basin, southeast Australia: a product of multistage alteration. *Australian Journal of Earth Science*, vol. 57. pp. 243–258.
- POWNCBEY, M.I., SPARROW, G.J., and FISHER-WHITE, M.J. 2008. Characterisation of ilmenites from western Eucla Basin heavy mineral concentrates. *Proceedings of the Ninth International Congress for Applied Mineralogy*. Australasian Institute of Mining and Metallurgy, Melbourne. pp. 537–544.
- POWNCBEY, M.I. and MACRAE, C.M. 2011. Electron beam analysis techniques used for the characterization of industrial minerals. *Advances in the Characterization of Industrial Minerals*, Christidis, G. (ed.). EMU Notes in Mineralogy, 9. European Mineralogical Union and the Mineralogical Society of Great Britain & Ireland. pp. 227–286.
- POWNCBEY, M.I. and MACRAE, C.M. 2016. Electron probe microanalyser. *Process Mineralogy*. Becker, M., Wightman, E.M. and Evans, C.L. (eds.). Julius Kruttschnitt Mineral Research Centre, University of Queensland, Indooroopilly. pp. 79–96.
- POWNCBEY, M.I., MACRAE, C.M., and WILSON, N.C. 2007. Mineral characterisation by EPMA mapping. *Minerals Engineering*, vol. 20. pp. 444–451.
- POWNCBEY, M.I., SPARROW, G.J., ARAL, H., SMITH, L.K., and BRUCKARD, W.J. 2015. Recovery and processing of zircon from Murray Basin mineral sand deposits. *Transactions of the Institution of Mining and Metallurgy C: Mineral Processing and Extractive Metallurgy*, vol. 124, no. 4. pp. 240–253.
- RANKIN, W.J. (ed.). 2013. *Mineral Sands. Australasian Mining and Metallurgical Operating Practices. The Maurice Mawby Memorial Volume*. 3rd edn. Australasian Institute of Mining and Metallurgy, Melbourne. vol. 2. pp. 1683–1718.
- REID, A.F., GOTTLIEB, P., MACDONALD, K.J., and MILLER, P.R. 1984. QEM*SEM® image analysis of ore minerals: volume fraction, liberation and observational variances. *Applied Mineralogy*. Park, W.C. Hansen, D.M. and Hagni, R.D. (eds). AIME, New York, NY. pp. 191–204.
- RHAMDHANI, M.A., AHMAD, S., POWNCEBY, M.I., BRUCKARD, W.J., and HARJANTO, S. 2018. Selective sulphidation of impurities in weathered ilmenite. Part 1 – Applicability to different ilmenite deposits and simulated Becher kiln conditions. *Minerals Engineering*, vol. 121. pp. 55–65.
- RICHARDS, R.G., MACHUNTER, D.M., GATES, P.J., and PALMER, M.K. 2000. Gravity separation of ultra-fine (-0.1 mm) minerals using spiral separators. *Minerals Engineering*, vol. 13, pp. 65–77.
- ROLFE, P.E. 1973. The modified metallurgical upgrading of ilmenite to produce high grade synthetic rutile. *Proceedings of the AusIMM Conference Series No. 2*, Perth, May 1973. Australasian Institute of Mining and Metallurgy, Melbourne. pp. 443–453.
- ROY, P.S., WHITEHOUSE, J., COWELL, P.J., and OAKES, G. 2000. Mineral sands occurrences in the Murray Basin, southeastern Australia. *Economic Geology*, vol. 95. pp. 1107–1128.
- SINHA, H.N. 1973. The Murso process for producing rutile substitute. *Titanium Science and Technology*. Jaffee, R.I. and Burte H.M. (eds.). Plenum Press, New York – London. pp. 233–245.
- SUTHERLAND, D. and GOTTLIEB, P. 1991. Application of automated quantitative mineralogy in mineral processing. *Minerals Engineering*, vol. 4. pp. 753–762.
- WILSON, N.C. and MACRAE, C.M. 2005. An automated hybrid clustering technique applied to spectral data set. *Microscopy and Microanalysis*, vol. 11, supplement 2, 434CD.
- WOODCOCK, J.T. (ed.). 1980. *Mineral sands. Mining and Metallurgical Practices in Australasia. The Maurice Mawby Memorial Volume*. Australasian Institute of Mining and Metallurgy, Melbourne. pp. 733–789.
- WOODCOCK, J.T. and HAMILTON, J.K. (eds). 1993. *Mineral Sands. Australasian Mining and Metallurgy. The Maurice Mawby Memorial Volume*. 2nd edn. Australasian Institute of Mining and Metallurgy, Melbourne. vol. 2. pp. 1250–1328. ◆



Online spiral grade control

A.M. Russell¹

Affiliation:

¹Mintek, Randburg, South Africa.

Correspondence to:

D. Phillpotts

Email:

davidph@mintek.co.za

Dates:

Received: 22 Aug. 2019

Revised: 17 Dec. 2019

Accepted: 14 Jan. 2020

Published: February 2020

How to cite:

Russell, A.M.

Online spiral grade control.

The Southern African Institute of Mining and Metallurgy

DOI ID:

<http://dx.doi.org/10.17159/2411-9717/892/2020>

This paper was first presented at *The Eleventh International Heavy Minerals Conference*, 5–6 August 2019, The Vineyard, Cape Town, South Africa.

Synopsis

Online control of gravity spiral concentrators has not been widely implemented, despite the scale of industrial spiral circuits and the associated labour requirements of manually adjusting the spiral splitter positions to counter disturbances. Previous industrial and academic attempts at automation initially showed some promising results, but have thus far not resulted in the implementation of large-scale control system at industrial sites. A new technique making use of jets of process water for the control of spiral product quality is proposed, and which is suitable for retrofitting to existing spiral circuits. A test programme carried out at a chromite plant processing UG2 flotation tailing at a site on the eastern limb of the Bushveld Complex in South Africa showed that online control of the spiral plant concentrate grade using this technique is feasible.

Keywords

spiral concentrator, optimization, online control, grade-recovery tradeoff.

Introduction

Gravity spiral separators are widely utilized for the physical separation of a number of ore types. In the South African context, gravity spirals are used extensively in the concentration of chromite, coal, and mineral sands. While the process flow sheets and operating conditions vary widely between these industries, the nature of the spirals used across different sectors is similar.

The most common types of spirals consist of a trough that twists downward in a helix (typically clockwise) about a central axis. A slurry mixture is fed to the top of the spiral from a distributor. As the material travels down the length of the spiral, a combination of gravity and hydrodynamic forces (Mishra and Tripathy, 2010) results in the lighter material being lifted and carried to the outer portion of the spiral while the heavier material remains on the inner portion of the spiral (Matthews, Fletcher, and Partridge, 1999). The disproportionate movement of heavy and light minerals results in the formation of regions of increased concentrations of heavy and light minerals.

In some designs, auxiliary splitters along the length of the trough allow heavy material at intermediate points down the spiral to be removed and sent directly to a product stream, thereby freeing processing capacity on the lower part of the spiral. An adjustable product splitter is installed at the base of the spiral, typically with two or three splitter blades. The relative positions of these splitter blades determine the proportions of the separated material that will report to the individual product streams.

The relative positions of the product splitter blades at the base of the spiral, as well as the positions of the auxiliary splitters along the length of the spiral, are manually adjusted. Since spiral concentrator plants typically make use of vast numbers of spirals comprising different processing stages, the manual adjustment of these splitters to counter fluctuations in plant operating conditions is time-consuming and impractical (Vermaak *et al.*, 2008). To ensure that product grades are maintained within specifications, the splitters are often positioned conservatively, thus resulting in mineral losses.

Background

There have been a number of attempts at implementing online measurement and control on spiral separators and related equipment such as shaking tables. A number of investigations have involved the use of the visual appearance of materials as a proxy for product quality or separation effectiveness, in many ways mimicking the measurements made by the operators on processing plants.

A patent application by Welsh and Deurbrouck (1973), details the use of a photoelectric sensor coupled with a mechanical sorting device to optimize the recovery of valuable material on a shaking

Online spiral grade control

table. An investigation by Gold (1991) sought to develop an algorithm to detect the interface position between mineral bands on a spiral. Recently, Nienaber, McCoy, and Auret (2017) used a statistical learning approach to improve the reliability of mineral band detection. High detection success rates were achieved in the case of ilmenite interfaces; however, much lower success rates were achieved on chromite samples.

A model of the relationship between the mineral band position and spiral feed properties such as flow rate, grade, solids composition, and viscosity was developed by Vermaak *et al.* (2008) for material with a low slimes content. The model was also used to predict the mineral band position for a sample where the mineral band interface cannot be optically detected due to the presence of slimes. Such a model would be useful for process control purposes; however, the necessary measurements are not available on most spiral concentrator plants.

The use of inflatable bladders to divert material on a spiral surface to the desired product port is described in a European patent by Cooke (2009). Similarly, the work by Thornton and Carnell (2018) details the use of pneumatically actuated splitters mounted above a spiral trough to influence the proportion of material flowing to the product and reject ports. In that work, plans to incorporate this actuation mechanism with online density measurements are mentioned, but no online control results are provided.

The use of solids density gradients (based on electrical conductivity measurements) to inform the mechanical manipulation of the product splitters was detailed by Mohanty, Wang, and Zhang (2014).

The limited investigations into spiral control have so far not resulted in feasible, long-term industrial implementations, despite promising results under laboratory conditions or pilot-scale industrial conditions. It is believed that this is mainly due to the complexity and cost involved in scaling a control system from the laboratory scale to an industrial scale. Furthermore, the cost and challenges associated with the maintenance of a complicated control system conflict with the relatively low capital and maintenance costs associated with gravity spirals, further deterring operational management from applying such a control system to a spiral circuit.

Engineering design

Spiral actuation using spray nozzles

A number of previous attempts have sought to manipulate the mass flows of material to the different product ports on a spiral by moving the installed product and/or auxiliary splitters using mechanical devices. While moving the product splitter in this way emulates the manual process of moving the splitter, a number of practicalities have to be considered.

- ▶ Each mechanical actuator requires the supply of utilities, including instrument air and electrical power.
- ▶ Spiral plant conditions are quite harsh, with large amounts of fine material present. In some cases salt water is used as a process medium, exacerbating corrosion. The maintenance requirements for a large installation of mechanical actuators would be a significant burden for many plants.
- ▶ Mechanical actuators require robust mounting points about which to act, a rarity on spiral plants.
- ▶ The cost of fitting mechanical actuators to a bank of spirals will be beyond the reach of many operating plants.

A novel actuation system that makes use of multiple spray nozzles creating jets of process water to manipulate the flow of material on a bank of spirals has been developed and patented. The mode of action of the spray nozzles is illustrated in Figures 1 and Figure 2.

The mode of action of the spray nozzles is as follows.

- ▶ Nozzles are statically mounted in an optimal position above each of the concentrate and gangue material regions on the spiral, upstream from either a product or auxiliary splitter.
- ▶ The impact of the water on the spiral surface creates a blast zone that is triangular in shape with a stationary apex. The location of this zone determines the point from which material will be shifted.
- ▶ The pressure of the water feeding the spray nozzles is manipulated to alter the width of the blast zone, and hence the degree to which material is pushed towards the alternative product port.
- ▶ The overall effect is such that the blast zone alters the

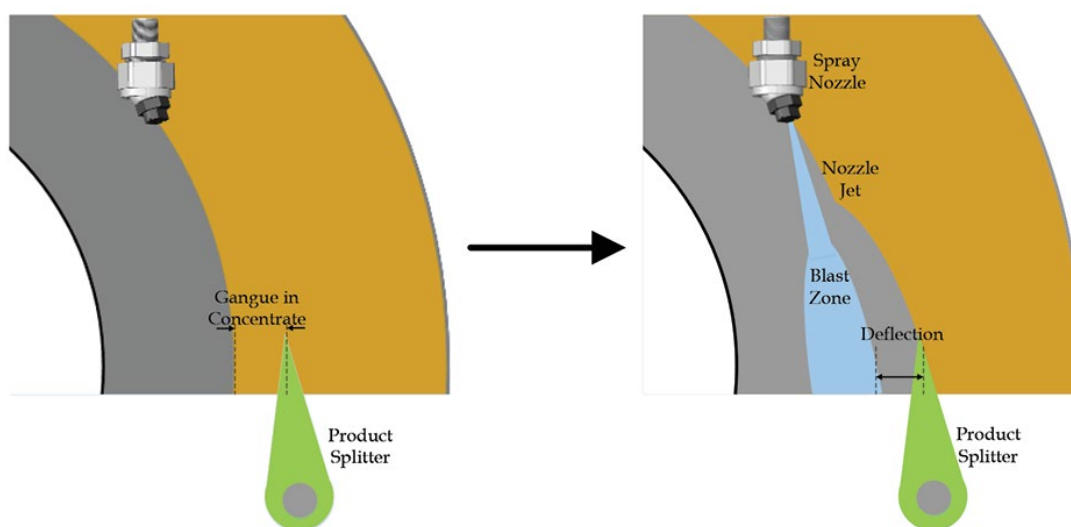


Figure 1—Mode of action of the spray nozzle on the material on the spiral when there is gangue material entering the concentrate product port

Online spiral grade control

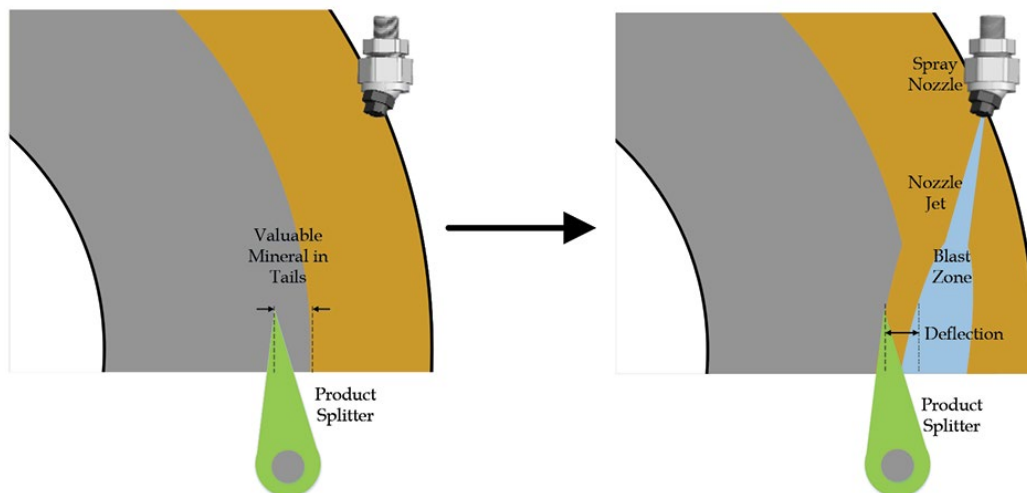


Figure 2—Mode of action of the spray nozzle on the material on the spiral when there is valuable mineral entering the tails port

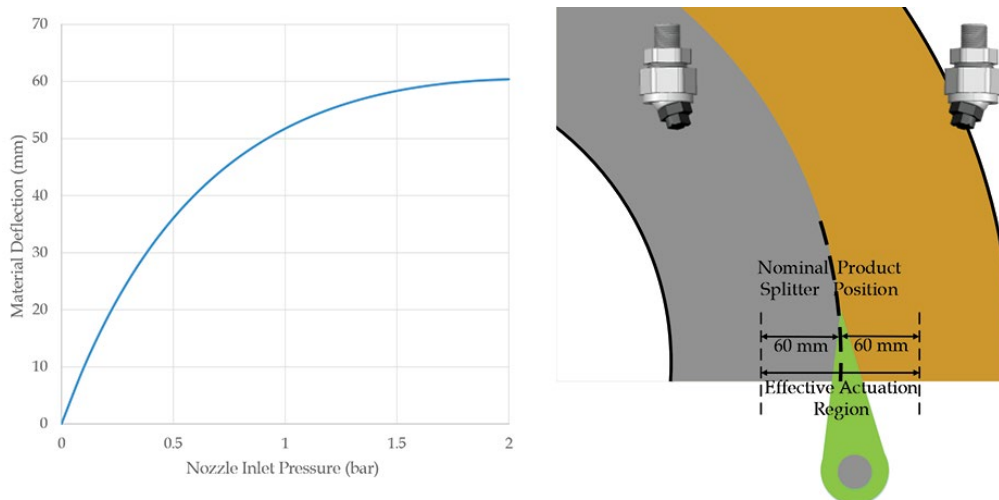


Figure 3—Theoretically achievable deflection versus the nozzle feed water pressure

trajectory of the material on the spiral to deflect it a certain distance from its original path. By varying the amount of deflection, the percentage of material entering a targeted port can be manipulated.

The amount of deflection theoretically achievable in relation to the nozzle feed pressure is shown Figure 3.

The maximum achievable deflection using the selected nozzles and the 2 bar water supply measured on industrial spirals is in the order of 60 mm (see Figure 3) and is similar to the magnitude of the splitter blade movements resulting from manual changes. Similarly, the resulting mass of material directed away from the concentrate or tails port is similar to that which would be achieved by a manual movement of the product splitter. Therefore, relatively large movements of the mineral band due to process disturbances such as density or feed flow rate fluctuations can be countered through the use of water spray nozzles.

The nozzles appear to be able to run for more than 2 months without requiring maintenance or replacement while using the test site's process water supply.

Laboratory tests show each nozzle requires the equivalent of 2 L/min or 2.5% of the total water on the spiral start for control within the typical variance of grade. This water also assists in

keeping the high-grade material mobile. This water addition can be compensated for by adding less dilution water elsewhere in the spiral circuit.

Integration with an online grade analyser

The spray nozzle mechanism described here was incorporated into an online control mechanism in combination with an online spectroscopic grade analyser. The analyser provides grade measurements every 15 seconds, which is at a much higher frequency than the concentrate grade variations experienced in practice, thereby providing sufficient closed-loop control performance.

The control system consists of the online grade analyser, a processing unit, a globe control valve, and a water distribution manifold. The opening of the control valve is determined by the difference between the online grade measurements and the applicable set-point. This in turn determines the pressure of the water feeding the spray nozzles, and hence the magnitude of the control action exerted on the spirals. The same control action is applied to all of the spirals in a bank, as it is assumed that differences in the performance of individual spirals can be ignored since they are fed from the same distributor. The schematic layout of the control system is shown in Figure 4.

Online spiral grade control

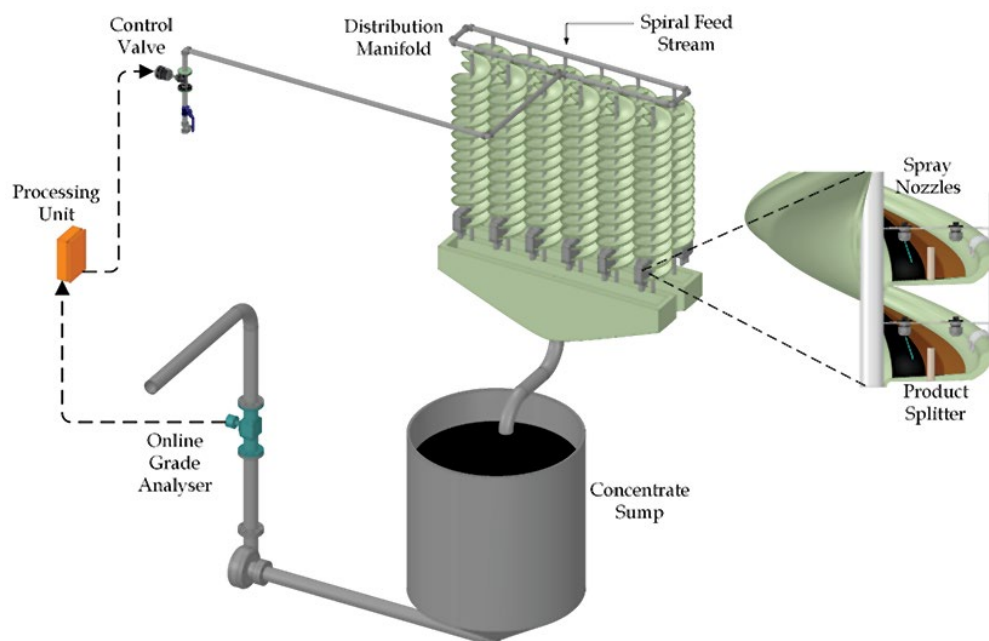


Figure 4—Schematic layout of the spiral grade control system

Experimental

Industrial test site

Testing of the control system was carried out on the chrome recovery spiral plant of a UG-2 platinum group metal concentrator on the eastern limb of the Bushveld Complex in South Africa. The spiral plant processes the final flotation tailings for the recovery of chromite. The process flow diagram of the plant is shown in Figure 5. The concentrates from both the mid-recleaner and recleaner banks are combined to form the final concentrate. The grade analyser measures this combined stream.

Under manual control conditions, the plant operators monitor the grade analyser reading and manually adjust the splitter positions of the mid-recleaner bank accordingly, albeit infrequently. This bank was therefore selected for the testing of the automated control system, as its manipulation would most closely resemble the manual control by the operators. Furthermore, this stream constitutes between 60% and 70% of the total concentrate mass flow, hence its manipulation will have a significant impact on the final concentrate grade. The mid-recleaner bank consists of 12 double-start spiral poles; a total of 24 spirals. Each of these spirals was fitted with a spray nozzle system for the test work.

Spray nozzle effectiveness

A sampling campaign was conducted to measure the maximum effectiveness of the spray nozzle system on the mid-recleaner bank of spirals. Here, the spray nozzles were activated at maximum control valve opening while crosscut samples of the feed, concentrate, and tails were taken from five separate spirals. These samples were analysed to determine the effects of the spray nozzles on the chromite grade and recovery of the specific spiral bank. This procedure was repeated for the scenario where the spray nozzles direct material towards the concentrate port, and for the scenario where they direct material towards the tails port.

Automated grade control

The online performance of the control system was evaluated by operating for 160 hours with the grade control system active, with comparisons drawn between the final concentrate grade stability observed under manual control conditions and under automated control conditions respectively. A 24-hour moving average of the concentrate grade was also calculated to represent the grade of the material on the product stockpile.

Operating results and discussion

The effect of spray nozzles on mineral grade and recovery

The maximum effectiveness of the spray nozzles when pushing material towards the tails port of the spiral is shown in Figure 6. Here it can be seen that while a 2.00% increase in the grade of the concentrate from the mid-recleaner bank was achieved, this was accompanied by a 15.05% decrease in the recovery of chromite for this bank. Simultaneously, the chromite feed grade to the mid-recleaner bank increased by 2.00% due to additional chromite-bearing material being pushed towards the tails port, and subsequently recycled back to the mid-recleaner bank via the re-scavenger concentrate. As a result, the upgrade ratio of the mid-recleaner bank remained largely unaffected.

The maximum effectiveness of the spray nozzles when pushing material towards the concentrate port is shown in Figure 7. Using the maximum control action, an 8.51% increase in chromite recovery to the concentrate was achieved, accompanied by a 2.33% decrease in the concentrate chromite grade. Here, the decrease in the concentrate grade was associated with a 1.30% decrease in the mid-recleaner feed chromite grade due to the reduced amount of chromite-bearing material being collected in the tails product, and thus recycled via the re-scavenger concentrate. The net result of this was a decrease in the chromite upgrade ratio of the mid-recleaner bank from 1.11 to 1.06.

Online spiral grade control

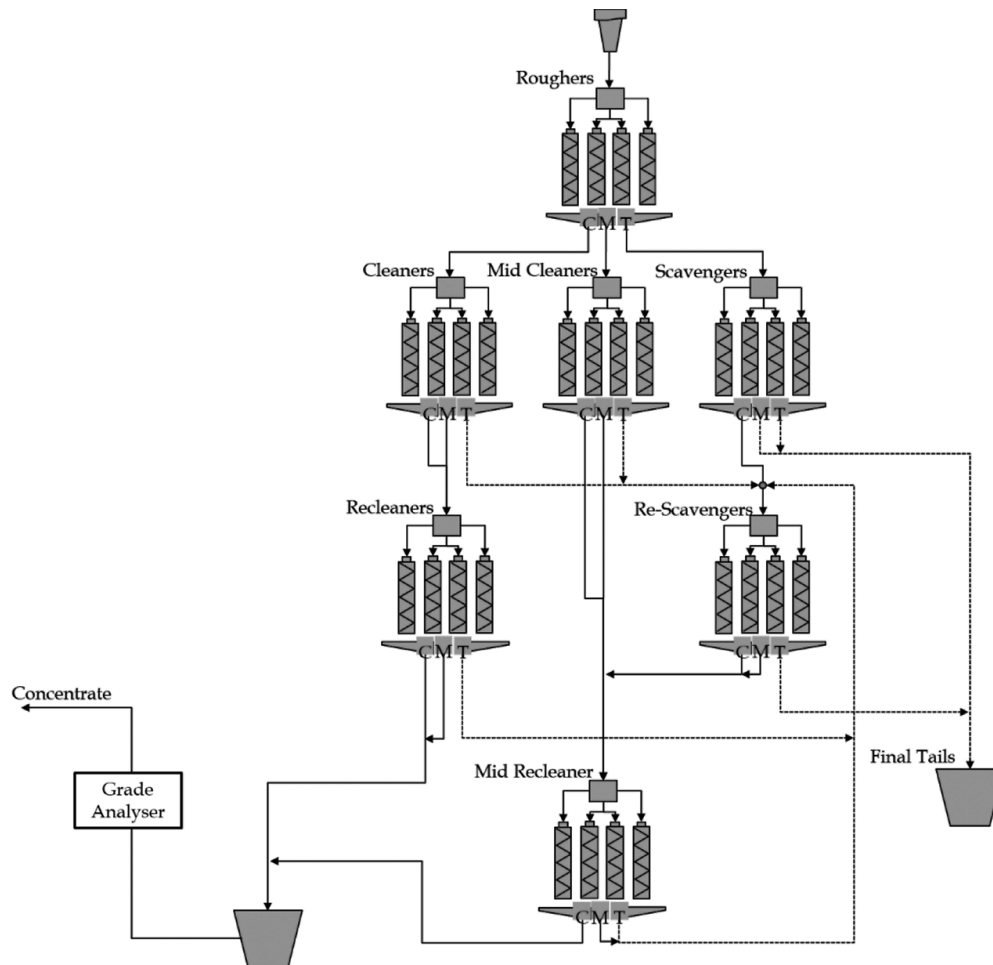


Figure 5—Chromite spiral plant process flow diagram

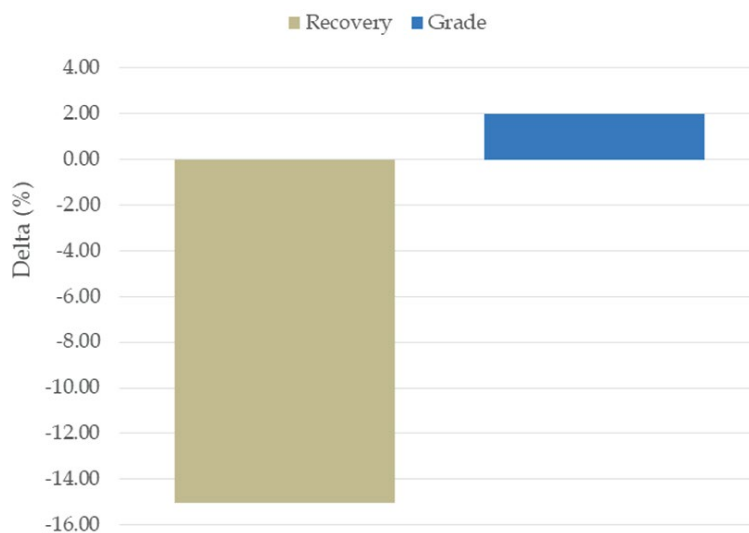


Figure 6—Effect of maximum control action pushing material towards the tails port

While the inverse relationship between the concentrate chromite recovery and chromite grade was to be expected, it is evident that the relationship between these two key variables

is nonlinear. The recovery decrease associated with an increase in concentrate grade is significantly greater (1.77 times) than the recovery increase associated with a decrease in concentrate

Online spiral grade control

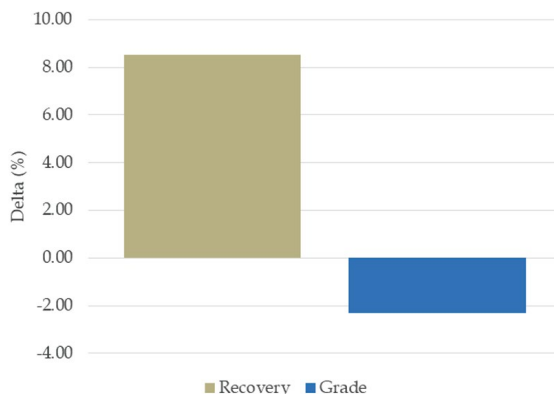


Figure 7—Effect of maximum control action pushing material towards the concentrate port

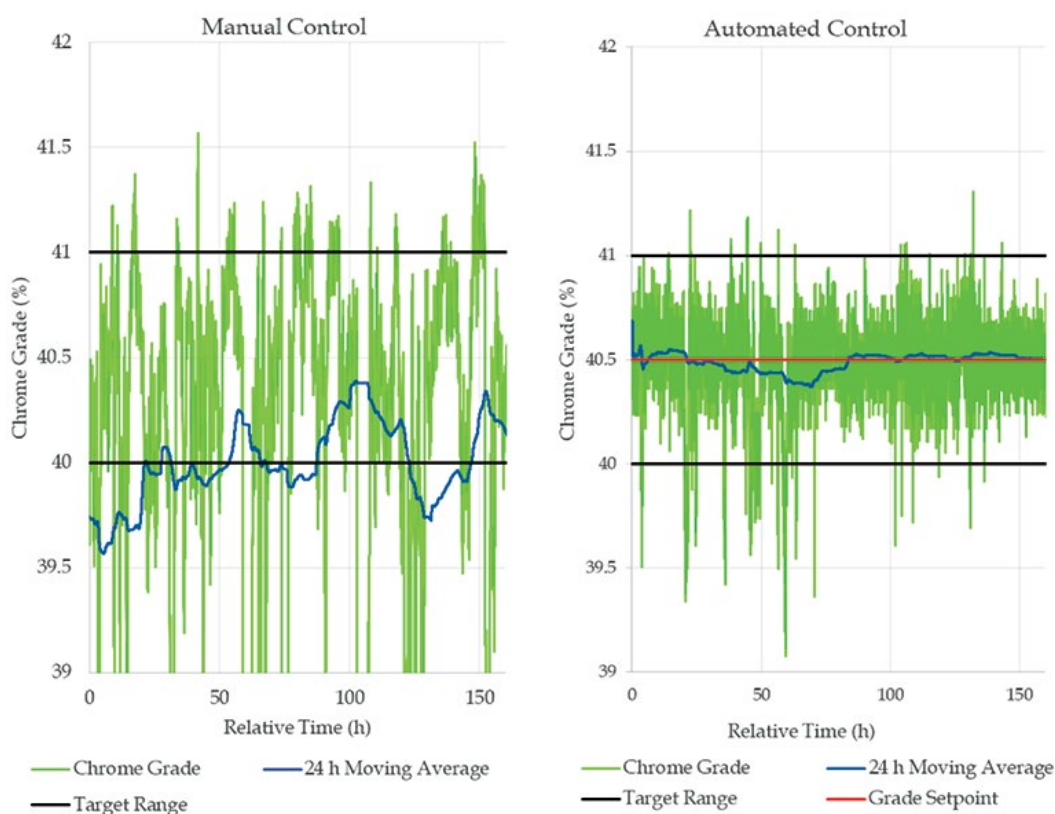


Figure 8—Comparison of the concentrate grade stability under manual and automated control

grade. This relationship is due to the nonlinear, sigmoidal profile of the chromite concentration across the spiral surface. Therefore, a balance between recovery optimization and grade protection should be sought.

Automated concentrate grade control

Subsequently, an automated grade control test was carried out to determine the effectiveness of the spray nozzles in controlling the final concentrate grade to a set-point. The results of this test are summarized in Figure 8 and Table I.

During the period under manual control, the moving average of the concentrate grade dropped below the minimum grade for the product specification. This indicates that the overall grade of the product on the stockpile was likely to be compromised in these instances.

Conversely, while under automated control, the moving average of the product grade was maintained within 0.15% of the set-point grade at all times, and well within the product specification limits. The standard deviation of the instantaneous concentrate grade was reduced more than threefold under automated control, while the standard deviation of the 24-hour moving average of the concentrate grade was reduced by more than sixfold, indicating significantly improved concentrate grade stability.

Chromite product specifications normally have a stipulated level for silica content, and therefore the control of the silica grade in the concentrate is also of concern in chromite production. Although control of the silica grade was not a primary objective of this control system, stability in the silica grade was brought about as a consequence of automated chromite grade control.

Online spiral grade control

Table I

Summary of the concentrate chromite grade stability under automated and manual control

Measure	Automated control	Manual control
Average grade (grade %)	40.49	40.24
Standard deviation (grade %)	0.20	0.70
24 h average standard deviation (grade %)	0.04	0.26

Table II

Summary of the concentrate silica grade stability under automated and manual control

Measure	Automated control	Manual control
Average silica grade (grade %)	3.90	3.77
Standard deviation (grade %)	0.32	0.58

Table II summarizes the silica content variability for the automated and manual control scenarios. The variability of the silica grade during automated control was less than half of that during manual control. By reducing the silica grade variability, the number of instances where the silica grade limits are violated will be reduced, lowering the risk of the product being out of specification.

Production benefits

A reduction in the variability of the concentrate grade will not significantly impact the productivity of a concentrator in isolation. However, improved stability will allow the safety margin between the targeted concentrate grade and the lower limit for the product specification to be reduced. In doing so, more valuable material can be recovered in the concentrate, thus increasing production and revenue.

For the test site evaluated here it is estimated, based on the UG2 tailings spiral performance characteristics presented by Dawson (2010), that a reduction in the target chromite grade of 0.5% would yield a 1.2% increase in chromite recovery to the concentrate. At a sale price of US\$150 per ton, this would result in a potential increase in revenue of around US\$52 000 per month.

Conclusions

A water-nozzle control system for gravity spiral concentrators has been developed and tested. Jets of water emanating from spray nozzles mounted above the spiral surface can be used to manipulate the mass flows of material between the ports of the spiral product splitter by displacing the material on the spiral surface about a blast zone. The dimensions of the blast zone can be altered based on the flow rate of the water leaving the spray nozzles, which is a function of the nozzle water pressure. By manipulating the water pressure, the degree of deflection of the material on the spiral surface can be controlled, to a maximum of 60 mm at a water pressure of 2 bar.

When applied to a chromite recleaner bank of spirals, the water nozzle system was capable of increasing the concentrate chromite grade of that specific bank of spirals by a maximum of 2.00% with an associated decrease in chromite recovery of 15.05% when grade protection was targeted. Conversely when chromite recovery protection was targeted, the concentrate chromite grade was decreased by a maximum of 2.33% with an associated increase in chromite recovery of 8.51%.

The water nozzle system was tested on an industrial site, in conjunction with an online grade analyser, forming a closed-loop control system. During the test period, the variability of the measured concentrate grade was decreased significantly, with the standard deviation of the instantaneous concentrate grade being reduced more than threefold compared with the manual control scenario. Furthermore, the standard deviation of the 24 hour moving average concentrate grade was reduced more than sixfold, indicating vastly improved stability of the product quality on the stockpile. In addition, the stability of the silica content of the concentrate was improved, with a twofold reduction in the standard deviation during automated control.

The improved grade stability could allow a plant to reduce the safety margin between the targeted concentrate grade and the lower limit of the product specification, thereby allowing more valuable mineral to be recovered. For this test site, the benefit derived from reducing the concentrate target grade by 0.5% would result in a recovery improvement of 1.2%, which would yield approximately US\$52 000 per month in additional revenue.

References

- COOKE, G. 2008. An adjustable spiral concentrator. European patent EP20090802279.
- DAWSON, N.F. 2010. Experiences in the production of metallurgical and chemical UG2 chromite concentrates from PGM tailings streams. *Journal of the Southern African Institute of Mining and Metallurgy*, vol. 110. pp. 683-690.
- GOLD, D. 1991. The investigation and design of a machine vision system for the detection and control of the separation in a spiral ore concentrator. MSc thesis, University of Cape Town, South Africa.
- MATTHEWS, B.W., FLETCHER, C.A.J., and PARTRIDGE, T.C. 1999. Particle flow modelling on spiral concentrators. *Proceedings of the Second International Conference on CFD in the Minerals and Process Industries*, Melbourne, Australia, 6-8 December 1999. CSIRO Minerals, Melbourne. pp. 211-216.
- MISHRA, B.K. and TRIPATHY, A. 2010. A preliminary study of particle separation in spiral concentrators using DEM. *International Journal of Minerals Processing*, vol. 94. pp. 192-195.
- MOHANTY, M.K., WANG, A.M., and ZHANG, B.J. 2014. Automated system for coal spiral. US patent 20140238096 A1.
- NIENABER, E.C., MCCOY, J.T., and AURET, L. 2017. Spiral concentrator interface monitoring through image processing: A statistical learning approach. *IFAC PapersOnLine*, no. 50-52. pp. 53-58.
- THORNTON, C. and CARNELL, M. 2018. Practical application of spiral automation technology. *Proceedings of the 17th Australian Coal Preparation Conference and Exhibition*. Australian Coal Preparation Society, Brisbane. pp. 271-283.
- VERMAAK, M.K.G., VISSER, H.J., BOSMAN, J.B., and KREBS, G. 2008. A simple process control model for spiral concentrators. *Journal of the Southern African Institute of Mining and Metallurgy*, vol. 108, no. 3. pp. 147-154.
- WELSH, R.A. and DEURBROUK, A.W. 1973. Product separator. US patent 3933249. ◆



HYDRAULIC BREAKERS

FXJ275



FXJ125 FXJ175 FXJ275 FXJ375 FXJ475

Distribution and Product Support by:



Download any QR reader/scanner from the Google Play or Apple App Store

Branches and Dealers throughout South Africa and Southern Africa

ELB PROMISE



Right Job



Right Time



Right Way

www.elbequipment.co.za

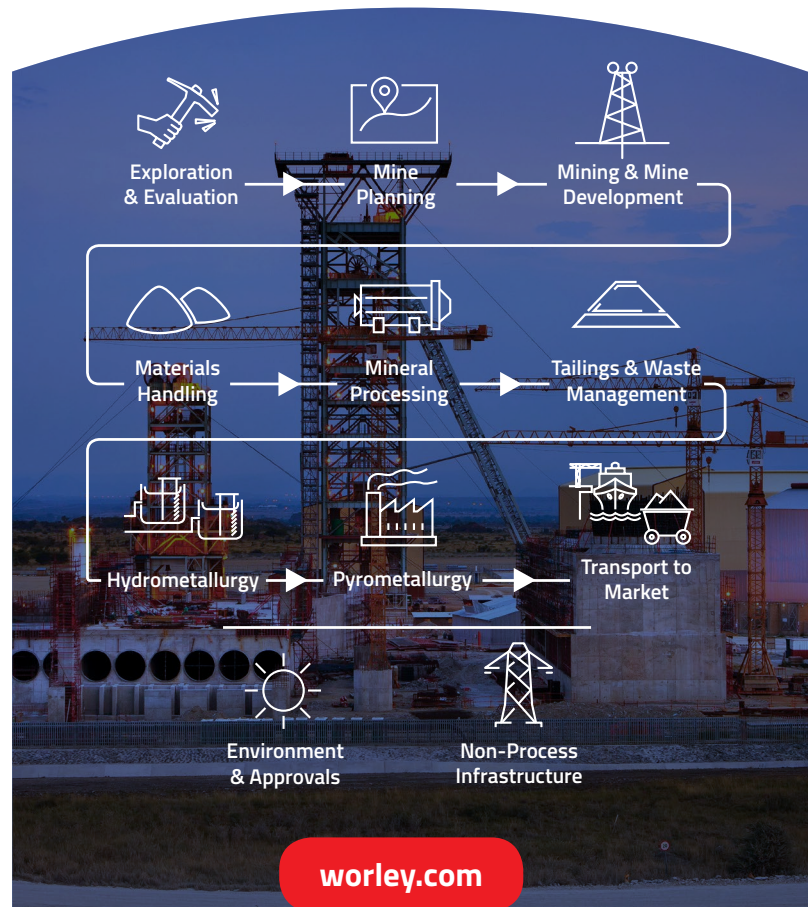


+27 (0)11 306 0700
elb@elbquip.co.za

Engineering and project management services to the mining industry

- Innovative solutions
- Efficient digital asset management from design through construction to operations
- Concept-to-completion
- Design expertise
- Project capabilities for all minerals
- Mining centre of excellence

Visit Worley
Mining Indaba 3- 6 February 2020
Stand 504





A literature review and interpretation of the properties of high-TiO₂ slags

H. Kotzé¹

Affiliation:

¹Consensi Consulting, Mtunzini, South Africa.

Correspondence to:

H. Kotze

Email:

hanlie.k@consensi.co.za

Dates:

Received: 23 Aug. 2019

Revised: 24 Jan. 2020

Accepted: 13 Feb. 2020

Published: February 2020

How to cite:

Kotzé, H.

A literature review and interpretation of the properties of high-TiO₂ slags.

The Southern African Institute of Mining and Metallurgy

DOI ID:

<http://dx.doi.org/10.17159/2411-9717/894/2020>

ORCID ID:

H. Kotzé

<https://orcid.org/0000-0002-8937-7511>

This paper was first presented at *The Eleventh International Heavy Minerals Conference*, 5–6 August 2019, The Vineyard, Cape Town, South Africa.

Synopsis

The properties of high-TiO₂ slags are markedly different from those of many other metallurgical slags. The objective of this paper is twofold: firstly, to assemble in one document the TiO₂ slag properties, including Ti³⁺/Ti⁴⁺ ratio, liquidus temperatures, heat capacity, density, viscosity, thermal conductivity, and electrical conductivity: all expressed in terms of temperature and composition dependency. Secondly, this paper attempts to correlate published experimentally measured data with theoretically based parameters, which will enable the application of the measured properties to wider slag compositions within the pseudobrookite-TiO₂ slag system.

Keywords

high-TiO₂ slag, properties.

Introduction

Slag properties are an essential tool in problem solving, both in equipment design and metallurgical process control. Experimental work on high-TiO₂ slags is particularly difficult because of their chemically corrosive nature and compositional sensitivity to oxygen partial pressure. While ample publications are available and are still being produced for silicate-based slags, comparatively few results are available for high-TiO₂ slags. The objective of this work is firstly to summarize the essential properties for liquid TiO₂ slags. Secondly, an attempt is made to derive correlations from the published experimental work which are based on a theoretical concept. In this way, it is believed that the experimental data can be cautiously extrapolated to other high-TiO₂ slags. To this end, a set of typical high-TiO₂ slags based on a data-set published in earlier work (Kotze and Pistorius, 2010) is used throughout this paper. The chemical composition of this set is given in Table I. Although 94%TiO₂ is not considered 'typical', it was included in the example slags because many producers migrate to higher TiO₂ slags.

The experimental data cited in this work is by no means claimed to be all-inclusive. Glimmers of work done in Eastern European countries are present, though not easily interpreted by English-speaking researchers. On occasion experimental data was not used because of a discrepancy in the data or experimental method.

Slag properties

Ti³⁺/Ti⁴⁺ ratio

Titania slag compositions are typically expressed as TiO₂ because analytical methods measuring the total titanium are fast and less cumbersome than the wet chemistry titration method required to measure Ti³⁺ (Tranell, Ostrovski, and Jahanshahi, 2002). When appreciable amounts of Ti₂O₃ are included in the TiO₂ value, titania is expressed as the equivalent TiO₂. In these instances, slag assays exceed 100 because the oxygen is overestimated. The assay total is therefore an indication of the level of reduction. Previous attempts by the author to correlate measured Ti³⁺ values with assay totals yielded unsatisfactory results.

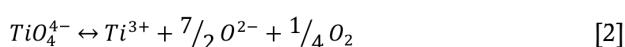
The balance between Ti⁴⁺ and Ti³⁺ follows Reaction [1] and like other transition elements, it is governed by a redox reaction such as the O-type behavior of Reaction [2] (Tranell, Ostrovski, and Jahanshahi, 2002). The Ti³⁺/Ti⁴⁺ ratio is therefore expected to be dependent on the oxygen partial pressure and the oxygen activity in the slag bath. Tranell and co-workers (Tranell, Ostrovski, and Jahanshahi, 1997, 2002) investigated these relationships in TiO₂-Ti₂O₃-SiO₂-CaO slags and found the Ti³⁺/Ti⁴⁺ ratio to depend on the oxygen partial pressure raised to the power of 0.21 (Tranell, Ostrovski, and Jahanshahi, 1997) and 0.23 (Tranel, Ostrovski, and Jahanshahi, 2002). Using optical basicity to represent oxygen activity, they derived a correlation using temperature, oxygen partial pressure, and optical basicity to calculate the Ti³⁺/Ti⁴⁺ ratio. This correlation yielded good results with all the slags they investigated, but not with those of other researchers.

A literature review and interpretation of the properties of high-TiO₂ slags

Table I

Compositions of example industrial TiO₂ slags based on the data-set given by Kotze and Pistorius, 2010

	TiO ₂ _{eq}	FeO	SiO ₂	Al ₂ O ₃	CaO	MgO	MnO
Slag 1	94.0	4.0	1.5	1.5	0.10	1.0	2.1
Slag 2	91.0	7.0	1.4	1.4	0.10	1.0	2.0
Slag 3	88.0	10.0	1.2	1.3	0.10	1.0	1.9
Slag 4	85.0	13.0	1.1	1.2	0.10	0.9	1.8
Slag 5	82.0	16.0	0.9	1.1	0.10	0.8	1.7



In this work, electronic polarizability was investigated as an alternative measure to predict the activity of oxygen. Electronic polarizability is described as the ‘ability of oxygen to transfer electron density to surrounding cations’ (Dimitrov and Komatsu, 2010). It is a measure of the propensity of compounds to donate charge from oxygen ions to the surrounding electron cloud (Duffy and Ingram, 1976). In this context, Ca²⁺ with a cation polarizability of 1.57 Å³ is ‘generous’ while Si⁴⁺ at 0.284 Å³ is comparatively ‘stingy.’ A few mutually exclusive data-sets exist to calculate electronic polarizability. The data used in this work is based on the large data-set of dynamic polarizabilities published by Shannon and Fischer (2016) which includes a value for the cation polarizability of Ti³⁺. The Ti³⁺/Ti⁴⁺ ratios of the CaO-SiO₂-TiO_x slags from Tranell were found to correlate well with the ratio of the polarizabilities of Ca²⁺ and Si²⁺, $R_\alpha = \frac{X_{CaO} \alpha_{Ca^{2+}}}{X_{SiO_2} \alpha_{Si^{4+}}}$ (polarizability Å³; mole fraction X). This result corroborates the polarizability ratio of Ca²⁺ and Si⁴⁺ as a measure of the oxygen activity in the bath. The Ti³⁺/Ti⁴⁺ ratios of the slags Tranell studied were subsequently calculated using a correlation with two parameters: the experimental oxygen partial pressure and the polarizability ratio R_α . Figure 1 shows the results of this correlation to compare well with the experimental Ti³⁺/Ti⁴⁺ ratios.

The validity of the correlation between oxygen partial pressure, electronic polarizability, and Ti valency was tested against industrial TiO₂ slags using measurements reported by Geldenhuys and Pistorius (1999). These workers measured the oxygen partial pressure in pilot plant TiO₂ slags and reported the

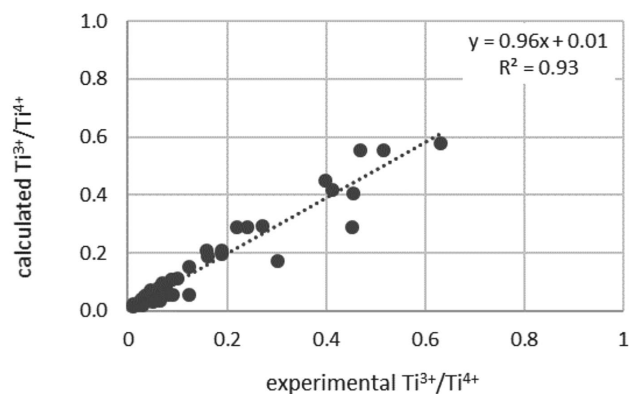


Figure 1 – Comparison of the experimental Ti³⁺/Ti⁴⁺ ratios (Tranell, Ostrovski, and Jahanshahi, 2002) against the calculated Ti³⁺/Ti⁴⁺ ratio

TiO₂ and Ti₂O₃ values of the slags at the time of measurement. Their measured oxygen partial pressures in the slags are plotted as the circles in Figure 2. Since the full assays of the slags used in the Geldenhuys study were not given, their results are compared with the calculated TiO₂ and Ti₂O₃ values of the example slags in Table I using the correlation derived from the work by Tranell. This is not ideal, but a reasonable replacement, as the impurity levels of the ilmenites used in the Geldenhuys study and those used in the Kotze (Kotze and Pistorius, 2010) study – on which the example slags were based were similar. The calculated results shown with the solid and broken lines in Figure 2 compare well with the experimental data. It is worthwhile to note that several studies found the same Ti³⁺/Ti⁴⁺ ratios in industrial slags as were found in the Geldenhuys pilot plant study. Few of these results are published such as the industrial slag data points given in Figures 4 to 6, but many are unpublished due to intellectual property rights.

The dependency of the Ti³⁺/Ti⁴⁺ ratio on the oxygen partial pressure and CaO/SiO₂ ratio (based on the work by Tranell) is summarized in Figure 3. Lower oxygen partial pressures lead to greater reduction and hence higher Ti³⁺/Ti⁴⁺ ratios. Higher CaO/SiO₂ ratios create higher oxygen activity, which in turn decreases the Ti³⁺/Ti⁴⁺ ratio. In a given smelting process the oxygen partial pressure is largely governed by the Fe-FeO equilibrium in the slag (Pistorius, 2007), while the CaO/SiO₂ ratio is determined by the raw material quality.

In an earlier paper Tranell also reports MgO to affect the Ti³⁺/Ti⁴⁺ ratio (Tranell, Ostrovski, and Jahanshahi, 1997). A correlation including the polarizability of Mg²⁺ did not fit the industrial data. The industrial data was a small set, though, and it does not exclude the potential of MgO (as possibly Al₂O₃) to – similarly to CaO and SiO₂ influence the Ti³⁺/Ti⁴⁺ ratio. Future work will investigate this possibility.

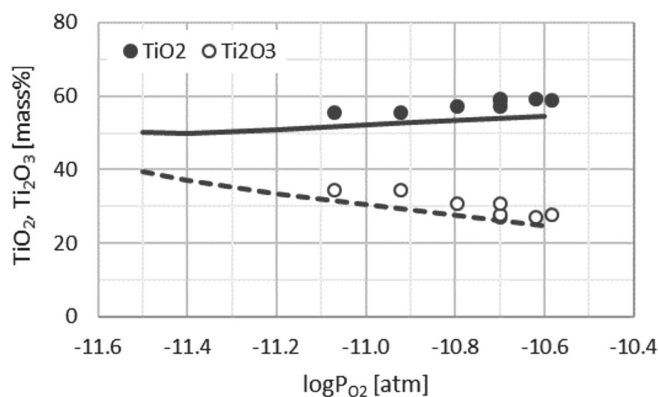


Figure 2 – Measured oxygen partial pressure in TiO₂ slags against equivalent TiO₂. Circles: pilot plant measurements (Geldenhuys and Pistorius, 1999), line: calculated in this work using the correlation derived from the work of Tranell, Ostrovski, and Jahanshahi (2002)

A literature review and interpretation of the properties of high-TiO₂ slags

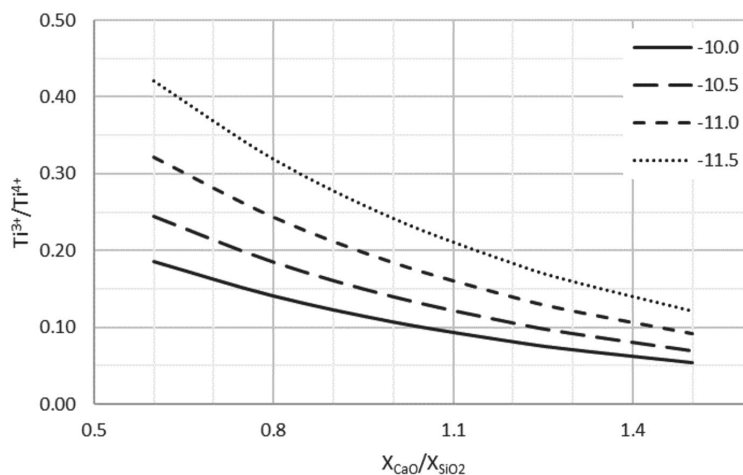


Figure 3—Ti³⁺/Ti⁴⁺ ratios calculated from the oxygen partial pressure (log Po₂ [atm] given in the legend) and CaO/SiO₂ molar ratio

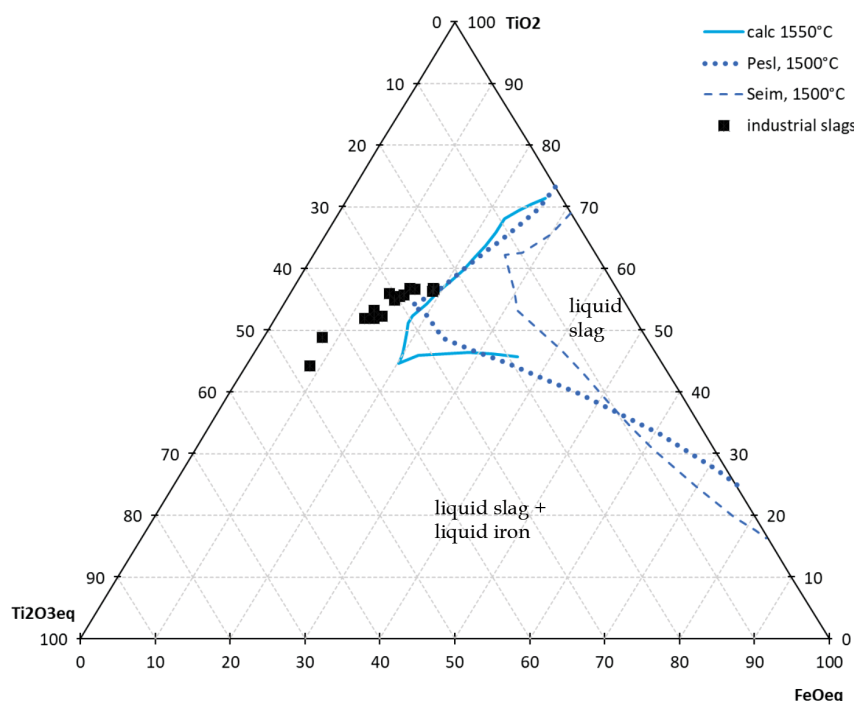


Figure 4—Liquidus isotherms at 1500°C from Pesl - dotted lines (Pesl and Eric, 1999), and Seim - broken lines (Seim, 2011). The solid line represents the isotherm for 1550°C calculated from the thermodynamic data of Eriksson (Eriksson and Pelton, 1993; Eriksson and Pelton, 1996). Axes are in mass%

Liquidus temperatures

Pesl and Eriç (1999) conducted experimental work on slags of the TiO₂-Ti₂O₃-FeO system, controlling the oxygen partial pressure with CO-H₂ gas mixtures, and calibrating slag samples at 1500°C and 1600°C in platinum or molybdenum crucibles for 6 to 8 hours before rapidly quenching them to capture the high-temperature phases. Their predicted liquidus isotherms for 1500°C and 1600°C are reproduced for axes in mass% and given in Figure 4 and Figure 5 as dotted lines. No accuracy or error prediction was reported.

Seim melted slags in an induction furnace with a slag freeze-lining to protect the crucible walls (Seim, 2011; Seim and Kolbensen, 2010). Experiments were conducted in an Ar atmosphere, using titanium metal and haematite additions to control the level of reduction. Liquidus temperatures were determined from cooling curves captured by a spectroprometer

looking down onto the upper surface of the slag. The tolerances for individual measurements on the iron-saturated samples are given as 4.9°C to 33.3°C. Seim modelled a liquidus surface for the FeTiO₃-Ti₂O₃-TiO₂ system using the measured liquidus temperatures of the iron-saturated slags and expanding the thermodynamic data-set with two optimized ternary parameters. The model is considered to accurately predict the measured liquidus temperatures of the iron-saturated slags. The liquidus temperature measurements on the iron-unsaturated samples were unexpectedly and unexplainably lower and not used in the modelling exercise. Despite this, the measured liquidus temperatures of the iron-unsaturated slags plot on average 108°C below the modelled liquidus and 59°C above the modelled solidus temperatures. The model isotherms for 1500°C, 1600°C, and 1700°C were reproduced to have TiO₂, Ti₂O₃, and FeO as corners of the ternary and are shown in Figure 4, Figure 5, and Figure 6 as broken lines.

A literature review and interpretation of the properties of high-TiO₂ slags

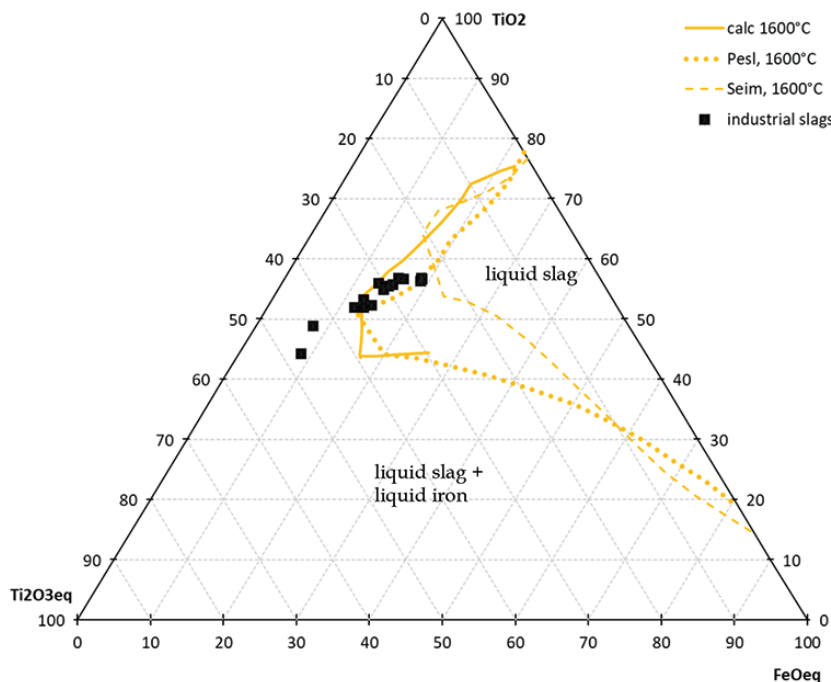


Figure 5—Liquidus isotherms at 1600°C from Peisl - dotted lines (Peisl and Eric, 1999), and Seim – broken lines (Seim, 2011). The solid line represents the isotherm for 1600°C calculated from the thermodynamic data of Eriksson (Eriksson and Pelton, 1993; Eriksson and Pelton, 1996). Axes are in mass%

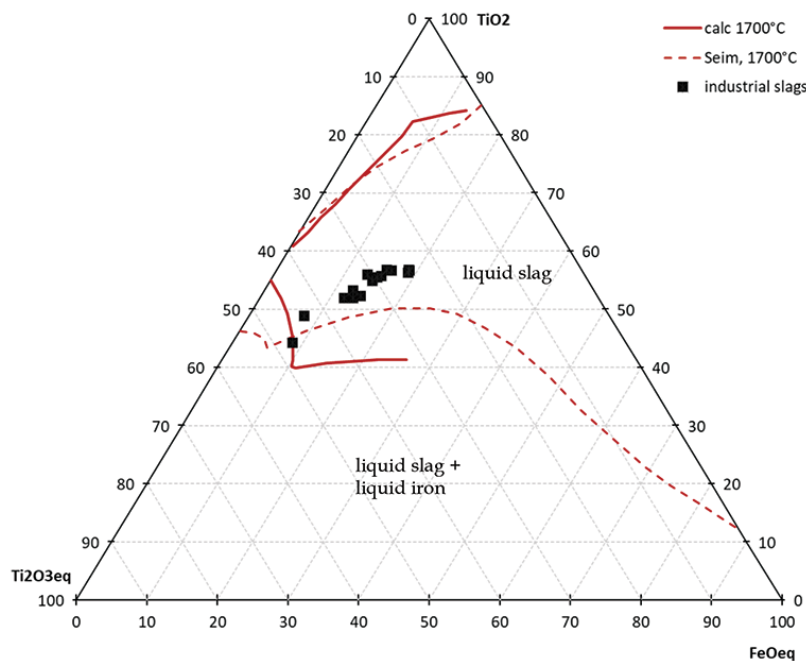


Figure 6—Liquidus isotherms at 1700°C Seim – broken lines (Seim, 2011). The solid line represents the isotherm for 1700°C calculated from the thermodynamic data of Eriksson (Eriksson and Pelton, 1993; Eriksson and Pelton, 1996). Axes are in mass%

Thermodynamic data for the binary systems TiO₂-FeO and Ti₂O₃-TiO₂ were published by Eriksson and Pelton (1993) and they illustrated the validity of using this data to calculate the solid phase relationships in the ternary system below 1400°C. They did not publish liquidus predictions (Eriksson and Pelton, 1996). The maximum inaccuracy of the data was given as ±20°C. In the present work the thermodynamic data from Eriksson were used in the Modified Quasichemical Approach (Pelton and Blander, 1986) to calculate the liquidus temperatures in the TiO₂-Ti₂O₃-FeO system. A temperature, dependent activity coefficient was calculated for the pseudobrookite M₃O₅ phase

from the experimental data by Peisl (Peisl and Eric, 1999). The calculated liquidus isotherms for 1550°C, 1600°C, and 1700°C are shown Figure 4, Figure 5, and Figure 6 as solid lines. The low-temperature trough these isotherms along approximately 55%TiO₂ is in line with the experimentally measured low melting point measured in argon by Brauer and Littke (1960) for the TiO₂-Ti₂O₃ binary: 1660°C between TiO_{1.70} and TiO_{1.75} (43% to 53% TiO₂).

All three isotherm sets show a liquid slag field with (i) an upper phase boundary with the liquid slag + TiO_x phase field, (ii) a lower phase boundary with the liquid slag + liquid iron phase

A literature review and interpretation of the properties of high-TiO₂ slags

field, and (iii) a boundary with the liquid slag + M₃O₅ + liquid metal phase field. The two upper phase boundaries at 1700°C (*i.e.* the calculated, and Seim prediction) are very similar, and so are the upper phase boundaries of these two sets for 1500°C and 1600°C up to 20%Ti₂O₃ – refer to Figure 7. Beyond 20% Ti₂O₃ the calculated isotherms predict the liquid slag phase field to extend towards TiO₂.Ti₂O₃, similar to the dotted 1600°C and 1500°C isotherms by Pesl. The lower boundary separating the liquid slag from the liquid slag + liquid iron phase field, is predicted to lie closer to the TiO₂ apex by the Seim model.

To place the liquidus isotherms in Figures 4 to 6 in context with industrial slags, compositions of typical as-tapped TiO₂ slags from three different smelters (Pistorius, 2002) are shown as dark squares on the ternaries. For the high-FeO slags the dotted 1500°C and 1600°C upper boundary isotherms by Pesl imply a 100°C drop in liquidus with a ±1% change in FeO (approximately 19% to 18%). This seems an unlikely discontinuity in the known FeO-liquidus temperature relationship of the system. The more likely case is a more gradual temperature gradient as shown by the calculated 50°C spaced isotherms in Figure 7. These are also in agreement with the isotherms by Seim – at least up to 20%Ti₂O₃.

According to the calculated isotherms the industrial slag series have liquidus temperatures ranging from 1550°C for 20%FeO_{eq} up to 1700°C for ±9%FeO_{eq}, while the broken line isotherms (Seim model) indicate a liquidus range starting somewhere above 1600°C to just over 1700°C. Given the stated tolerances and inaccuracies, the different sets of isotherms are regarded to give similar results, especially in the area of concern for typical industrial TiO₂ slags. It will be worthwhile, though, to clarify the discrepancy in the size of the liquid slag phase fields as predicted by the different sets of isotherms.

Figure 7 shows how the liquidus increases with decreasing %FeO: higher reduction yields a higher slag liquidus. However, for a given FeO content, *e.g.* 10mass%, higher reduction will increase the Ti³⁺/Ti⁴⁺ ratio, which will decrease the liquidus, until the Ti³⁺/Ti⁴⁺ ratio crosses the low liquidus trough between TiO₂ and Ti₂O₃. On the lower TiO₂ and higher Ti₂O₃ side of this trough, the liquidus will increase again with increasing Ti³⁺/Ti⁴⁺. In practice, where a process receives a stable ilmenite quality, higher reduction will lead to a simultaneous decrease in FeO and an increase in Ti₂O₃, and the net effect will be an increase in liquidus, though smaller in size than what would have resulted from a decrease in FeO only.

To apply phase temperature behaviour from the ternary FeO-TiO_x (Figure 7) system to industrial slags, the gangue oxides are grouped into the so-called equivalent FeO and equivalent Ti₂O₃ values, calculated with Equations [3] and [4] (percentages as mass%, molecular weight M [g/mol]) (Pistorius, 2007). FeO_{eq} and Ti₂O₃_{eq} were shown to correlate, following the stoichiometric relationship of the pseudobrookite solid solution TiO₂.(Ti³⁺+Al³⁺+Cr³⁺)₂O₃ (Fe²⁺Mg²⁺Mn²⁺)O.2TiO₂, in short referred to as M₃O₅. Researchers have shown MgO, MnO, and Al₂O₃ to partition to the dominant M₃O₅ (pseudobrookite) phase thereby stabilizing this phase (Borowiec, 2009; Pistorius, 2002). There are indications that MnO does not fully partition to the M₃O₅ phase but that a potentially significant portion thereof separates to the silicate phase (Seim, 2011; Pesl and Eric, 2002). Without quantitative data on the behaviour of MnO though, the correlation showed by Pistorius is followed. The liquidus isotherms in Figure 7 can therefore applied to industrial slags when the FeO and Ti₂O₃ are expressed in their equivalent forms. The FeO_{eq} and Ti₂O₃_{eq} of the example slags (Table I), together with their calculated liquidus temperatures, are listed in Table II.

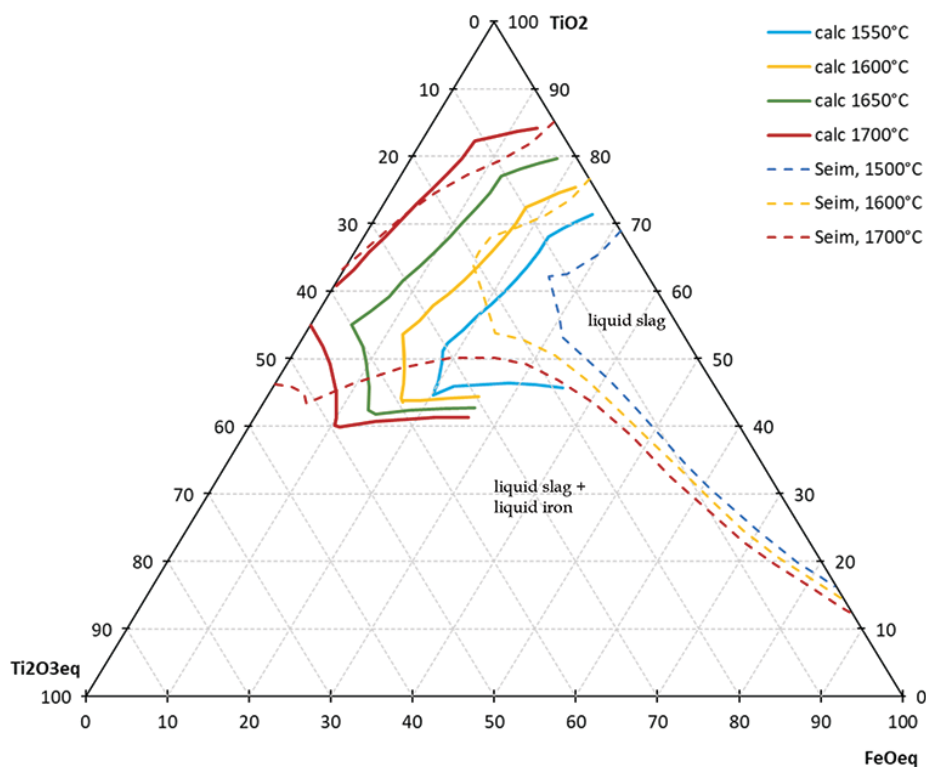


Figure 7—Calculated liquidus isotherms between 1550°C and 1750°C at 50°C intervals. Axes are in mass%

A literature review and interpretation of the properties of high-TiO₂ slags

Table II

Calculated liquidus temperatures (°C) of the example industrial slags from Table I, using the FeO_{eq} and Ti₂O_{3 eq} [mass%]

	TiO _{2 eq}	TiO ₂	FeO _{eq}	Ti ₂ O _{3 eq}	T _{liquidus}
Slag 1	94.0	50.1	7.9	40.9	1628
Slag 2	91.0	49.9	10.8	38.3	1604
Slag 3	88.0	51.0	13.7	34.6	1588
Slag 4	85.0	52.8	16.4	30.2	1571
Slag 5	82.0	54.5	19.1	25.8	1555

$$\%FeO_{eq} = \%FeO + \left(\frac{\%MgO}{M_{MgO}} + \frac{\%MnO}{M_{MnO}} \right) M_{FeO} \quad [3]$$

$$\%Ti_2O_{3 eq} = \%Ti_2O_3 + \left(\frac{\%Cr_2O_3}{M_{Cr_2O_3}} + \frac{\%V_2O_5}{M_{V_2O_5}} + \frac{\left(\%Al_2O_3 - \frac{SiO_2}{3} \right)}{M_{Al_2O_3}} \right) M_{Ti_2O_3} \quad [4]$$

High-TiO₂ slags have a narrow gap between liquidus and solidus temperatures. Seim measured the liquidus and solidus temperatures on synthetic slags using differential thermal analysis/thermal gravity analysis (Seim, 2011). For a TiO₂-Ti₂O₃-5.6%FeO slag the liquidus and solidus were 1696°C and 1682°C respectively, and for a TiO₂-Ti₂O₃-16.9%FeO slag, 1664°C and 1644°C respectively. These results imply a narrow temperature gap of 14°C to 20°C between liquidus and solidus. Borowiec (2009) measured solidus and liquidus temperatures on slags with 11–12%, 6–7%, and 2% gangue impurities (the publication gives the impurities for the first and third slag, while impurities for the second slags were deduced from other publications using the same slag). The temperature differences were 136°C, 83°C, and 66°C respectively (Borowiec, 2009). Provided the SiO₂ content in the gangue impurities is low (*i.e.* <5% in >10% total gangue, and <3% in <7% total gangue), these differences are indications of the solidus temperatures of high-TiO₂ slags.

Heat capacity

The heat capacities of liquid TiO₂ slags were reported by Kotze and Pistorius (2010) and are repeated here, Equation [5] (*C_p* in J/kg.K). The heat capacity values for the example slags in Table I are listed in Table III.

$$C_p = 0.0561(\%FeO_{eq})^2 - 3.3668(\%FeO_{eq}) + 1044.4 \quad [5]$$

Density

With most liquid slag systems, a density calculation needs to incorporate the enthalpy of mixing. For slags with only a small deviation from ideality, such as high-TiO₂ slags (Eriksson and Pelton, 1993; Gaskell, 2008, p. 247), a weighted average of the densities of the pure liquids suffices. The density of liquid TiO₂ was taken as 3.3 g/cm³ at 1600°C from the measurements by Dingwell (1991). The density of liquid Ti₂O₃ was measured by Ikemiya *et al.* under an Ar-H₂ gas mixture (1993); extrapolated to 1600°C, Ti₂O₃ has a density of 4.0 g/cm³. Finally, the density of liquid FeO was taken as 4.4 g/cm³ at 1600°C based on the measurements done by Xin *et al.* (2019). The resultant calculated densities for the example slags (Table I) are given in Figure 8. It is concluded that typical high-TiO₂ slags have a density range

Table III

Heat capacities (J/kg.K) of the example slags in Table I, liquid phase

Slag 1	Slag 2	Slag 3	Slag 4	Slag 5
1021	1015	1009	1004	1001

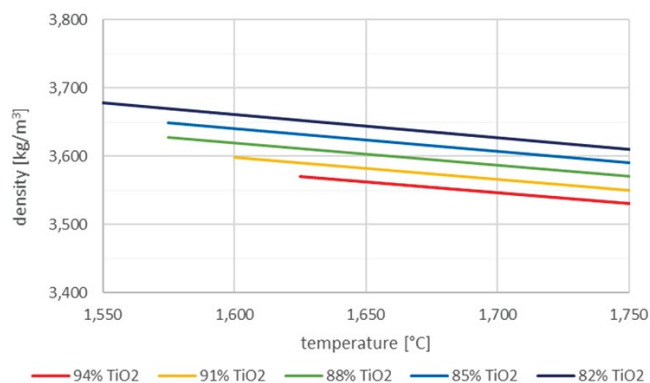


Figure 8—Calculated densities of the example slags in Table I, liquid state. The legend indicates TiO_{2 eq}.

of 3.5 g/cm³ to 3.7 g/cm³. This is lower than the temperature-independent value of 3.8 g/cm³ often cited in literature (Kotze and Pistorius, 2010; Zietsman and Pistorius, 2006). Figure 8 shows that the slag densities decrease with increasing temperature, as well as with increasing total TiO₂.

Electrical conductivity

The experimental measurements of the electrical conductivities of TiO₂ slags by Desrosiers are reproduced in Figure 9 (Desrosiers, Ajersch, and Grau, August 1980). The electrical conductivity of TiO₂ slags is exceptionally high compared to silicate slags, which have conductivities in the order of 0.1 up to less than 10 Ω⁻¹.cm⁻¹. High-FeO slags (>70%FeO) have similar and even higher electrical conductivities compared to the titania slags (Jiao and Themelis, 1988; Frederikse and Hosler, 1973). The Desrosiers slags form two distinct groups: those with low gangue (oxides excluding Fe and Ti oxides: 5–6%, 66% to 79%TiO_{2 eq}), and high gangue (15–17% gangue, 80% to 88%TiO_{2 eq}).

Since electrical conductivity is the movement of electron charges, the concept of electronic polarizability was tested against the experimental electrical conductivity measurements. By using the polarizability of the oxide components (Table IV), it was possible to reproduce the electrical conductivities of the high-gangue TiO₂ slags using a correlation of the form given in Equation [6] (electrical conductivity σ [Ω⁻¹.cm⁻¹]; electronic polarizability of the slag α_{slag} [Å³] calculated with Equation [7] and the oxide polarizabilities given in Table IV; *a* a constant; and *n* a temperature-dependent constant). The calculated electrical conductivities for the high-gangue group (lower TiO_{2 eq}) are given by the broken lines in Figure 9: these calculated values correspond remarkably well with the measured data from Desrosiers.

$$\sigma_{high\ gangue} = a \left(\frac{\alpha_{slag}}{10} \right)^n \quad [6]$$

A literature review and interpretation of the properties of high-TiO₂ slags

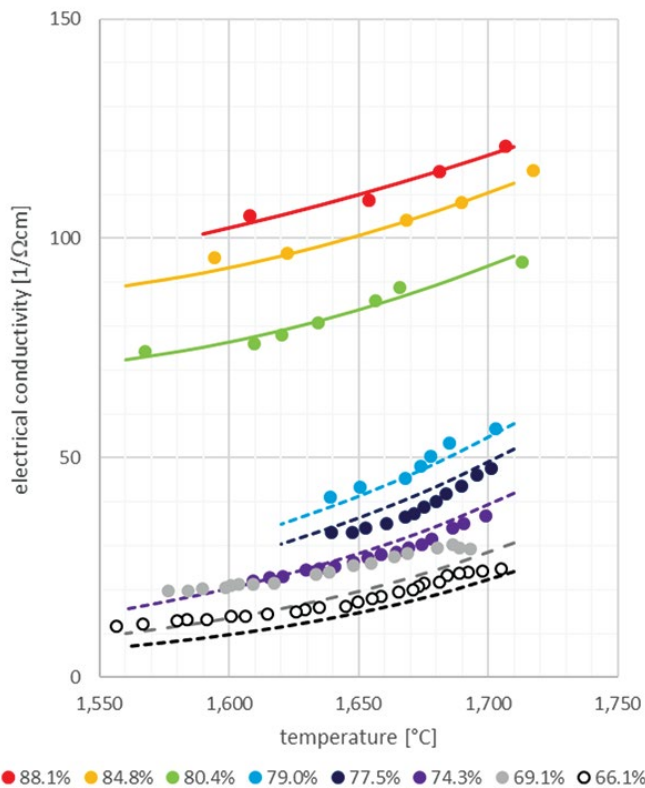


Figure 9—Electrical conductivities of liquid TiO₂ slags. Circles are experimental measurements (Desrosiers, *et al.*, August 1980); lines are calculated values (this work). Broken lines are calculated using Equation [6]; solid lines used Equation [6] combined with [8]. The legend indicates %TiO_{2 eq}.

Table IV

Electronic polarizabilities of oxides calculated from cation and oxygen anion polarizabilities (Shannon and Fischer, 2016)

	TiO ₂	Ti ₂ O ₃	FeO	Al ₂ O ₃	CaO	MgO	MnO	SiO ₂	Cr ₂ O ₃
α_i (Å ³)	8.590	12.570	3.830	6.306	3.360	2.441	3.864	3.864	11.410

$$\alpha_{slag} = \sum (X_i \alpha_i) \quad [7]$$

$$R_{valency} = \frac{(X_{Fe^{2+}} + X_{Ti^{3+}})}{(X_{Fe^{2+}} + X_{Ti^{3+}} + X_{Ti^{4+}})} \quad [8]$$

Applying Equation [6] to the low-gangue group (high-TiO_{2 eq}) yielded fair, but not, good results. The addition of a temperature-dependent valency ratio $R_{valency}$, Equation [8], improved the calculation significantly: the results are shown by the solid lines in Figure 9.

The electrical conductivities calculated for the example slags (Table I) are shown in Figure 10. The results of the 82%, 85%, and 88%TiO_{2 eq} slags correspond with the measured values of similar slags shown in Figure 9. The predicted electrical conductivities for the 91% and 95% TiO₂ slags cannot be verified against experimental data, but since the calculation is based on parameters which supports the theory of electrical conductivity in slags, the prediction carries some level of confidence. Judging from the intervals between the lines of the five example slags, the increase in electrical conductivity accelerates with increasing TiO_{2 eq}. A similar phenomenon is shown for high-FeO slags up to 100% FeO (Jiao and Themelis, 1988).

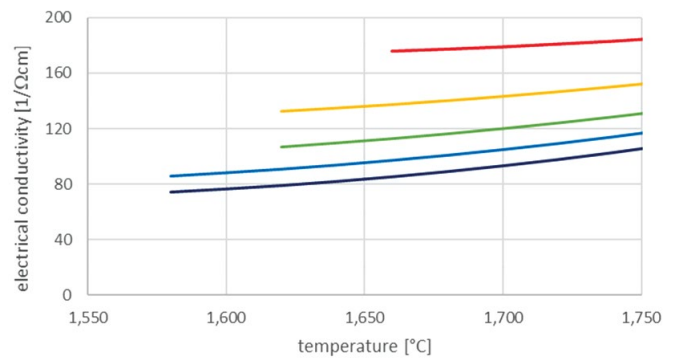


Figure 10—Calculated electrical conductivities for the example slags (Table I), liquid state. The legend indicates %TiO_{2 eq}.

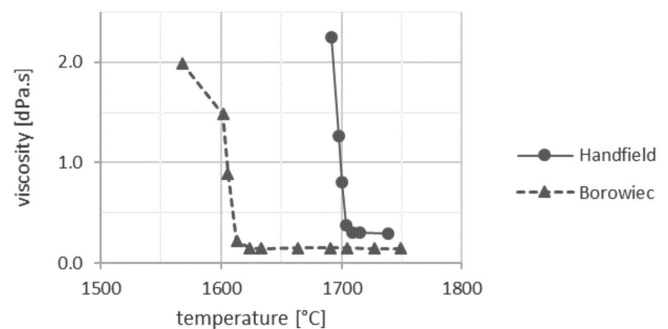


Figure 11—Measured viscosities of TiO₂ slags reproduced from Handfield (Handfield and Charette, 1971) and Borowiec (Borowiec, 2009)

Viscosity

The viscosity of slags is known to be structure-dependent and high-TiO₂ slags are no different: above their liquidus temperatures TiO₂ slags dissociate into Ti⁴⁺, Ti³⁺, and Fe²⁺; these have no structure such as SiO₂ networks provide for silicate slags. Consequently, fully liquid TiO₂ slags have very low viscosities. The measured data for ‘low-FeO’ Sorel slag (Handfield and Charette, 1971) and 95%QMM slag (Borowiec, 2009) are reproduced in Figure 11: above their liquidus temperatures these slags measured 0.3 dPa.s and 0.15 dPa.s. A recent study reports 0.6 dPa.s for fully liquid slags (Hu *et al.*, 2018). Though these numbers are different, they are all very low and not sensitive to composition or temperature. A second point of importance is that the critical temperature where viscosity increases sharply is only slightly below the slags’ liquidus temperatures (Borowiec, 2009; Hu *et al.*, 2018).

Considering these results, the viscosities of the example slags (Table I) are estimated as shown in Figure 12. The dominant feature in these viscosity curves is the sharp upwards turn, the estimated positioning of which, was based on the calculated liquidus temperatures of the example slags given in Table II.

In industrial smelting the slag bath is likely to contain some unreacted reagent. The Einstein-Roscoe equation was used to quantify the impact thereof on the viscosity of the liquid bath (Equation [9]: viscosity of the liquid with solids, η [Pa.s]; viscosity of fully liquid phase η_0 [Pa.s]; f volume fraction of the solids; assumed density for reductant 0.9 g/cm³). This is an approximation because the Einstein-Roscoe equation was derived for solid spheres and reductants are often angular. The calculated

A literature review and interpretation of the properties of high-TiO₂ slags

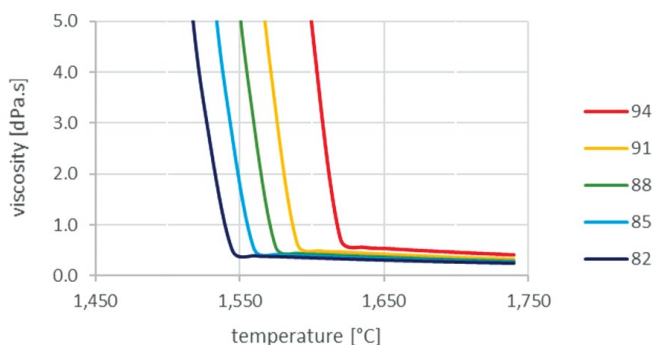


Figure 12—Estimated viscosities for the example slags in Table I. The legend indicates %TiO₂

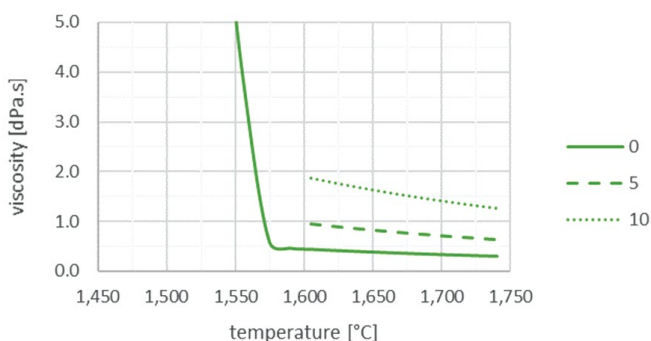


Figure 13—Calculated viscosities for fully liquid slag (88%TiO₂) containing 0%, 5% and 10 mass% reductant

viscosities for 0%, 5%, and 10mass% reductant in the 88%TiO₂ fully liquid slag are shown in Figure 13. At 10mass% reductant the viscosity of the slag bath increases from around 0.4 dPa.s to 1.5 dPa.s. This is similar to a change from olive oil at 35°C to maple syrup at 25°C (Nierat, Musameh, and Abdel-Raziq, 2014; Ngadi and Yu, 2004): not unmanageable – as Handfield points out: blast furnace slags are still tappable at 5 dPa.s, but also not insignificant considering the foaming tendency of TiO₂ slag baths.

$$\eta = \eta_0(1 - 1.35f)^{-2.5} \quad [9]$$

Thermal conductivity

The thermal conductivity of solid TiO₂ slags was reported as $0.00175T + 0.3$ W/m°C, which gives a thermal conductivity range of 1.0 to 2.9 W/m°C from 400°C to 1500°C (Kotze and Pistorius, 2010). Thermal conductivity measurements on solid TiO₂ slags from room temperature to 1050°C varied from just above 1 W/mK to approximately 2.5 W/mK with mostly, but not always, a positive relationship with temperature (Heimo, 2018). A single measurement in the same study gave 5 W/m°C at 1400°C. In the absence of data for liquid slag, 1 W/m°C is sometimes used in modelling (Zietsman and Pistorius, 2006). In the following paragraphs an attempt is made to approximate the thermal conductivity of high-TiO₂ slags based on the structure of these slags and their optical properties.

The thermal conductivity of slags is a combination of lattice k_{latt} , radiation k_{rad} , and electronic conduction k_e (Mills and Susa, 1992). Lattice conduction is structure-dependent because it relies on the velocity of phonons v through the slag, and the mean free path of phonons L through the slag, (Equation [10];

heat capacity at constant pressure C_p). In solids the crystal lattice provides the structure along which phonons travel; in silicate slags, the SiO₂ network provides the means. Thermal conductivity values measured with the transient hot wire method, a technique which isolates lattice conductivity, range from 0.03 to 1 W/mK for silicate slags (Glaser and Sichen, 2013; Kang *et al.*, 2012). Lattice thermal conductivities decrease with increasing temperature, reflecting the diminishing slag structure with increasing temperature. In TiO₂ slags – judging from the low viscosities above liquidus temperatures – no significant structure exists. Lattice thermal conductivities in high-TiO₂ slags are therefore expected to be small. Nevertheless, the lattice conductivity where estimated from a correlation between reported transient hot wire thermal conductivities and calculated viscosities of silicate slags. The model used for viscosity calculations is based on the work by Zang (Zhang *et al.*, 2012, Zhang and Chou, 2012), a little-known model for SiO₂-Al₂O₃-CaO-MgO-FeO-MnO-K₂O slags, but with good reproducibility of experimental data, and with potential to be expanded to more oxide components (Kotze, 2017).

$$k_{latt} = \frac{1}{3}C_p vL \quad [10]$$

The radiative component of thermal conductivity k_{rad} is calculated with Equation [11] (Mills and Susa, 1992) (Stefan Boltzmann constant $\sigma = 5.67 \times 10^{-8}$ W/m²K⁴; refractive index of the slag n [dimensionless]; temperature T [K]; absorption coefficient β [cm⁻¹] usually denoted as α in the literature but changed here to avoid confusion with the earlier mentioned electronic polarizability). The refractive indexes of the transition metal oxides are generally higher: 2 and more, compared to 1.535 for SiO₂, 1.805 for CaO, 1.715 for MgO, and 1.79 for Al₂O₃. Based on this the radiative component in the TiO₂ slags could be expected to be higher than for silicate slags. However, the absorption coefficient for FeO is two orders of a magnitude higher (Susa, Nagata, and Mills, 1993), and that of Ti₂O₃ three orders of a magnitude higher (Li, 2016) than those of SiO₂, CaO, MgO and Al₂O₃. Consequently, the radiative component of high-TiO₂ slags is low compared to low FeO silicate slags.

$$k_{rad} = \frac{16\sigma n^2 T^3}{3\beta} \quad [11]$$

The electronic thermal conductivity k_e was calculated with the Wiedemann-Franz formula (Ok *et al.*, 2018) (Equation [12], electrical conductivity σ [Ω⁻¹m⁻¹]; Lorenz number $L = 2.44 \times 10^{-8}$ W/ΩK²; temperature T [K]). Due to the high electrical conductivity of TiO₂ slags, electronic conductivity, which is negligible in silicate slags, can be significant for TiO₂ slags.

$$k_e = \sigma LT \quad [12]$$

The estimated lattice, and calculated radiative and electronic conductivities of example slags 1, 3, and 5 (94%, 88%, and 82% TiO_{2 eq}) are shown in Figure 14. Total thermal conductivities are shown with the thicker solid lines. The total thermal conductivity for liquid high-TiO₂ slags is estimated to range from 0.4 W/mK to close to 1 W/mK over the liquid temperature range. The thermal conductivity is predicted to increase non-linearly with increasing TiO_{2 eq} (Figure 15) which is attributed to the increase in electronic conduction with increasing TiO_{2 eq}.

Summary

Experimentally measured properties of high-TiO₂ slags were

A literature review and interpretation of the properties of high-TiO₂ slags

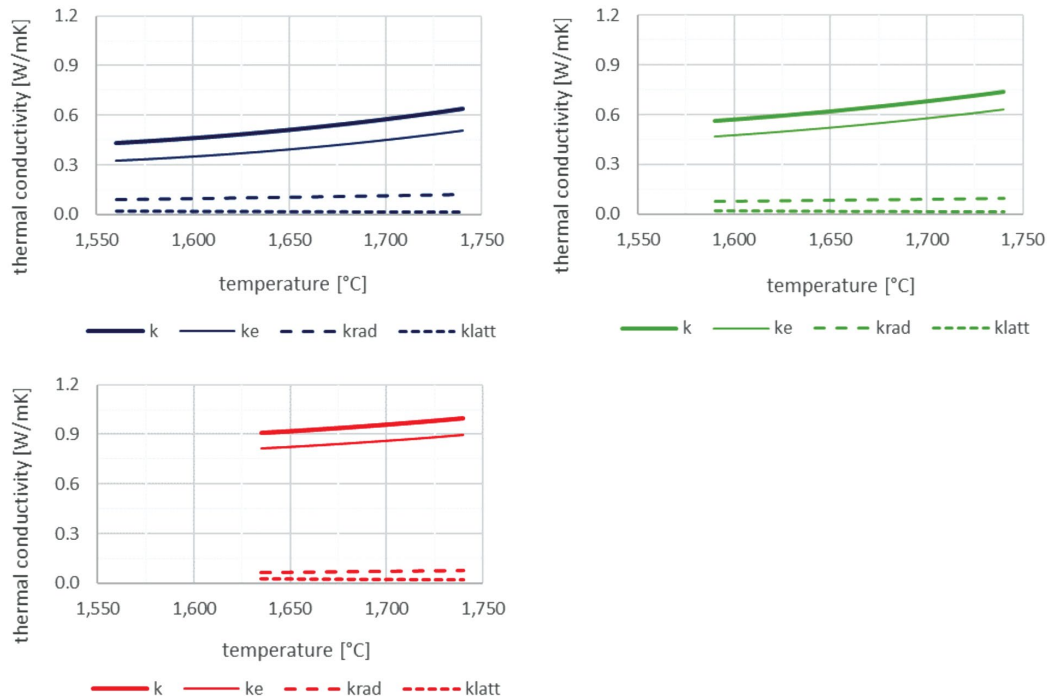


Figure 14—Estimated total, lattice, radiative, and electronic thermal conductivity. Top left; 82% TiO_{2,eq}; top right 88% TiO_{2,eq}; bottom: 94%TiO_{2,eq}.

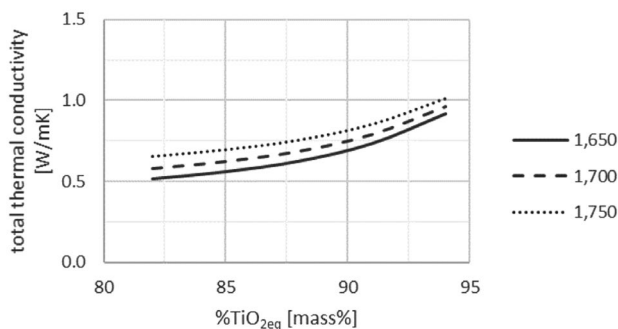


Figure 15—Estimated total thermal conductivity for the example slags at 1650°C, 1700°C and 1750°C

investigated and correlated with theoretically based parameters. Based on these correlations, the properties for five typical high-TiO₂ slags were calculated.

- The Ti³⁺/Ti⁴⁺ ratio of the liquid slags depends on the oxygen partial pressure and the oxygen activity in the bath. The polarizability ratio between Ca²⁺ and Si⁴⁺ cations was found to be a good parameter to quantify the oxygen activity. Future work will endeavor to investigate this concept against more TiO₂ slag data and other slag systems.
- Liquidus temperatures increase with decreasing FeO, but can increase or decrease with increasing Ti₂O₃ depending on the ratio between Ti³⁺ and Ti⁴⁺. Following on from the Ti³⁺/Ti⁴⁺ correlations, liquidus temperatures depend therefore on FeO, oxygen partial pressure, and the CaO and SiO₂ impurities. Other impurities such as MgO, MnO, Al₂O₃, Cr₂O₃, and V₂O₅ also affect liquidus values when they stabilize the M₃O₅ pseudobrookite phase. The partitioning of MnO between the M₃O₅ and silicate phases needs to be reviewed.

- The heat capacity of liquid high-TiO₂ slags cover a narrow range from 1000 to 1020 J/kgK.
- Liquid slag densities range from 3.5 to 3.7 g/cm³, with the lower range applying at higher temperatures and to higher TiO_{2,eq} slags.
- The electrical conductivities of liquid high-TiO₂ slags are one to two order of magnitudes higher than those of silicate slags and increase with increasing temperature. This is an important point for both AC and DC furnace design. The electrical conductivity of high-gangue TiO₂ slags correlates with the slags' electronic polarizability, while for low-gangue TiO₂ slags (high-TiO_{2,eq}), the electrical conductivity was reproduced by using the slags' electronic polarizability and the valency ratio between Fe and Ti cations.
- The viscosities of high-TiO₂ slags above liquidus temperatures are very low but increase sharply just below liquidus temperatures. Though the viscosities of fully liquid slags are low, the presence of unreacted reductant in the bath will increase its viscosity.
- The thermal conductivities of liquid high-TiO₂ slags were derived from their viscosities and optical properties. For the example slags the thermal conductivities are estimated to range from 0.5 to 1 W/mK. Electronic thermal conduction is dominant and contributes to most to the total thermal conductivity.

Though the intention of this paper is to create a basis for extrapolation to TiO₂ slags not covered in the specific set of experimental work, the correlations derived here are still only applicable to the typical TiO₂, pseudobrookite M₃O₅ slags.

Slag properties are evasive: the need to estimate the thermal conductivity of the TiO₂ slags from theoretical considerations is a point in case. It is a complex field but our understanding of slag properties has expanded over the last approximate two decades. It is the author's hope that many a publication on the properties of TiO₂ slags is still to see the light.

A literature review and interpretation of the properties of high-TiO₂ slags

Acknowledgements

I would like to express sincere gratitude to all the researchers who contribute to the field of slag properties. My gratitude also goes to the referees who fulfilled their duty to challenge my thoughts and assumptions. And to all the designers and producers who apply this understanding of slag properties to optimize their processes: thank you for your support.

References

- BOROWIEC, K. 2009. *Partition of impurities within titania slag*. Santiago, Chile, s.n., pp. 23–31.
- BRAUER, G. and LITKE, W. 1960. On the melting point and thermal dissociation of titanium dioxide. *Journal of Inorganic and Nuclear Chemistry*, vol. 16. pp. 67–76.
- DESROSIERS, R., AJERSCH, F., and GRAU, A. August 1980. *Electrical conductivity of industrial slags of high titania content*. Halifax, Nova Scotia, s.n.
- DIMITROV, V. and KOMATSU, T. 2010. An interpretation of optical properties of oxides and oxide glasses in terms of the electronic ion polarizability and average single bond strength. *Journal of the University of Chemical Technology and Metallurgy*, vol. 45, no. 3. pp. 219–250.
- DINGWELL, D.B. 1991. The density of titanium(IV) oxide liquid. *Journal of the American Ceramic Society*, vol. 74, no. 10. pp. 2718–2719.
- DUFFY, J. and INGRAM, M. 1976. An interpretation of glass chemistry in terms of the optical basicity concept. *Journal of Non-Crystalline Solids*, vol. 21, pp. 373–410.
- ERIKSSON, G. and PELTON, A.D. 1993. Critical evaluation and optimization of the thermodynamic properties and phase diagrams of the MnO-TiO₂, MgO-TiO₂, FeO-TiO₂, Ti₂O₃-TiO₂, Na₂O-TiO₂, and K₂O-TiO₂ systems. *Metallurgical Transactions B*, October, Volume 24B, pp. 795–805.
- ERIKSSON, G. and PELTON, A.D. 1996. Measurement and thermodynamic evaluation of phase equilibria in the Fe-Ti-O system. *Ber. Bunsenges Phys Chem*, vol. 100, no. 11. pp. 1839–1849.
- FREDERIKSE, H. and HOSLER, W. 1973. Electrical conductivity of coal slag. *Journal of the American Ceramic Society*, August, pp. 481–419.
- GASKELL, D.R. 2008. *Introduction to the Thermodynamics of Materials*. Fifth edition ed. New York, London: Taylor & Francis.
- GELDENHUIS, J. and PISTORIUS, P. 1999. The use of commercial oxygen probes during the production of high titania slags. *Journal of the South African Institute of Mining and Metallurgy*, January/February, pp. 41–48.
- GLASER, B. and SICHEN, D. 2013. Thermal conductivity measurements of ladle slag using transient hot wire method. *Metallurgical and Materials Transactions B*, February, vol. 44B. pp. 1–4.
- HANDFIELD, G. and CHARETTE, G. 1971. Viscosity and structure of industrial high-TiO₂ slags. *Canadian Metallurgical Quarterly*, vol. 10, no. 3. pp. 235–243.
- HEIMO, J. 2018. Thermal conductivity of titanium slags. Aalto: Aalto University.
- HU, K. *et al.*, 2018. Viscosity of TiO₂-FeO-Ti₂O₃-SiO₂-MgO-CaO-Al₂O₃ for high-titania slag smelting process. *Metallurgical and Materials Transactions B*, August, vol. 49B. pp. 1963–1973.
- IKEMIYA, N., UMEMOTO, J., HARA, S., and OGINO, K. 1993. Surface tension and densities of molten Al₂O₃, Ti₂O₃, V₂O₅ and Nb₂O₅. *ISIJ International*, vol. 33, no. 1. pp. 156–165.
- JIAO, Q. and THEMELIS, N. 1988. Correlations of electrical conductivity to slag composition and temperature. *Metallurgical Transactions B*, February, vol. 19B. pp. 133–140.
- KANG, Y. *et al.*, 2012. Thermal conductivity of the molten CaO-SiO₂-FeOx system. *Metallurgical and Materials Transactions B*, December, vol. 43B. pp. 1420–1426.
- KOTZE, H. 2017. *Comparison between viscosity models*, Consensi internal study.
- KOTZE, H. and PISTORIUS, P. 2010. A heat transfer model for high titania slag blocks. *Journal of the South African Institute of Mining and Metallurgy*, February, vol. 110. pp. 57–66.
- LI, Y. 2016. *Investigation of titanium sesquioxide Ti₂O₃: synthesis and physical properties*, Thuwal, Kingdom of Saudi Arabia.
- MILLS, K. and SUSA, M. 1992. *Thermal Conductivities of Slags*, Teddington, United Kingdom: National Physical Laboratory.
- NGADI, M. and YU, L. 2004. Rheological properties of Canadian maple syrup. *Canadian Biosystems Engineering*, vol. 46. pp. 3.15–3.18.
- NIERAT, T., MUSAMEH, S., and ABDEL-RAZIQ, I. 2014. Temperature-dependence of olive oil viscosity. *Materials Science An Indian Journal*, vol. 11, no. 7. pp. 233–238.
- OK, K.M. *et al.*, 2018. Effect of point and planar defects on thermal conductivity of TiO_{2-x}. *Journal of the American Ceramic Society*, vol. 101. pp. 334–346.
- PELTON, A.D. and BLANDER, M. 1986. Thermodynamic analysis of ordered liquid solutions by a modified quiasochemical approach - application to silicate slags. *Metallurgical Transactions B*, December, vol. 17B. pp. 805–815.
- PESL, J. and ERIC, R. 2002. High temperature carbothermic reduction of Fe₂O₃-TiO₂-M_xO_y oxide mixtures. *Minerals Engineering*, vol. 15. pp. 971–984.
- PESL, J. and ERIC, R.H. 1999. High-temperature phase relations and thermodynamics in the iron-titanium-oxygen system. *Metallurgical and Materials Transactions B*, August, vol. 30B. pp. 695–705.
- PISTORIUS, P. 2007. Ilmenite smelting: the basics. s.l. *The Southern African Institute of Mining and Metallurgy*, pp. 75–84.
- PISTORIUS, P. C. 2002. The relationship between FeO and Ti₂O₃ in ilmenite smelter slags. *Scandinavian Journal of Metallurgy*, vol. 31. pp. 130–125.
- SEIM, S. 2011. Experimental investigations and phase relations in the liquid FeTiO₃-Ti₂O₃-TiO₂ slag system, Trondheim.
- SEIM, S. and KOLBENSEN, L. 2010. Update on the equilibrium between liquid Fe-Ti-O slags and metallic iron. *Steel Research International*, vol. 81, no. 12. pp. 1051–1055.
- SHANNON, R.D. and FISCHER, R.X. 2016. Empirical electronic polarizabilities of ions for the prediction and interpretation of refractive indices: oxides and oxysalts. *American Mineralogist*, vol. 101, pp. 2288–2300.
- SUSA, M., NAGATA, K., and MILLS, K. 1993. Absorption coefficients and refractive indices of synthetic glassy slags containing transition metal oxides. *Ironmaking and Steelmaking*, vol. 20, no. 5. pp. 372–378.
- TRANELL, G., OSTROVSKI, O., and JAHANSHAH, S. 1997. *The thermodynamics of titanium in CaO-MgO-Al₂O₃-SiO₂-TiO_x slags*. Sydney, pp. 501–506.
- TRANELL, G., OSTROVSKI, O., and JAHANSHAH, S. 2002. The equilibrium partitioning of titanium between Ti³⁺ and Ti⁴⁺ valency states in CaO-SiO₂-TiO₂ slags. *Metallurgical and Materials Transactions B*, February, vol. 33B. pp. 61–67.
- XIN, J., GAN, L., WANG, N., and CHEN, M. 2019. Accurate density calculation for molten slags in SiO₂-Al₂O₃-CaO-MgO-FeO-Fe₂O₃ systems. *Metallurgical and Materials Transactions B*, 50B(December). pp. 2828–2842.
- ZHANG, G.-H. and CHOU, K.-C. 2012. Measuring and modeling viscosity of CaO-Al₂O₃-SiO₂-(K₂O) melt. *Metallurgical and Materials Transactions B*, August, vol. 43B. pp. 841–848.
- ZHANG, G.-H., CHOU, K.-C., and MILLS, K. 2012. Modelling viscosities of CaO-MgO-Al₂O₃-SiO₂ molten slags. *ISIJ International*, vol. 52, no. 3. pp. 355–362.
- ZHANG, G.-H., CHOU, K.-C., XUE, Q.-G., and MILLS, K. C. 2012. Modeling viscosities of CaO-MgO-FeO-MnO-SiO₂ molten slags. *Metallurgical and Materials Transactions B*, February, vol. 43B. pp. 64–72.
- ZIETSMAN, J. H. and PISTORIUS, P. 2006. Modelling of an ilmenite-smelting DC arc furnace process. *Minerals Engineering*, vol. 19. pp. 262–279. ◆



A geometallurgical approach to enhance the gravity beneficiation of a strontium deposit

A. Perroton¹, T. Wallmach¹, S.B. Blancher¹, and G. Rameau¹

Affiliation:

¹Eramet Ideas, Trappes, France.

Correspondence to:

A. Perroton

Email:

arthur.perroton@eramet.com

Dates:

Received: 23 Aug. 2019

Revised: 21 Jan. 2020

Accepted: 7 Feb. 2020

Published: February 2020

How to cite:

Perroton, A., Wallmach, T., Blancher, S.B., and Rameau, G. A geometallurgical approach to enhance the gravity beneficiation of a strontium deposit. The Southern African Institute of Mining and Metallurgy

DOI ID:

<http://dx.doi.org/10.17159/2411-9717/896/2020>

This paper was first presented at *The Eleventh International Heavy Minerals Conference*, 5–6 August 2019, The Vineyard, Cape Town, South Africa.

Synopsis

Mineralogical analyses and QEMSCAN® process simulation were used to characterize a heavy mineral concentrate of celestine originating from the Beni Mansour deposit in Algeria, and to model a gravity separation process to remove Sr-, Ba-, and Ca-bearing impurity phases. By analysing the partitioning of Ba, it was shown that the very small amounts of barite present in the sample could not account for the chemically derived Ba concentration in the total sample. It was therefore decided to investigate the presence of Ba that could replace the Sr in celestine in the form of solid solution substitution. It was found that some celestine particles displayed zonation textures with respect to Ba, resulting in difficulties in meaningfully reducing the Ba content without a significant loss of Sr. It was shown that the removal of all barite would lead to a minimum of 0.65 wt% Ba in the final celestine concentrate. Density separation modelling by QEMSCAN® software showed that the 3.5–4.0 g/cm³ density fraction had higher Sr and celestine concentrations, as high as 46.33 wt% Sr. In this particular fraction, the Ba and Ca contents could be reduced to 0.72 wt% and 0.49 wt% respectively.

Keywords

process mineralogy, geometallurgy, modelling, density separation, QEMSCAN®.

Introduction

Chemical surveys performed on Beni Mansour deposit in the past for resource estimation did not include detailed mineralogical information and interpretation. By including this information, it is possible to predict the process behaviour of minerals in a way that can make the difference between a mineral resource of potential economic interest and a mineral reserve of definite economic value. Mine planning is increasingly performed based on mineralogical and process-related factors that can be simulated with the QEMSCAN® software. The literature provides numerous examples of applications and case studies to indicate how automated mineralogy can add value to process improvement. Within the past few years a large number of papers and communications have been published on the interactions of automated mineralogy, ore processing, and geometallurgy (Lotter *et al.*, 2011; Schouwstra and Smit, 2011; Baum, 2014; Gu, Schouwstra, and Rule, 2014; Zhou and Gu, 2016; Becker, Wightman, and Evans, 2016; Delaporte *et al.*, 2018, 2019).

Study aims

The sample was provided by an Eramet Ideas external customer in order to demonstrate the QEMSCAN® application for mineral characterization and to provide process-related information.

The celestine concentrate was analysed with respect to its chemical and mineralogical composition. The objectives of these analyses were to:

- Identify the minerals present in the sample
- Identify mineral impurities, particularly those containing Ca and Ba
- Propose physical methods to improve the quality of the Sr concentrate.

The provided sample had a high Sr concentration of 46 wt%. This corresponds with the very high content of celestine, amounting to 97 wt%. The barium content amounted to 0.78 wt%, and calcium to 0.90 wt%. These impurities should be reduced as much as possible to meet the tight specifications of the chemical industry. As the client is currently in a qualification process for its product, the authors were asked to determine the minimum concentrations of Ba and Ca that could be reached in the concentrate by using physical beneficiation techniques.

A geometallurgical approach to enhance the gravity beneficiation of a strontium deposit

This paper aims to show how mineralogical information can aid in making mineral processing decisions, and how SEM/QEMSCAN® analyses can be used to identify and quantify trace elements that affect the ore quality.

Geological context and identification of the sample

The sample originated from the Beni Mansour deposit in Wilaya de Béjaia, 170 km southeast of Algiers (Algeria). This Triassic complex hosts an important occurrence of celestine mineralization. The mineralization occurs within an elongated Triassic structure trending N80°E, deep-seated in Albian and Cenomanian formations. This Trias consists of monogenic and polygenic breccias cemented by celestine and characterized by various authigenic minerals and several generations of calcite (Moulla and Thibieroz, 1995).

The mine is owned and operated by TBRHO, part of the Zergoun Brothers Group. A 500 g sample of a heavy mineral concentrate, generated by reference shaking table tests, was submitted and studied. Prior to the shaking table tests, the sample was subjected to a three-stage crushing process to reduce the particle size to below 5 mm (TBRHO internal report, 2014). The heavy mineral concentrate was split in two twin samples, one for chemical analyses and one for the mineralogical study

For microscopic observations, in order to obtain a homogeneous and representative polished section, the sample was embedded in liquid epoxy resin. After polymerizing, the resin-mineral mixture was cut perpendicular to its surface, then re-embedded, polished, and carbon coated. This method allows representative analyses of the sample even if particle segregation occurred after placing the sample material into the epoxy resin.

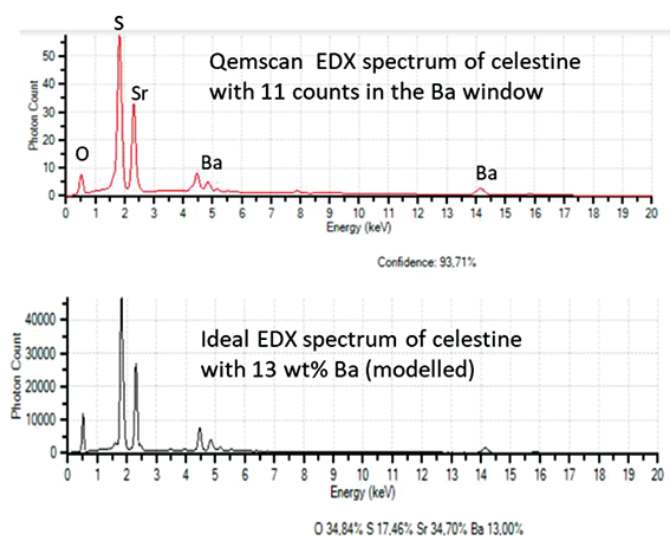
Experimental and analytical methods

The mineralogical characterization was performed using QEMSCAN®, scanning electron microscopy, and electron microprobe analyses. QEMSCAN® is an automated technique for the detailed and statistically significant characterization of mineral and noncrystalline phases, using polished sections, by means of scanning electron microscopy (SEM) coupled with chemical microanalyses by energy-dispersive spectrometry

(EDS). Characteristic EDS spectra generated by the electron beam impinging on the sample are used for the characterization of minerals and phases. The characterization addresses physical, chemical, and textural properties of minerals and phases in order to statistically evaluate this information, individually or in combinations of individual grains or particles (Gottlieb *et al.*, 2000). QEMSCAN® analyses for this project were carried out at the Eramet Ideas Geometallurgy Department using a FEI Quanta 650F SEM platform fitted with two Bruker Xflash 30 mm silicon drift energy-dispersive detectors.

For QEMSCAN® analyses, the sample was divided into six twin fractions, each of which was analysed separately to confirm the representativeness of analyses. Analyses were performed using 2 µm steps to obtain 21 million EDX analyses for classification and grouping, with respect to corresponding minerals or mineral groups that constituted the building blocks of a mineralogical database that served as the basis for QEMSCAN® data treatment and interpretation. The creation of a reliable species identification protocol (SIP) for an ore deposit, which is a mineralogical database, is one of the most critical requirements for precise analyses of any sample. Chemical and physical properties of minerals, such as densities, can be treated with high statistical significance, as discussed in the following sections. A total of 5500 particles were analysed during 46 hours with a working distance of 13 mm and a spot size of 1.2 nm. The results presented in the paper represent the aggregate of these 5500 particles.

The development of a quantitative database needs to be addressed briefly as a rarely applied methodology for QEMSCAN® analyses was used in this investigation. Each SIP entry is based on EDX images generated from photon counts in the SEM detectors. These analyses can be grouped into compositional classes. An example is presented in Figure 1. The counts for Sr, Ba, S, and oxygen for a celestine analysis are presented in this figure (red spectrum). These counts do not directly refer to weight percentages as oxygen is very frequently underrepresented in EDX analyses. Additionally, matrix effects of minerals involving light and heavy elements play a role in the liberation of photons during analysis. The black EDX spectrum in Figure 1 represents



	counts	SIP definition
Sr	49.79	Must Have (In Range: 45.0 - infinity)
Ba	11.77	Must Have (In Range: 11.0 - 12.0)
S	17.95	Must Have (In Range: 10.000 - infinity)
O	6.54	Any amount

Modelled concentrations

Used Elements	
Element	Weight Percentage
O	34,841
S	17,457
Sr	34,702
Ba	13

Figure 1—Comparison of QEMSCAN®-generated EDX spectrum (red) with a modelled ideal EDX spectrum of celestine containing 13 wt% Ba

A geometallurgical approach to enhance the gravity beneficiation of a strontium deposit

ideal celestine with precise quantities of elements in weight percentages. The amount of Ba in celestine can be quantified by adding Ba replacing Sr into the simulation software in order to attain an EDX pattern that corresponds to the actual QEMSCAN® analysis. In the case presented in Figure 1, 13 wt% of Sr has been replaced by Ba, resulting in a close match of the QEMSCAN®-generated EDX pattern for this analytical point. It can also be shown that 11.7 photon counts represent 13 wt% Ba in this analysis. In this way, photon counts of Ba in a celestine matrix were converted into weight percentages in the range of 0–10 wt% Ba in celestine. The Ba photon counts are therefore underrepresented in QEMSCAN® analyses, whereas Sr is overrepresented. This is due to the fact the heavier Ba (elemental mass 137.33) is less susceptible for the liberation of photons during QEMSCAN® analyses than lighter Sr (elemental mass 87.62). As mentioned above, the deficiency in oxygen in SEM analyses must also be considered. For precise Sr concentrations in this analysis, a conversion from photon counts into weight percentages is also required. Obtained weight percentages of refined elemental compositions of Ba-bearing celestine were used in the textural interpretations presented in this paper.

Chemistries and densities of the individual phases are entered into the so-called primary list in order to convert area percentages

from the image information into weight percentages. The quality of the database can be shown by the very low amount of unidentified minerals (<0.05 wt% 'others') and by comparing the bulk chemical analyses of the sample (XRF) with the recalculated chemistry based on the mineralogical composition. A good correlation ($R^2 > 0.95$) is presented in Figure 2.

Identification of impurities

Barium and calcium department

One of the original aims was to trace Ca- and Ba-bearing minerals in the sample. The very small amounts of calcite, dolomite, and barite in the sample (Figure 2) cannot account for the chemically derived concentrations in the analysed sample. It was therefore decided to investigate the possibility of Ba and Ca replacing the Sr in celestine in the form of solid solutions.

The partitioning of Ba and Ca is shown in Figure 3. The X-axes represent QEMSCAN® inferred concentrations of barium (0.8 wt%) and calcium (0.9 wt%). These elements are hosted by various minerals that are represented in different colours. Barium is 85% hosted by celestine (green), replacing Sr in its mineral lattice (Figure 3A). Calcite (cream) and dolomite (blue) host only half the Ca present in the sample (Figure 3B). The remainder of Ca is hosted by celestine, where it replaces some of the Sr. The

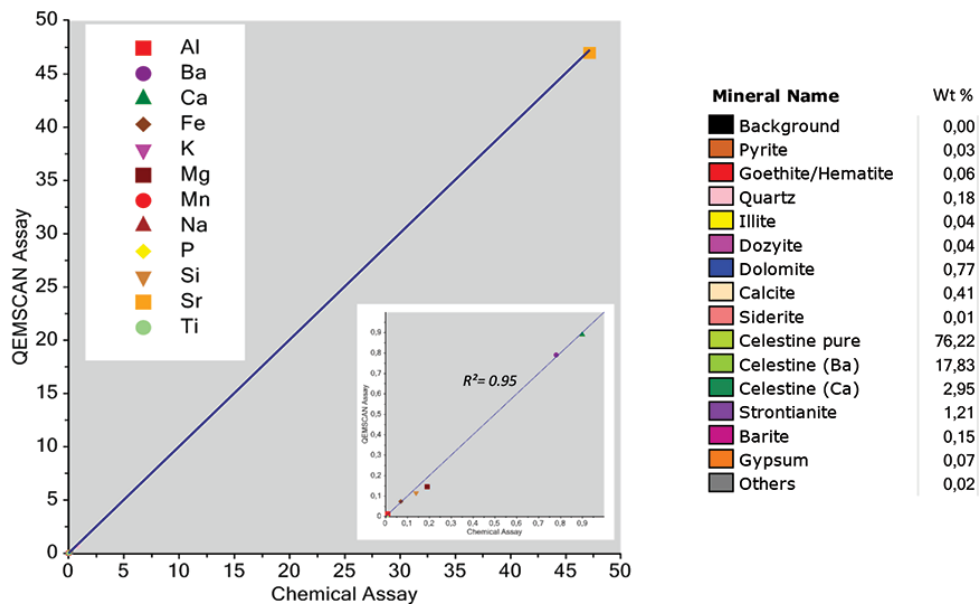


Figure 2—Chemical assay reconciliation with QEMSCAN® recalculated element concentrations. A good correlation ($R^2 > 0.95$) is necessary to confirm a good mineral identification. The mineralogical composition of the investigated sample (in wt%) is presented on the right hand side of the figure

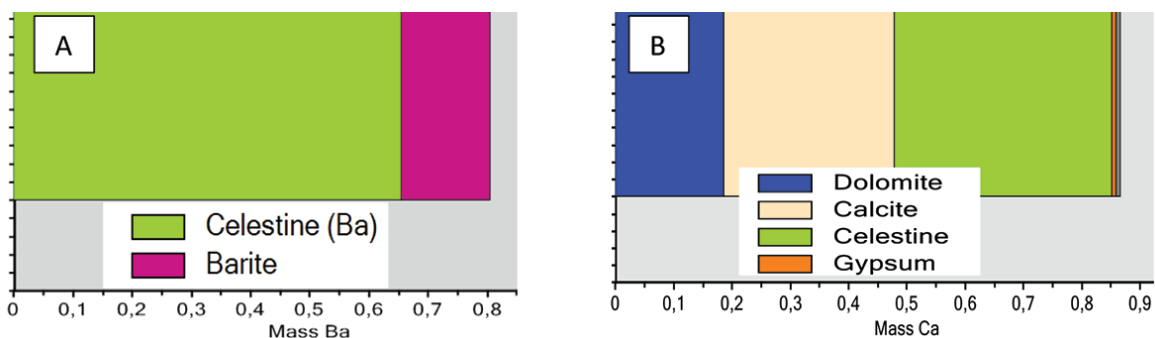


Figure 3—Partitioning of Ba and Ca. The majority of Ba is replacing Sr in celestine (A). Calcium is partitioned equally in CaMg carbonates (calcite and dolomite) and celestine (B)

A geometallurgical approach to enhance the gravity beneficiation of a strontium deposit

celestine mineral phase is therefore a solid solution between three end-members: SrSO_4 (celestine ss), BaSO_4 (barite), and CaSO_4 (anhydrite). These two figures show that without any loss of celestine, barite, calcite, and dolomite can be further removed to attain concentrations of 0.65 wt% Ba and 0.37 wt% Ca.

Ba-celestine and Ca-celestine analyses

Celestine particles display Ba-rich zonation textures. Calcium occurs more randomly in small amounts within celestine, but is concentrated in Ba-free parts. Some celestine particles display quasi-rhythmic zonation and the Ba contents can reach several wt% (up to 4 wt%) in distinct zones (Figures 4 and 5).

Association and liberation considerations

Barite, dolomite, and calcite were identified and are present either as liberated minerals or as inclusions in celestine. Some selected QEMSCAN® particle views showing the textural relationships of these minerals with celestine are presented in Figure 6.

The textural relationships presented in Figure 6 can be quantified. Figure 7 presents an association diagram that shows the 'coexistence' (inclusions or attachment to adjacent phases) and the purity of the individual particles. The X-axis presents the analysed minerals; the Y-axis shows the percentage association

of each mineral with the same mineral, indicating its purity in particles where it is present, and with other minerals. Celestine is almost completely free of inclusions of other phases. Pure celestine is associated with up to 10% Ba-bearing celestine and up to 2% with Ca-bearing celestine. Barite is associated with up to 30% celestine. Calcite is 70% pure and associated with only small amounts of celestine and strontianite, together totalling 20%.

The association diagram presented in Figure 8 represents interfaces of minerals and the interface of the mineral with the background (free surface). In this approach the purity of a mineral is not displayed. Instead, the diagram presents a quantification of mineral interfaces between texturally associated minerals. The association with the background (free surface, represented by the black portion of each column) carries important information for mineral processing. Should, for instance, calcite or dolomite be removed by flotation or acid leaching, it would be necessary for these minerals to be well liberated with a high percentage of free surface area. In the case of the analysed sample, dolomite and calcite are not very well liberated and show free surfaces of only 8% for calcite and 15% for dolomite. Even if the two minerals are grouped together

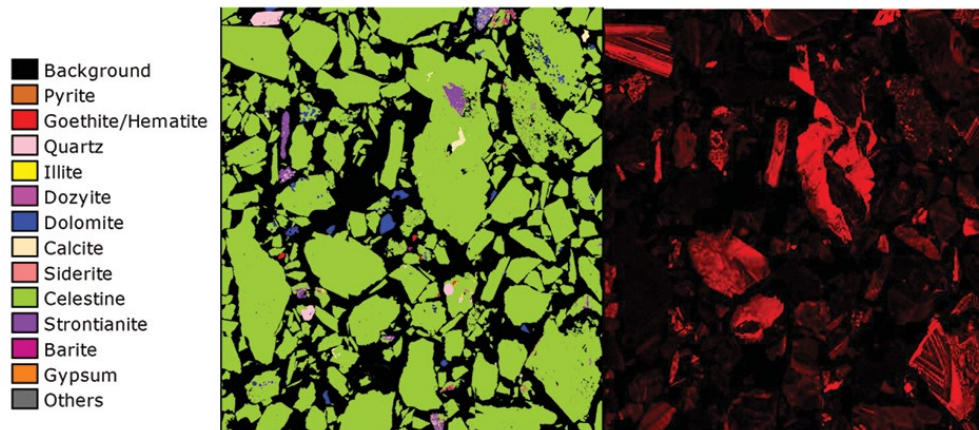


Figure 4—The QEMSCAN® image on the right shows those microanalyses that contain minor amounts of barium (red). Barium is zoned in some particles (bottom right and top left corners)

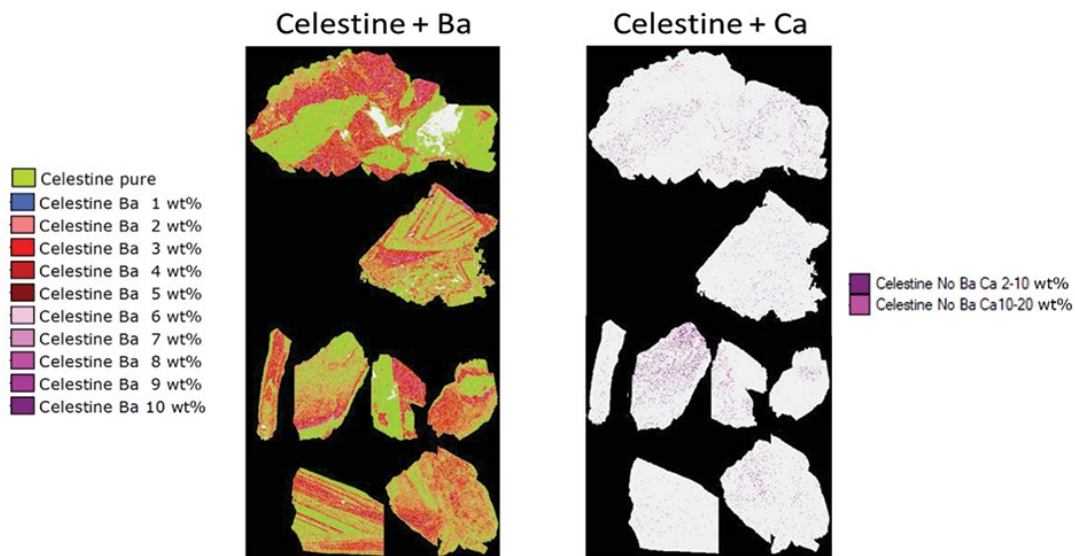


Figure 5—Ba and Ca distribution in celestine particles. Left: celestine particles with highlighted Ba zonation patterns. Right: Ca distribution in celestine particles

A geometallurgical approach to enhance the gravity beneficiation of a strontium deposit

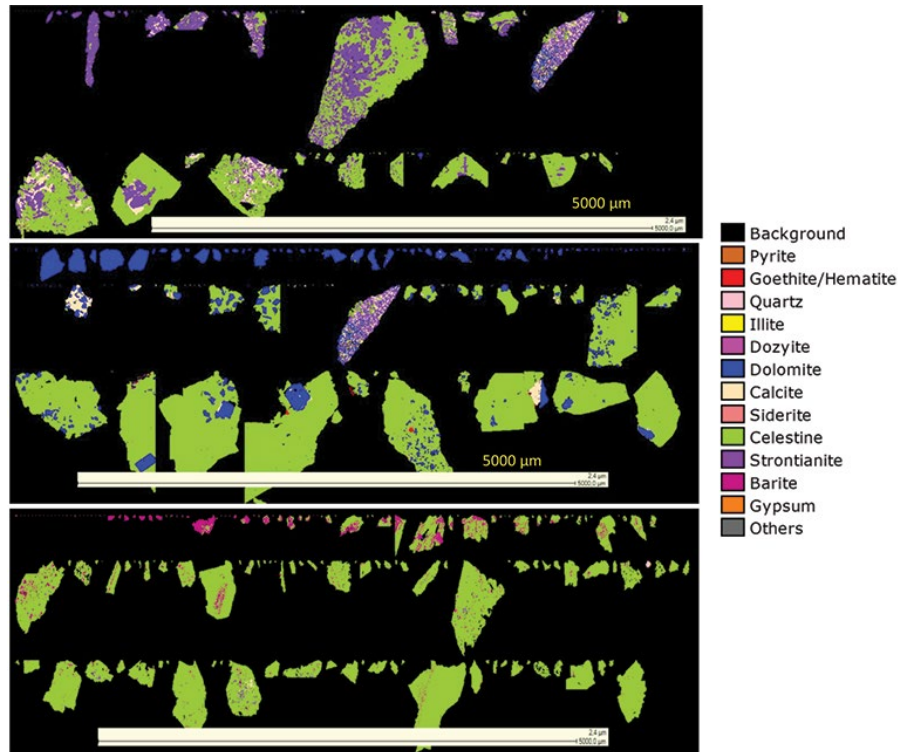


Figure 6—Selected QEMSCAN® views of celestine particles (green) that host strontianite (purple, at the top), dolomite (blue, in the middle), calcite (orange, in the middle), and barite (pink, at the bottom). These minerals are either well liberated or occur as inclusions in celestine

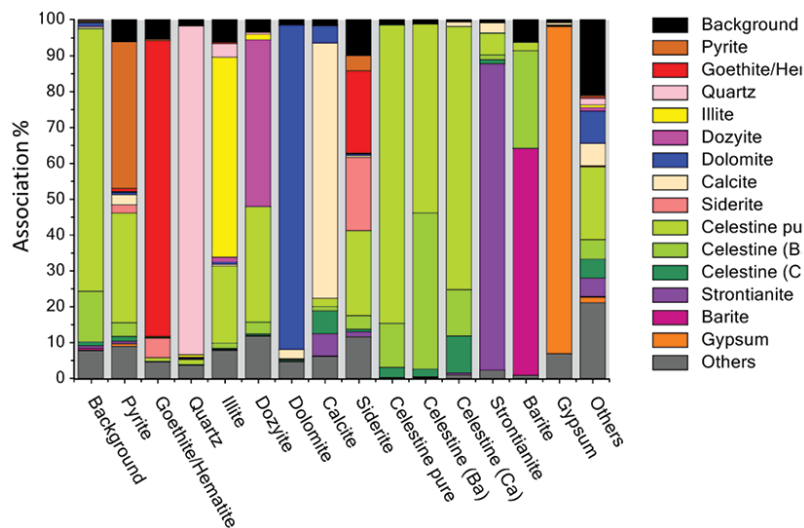


Figure 7—Mineral association diagram normalized to 100% for each mineral. The X-axis represents the identified minerals, each of which is normalized to 100%. The Y-axis shows the association percentage of each mineral with other minerals that occur as inclusions or adjacent (touching) mineral grains

the free surface will not exceed 20%. The majority of these two minerals are locked as inclusions in other minerals, and therefore they are not good candidates for physical separation methods.

Barite appears to be largely texturally associated with celestine, which again indicates that it will be difficult to significantly reduce the Ba levels in the concentrate. Dolomite and calcite are less frequently associated with celestine and thereby have a greater potential for being removed from the concentrate.

Celestine displays 80% free surface and is by far the best liberated mineral in the sample, indicating a good potential for physical separation methods to be employed in the beneficiation process.

Process modelling as a first indicator to increase the economic quality of samples

The QEMSCAN® software offers a number of process modelling options. The modelling of density separation of particles is of particular interest for this geometallurgical application. Each particle can contain several phases or grains of different densities, chemical compositions, and sizes. The sum of all these variables is taken into consideration in the modelling software.

Density modelling indicates that there is still potential to improve the quality of celestine concentrates. As the analysed concentrate already has a very high content of Sr (45.57 wt%)

A geometallurgical approach to enhance the gravity beneficiation of a strontium deposit

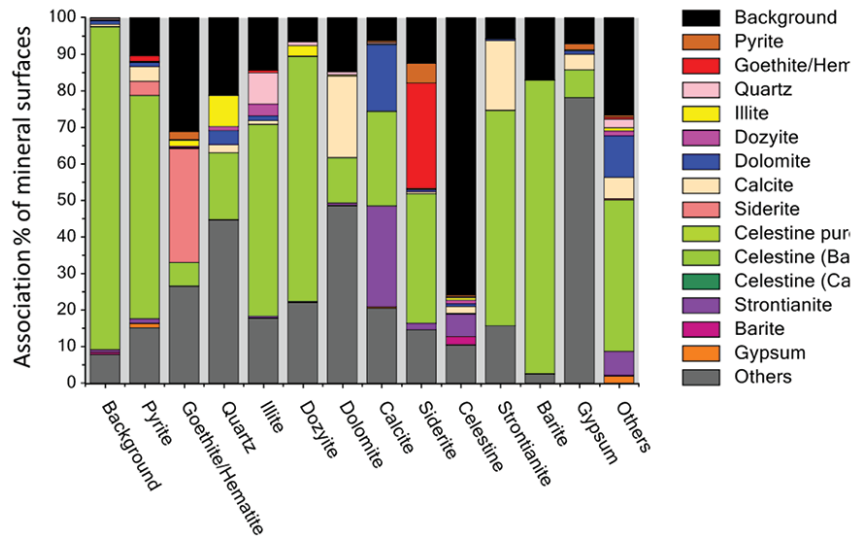


Figure 8—Mineral association diagram displaying the mineral interface percentages (normalized to 100%). Celestine, with 80% association (black portion of the celestine column), is the best liberated mineral in the analysed sample. Calcite and dolomite are not well liberated in terms of free surface, and occur mainly locked in other minerals

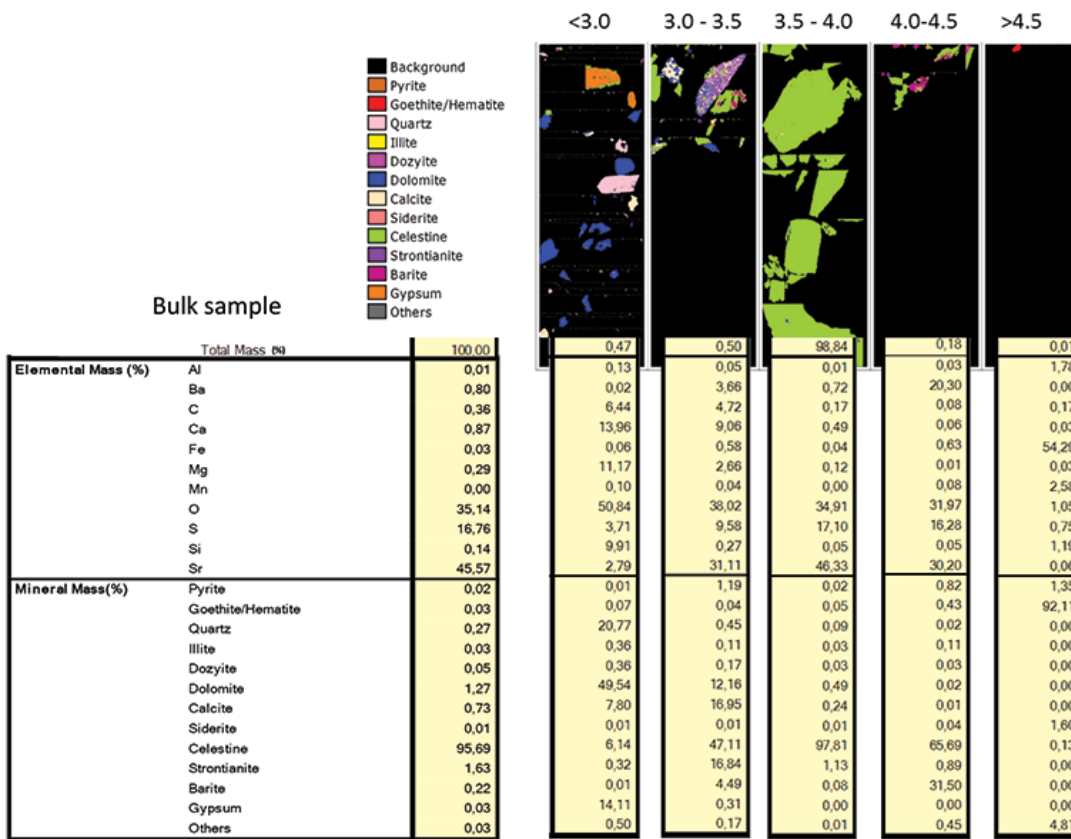


Figure 9—Density separation modelling using density steps of 0.5 g/cm³, from < 3.0 g/cm³ to > 4.5 g/cm³. Each fraction can be represented in terms of chemistry and mineralogy. The mass percentage of each fraction is also indicated on the top of each density fraction

and celestine (95.69 wt%), the potential for improvement is limited. Nevertheless, the density separation modelling data (Figure 9) confirms that is theoretically possible to concentrate the minerals of economic interest. The amount of Sr and celestine is highest in the 3.5–4.0 g/cm³ density fraction and is, at 46.33 wt% Sr, slightly higher than in the original bulk sample, which contained 45.57 wt% Sr. This improvement is also reflected by the increase from 95.69 wt% celestine in the bulk sample

to 97.81 wt% in the 3.5–4.0 g/cm³ density fraction. The mass percentage of each fraction is indicated above each density fraction on Figure 9. The 3.5–4.0 g/cm³ fraction represents 98.84 mass% of the bulk sample, indicating that there will be good recovery of the economic minerals and little waste to process.

The QEMSCAN® software, in combination with a well-developed database and element concentration calibrations, allow granulo-density and granulo-chemistry modelling to be

A geometallurgical approach to enhance the gravity beneficiation of a strontium deposit

performed. The results are important for simulation prior to actual ore processing tests. The concentrate is simulated from the feed materials by physical parameter processing before using more expensive processing techniques (*e.g.* hydro- and pyrometallurgy).

The software also allows a particle size distribution to be calculated, in which each particle size fraction of choice can be used for showing chemical and mineralogical compositions, as well as fractioned densities. This can save weeks of physical test work and provides process engineers with valuable information when performing and evaluating physical tests. Some selected results that could be important for celestine and Sr enrichment are presented in Figure 10 and Figure 11. Mass and mass percentages of Ca and Sr as function of density and particle sizes are shown. Mass of an element refers to the concentration of an element with respect to the overall sample. Mass percentage of an element refers to the concentration of an element in the respective size and density fraction. An element may, for instance, be highly enriched in a certain size or density fraction, the mass of which is small with respect to the overall sample. A low concentration in a fraction that represents a significant mass of the sample may dominate the overall mass balance of this element. Mass and mass percentage of Ca in the analysed sample are shown in Figure 10. The mass of Ca represents the concentration of an element with respect to the overall sample chemistry. The mass percentage of an element represents the concentration of an element with respect to the fraction chemistry without taking the relationship with the overall sample chemistry into account. The Ca mass in the sample is concentrated in the < 400 μm and < 4.0 g/cm^3 fraction. In terms of mass percentage, the highest concentration of Ca occurs in the lower density fractions. As they are of minor significance with respect to the overall mass of the sample, these fractions contrast with the mass of Ca in the sample. The lower density fractions represent Ca partitioned in calcite and dolomite, whereas the higher density fractions

represent Ca in celestine. In the case of less concentrated samples, this information would help to decrease the amount of Ca by reducing the small size and low density fractions.

The same concept applies to the partitioning of Ba. It can be seen that the small size and low density fractions are enriched in impurities, unwanted elements, or minerals from celestine concentrates.

Summary and conclusion

Acid leaching processes are commonly applied to reduce elevated concentrations of Ca and Mg through carbonate dissolution. It can be shown that alternative methods, based on physical concentration of the ore, can be applied to reduce the concentrations of barium, magnesium, and calcium.

The presented example demonstrates the importance of automated mineralogy for the extraction of critical information for mineral processing of a celestine-rich strontium ore sample. Based on detailed mineralogical and microtextural analyses, it was possible to simulate how physical mineral separation can increase the quality of the concentrate. The QEMSCAN® model confirms that density separation can increase the concentrations of economic elements. The amount of Sr is highest in the 3.5–4.0 g/cm^3 density fraction and is, at 46.33 wt% Sr, slightly higher than in the original bulk sample, which contained 45.57 wt% Sr. Barium occurs only in small amounts and cannot be decreased significantly. Using a simulated 3.5 g/cm^3 cut-off density, the calcium content can be decreased in the heavy fraction from 0.87 wt% to 0.49 wt%. This is because the calcium-bearing minerals calcite and dolomite report to the light fraction. Granulometry modelling has shown that at a cut-off at 400 μm the calcium content can be reduced, but this will come at the cost of a significant loss of strontium.

Similar process modelling can be performed on any ore type for improving grades and recoveries of economically valuable elements by using chemical and physical differences

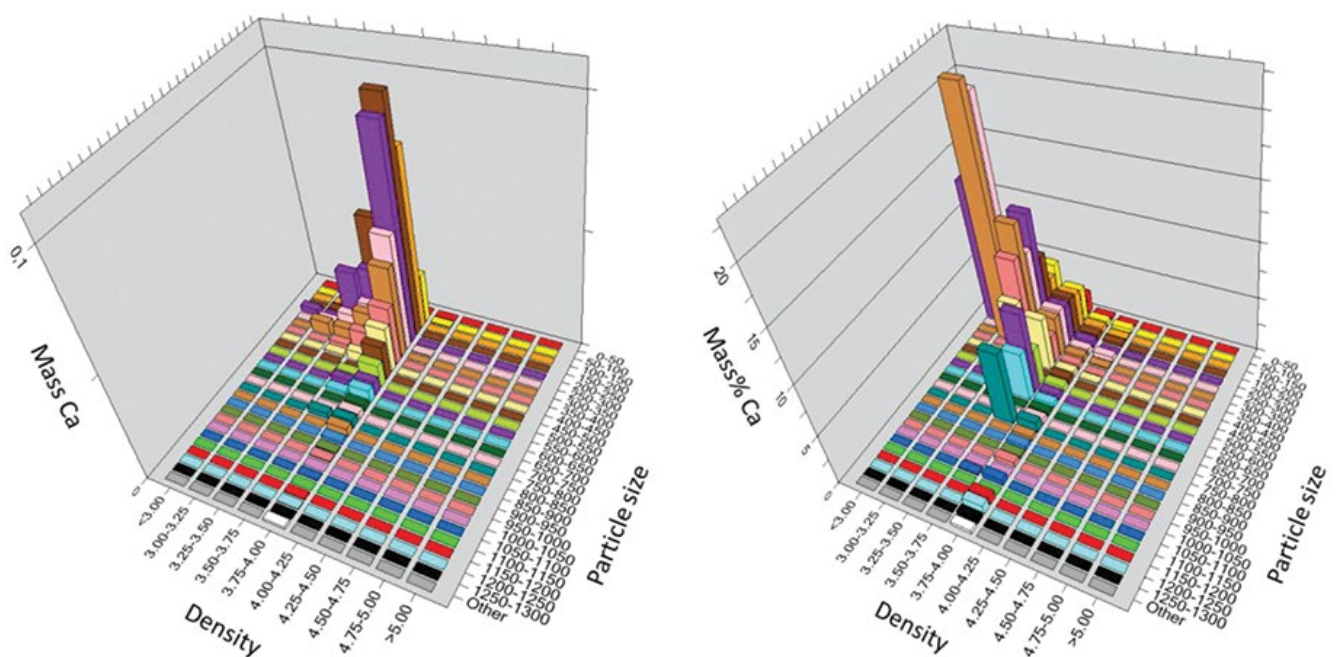


Figure 10—Ca partitioning in density and particle size fractions. The left hand diagram shows Ca concentrations with respect to the overall sample. The right hand diagram shows the Ca percentage in each fraction irrespective of the mass% of this fraction in the overall sample

A geometallurgical approach to enhance the gravity beneficiation of a strontium deposit

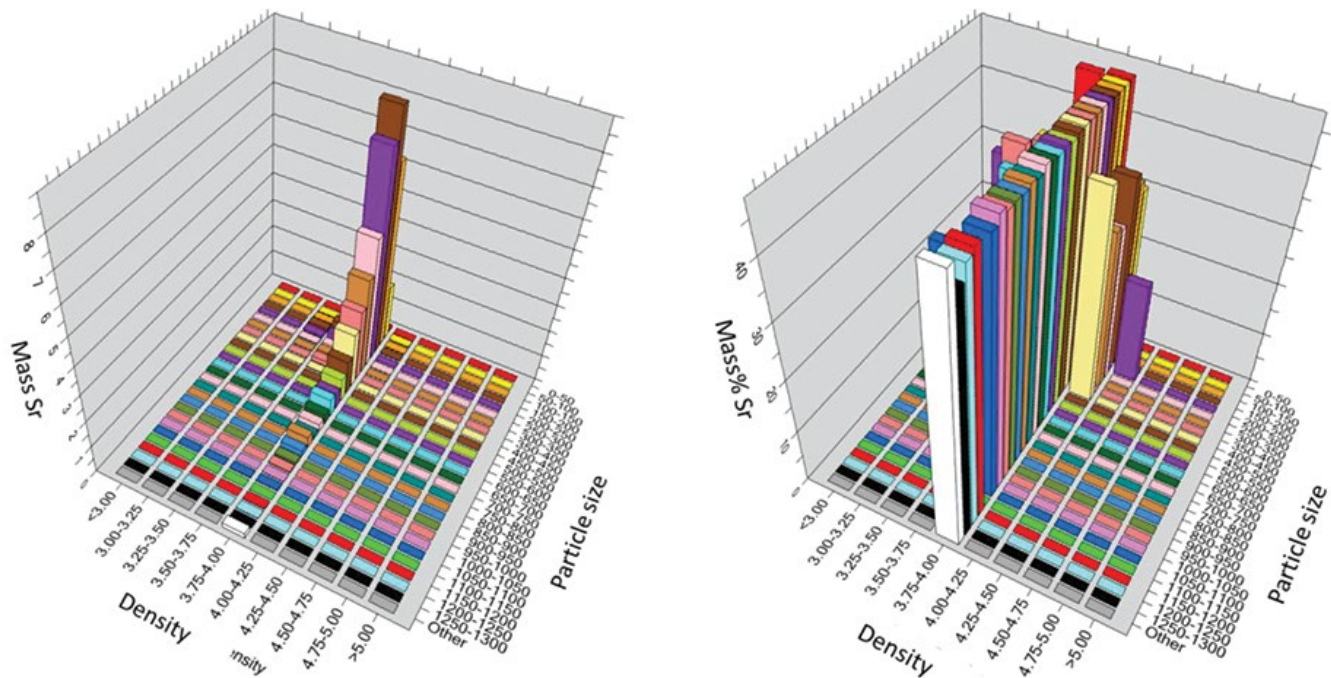


Figure 11 – Sr partitioning in density and particle size fractions. The left hand diagram shows Sr concentrations with respect to the overall sample. The right hand diagram shows the Sr percentage in each fraction irrespective of the mass% of this fraction in the overall sample

of particles and minerals in particles. It must be kept in mind that the proposed process options are theoretical, and even sometimes hypothetical. Any proposed process option suggested by process modelling needs to be verified by physical tests, which are performed under real conditions that differ from ideal and computed modelling tests. The interactions of particles with different chemical and physical properties during mineral processing are important, difficult to simulate, and may lead to results that do not correspond to the modelling results. Nevertheless, the modelling provides a good starting point and roadmap guiding process engineers in performing their tasks. In the past, and even still nowadays, mineral processing tests were performed on an almost trial-and-error basis. Long testing cycles, accompanied by chemical analyses, which are not always immediately available, are time- and energy-consuming. This situation can be vastly improved by using automated mineralogy and geometallurgy concepts.

This study addressed the mine operator's major concerns:

- Minerals in the sample have been identified and their proportions calculated.
- Impurities have been precisely located. Barium is hosted mainly in celestine, replacing Sr. Calcite and dolomite host half the Ca present in the sample. The remainder of the Ca is hosted by celestine, replacing some of the Sr.
- A density separation has been proposed to enhance the valorization of the deposit by increasing the strontium content and decreasing the calcium concentration.

References

BECKER, M., WIGHTMAN, E.M., and EVANS, C.L. (eds). 2016. Process Mineralogy. *JKMRC Monograph Series in Mining and Mineral Processing*, no. 6. Julius Kruttschnitt Mineral Research Centre, Brisbane, Australia. 470 pp.

BRAUN, W. 2014. Ore characterization, process mineralogy and lab automation, a road map for the future. *Minerals Engineering*, vol. 60. pp. 63–73.

DELAPORTE, A., BLANCHER, S.B., GONCALVES, P., and WALLMACH, T. 2018. Physical property changes of Fe-Ti oxides along their alteration: a geometallurgical study to improve the yield of a mineralurgical plant. *Proceedings of the XXIX International Mineral Processing Congress*, Moscow, Russia. International Mineral Processing Council.

DELAPORTE, A., BLANCHER, S.B., PERROTON, A., and WALLMACH, T. 2019. Detailed mineralogical characterization of leucoxene: a base for physical beneficiation to improve rutile recoveries. *Proceedings of Heavy Minerals 2019*, Cape Town, South Africa. Southern African Institute of Mining and Metallurgy, Johannesburg.

GOTTLIEB, P., WILKIE, G., SUTHERLAND, D., HO-TUN, E., SUTHERS, S., PERERA, K., JENKINS, B., SPENCER, S., BUTCHER, A., and RAYNER, J. 2000. Using quantitative electron microscopy for process mineralogy applications. *Journal of the Minerals, Metals, and Materials Society*, vol. 52, no. 4. pp. 24–25.

GU, Y., SCHOUWSTRA, R.P., and RULE, C. 2014. The value of automated mineralogy. *Minerals Engineering*, vol. 58. pp. 100–103.

LOTTER, N.O., KORMOS, L.J., OLIVEIRA, J., FRAGOMENI, D., and WHITEMAN E. 2011. Modern process mineralogy: two case studies. *Minerals Engineering*, vol. 24. pp. 638–650.

MOULLA, S. and THIBIEROZ, J. 1995. Le gisement de célestine du Trias extrusif de Béni-Mansour (Béjaïa, Algérie): traces, cathodoluminescence et inclusions fluides dans les carbonates et sulfates. *Bulletin du Service Géologique de l'Algérie*, vol. 6, no 2. pp. 161–177.

SCHOUWSTRA, R.P. and SMIT, A.J. 2011. Developments in mineralogical technique – what about mineralogists? *Minerals Engineering*, vol. 24. pp. 1124–1228.

ZHOU, J. and GU, Y. 2016. Geometallurgical characterization and automated mineralogy of gold ores. *Gold Ore Processing (2nd edn)*. Adams, M. (ed.). Elsevier. pp. 95–111. ◆



Assessment of errors in the transmission of the orientation and cartographic system from the surface to an underground mine

L. Sanmiquel¹, M. Bascompta¹, and J.M. Rossell¹

Affiliation:

¹Polytechnic University of Catalonia, Manresa, Spain.

Correspondence to:

L. Sanmiquel

Email:

alluis.sanmiquel@upc.edu
bmarc.bascompta@upc.edu
cjosep.maria.rossell@upc.edu

Dates:

Received: 10 Jul. 2019
Revised: 5 Nov. 2019
Accepted: 29 Nov. 2019
Published: February 2020

How to cite:

Sanmiquel, L., Bascompta, M., and Rossell, J.M. Assessment of errors in the transmission of the orientation and cartographic system from the surface to an underground mine. The Southern African Institute of Mining and Metallurgy

DOI ID:

<http://dx.doi.org/10.17159/2411-9717/826/2020>

Synopsis

An accurate transmission of the orientation between surface and underground workings, by means of vertical shafts, is a major challenge in the mining industry, especially for deep mines. We assessed the accuracy of this operation in a case study using the two-shaft plumbing and gyroscopic methods in order to compare and analyse the planimetric displacement of the baseline due to different sources of error in each method. The advantages and disadvantages of both methods are discussed. Some disadvantages in each method have been reduced thanks to technological progress, especially in the two-shaft plumbing method. The different sources of error that affect the measurements are analysed in detail with the aim of compensating them and achieving the required precision for an underground infrastructure. Mine ventilation has been identified as one of the most important sources of error in the plumbing method due to intake and return air flow producing a significant displacement of the verticality of the plumbs in the shafts. In this regard, we describe some measures to reduce the influence of ventilation and give details of a compensation method.

Keywords

shaft plumbing, ventilation, plumb oscillation, gravity, Earth rotation.

Introduction

An adequate development of an underground mine or the construction of a tunnel requires the transmission of the cartographic system and orientation from the surface to underground with high accuracy (Stiros, 2009). Maintaining the correct alignment over time is crucial to avoid cost overruns and delays (Yao *et al.*, 2019). Currently, optimization of the measurements is also an important topic in a wide variety of sectors, such as surveying (Štroner, Michal, and Urban, 2017) or civil engineering and construction (Zhang *et al.*, 2018). In the case of deep mining, this task is particularly complex when there is not an existing tunnel connected to the surface, necessitating the use of special techniques (Chrzanowski and Robinson, 1967; Benecke and Kalz, 2006).

However, each mine presents different characteristics: depth, ventilation layout, cross-sections and number of shafts, environmental conditions, presence of water *etc.* These conditions, together with the required level of accuracy, will affect the method used to transmit the orientation and cartographic system to underground. Hence, there is no standard procedure but different possibilities arise, depending on each case.

Verticality and its control is also important in many sectors and applications, such as buildings and infrastructure. The most widespread system used is based on satellite geo-localization (GPS, GLONASS, Galileo, *etc.*), which is capable of highly accurate measurements. This system allows different combinations of sensors and surveying equipment to deliver precise and reliable coordinates (van Cranenbroeck, 2010). Unfortunately, it is not possible to use it in mine shafts because the signals do not propagate underground.

This paper presents a detailed case study with an extensive analysis of the advantages and disadvantages of two commonly used methods – the two-shaft plumbing and gyroscopic methods. The mine assessed is located in Suria, northwest of Barcelona, Spain. It has a depth from 600 to 1000 m below the surface and access is by means of two vertical shafts, each 5 m in diameter and 680 m deep. The first shaft, called Shaft 2, is used for staff access and ventilation intake, while the second, Shaft 3, is used to extract the ore and for ventilation return. The two shafts are around 100 m apart (Figure 1).

The company is planning to connect the underground workings to the surface by a ramp. Several surveys have been done with the idea of transmitting the orientation and the cartographic system from the surface to the beginning of the ramp underground, which is 3500 m away from the shafts. For this reason, it is necessary to ensure that the error in the axis of the tunnel is acceptable, both horizontally

Assessment of errors in the transmission of the orientation and cartographic system

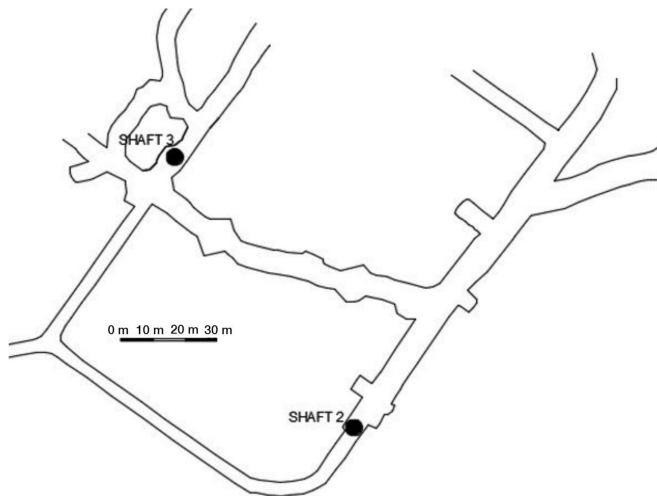


Figure 1—Mine layout in the area where measurements were taken

and vertically. However, high-accuracy coordinates and orientation is usually one of the main problems in tunnel surveying and underground constructions (Urban and Jiřikovský, 2015). There are two different options for transmitting topographical information from surface to underground.

- ▶ The two plumbs method is the best option when two shafts are accessible and a gyroscope is not available (Staley, 1964; Estruch and Tapia, 2003). Each plumb is connected to a wire, in the conventional system, running from the top of the shaft to the bottom. This allows reliable results to be obtained in deep shafts. The other option, a laser/optical system, is not as precise owing to the pressure and temperature differences between the top and the bottom of the shaft, which can create a deviation in the verticality of the laser. However, it is perfectly feasible in the case of shallow shafts, such as at the underground coal mine in Digwadih (Bahuguna, 2003). All activity in the shaft has to be stopped before the operation can be carried out.
- ▶ The gyroscopic survey method is widely used for the transmission of orientations with high accuracy, being able to define absolute directions at any measurement point and eliminate systematic errors (Benecke and Kalz, 2006).

As there are two shafts at the study site and it was important to ensure the accuracy of the measurements, it was decided to use both methods to analyse and validate the results.

Material and methods

Set-up

In the case of the plumb method, one of the main problems is the projection of a point from the top to the bottom of the shaft. It is important to ensure the plumb verticality, with either an optical or a conventional plumb using a cable. The conventional system was used in this study due to some intrinsic characteristics of the mine that are detailed further on. The following preparations were necessary before the measurements:

- ▶ Cover the tops of both shafts with a canvas to reduce the ventilation effect. The remaining ventilation effect is compensated
- ▶ Secure an anti-rotating steel cable 3 mm in diameter at the top of the shaft

- ▶ Connect a 64.4 kg plumb bob with several blades attached to the bottom of the steel cable. The plumb bob is placed inside a 1 m³ tank filled with oil to reduce oscillation
- ▶ Place a 10 × 10 cm bullseye on the cable to increase the accuracy of the measurements. This is because of the adverse environmental conditions (dust, pollutants, high temperature) in the drift.

This arrangement allows the coordinates to be projected in each of the two shafts. The bullseye enables easier and more accurate measurement with total stations when it is not possible to use a prism to measure distances, having a maximum measurement range of 25 m. Finally, the projected points of both shafts were connected by a polygon. The results obtained can be compared to those obtained by the gyroscope method and used to verify them.

The combination of both methods allowed any alignment of the polygon to be chosen for use with the gyroscope method. In this case, the best alignment was INT3-INT2 (Figure 4) due to logistical constraints. The equipment used is detailed below.

Total station Leica TCRP1201:

Angular accuracy: 1" (3s)

Linear accuracy: 1 mm ±1.5 ppm

Maximum distance measurement without prism: 250 m

Transit level accuracy: 30"

Gyroscope GYROMAX-AK-2M-TM:

Accuracy: 20" (60s)

The technical characteristics of the total station used specify a maximum error of 1 mm ±1.5 ppm, with prism and without prism if a bullseye is used. Before starting with the study, several measurements were taken to verify the precision of the equipment. Two sets of 10 measurements were obtained in two different alignments on two consecutive days, one alignment close to Shaft 2 and the other close to Shaft 3. Moreover, every measurement was taken with a time interval of 30 seconds (Table I).

The standard deviation (SD) from the sets of measurements is lower than 1 mm. Therefore, the technical specifications of the equipment have been verified. Zamecnikova *et al.* (2014) stress the importance of the type of surface from which the laser signal is reflected to avoid errors, being crucial to either the distance or the reflectivity. The use of a bullseye reduces this potential source of error, as can be concluded from the results in Table I.

Two-shaft plumbing method

A plumb was suspended in each shaft and the two were connected by means of an underground traverse. These will be referred to as plumb P1 for Shaft 3 and plumb P2 for Shaft 2.

Two sets of measurements were taken after eight hours without artificial ventilation in Shaft 2 – one set with the entrance of the shaft uncovered and another with the entrance almost completely covered with canvas to minimize the effect of natural air flow on the plumb and quantify its influence to the plumb verticality. The difference in the verticality of the plumbs between the shaft covered and uncovered was 1 cm. Hence, the set of measurements with the shaft covered was taken as correct.

Shaft 3 (the ventilation return shaft) could not be covered since the cover generated turbulence which affected the plumb stability. Hence, the ventilation effect was compensated by several sets of measurements at the bottom of the shaft.

The necessary weight for the plumb bob was calculated from the equation derived by Taton (1966):

Assessment of errors in the transmission of the orientation and cartographic system

Table 1
Distance measurements in two alignments without prism

Measurement	First day		Measurement	Second day	
	Alignment 1	Alignment 2		Alignment 1	Alignment 2
M1	16.595	22.558	M1	16.594	22.560
M2	16.594	22.559	M2	16.595	22.561
M3	16.595	22.559	M3	16.594	22.559
M4	16.595	22.559	M4	16.594	22.559
M5	16.595	22.558	M5	16.595	22.558
M6	16.595	22.558	M6	16.596	22.560
M7	16.595	22.559	M7	16.595	22.560
M8	16.596	22.559	M8	16.595	22.559
M9	16.595	22.559	M9	16.595	22.559
M10	16.595	22.559	M10	16.596	22.560
Average	16.595	22.559	Average	16.595	22.559
SD	0.0005	0.0003	SD	0.0007	0.0006

$W = 10 + 0.08L$, where L is the length of the shaft.

After evaluating the mine, the conventional plumb method was chosen instead of the optical method, based on two main reasons:

- Characteristics of the shafts. Water is falling down the shaft, and there are considerable levels of pollutants and dust. In addition, the temperature and pressure change during the day and there is an air flow despite the fans having been turned off. Furthermore, the cage and equipment inside the shafts make it very difficult to install the optical plumb with the necessary precision. All these factors could have an influence on the verticality of the optical plumb and, therefore, on the precision of the measurements.
- Safety issues. Falling rocks and other objects in the shaft have previously been reported and observed *in situ*. The installation of the optical plumbs requires precise tasks at the bottom of the shaft to ensure the accuracy. On the other hand, the conventional plumb can be installed using a more mechanized and easier process.

Gyroscopic method

The system is able to calculate true north with an accuracy of 20" (60s) in a single measurement according to the supplier. However,

after 10 tests with a series of five measurements, the standard deviation was found to be around 13.3" (40s). Therefore, the maximum precision of the gyroscope used has been taken as 40s in this case. In fact, the gyroscopic method is commonly used to correct the error accumulation of the traverses, and this is an effective method for improving the precision of the traverse control network and ensuring breakthrough of long tunnels (Shi, Ma, and Yang, 2016). Two sets of five measurements were taken at the surface base, called C4-C3, for the calibration and the underground base, called INT3-INT2, used for the underground traverse between the plumbs.

Propagation of measurement errors in the traverses

Consider a traverse based on a framework of coordinates as shown in Figure 2. Taking into account the propagation of errors in the measurement of angles (β_k) and distances (d_k) along the traverse, the coordinates (x_k, y_k) of the last station k can be obtained. The initial station $0 = (x_0, y_0)$ is treated as an error-free point, but the coordinates for any other point (x_k, y_k) are probabilistic and estimated as $(x_k \pm \alpha\sigma_{x_k}, y_k \pm \alpha\sigma_{y_k})$, with a probability of 68.3% for $\alpha = 1$, 95.5% for $\alpha = 2$, and 99.7% for $\alpha = 3$, where σ_{x_k} and σ_{y_k} are the standard deviations of x_k and y_k , respectively.

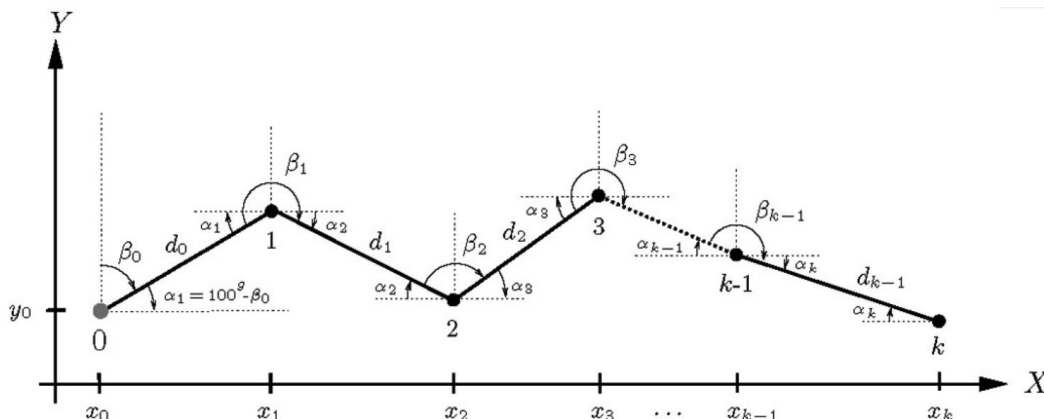


Figure 2—Measurement of angles and distances in a traverse

Assessment of errors in the transmission of the orientation and cartographic system

By applying the theory of error propagation (Davis *et al.*, 1981; Stiros, 2009), the coordinates (x_k, y_k) for a point k have the following form:

$$x_k = x_0 + \sum_{i=0}^{k-1} d_i \sin(\beta_0 + \beta_1 + \dots + \beta_i - 200^g i) \quad [1]$$

$$y_k = y_0 + \sum_{i=0}^{k-1} d_i \cos(\beta_0 + \beta_1 + \dots + \beta_i - 200^g i) \quad [2]$$

where β_0 is measured clockwise from north. The angles β_i , for $i = 1, \dots, -1$, are the horizontal angles between consecutive legs. Assuming that standard errors of angle and distance measurements satisfy $\sigma_{\beta_1} = \dots = \sigma_{\beta_{k-1}} = \sigma_\beta$ and $\sigma_{d_1} = \dots = \sigma_{d_{k-1}} = \sigma_d$, respectively, the following variances and covariance of the coordinates (x_k, y_k) result:

$$\sigma_{x_k}^2 = \sigma_\beta^2 \sum_{i=1}^k (y_k - y_{i-1})^2 + \sigma_d^2 \sum_{i=1}^k \left(\frac{x_i - x_{i-1}}{d_i} \right)^2 \quad [3]$$

$$\sigma_{y_k}^2 = \sigma_\beta^2 \sum_{i=1}^k (x_k - x_{i-1})^2 + \sigma_d^2 \sum_{i=1}^k \left(\frac{y_i - y_{i-1}}{d_i} \right)^2 \quad [4]$$

$$\sigma_{x_k y_k}^2 = -\sigma_\beta^2 \sum_{i=1}^k (y_k - y_{i-1})(x_k - x_{i-1}) + \sigma_d^2 \sum_{i=1}^k \left(\frac{(y_i - y_{i-1})(x_i - x_{i-1})}{d_i^2} \right) \quad [5]$$

Error ellipse

The variances and covariance allow any point $k = (x_k, y_k)$ to be confined to an error ellipse with a certain probability. To do this, Equation [6] is applied:

$$\lambda^2 - (\sigma_{x_k}^2 + \sigma_{y_k}^2) \lambda + (\sigma_{x_k}^2 \sigma_{y_k}^2 - \sigma_{x_k y_k}^2) = 0 \quad [6]$$

with $\sigma_{x_k}^2$, $\sigma_{y_k}^2$ and $\sigma_{x_k y_k}^2$ computed in Equations [3] to [5]. Denote λ_1, λ_2 the roots of Equation [6]. Then, the semi-axes of the error ellipse are given by $\tau\lambda_1, \tau\lambda_2$, with a probability depending on τ . Thus, for $\tau = 1$ the probability is 39%; for $\tau = 2.15$ it is 90%, and for $\tau = 2.45$ it is 99%. Moreover, the orientation of the error ellipse can be obtained as:

$$\tan 2\theta = \frac{\sigma_{x_k y_k}}{\sigma_{x_k}^2 - \sigma_{y_k}^2} \quad [7]$$

where θ is the angle between the major semi-axis and the X-axis (Mikhail, 1976).

Results

Errors in the measurements taken in the two shaft plumbing method

This method requires some operations to perform the connection survey that generate errors (Chrzanowski, Derenyi, and Wilson, 1967; Estruch and Tapia, 2003) as well as the overall error given by Equation [8]:

$$m_\alpha = \sqrt{m_s^2 + m_b^2 + m_p^2} \quad [8]$$

where m_α is the global error, m_s is the error produced in the surface works to determine the orientation and coordinates of the plumb at the surface, m_b is the error from the underground topographic survey to connect both plumbs or between the plumbs, and m_p is the vertical error of the plumb.

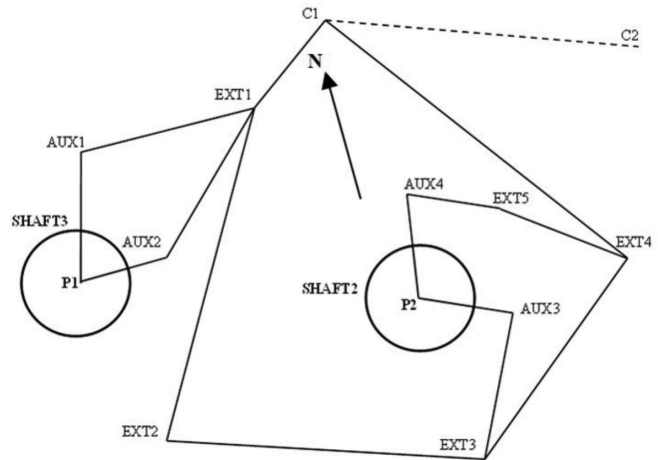


Figure 3—Surface traverse

The surface traverse (Figure 3) between base C1-C2 and plumbs P1 and P2 was a closed traverse, which allowed calculation the total error due to the angular and linear errors in the polygonal axis. The polygon had the following characteristics:

- Length: 436.374 m
- Number of legs: 5
- Error in X: -0.0015 m
- Error in Y: -0.0007 m.

The accumulation of angular and linear error in the axis, when the traverse was completed, produced a displacement of the final station (C1):

$$E_{tr} = \sqrt{e_x^2 + e_y^2} = \sqrt{0.0015^2 + 0.0007^2} \quad [9]$$

Coordinates of the plumbs (P1 and P2) were calculated through two different branches. Table II shows the error between measurements in each plumb.

The real squared error of the base P1-P2 was:

$$\text{Error in P1} = \sqrt{0.000^2 + 0.003^2} = 0.003 \text{ m} \quad [10]$$

$$\text{Error in P2} = \sqrt{0.000^2 + 0.000^2} = 0.000 \text{ m} \quad [11]$$

$$\text{Error in P1 - P2} = \sqrt{0.003^2 + 0.000^2} = 0.003 \text{ m} \quad [12]$$

The small differences in the plumbs' coordinates, as well as the angular and linear errors in the exterior closed traverse, indicate the accuracy of these measurements because the real error in the exterior base P1-P2 was lower than the theoretical error. This theoretical error in bases P1 and P2 regarding the external survey was calculated taking into account the

Table II

Error in the coordinates of plumbs P1 and P2 at the shaft top

Plumb	Error X (m)	Error Y (m)
P1	0.000	0.003
P2	0.000	0.000

Assessment of errors in the transmission of the orientation and cartographic system

Table III

Error ellipse characteristics at the final point of the exterior traverse

Exterior traverse	Point	Sx (m)	Sy (m)	Major axis (m)	Minor axis (m)	Max. error
C1-EXT1-AUX1-P1	P1	0.0001	0.0001	0.00028	0.00018	0.0003
C1-EXT1-AUX2-P1	P1	0.0001	0.0001	0.00029	0.00017	0.0003
C1-EXT1-EXT2-EXT3-AUX3-P2	P2	0.0002	0.0002	0.00064	0.00053	0.0008
C1-EXT1-EXT2-EXT3-EXT4-EXT5-AUX4-P2	P2	0.0017	0.0015	0.00465	0.00410	0.0062

topographic instruments and the leg characteristics. Its value will be the quadratic sum of the error ellipses in the semi-axis per leg. These error ellipses were calculated according to the methods used by Anderson and Mikhail (1998), Stiros (2009); and Mikhail (1976).

Error calculation

(a) Error m_s

Table III displays the error ellipse characteristics, at the end of the external survey, for plumbs P1 and P2, which were obtained by means of the topographical software TCP-MDT version 7.

Hence, the maximum theoretical error in P1 and P2 coordinates due to the exterior measurements was:

$$P1 = 0.0003 \text{ m (average error between two legs)}$$

$$P2 = 0.0035 \text{ m (average error between two legs)}$$

Consequently, the total theoretical error of the base P1-P2:

$$m_s = \sqrt{0.0003^2 + 0.0035^2} = 0.00353 \text{ m} \quad [13]$$

As can be seen from the previous sections, the theoretical error is higher than the real error. The most unfavourable, the theoretical one, will be taken into account in the underground survey.

(b) Error m_b

Figure 4 details the closed traverse (INT1-INT2-INT3-INT4-INT1) in the underground survey, used to transmit the coordinates of P1 and P2, which has the following characteristics and total errors:

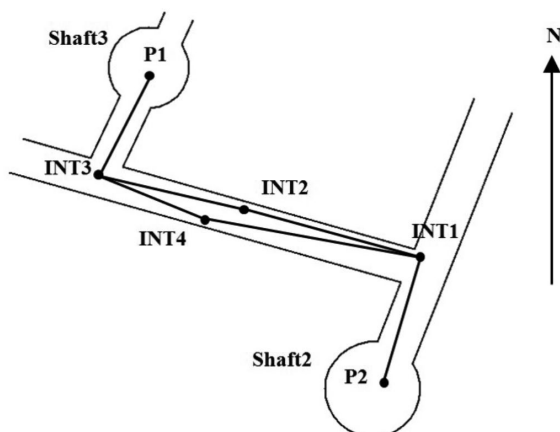


Figure 4—Underground traverse connecting plumb P2 and plumb P1

Length: 187.270 m

No. of legs = 4

Total error in X = 0.0030 m

Total error in Y = -0.0015 m.

The angular and linear error accumulations in the different axes produced the next final station displacement:

$$E_{tr} = \sqrt{e_x^2 + e_y^2} = \sqrt{0.0030^2 + 0.0015^2} = 0.0034 \text{ m} \quad [14]$$

Table IV reveals the adequacy of the angular and linear errors in the closed underground traverse. The error determination was done following the same procedure as for the surface measurements.

In this case, the maximum theoretical error in the base P1-P2 was, directly, the average error in the two legs of the underground traverse between P2 and P1, $m_b = 0.0057 \text{ m}$, which is larger than the real error obtained in the measurements of the closed traverse (INT1-INT2-INT3-INT4-INT1). Once again, it is considered the most adverse case.

(c) Error m_p

The sources of error, m_p , that could affect the verticality of the plumbs are quite complex and have to be thoroughly studied. These errors are especially important in the orientation transmission (α) because it is an angular measurement and the final linear error increases with the length of the traverse. Therefore, the plumbs have to be separated as far as possible in order to reduce the potential error. It is very difficult to do this with only one shaft, but in the case study the two shafts are separated by 100.618 m. This enables the angular error to be reduced significantly. The following paragraphs detail the factors that cause this error and the ways to calculate it and compensate for it, based on previous studies (Chrzanowski and Robinson, 1953; Chrzanowski, Derenyi, and Wilson, 1967). It was also demonstrated that the verticality of a plumbline in a shaft is affected by: ventilation, oscillation and vibration of the plumb, cross-sectional shape of the cable, and the effect of gravity.

Table IV

Error ellipse characteristics at the final point of the underground traverse

Underground traverse	Point	Sx (m)	Sy (m)	Major axis (m)	Minor axis (m)	Max error
P2-INT1-INT2-INT3-P1	P1	0.0012	0.0016	0.00456	0.00346	0.0057

Assessment of errors in the transmission of the orientation and cartographic system

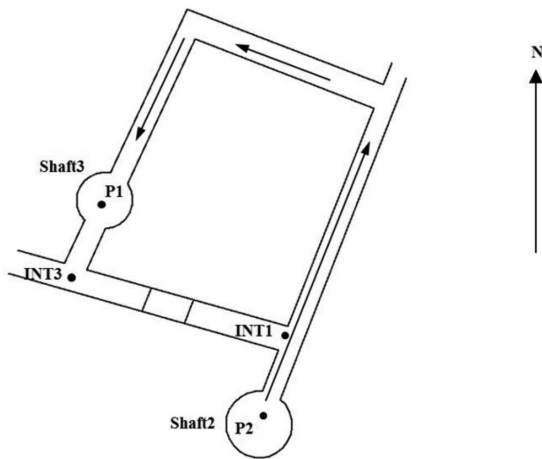


Figure 5—Direction and sense of the ventilation

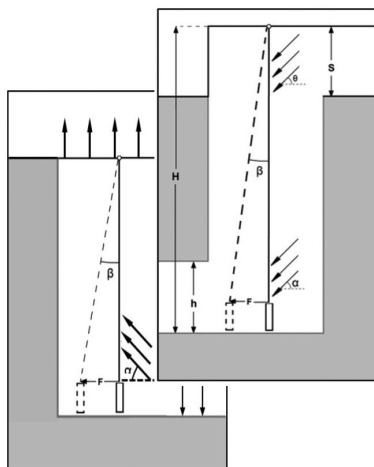


Figure 6—Diagram showing the ventilation effect on plumb P1 (shaft 3, left) and plumb P2 (shaft 2, right)

Influence of ventilation

The air flow in an underground mine can produce a significant displacement in the verticality of the plumb lines. Hence, it is essential to switch off the artificial ventilation system so as to minimize that the verticality error. The air speed dropped to 1.90 m/s at the bottom of Shaft 2 eight hours after the fans were switched off. Then, about 95% of the shaft entrance was covered, and consequently the air speed at the bottom was reduced from 1.90 m/s to 0.79 m/s. Two sets of 20 measurements were carried out, the first set with the shaft uncovered and the second with the shaft covered, two hours later. The air speed in Shaft 3 was reduced to 1.2 m/s at the bottom of the shaft 31 hours after the fans were stopped. Hence, the four sets of 20 measurements were done under similar conditions of air speed. Figure 5 details the relative position of both shafts and the flow direction in the ventilation circuit.

Mine ventilation is one of the main sources of error when using the plumbing method, and different procedures are used to compensate for this potential error. According to Chrzanowski

Table V

Variables description from Equation [15] and the case study

Parameter	Definition	Value
ρ_A (kg/m ³)	Air density	1.16
v_{int} (m/s)	Air velocity at the bottom of the shaft	1.2
C_f	Friction coefficient	1.3
D (m)	Wire diameter	0.003
H (m)	Length of wire exposed in the gallery	4
α (°)	Air angle of incidence	45
H (m)	Length of the plumb wire	680
G (m/s ²)	Gravitational acceleration	9.8
m_c (kg)	Weight of the wire	37.7
m_p (kg)	Weight of the plumb bob	64.4
F_{P1} (m)	Horizontal displacement of the plumb in Shaft 3	0.0054

(1967), the calculation of plumb displacement caused by ventilation has to take into account the air speed during the measurements in each shaft, depth of the shafts, plumb bob weight, and section of the shaft and tunnel, among other factors. Figure 6 shows how the ventilation varies the position of the plumb.

The equation for calculating F_{P1} is based on physical principles and it allows calculation of the plumb displacement owing to the ventilation (Figure 6). The calculation gave a horizontal displacement in plumb P1 of 5.4 mm (Table V).

$$F_{P1} = \frac{\frac{1}{2} \rho_A v_{int}^2 \cdot C_f \cdot D \cdot h (\cos \alpha)^2 \left(H - \frac{h}{2} \right)}{g \left(\frac{m_c}{2} + m_p \right)} \quad (m) \quad [15]$$

The covering of the shaft and its geometry affected the

Table VI

Variables description from Equation (16) and the case study

Parameter	Definition	Value
ρ_A (kg/m ³)	Air density	1.16
v_{int} (m/s)	Air velocity at the bottom of the shaft	0.79
v_{ext} (m/s)	Air velocity at the head of the shaft	8
S (m)	Square opening at shaft entrance	0.5
C_f	Friction coefficient	1.3
D (m)	Rope diameter	0.003
H (m)	Length of rope exposed in the gallery	4
α (°)	Air angle of incidence at the bottom of the shaft	45
θ (°)	Air angle of incidence at the head of the shaft	45
H (m)	Length of the plumb rope	680
G (m/s ²)	Gravitational acceleration	9.8
m_c (kg)	Weight of the rope	37.7
m_p (kg)	Weight of the plumb	64.4
F_{P2} (m)	Horizontal displacement of the plumb in the Shaft2	0.0024

Assessment of errors in the transmission of the orientation and cartographic system

Table VII

Standard deviation in each set of measurements from Shaft 2

Plumb P2 in Shaft 2	First set of measurements (1°) (n = 20)			Second set of measurements (2°)		
	X (m)	Y (m)	Total (m)	X (m)	Y (m)	Total (m)
P2 standard deviation	0,0016	0,0008	0,0018	0,0006	0,0006	0,0008

Table VIII

Standard deviation in each set of measurements from Shaft 3

Plumb P1 in Shaft 3	All series of measurements n = (80)		
	X(m)	Y(m)	Total(m)
Standard deviation in P1	0,0008	0,0019	0,0021

ventilation and, as a consequence, the plumb was also affected. The equation for calculating F_{p2} (Figure 6) has been used in this case. The angles θ and α created by the air and the horizontal can be determined graphically depending on the way the ventilation system introduces the air to the shaft and the intersection between the bottom of the shaft and the underground tunnel. However, a standard value of 45° can be adopted in the majority of the cases, as has been done in this survey. The deviation of plumb P2 was 2.4 mm (Table VI).

$$F_{p2} = \frac{\frac{1}{2} \cdot \rho_A \cdot C_f \cdot D \cdot \left[h \cdot v_{air}^2 \cdot (\cos \alpha)^2 \left(H - \frac{h}{2} \right) + \left(v_{air}^2 \cdot (\cos \theta)^2 \cdot \frac{S^2}{2} \right) \right]}{g \cdot \left(\frac{m_c}{2} + m_p \right)} \quad [16]$$

F_{p1} and F_{p2} values indicate the distance to compensate due to ventilation. However, it is necessary to know the direction and sense for the compensation. Previous studies indicated several methods that allowed the calculation of this direction, but they are laborious, complicated, and dangerous because employees have to work around the bottom of the shaft. Fortunately, the current surveying stations allow distances to be measured without the prism, after which the compensation is applied. The movement direction of the plumb in Shaft 2 was deduced from two points, 1° and 2°, obtained by the mean value of each set of measurements. There was an important air speed reduction between the first set of measurements (1.90 m/s) and the second (0.79 m/s once the shaft was covered). This reduction produced

Table IX

Linear error of the connecting underground traverse between plumbs P2 and P1

	Real measurements	Compensated measurements
Error X	-8.3 mm	-6.6 mm
Error Y	12.3 mm	9.7 mm
Linear error	14.8 mm	11.8 mm

a displacement of 1 cm between both points. Tables VII and VIII display the standard deviation in each set according to several studies (Box and Hunter, 2005; Ebdon, 1985).

Once the displacement of P2 is calculated, its coordinates without the ventilation effect can be obtained. This point is called P2N and it was determined by means of the second set mean value, orientation, and horizontal displacement, F_{p2} from Table VI. Finally, it was possible to calculate the new horizontal angle and distance towards P2 from the traverse station INT1.

Plumb P1 was determined by the procedure previously detailed, obtaining the average point P1N. Based on the coordinates from point P1N, the new horizontal angle and distance towards P1 from station INT3 of the underground traverse were calculated.

Table IX shows the linear error of the underground traverse with and without the ventilation compensation. It reflects a reduction of over 20% in the linear error, from 14.8 to 11.8 cm.

Hence, it is very important to take into account the compensation due to the ventilation effect in this kind of survey, particularly when it is not possible to cover the shaft or the natural ventilation is considerable. Besides, the angular and distance measurements have to be taken at the same time from the total station to the plumbs, and many times (two set of 20 measurements to plumb P2 in Shaft 2, and four sets of 20 measurements to plumb P1 in Shaft 3). For that purpose, it was necessary to use a laser capable of measuring the distance when aimed at a cable with a diameter of 3 mm from at least 10 m away.

Apart from the method described here, there are other options available such as applying a vertical load to the plumbs in order to reduce the ventilation effect (Schätti and Ryf, 2004).

Influence of plumb oscillation

The plumb was equipped with special wings to increase its stability. P2 measurements began five hours after the plumb bob was immersed in a tank full of oil. P1 measurements, on the other hand, started one hour after immersion. The centre point of the pendulum movement was found in both cases because of the number of measurements carried out.

Influence of vibrations and shape of the cable

Errors due to vibration and the shape (cross-section) of the cable were considered negligible because of several measures taken to reduce these: the wings, the tank of oil, and an anti-rotation cable.

Effect due to gravity and Earth's rotation

The distance between two plumbs varies slightly with depth

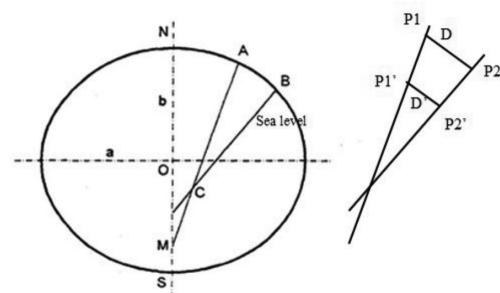


Figure 7—Plumb convergence due to gravity and centrifugal force

Assessment of errors in the transmission of the orientation and cartographic system

Table X

Error analysis of the underground traverse

	Without compensation	Ventilation compensation	Ventilation and Earth's gravity compensation
Error X	-8.3 mm	-6.6 mm	-0.5 mm
Error Y	12.3 mm	9.7 mm	0.7 mm
Linear error	14.8 mm	11.8 mm	0.9 mm

because they are not exactly parallel, and if they were extended to the centre of the Earth they would converge under the influence of gravity. However, the existence of a centrifugal force changes the direction of the plumbs and they do not converge towards the centre of the Earth but towards another intermediate point as indicated in Figure 7 (Estruch, 2001; Martin, 1983).

The distance in an alignment projection at a certain depth is deduced from the following equation

$$D = D' + \left[D' \frac{H}{R_o} + D' \frac{H^2}{R_o^2} \right] \text{ (m)} \quad [17]$$

where D is the distance of the alignment in the surface (m), D' is the distance of the alignment in a certain depth (m), H is the depth of the projection of the surface alignment (m), and R_o is the average radius of the Earth (6 375 000 m in this study).

Using the data from the case study, where D is 100.618 m and H is 680.591 m, D' will be 100.607 m with an error of 0.011 m. This error has been compensated by increasing each distance of the underground traverse between P1 and P2 by a value calculated applying the indicated equation according to previous studies by Chrzanowski and other authors. In this case, this error has been the most important. However, its compensation is very simple.

Other errors affecting the plumb verticality

Some authors consider the possibility that the plumbs could be affected in their displacement by their masses, but King and Habberjam (1951) stated that the attraction between the masses and the plumb is insignificant when the shaft is less than 1000 m deep. It is also said that the attraction of two plumbs is different if they are separated by more than 1500 m (King and Habberjam, 1951). As the plumbs in the case study were separated by 100 m at a depth of 680 m, the deviation due to the attraction between the plumbs and the ground does not influence the verticality, nor transmission of the orientation and cartographic system.

Table XI

Gyroscope measurements

	Underground axis INT3-INT2	Underground axis INT3-INT2
Number of measurements	5	5
Average true north orientation	128.0780 ^o	128.0844 ^o
Standard deviation	37 ^s	45 ^s
Final meridian convergence	0.9217 ^s west	0.9171 ^s west
Projected north orientation system UTM	128.9997 ^o	129.0015 ^o

(d) Quality control

The closing error of the underground traverse between P2 and P1 has been used as a quality control in the survey. This linear traverse closing error in the traverse P2-INT1-INT2-INT3-P1 is an indicator of the global precision, because it accumulates the errors occurring on the surface and in the plumb verticality. Table X summarized the linear error of the underground traverse between the plumbs before and after applying the compensations.

Error M_α

All the errors that compose the plumb vertical deviation m_p could be compensated with the equations of F_{p1} and F_{p2} , achieving an error m_p practically nullified. Therefore, the total error m_α affecting the orientation from the base P1-P2 to the underground tunnel would be detailed as follows:

$$m_\alpha = \sqrt{m_s^2 + m_b^2 + m_p^2} = \sqrt{3.5^2 + 5.7^2 + 0.9^2} = 6.75 \text{ mm} \quad [18]$$

It was possible to find the angular error with the length of the base from the lineal error m_α :

$$\text{Error} = \frac{0.00675 \text{ m}}{100.618 \text{ m}} = 6.670762 \cdot 10^{-5} \cdot \frac{636620^s}{1 \text{ rad}} = 43^s \quad [19]$$

Errors in the measurements taken by the gyroscopic method

Errors in the orientation generated by the gyroscope depend on its precision. In this case, it has an accuracy of 60^s in a single measurement according to the specifications of the supplier. However, a set of measurements can have a standard deviation about 40^s as indicated in the section 'Two shaft plumbing method'.

Measurements done with the gyroscope consisted of two sets of measurements of the underground base INT3-INT2 on different days. Each set consisted of five measurements: three with the gyroscope located at the point INT3 measuring INT3-INT2 and two with the gyroscope located at INT2 measuring INT2-INT3.

Table XI shows the results and accuracy of the measurements. The standard deviation has been calculated according to the method of Box and Hunter (2005) and Ebdon (1985).

The mean value of base INT3-INT2 using the gyroscope was 129.0003^s. The final meridian convergence is calculated from the theoretical meridian corrected by the data obtained from the calibration baseline (C4-C3). The theoretical meridian convergence in point of known coordinates is obtained by a software application from the Cartographic and Geological Institute of Catalonia website and equations by Estruch (2001). The convergence has been taken into account in determining the final orientation.

If only the gyroscopic method was applied, the coordinates of a known point would have to be projected to the underground tunnel from the surface using a conventional method, one plumb in a shaft for transmitting the cartographic system. Hence, there

Table XII

Error ellipses on the final leg of the underground traverse between P1 and INT2

Underground traverse	Point	Sx (m)	Sy (m)	Major axis (m)	Minor axis (m)	Max. error
P1-INT3-INT2	INT2	0.0007	0.0008	0.00228	0.00191	0.0030

Assessment of errors in the transmission of the orientation and cartographic system

Table XIII

Variation of the orientation in the underground base INT3-INT2

	Orientation without compensation	Ventilation compensation	Ventilation and gravity compensation
Plumb method with 2 shafts	128.9932g	128.9959g	128.9959g
Gyroscope	129.0003g	129.0003g	129.0003g
Difference	71 ^s	44 ^s	44 ^s

will be two sources of errors: the true north orientation to the underground base and the transmission of the cartographic system from the surface.

The error generated by the gyroscope affects the orientation of the base measured, while the errors of the cartographic system transmission have been described in the section 'Errors in the measurements taken in the two shaft plumbing method', but regarding only one plumb. The global error m_{α} is also determined by Equation [8].

Considering that the cartographic system is transmitted by plumb P1, the error in the surveying works on the surface according to the section 'Error m_s ' is 0.0003 m (Table XII). Therefore, m_s is 0.0003 m.

For calculating the error in the underground leg INT3-INT2 it is necessary to indicate that the underground traverse to find the coordinates of points INT3 and INT2 was the traverse P1-INT3-INT2. In short, only two legs. In this way the error ellipse in INT2 was as shown in Table XII.

Therefore, the maximum theoretical error of base INT2 in the underground topographic survey was, directly, the error in the leg of the underground traverse between P1 and INT2:

Overall, Equation [20] includes the error generated to transmit the cartographic system through plumb P1 to the base INT3-INT2:

$$m_{\alpha} = \sqrt{m_s^2 + m_b^2 + m_p^2} = \sqrt{0.3^2 + 3.0^2 + 0.9^2} = 3.1 \text{ mm} \quad [20]$$

It must be pointed out that this error does not affect the orientation of the baseline INT3-INT2; it only produces a displacement of the coordinates. The error in the orientation is the standard deviation, 41^s, of the measurements done by the gyroscope.

Discussion

The underground orientation of the base INT3-INT2 varies because of the ventilation compensation, but it is not affected by the gravity force compensation (Table XIII). It can also be observed that the difference between both methods is only 44^s after the compensations.

Both methods have advantages and disadvantages, but they have similar accuracies.

- The two shaft plumbing method is operationally more laborious than the gyroscopic alternative. It needs to transmit the orientation and cartographic system from two shafts, whereas the gyroscope needs only one. This fact necessitates several hours of work around the shafts, increasing the risk to the staff.

- The plumbing method also needs more surface and underground surveying. However, the closed traverse in this method allows the accuracy of the values to be checked, whereas with the gyroscope the results can be verified only by doing an extra set of measurements.
- The most dangerous measurements are those around the shaft, especially those at the shaft bottom to calculate the central position of the plumb during its pendulum movement, due to falling rocks and other objects. However, the use of a total station without prism avoids this situation.
- Despite the plumbing method takes a few hours longer than the gyroscopic option, in the case study the plumbing took 20 hours and the gyroscopic measurements 31 hours. This discrepancy is due to the verification measurements done in the second case, while the two shaft plumbing method does not need verification. This time is subdivided into the following operations:
 - Plumbing method: 20 hours
 - a) 11 hours in Shaft 2
 - b) 9 hours in Shaft 3
 - Gyroscope: 31 hours with verification measurements and 19 hours without them
 - a) 7 hours in Shaft 3 (work for transmitting the cartographic system from the exterior to underground in the case that the two shaft method was not applied)
 - b) 2 × 5 hours calibration base C4-C3 and verification
 - c) 2 × 7 hours underground measurement INT3-INT2 and verification.

Conclusions

The study has described some adaptations of existing procedures, applied in studies some time ago, by means of new technologies, improving the accuracy of the measurements and safety levels during the survey because of the shorter time spent working around the shafts. In addition, the two shaft plumbing and the gyroscopic method have been analysed, emphasising the characteristics of both options. The comparison revealed similar accuracy levels, with a difference of only 44^s between the two methods. This confirms the reliability of the measurements made in the study and the suitability of both options.

The study suggests that the most important source of error in the two shaft plumbing method is the ventilation factor. Therefore, it is important to stop the artificial ventilation at least 24 hours before taking the measurements to reduce the air flow as much as possible. Unfortunately, it is very difficult to stop the operating fans for such a long time, and covering the intake shaft is an alternative. It is still necessary to compensate for the deviation of the plumb due to the ventilation effect caused by the remaining air flow.

It has also been found necessary to compensate the projected distances for a certain depth because of gravity and rotational forces, achieving a reduction in the linear error of the traverse between plumbs in both shafts in large part. Although this is very important in terms of error, compensation is much easier than in the ventilation effect.

The conventional plumblines method has proven to be a good choice when there are two shafts with depths greater than 500 m, and with some of the problems within the shaft as detailed

Assessment of errors in the transmission of the orientation and cartographic system

in the paper: pollutants, dust, remaining air flow, the possibility of rocks and other objects falling, water, limited physical space, and temperature and pressure changes during the measurement period. All these elements are potential sources of error in the verticality of an optical plumb as well as an avoidable occupation hazard. In the other cases the optical plumb is an adequate alternative due to its speed of installation.

It can be concluded that the conventional plumb method combines higher precision measurements and safer working conditions than the optical plumb method in the case study conditions. In addition, the combination of both methods, gyroscopic and plumbing, has been verified as an appropriate approach when high-precision measurements are needed.

Acknowledgements

The authors would like to thank ICL Iberia for their cooperation, especially the head of the surveying department, as well as the technical support of Carles Xandri from Maptek Pty Ltd.

References

- ANDERSON, J. and MIKHAIL, E. 1998. Surveying, Theory and Practice. 7th edn. WCB/McGraw-Hill, Boston.
- BAHUGUNA, P.P. 2003. Correlation survey for shaft deepening in Digwadih underground coal mine. *Journal of Surveying Engineering*, vol. 129, no. 1. pp. 33–36.
- BENECKE, N. and KALZ, U. 2006. Ensuring tunnel navigation by cost-effective gyroscope control measurements. *Tunnelling and Underground Space Technology*, vol. 21. p. 253.
- BOX, G.E.P., HUNTER, J.S., and HUNTER, W.G. 2005. Statistics for Experiments. Design, Innovation and Discovery. Wiley, Hoboken, NJ.
- CHRZANOWSKI, A., DERENYI, E., and WILSON, P. 1967. Underground survey measurements: Research for progress. *Canadian Mining and Metallurgical Bulletin*, vol. 60, no. 662. p. 643.
- CHRZANOWSKI, A. and ROBINSON, A. 1953. Surveying, Theory and Practice. McGraw-Hill, New York.
- DAVIS, R., FOOTE, F., ANDERSON, J., and MIKHAIL, E. Surveying. Theory and Practice (sixth ed.), McGraw-Hill, 1981.
- EBDON, D. 1985. Statistics in Geography. Blackwell. Hoboken, NJ.
- ESTRUCH, M. and TAPIA, A. 2003. Topografía Subterránea para Minería y Obras. Ediciones UPC, Barcelona.
- ESTRUCH, M. 2001. Cartografía Minera. Ediciones UPC, Barcelona.
- KING, H.J. and HABBERJAM, G.M. 1951. Displacement of Shaft Plumb Lines. Colliery Engineer, London.
- MARTIN, F. 1983. Geodesia y Cartografía Matemática. Paraninfo S.A., Madrid.
- MIKHAIL, E.M. 1976. Observations and Least Square. IEP, New York.
- SCHÄTTI, I., and RYF, A. 2004. Hochpräzise Lotung im Schacht Sedrun des Gotthard-Basistunnels. *Proceedings of the 14th International Conference on Engineering Surveying*, Zürich. <http://doi.org/10.5169/seals-236146>
- SHI, Z., MA, J., and YANG, Z. 2016. A study on the optimized adjustment method of maglev gyro control traverse under non-weighted measurement in long and large tunnels. *Modern Tunnelling Technology*, vol. 53, no. 2. pp. 44–47.
- STALEY, W.W. 1964. Introduction to Mine Surveying. Stanford University Press.
- STROS, S.C. 2009. Alignment and breakthrough errors in tunneling. *Tunnelling and Underground Space Technology*, vol. 24. pp. 236–244.
- ŠTRONER, M., MICHAL, O., and URBAN, R. 2017. Maximal precision increment method utilization for underground geodetic height network optimization. *Acta Montanistica Slovaca*, vol. 22, no. 1. pp. 32–42.
- TATON, R. 1966. Topographie Souterraine. Editions Eyrolles, Paris.
- URBAN, R. and JIRIKOVSKÝ, T. 2015. Accuracy analysis of tunneling measurements in UEF Josef. *Proceedings of the 15th International Multidisciplinary Scientific GeoConference*, SGEM, Sofia, vol. 2, no. 2. pp. 35–42.
- VAN CRANENBROECK, J. 2010. Controlling vertical towers. *Reporter 63: The Global Magazine of Leica Geosystems*. pp. 29–31.
- YAO, Y., LU, N., YANG, Y., CAO, Y., and YU, H.S. 2019. Study of long-termed displacements of a tunnel boring machine during its stoppage. *Tunnelling and Underground Space Technology*, vol. 84. pp. 432–439.
- ZAMEČNIKOVA, M., WIESER, A., WOSCHITZ, H., and RESSL, C. 2014. Influence of surface reflectivity on reflectorless electronic distance measurement and terrestrial laser scanning. *Journal of Applied Geodesy*, vol. 4. pp. 311–325.
- ZHANG, X., ZHANG, Y., LI, B., and QIU, G. 2018. GNSS-based verticality monitoring of super-tall buildings. *Applied Sciences*, vol. 8, no. 6. doi:10.3390/app8060991



5 STAR

Incentive Programme

About the SAIMM 5 Star Incentive Programme:

The SAIMM are proud to welcome you to our Incentive programme where we have negotiated to provide you with more benefits. These benefits include:

1. **Top 5 Proposers** for the current financial year are to be given a free ticket to the SAIMM Annual Banquet with mention at the Annual General Meeting.
2. **Top 5 Referees** for the financial year are to be given a free ticket to the SAIMM Annual Banquet with mention at the Annual General Meeting.
3. Access to discounts offered by **Service providers** that have negotiated discounted rates and special offers for you our valued member.
4. **Conference attendance** within a 2 year period and applies to events that are paid for. If you attend 3 events you get the next conference that you register for at no cost.
5. The author with the **most number of papers published in the SAIMM Journal in the previous financial year** would be recognised at the Annual General Meeting and will receive a free ticket to the SAIMM Annual Banquet.

How it works:

1. Collect your membership card from the SAIMM
2. Visit the SAIMM Website partner page to view all the deals available
3. Present it to the selected providers on the page behind this to qualify for the discount or offer.



Identifying barriers to growth in mineral value chains

H.J. Van Zyl¹, W.G. Bam¹, and J.D. Steenkamp^{2,3}

Affiliation:

¹Department of Industrial Engineering, Stellenbosch University, South Africa.

²Pyrometallurgy Division, Mintek, Randburg, South Africa.

³Department of Chemical and Metallurgical Engineering, University of the Witwatersrand, Johannesburg, South Africa.

Correspondence to:

H.J. Van Zyl

Email:

hman.v.zyl@gmail.com

Dates:

Received: 21 Sep. 2018

Revised: 26 Nov. 2019

Accepted: 28 Nov. 2019

Published: February 2020

How to cite:

Van Zyl, H.J., Bam, W.G., and Steenkamp, J.D.

Identifying barriers to growth in mineral value chains.

The Southern African Institute of Mining and Metallurgy

DOI ID:

<http://dx.doi.org/10.17159/2411-9717/341/2020>

Synopsis

Despite the importance that barrier identification has for policy-making and industry stakeholders alike; little guidance exists on consistent processes to systematically identify barriers that are hindering the different sectors of a value chain's expansion and growth. This article describes the development of a framework that supports the identification of barriers to growth in mineral value chains. The resultant process was applied to the case of the manganese value chain in South Africa, and revealed 31 barriers within this industry. The results were validated by a panel of experts and the feedback was used to rework and improve the framework.

Keywords

beneficiation, policy-making, barriers, manganese, case study, South Africa.

Introduction

Many of the world's mineral-rich countries are developing nations. In these countries, the mineral industry tends to make a large contribution to the annual gross domestic product and state income (UNCTAD, 2013). For these countries, it is imperative that proper mineral management strategies are put in place to ensure that the best developmental value is obtained from these industries (Bam and de Bruyne, 2017; Kahn, 2013). The various sectors comprising the mineral industry can generate a multitude of jobs, both directly and indirectly, contribute to the transfer of technologies and knowledge while also providing a substantial income (Coe, Dicken, and Hess, 2008; Gereffi and Fernandez-Stark, 2011). These developmental and economic benefits can also provide governments with the financial foundation for infrastructure development, which can lead to improved delivery of social services such as education and health care to improve the living conditions of the national citizenry (Gereffi and Fernandez-Stark, 2011; OECD, WTO, and World Bank Group, 2014).

The mineral industry, however, also has certain precarious characteristics, such as volatility, uncertainty, and exhaustibility, which pose many challenges to businesses, and policy-makers alike. A commonly stated anomaly that has been put forward is that countries with abundant natural resources often register lower economic growth than those without these natural resources (Alba, 2009; Callaghan, 2014; Department of Mineral Resources, 2011). This observation, its causes, and its validity has also given rise to a debate surrounding the possible existence of a so-called 'resource curse' and how to avoid it (Gilberthorpe and Papyrakis, 2015; Sachs and Warner, 1995; Stijns, 2005).

Within this context, beneficiation (broadly defined) is often viewed as being of strategic importance to mineral-producing countries. Specifically, beneficiation is often considered to be a key driver of industrial diversification (Bam and de Bruyne, 2017). Nonetheless, the beneficiation industries are exposed to various cyclical and systemic constraints that can hinder the ability of mineral-producing countries to establish and sustain these industries, with the capabilities that support effective mining differing from those that support effective beneficiation (Bam and de Bruyne, 2019; Hausmann, Klinger, and Lawrence, 2008). This is complicated by the constant emergence of new barriers to growth and the divergence of barriers faced by the different tiers of the mineral value chain. This makes it particularly difficult for policy-makers to firstly identify and, secondly, react to challenges that the different sectors of the mineral industry might face. In developing countries, these challenges are exacerbated by limited state resources and capacity. In many instances, and especially in developing countries, mistrust may also exist between government and industry, further complicating effective policy-making (Humphreys, 2013; Kahn, 2013).

Identifying barriers to growth in mineral value chains

Despite the importance that being able to identify barriers has for policy-making, little guidance exists on consistent systems or frameworks which enable researchers, policy-makers, and analysts to systematically identify the barriers (in a broad sense) that are hindering expansion and growth in various sectors of a value chain and to support proactive action by policy-makers to address these barriers (Bam and de Bruyne, 2017). The development of a systematic and comprehensive framework that could enable the proactive identification of the custom sets of barriers faced in mineral value chains (MVCs) could assist policy-makers to more efficiently determine which barriers are hindering growth on a periodic basis. The aim of this research is thus to develop such a framework which supports specialized barrier analysis for each subsector in an MVC. The goal is to improve the efficiency with which researchers, policy-makers, and other stakeholders can evaluate the binding constraints on an MVC in order to formulate effective responses to address these constraints.

Given the above, this paper provides a literature review of value chain analysis approaches and the shortcomings they have concerning the identification of specific barriers to growth (*Theoretical background*). To address these shortcomings, a novel framework for guiding the identification of barriers in MVCs was developed and applied to a case study of manganese in South Africa. An outline of the methodology used for developing this framework is presented in the *Framework development* section. This is followed by an exposition of the developed framework (*Framework design*). The application of the framework is presented in the *Case study* section and the methods used to validate the framework are discussed in the *Framework validation* section. The paper is concluded by discussing the outcomes and implications of the research.

Theoretical background

Various methods have been employed to analyse MVCs and how governments can support them. One of the dominant frameworks used for mineral development analysis has been *linkage theory*, based on the work by Hirschman (1981). This has been extended to a value chain perspective by authors such as Kaplinsky, Morris, and Kaplan (2011) using the global value chain (GVC) approach based on the work by Gereffi, Humphrey, and Sturgeon (2005), among others. Other works focusing on MVCs extend linkage theory with value chain analysis and a growth pole perspective (*e.g.* Callaghan, 2013).

The GVC analysis framework has become an increasingly important policy analysis tool (Gereffi, 2019). It effectively links producers and consumers from around the world into an integrated analysis framework. This provides a powerful departure point for understanding increasingly global links between firms. The GVC framework specifically provides insight as to how global firms are coordinated by investigating the structure and dynamics of the role-players involved in a specific chain. This methodology is often used as a tool to trace global production, link geographically dispersed activities and role-players, and determine the roles they play within the industry (Gereffi and Fernandez-Stark, 2011). The basic framework consists of four basic artefacts, namely: the input-output structure (a map showing the process of transforming raw materials into final products); the geographic scope of processing activities and supply and demand of products; governance structure (which explains how value chains are controlled); and institutional context (which investigates the characteristics and

attributes of the environment the value chain is embedded in) (Gereffi and Fernandez-Stark, 2011).

The VC perspective, and GVC perspective in particular, is very useful for facilitating the conceptualization of industry value chains and these frameworks have been seeing increasing use in the realm of policy analysis. The strengths of these frameworks include the fact that they:

- Provide a comprehensive description of the entire scope of the value chain (Gereffi and Fernandez-Stark, 2011; Porter, 1985)
- Identify the key role-players involved within the chain as well as the relationship they have with one another (Schmitz, 2005)
- Identify the value-adding processes within the chain (Kaplinsky and Morris, 2001); investigate the value added in different stages of the value chain (Gereffi and Fernandez-Stark, 2011; Porter, 1985)
- Describe the value chain in a global context (Gereffi and Lee, 2012)
- Include a value chain mapping structure (Gereffi and Fernandez-Stark, 2011; Kaplinsky and Morris, 2001)
- Consider chain governance structures (Humphrey and Schmitz, 2001); and consider the institutional attributes of the chain (Gereffi and Fernandez-Stark, 2011; Schmitz, 2005).

However, these approaches have certain shortcomings that need to be considered. They lack a clear purpose and structure (which allows flexibility, but requires additional analyst expertise, time, and resources); they are not consistently repeatable (particularly because they mostly rely on qualitative data and few quantitative measures have been proposed); and they specifically focus on governance and value capture issues (this implies that they potentially exclude the consideration of other factors that may also be hindering growth in the value chain). GVC (and related GPN) analysis is a suitable tool for retrospective investigation of a value chain and to identify the current extent of downstream processing (as well as the power relations between actors), but lacks a form of foresight analysis or explanations for the barriers to growth within the chain (Neilson *et al.*, 2018).

Literature on both local and foreign mineral industries suggest that many barriers exist that prohibit economic growth in the sector (*e.g.* Elliot, 2015; Edinger, 2014; Ford, Hobbs, and Urquart, 2007). Despite this acknowledgement, there is no comprehensive framework that can be used systematically to identify these barriers in value chains. A simple, proven, and reliable framework would allow policy-makers to identify such barriers more efficiently. Some significant issues in this field have not been addressed:

- Often only a single sector of the value chain is investigated, without consideration of the other sectors also comprising the chain (EY, 2019; von Below, 1992)
- The GVC analysis methods used in several mineral investigations do not specifically focus on the identification and prioritization of barriers
- GVC analysis and other qualitative methods are usually not systematically structured and require considerable analyst interpretation
- The data for quantitative approaches is often not available or limited, especially with regard to different sectors and developing countries (Gajigo, Mutambatsere, and Adjei, 2011; International Manganese Institute and RPA, 2015; Poole and Mhelembe, 2014)

Identifying barriers to growth in mineral value chains

- The scope of investigation is often too broad, restraining a full analysis of the chain and making it possible to provide only an overview of certain barriers (D'Harambure, 2015; EY, 2013)
- An analysis of the complete impact of the identified barriers is often lacking (D'Harambure, 2015; EY, 2019).

Methodology overview

Given the aim of developing a framework that supports the identification of barriers to growth in MVCs, a systematic approach was adopted in order to determine the requirements for the proposed framework (see Figure 1). Using GVC analysis literature as a basis for identifying requirements, a number of design requirements were identified, and corresponding analysis tools incorporated into the framework to address them. This framework (consisting of numerous VC analysis tools) was then applied to a comprehensive illustrative case study in order to attain insights regarding the practical application of the developed framework.

The research methodology can thus be divided into three stages:

- *Framework requirement and tool identification*, which includes the process of identifying the design requirements and tools required to identify barriers in the MVC (the development of the framework design requirements and potential analysis tools were based on parameters which were identified from the GVC and related literature)
- *Framework design and application* in order to determine the practical use of the framework in a real scenario and capture results for validation (through this exploratory case study, specific MVC characteristics were captured in a consistent and coherent manner)
- *Validation of the framework performance* through expert analysis of the case study and the framework itself (which enabled a review of the framework's capabilities and led to the refinement of the integrated MVC analysis process framework).

For the first step of the first phase of the methodology, the framework design requirements were identified. This was done by investigating the strengths and shortcomings of existing value chain analysis approaches through a literature review. The results of this phase are presented in the section *Framework development*. Supplementary tools were also identified to address the key shortcomings of the existing value chain approaches in relation to identifying barriers in MVCs. These tools were integrated within a systematic process to form an overarching

framework to identify barriers for different sections comprising mineral value chains (further described in *Framework design*).

During the second stage, the framework was applied to the case study (the results of which are presented in the *Case study section*). Each framework tool, as identified in the previous stage, was applied to the South African manganese MVC. The results from each phase were gathered and analysed in order to ultimately identify the barriers to growth throughout the value chain. These barriers were then categorized according to their severity and prevalence, which revealed the top ten barriers faced in each sector of the value chain.

The final stage of the methodology consisted of validating the results and the proposed framework. The framework structure and case study results were validated through expert analysis (described in the *Framework validation section*). Validation questionnaires were employed, and interviews conducted with experts from diverse fields of mineral value chain analysis. Their feedback with regard to the framework's usefulness, strengths, and shortcomings was reviewed and the necessary changes were incorporated within the framework.

Figure 2 is a visual representation of the framework design process followed to determine the tools to be incorporated into the proposed framework.

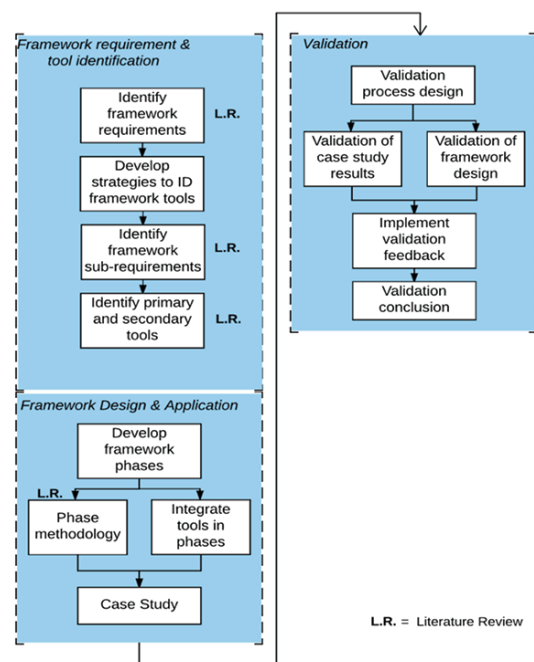


Figure 1—Overview of the implemented research methodology

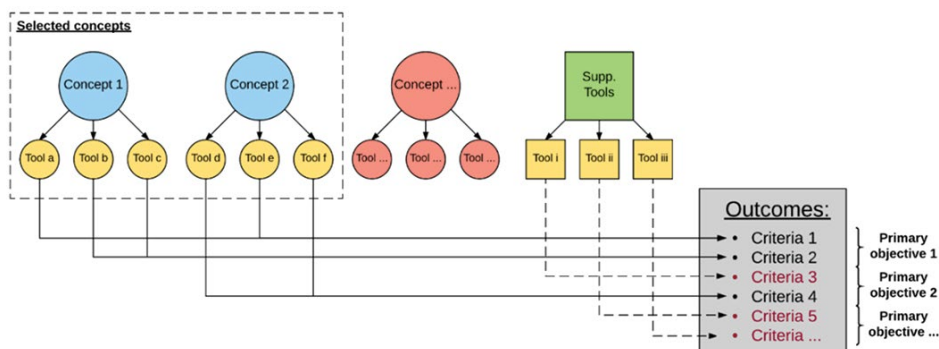


Figure 2—The framework design process

Identifying barriers to growth in mineral value chains

Framework development

The results from each of the steps included in the framework design process are described in this section, namely identifying the framework design requirements, identifying the supplementary tools, and integrating these tools in an overarching framework.

It is evident from investigating the various value chain analysis methods that each approach has characteristics that need to be investigated to ascertain its suitability for supporting the identification of barriers in MVCs. Supplementary analysis tools were also deemed necessary to address the limitations of the existing value chain analysis methods. The framework component requirements for describing an MVC were identified from the GVC and value chain literature, with new requirements proposed to address the limitations of the prevailing frameworks. These framework requirements are summarized in Table I.

Framework design

The framework consists of five phases which group specific tools together to make it more user-friendly and simpler to implement, with each phase focusing on a specific element of analysis. Table X in Appendix A provides an overview of the aim, detail, and outcome of each of the five phases. Once all of these phases are integrated, an overview of the proposed framework can be presented, as seen in Figure 3.

Primary data to identify barriers within the MVC can be collected by conducting interviews and surveys. This can be reliably done by following the Delphi technique. The technique aims to achieve a convergence of opinion on a specific real-world issue through a group communication process. The data collected from the interviews can then be used to compile a comprehensive list of sector-specific barriers across the industry. Each round of

the Delphi process as implemented in the exploratory case study is summarized in Table XI in Appendix B.

Once the barriers have been identified from the Delphi process, these barriers can be analysed by assessing their severity and prevalence, classifying them according to priority, reviewing the high-priority barriers, and determining the causal factors of the high-priority barriers. The implementation of these steps is further clarified in the case study section that follows.

Case study

This section reviews the case selection rationale and presents the results of the case study according to the five phases of the framework. The South African manganese industry was selected as a case study for the following reasons:

- Manganese has significant commercial importance, especially for the production of steel. Thus the results gathered from the case study will be of significant value
- Manganese is mainly used as an alloying element, hence this industry is analogous to many other mineral industries, such as chrome and iron, which are also primarily used in the manufacturing of alloys for steel
- South Africa is major player in the manganese industry, making information for the study more accessible and readily available
- Manganese is predominantly used only in steel manufacturing, which limits the product scope and simplifies the analysis required for the study.

An international perspective was also incorporated into the study to determine South Africa's global market presence. Since the entire value chain is very extensive and becomes increasingly intricate further down the chain, the scope of the value chain analysis was limited to activities involving the primary processing of the ore for product manufacturing. Each

Table I

Framework requirements

Strategic framework requirement no.	Requirement	Rationale and source
SFR1	Background knowledge on the specific mineral industry	Proposed to provide a knowledge base of the MVC that is to be investigated
SFR2	Identification of activities in the value chain	Key to describing value chain. Builds on Porter's value chain approach (Porter, 1985)
SFR3	Identification of the value chain role-player structure	Key to describing value chain. Builds on Porter's value chain (Porter, 1985) and GVC analysis (Gereffi and Fernandez-Stark, 2011; Gereffi, Humphrey, and Sturgeon, 2005)
SFR4	Identification of the different sectors comprising the industry	Proposed to enable the identification of sector-specific barriers
SFR5	Identification of the process-level flow of inputs, outputs, and intermediate products in the value chain	Proposed to elaborate upon Porter's value chain (Porter, 1985) in order to reveal the relationships among the role-players involved in the MVC through modelling the industry's high-level interaction between the various stakeholder involved
SFR6	Evaluation of domestic industry's global market position	Key to understanding context of barriers. Builds on GVC analysis (Gereffi, 2011; Gereffi and Fernandez-Stark, 2011; Sturgeon and Gereffi, 2009)
SFR7	Evaluation of the geographic scope of operations in the mineral value chain	Key to understanding context of barriers. Builds on GVC analysis (Gereffi, 2011; Gereffi and Fernandez-Stark, 2011)
SFR8	Evaluation of the power relationship between role-players	Key to understanding context of barriers. Builds on GVC analysis (Gereffi, 1994; Gereffi and Fernandez-Stark, 2011; Gereffi, Humphrey, and Sturgeon, 2005)
SFR9	Evaluation of the industry's current state of affairs	Proposed in order to gain an initial qualitative understanding of the impact that the barriers have on the industry, as well as to determine their possible causes
SFR10	Identification of the latest barriers across the different sectors in the value chain	Additional framework requirements to address the research objective of identifying barriers to growth in mineral value chains
SFR11	Evaluation of the severity of the barriers	
SFR12	Evaluation of the prevalence of the barriers	
SFR13	Analysis of cross-sector results	
SFR14	Categorization of barriers	

Identifying barriers to growth in mineral value chains

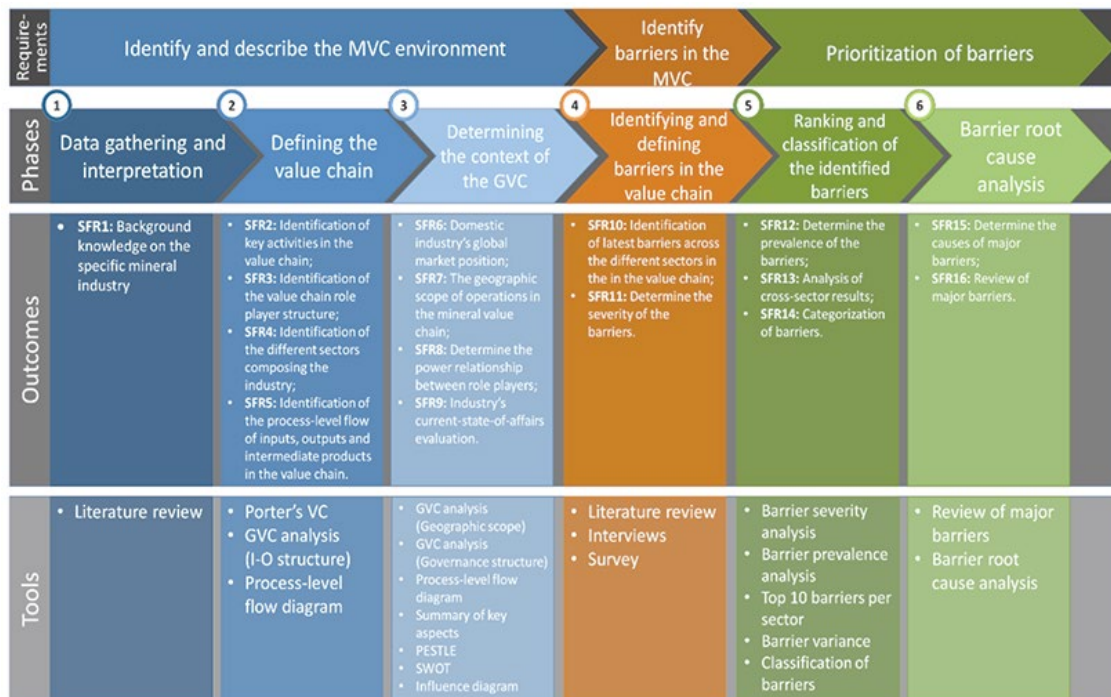


Figure 3—Proposed framework to guide the process of identifying barriers in MVCs

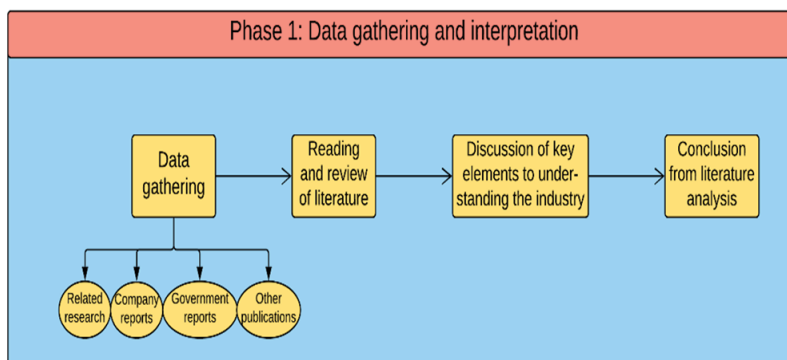


Figure 4—Overview of Phase 1 of the proposed framework

of the value chain activities up to this point formed part of the analysis and description of the MVC environment. This scope was deemed to be broad enough to illustrate and test the framework's capabilities, without the study becoming unduly complex. The rest of this section presents the results from the case study according to the five phases of the framework.

Phase 1: Data gathering and interpretation

A literature review was conducted on the manganese industry, specifically within the context of the South African market, which provided an overview of the relevant background information, disciplines, and theories relating to the specific industry. This information was used firstly to provide a solid platform to understanding the various aspects of the industry. An overview of the methodology followed in this phase is presented in Figure 4.

Since the literature review on the South African manganese value chain included a great deal of information, only the major findings are summarized here. South Africa is the dominant producer of manganese, possessing between 75 and 80% of the world's identified resources and approximately 24% of

the world's reserves. Over 90% of the reserves are located in the Kalahari Manganese Field (KMF) located in the Northern Cape Province, which has an estimated 4 Gt of manganese reserves (Ratshomo, 2013). The primary use of manganese is in manufacturing alloys that are used in steel production (International Manganese Institute and RPA, 2015). High-carbon ferromanganese, refined ferromanganese, and silicomanganese, are the major manganese alloys produced in South Africa (International Manganese Institute, 2014a; Olsen, Tangstad, and Lindstad, 2007). Manganese is also used to a lesser extent in the production of batteries, and very small quantities are used in numerous chemical products (Gajigo, Mutambatsere, and Adjei, 2011; International Manganese Institute and RPA, 2015).

Phase 2: Defining the MVC

During this phase, the various activities comprising the value chain were identified, as well as the role-player structures for each segment of the chain. A process flow diagram was developed, which provides an overview of the entire chain and the products that are produced throughout. The steps in this phase are illustrated in Figure 5.

Identifying barriers to growth in mineral value chains

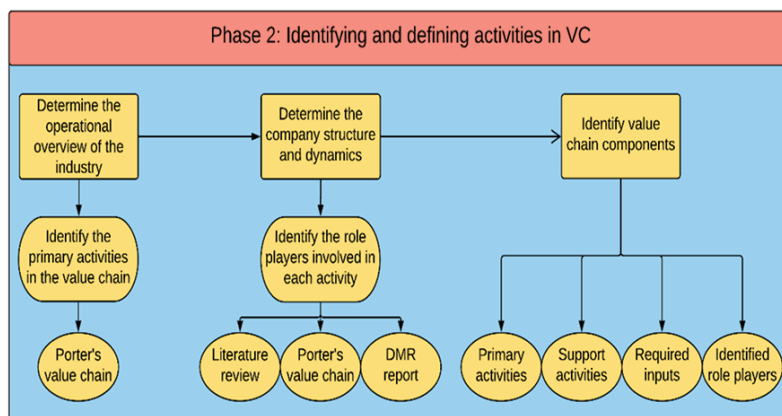


Figure 5—Overview of Phase 2 of the proposed framework

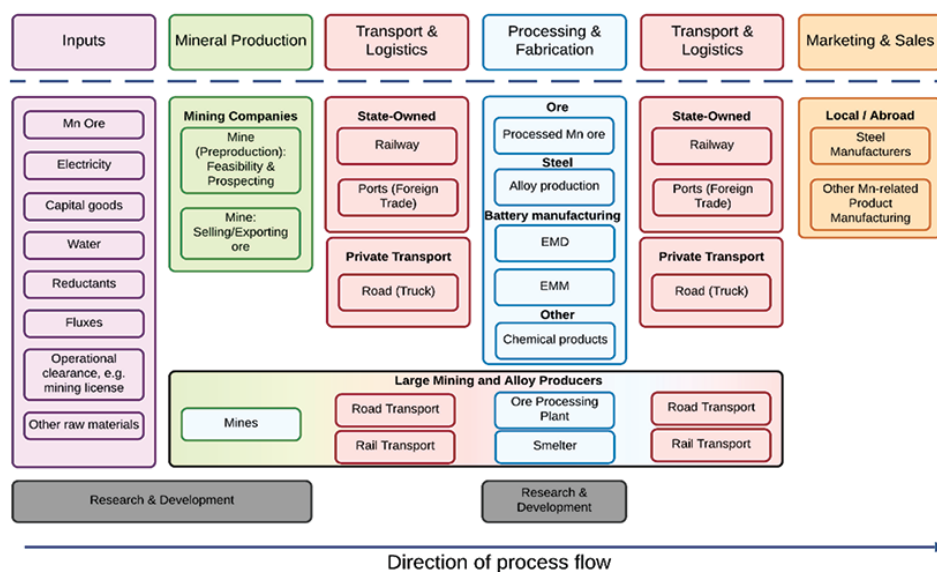


Figure 6—The South African manganese value chain

Porter's value chain and Gereffi's input-output structure approaches served as the foundation for developing the manganese MVC. Figure 6 outlines the various segments of the South African manganese value chain and the types of role-players involved in each step. It also provides a representation of the local structure of the industry, the required inputs for the processes, and the activities involved in each segment.

A process-level flow diagram was also developed in this phase to illustrate how materials are transformed throughout the value chain in terms of inputs and outputs. This diagram reveals the relationships among and between the various sectors and role-players in the manganese mineral industry. The small white blocks represent a specific output or product, which in turn, in most cases, is the input to the next process. These products are grouped by colours that represent different product types. The products are connected through arrows which indicate the process flow. It is useful to add the size (volume) of each output to the diagram, if this information is available, in order to place the proportion of these outputs into perspective. The final process-level diagram is shown in Figure 7.

The various sectors of the manganese industry are easily identifiable in the diagram. The industry consists of:

- Ore / mineral production
- Non-ferrous, electrolytic manganese dioxide, (EMD) and electrolytic manganese metal (EMM) production
- Ferrous / alloy manufacturing
- Slag-related product manufacturing
- Steel manufacturing
- Other chemical product manufacturing.

Due to the fact that the majority of manganese is used for metallurgical purposes (with 90 to 95% used in alloy manufacturing and approximately 5% in EMD and EMM production), the sectors that were investigated in this industry were: mineral production (mining sector), alloy manufacturing, EMD production, and EMM production.

Phase 3: Determining the context of the global value chain

This phase focused on integrating the manganese MVC within a global context by analysing the essential characteristics that define the chain environment. The activities in the phase are summarized in Figure 8.

To understand South Africa's position in the global manganese industry, the context of the country's role, and where

Identifying barriers to growth in mineral value chains

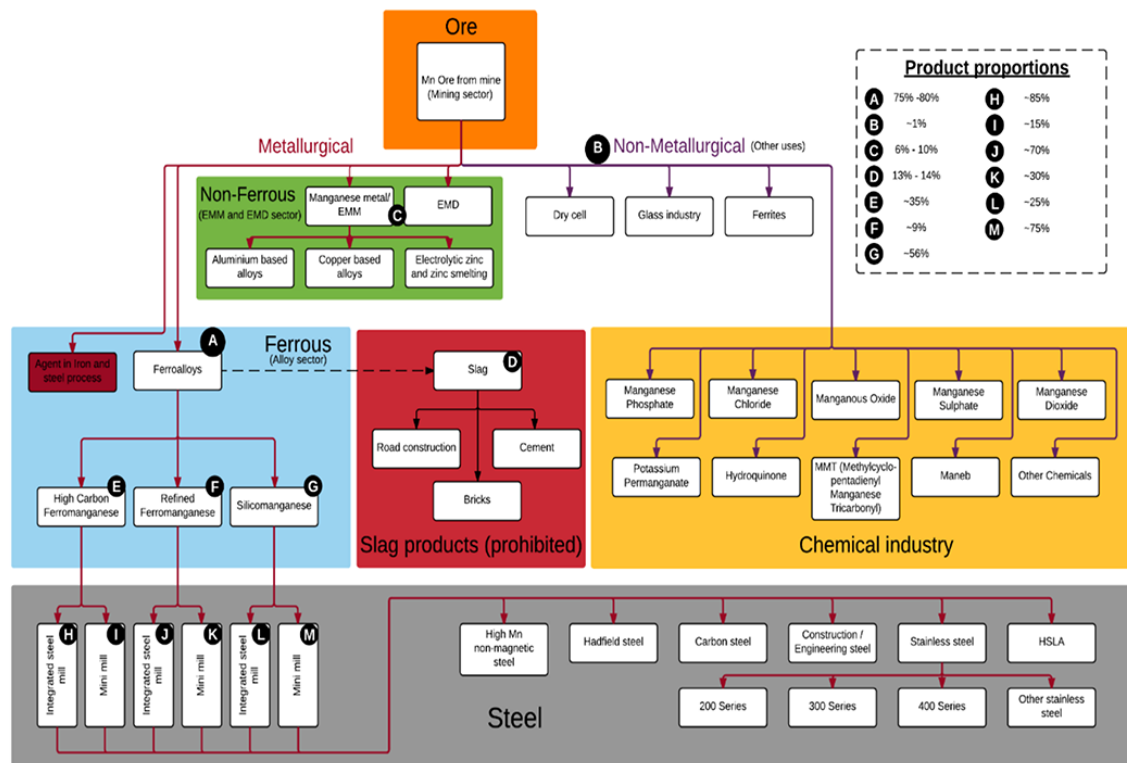


Figure 7—Manganese industry process-level flow diagram (van Zyl, Bam, and Steenkamp, 2016)

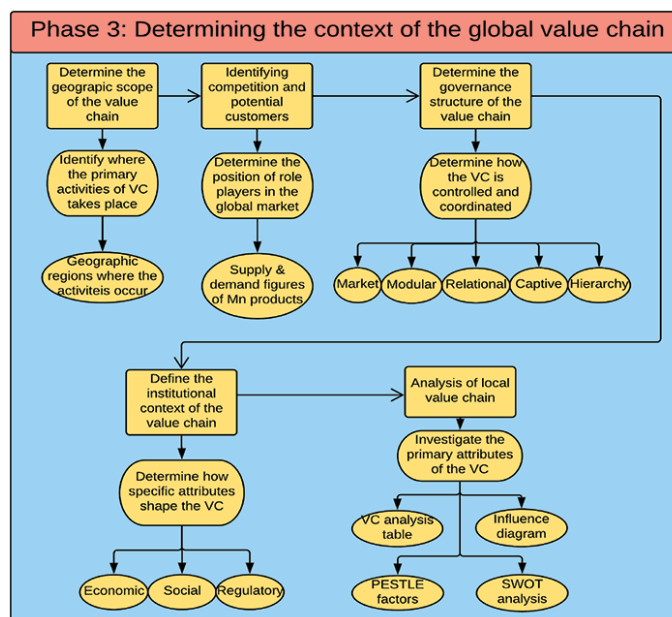


Figure 8—Overview of Phase 3 of the proposed framework

the barriers to economic growth lie, the global value chain of manganese and manganese-related products was examined. The findings are shown in Table II.

Table III lists the major global producers of manganese-related products and the total of number of countries producing each product.

Since manganese alloy producers do not have a differentiation advantage over competitors, as the alloys are commonly used in steel and widely produced around the world, they must focus primarily on gaining a cost advantage in order

to improve their competitive advantage. This primarily results in the top of the chain taking on a 'market' structure (as defined in Table IV). Producers are thus under pressure to constantly adjust their business strategy to cut costs, and one way of doing this is by ensuring they have the best trade agreement with ore providers, which places mining companies in a stronger trade position. This is highlighted by the fact that alloy producers also have to contend with rising electricity tariffs, labour issues, and other operational costs which are currently a number of South Africa's largest barriers to growth.

Identifying barriers to growth in mineral value chains

Table II

South Africa's production and consumption of manganese products

Product	Production			Consumption		
	Global rank	Volume (Mt Mn units)	% of global total	Global rank	Volume (Mt Mn units)	% of global total
Mn ore	1	4.64	24.9	9	0.325	1.8
HC FeMn	3	0.457	10.1	28	0.27	0.56
Ref. FeMn	5	0.102	5.9	31	0.10	0.59
SiMn	14	0.134	1.0	30	0.30	0.22
Steel	21	7.22	0.45	221	5.40	0.36

Sources: International Manganese Institute, 2014b; World Steel Association, 2014

Table III

Countries producing manganese-related products

Country	Ore			Alloys			Slag products	Steel	EMD	EMM
	Low	Med	High	HCFeMn	Ref. FeMn	SiMn				
South Africa	X	✓	✓	✓	✓	✓	X	✓	X ¹	✓
China	✓	X	X	✓	✓	✓	✓	✓	✓	✓
USA	X	X	X	✓	✓	✓	✓	✓	✓	X
Australia	X	✓	✓	✓	X	✓	✓	✓	✓	X
Brazil	✓	✓	✓	✓	✓	✓	✓	✓	X	X
Ukraine	X	✓	X	✓	✓	✓	✓	✓	X	X
Gabon	X	✓	✓	X	X	X	✓	X	X	X
Japan	X	X	X	✓	✓	✓	✓	✓	✓	X
India	✓	✓	✓	✓	✓	✓	X	✓	X	X
South Korea	X	X	X	✓	✓	✓	✓	✓	X	X
Total producing countries	9	16	6	21	11	21	- ²	91	8	2

Sources: Ore and alloys (International Manganese Institute, 2014a), slag (FICCI, 2014; Global Slag, 2015), Steel (World Steel Association, 2014), EMD (US International Trade Commission, 2003), EMM (MMC, 2016), Interviews.

¹South Africa stopped EMD production in 2015.

²No data available on countries that manufacture products from ferro-slag.

Table IV

Key characteristics of global value chain governance (source: (Gereffi, Humphrey, and Sturgeon, 2005))

Value chain governance type	Complexity of transactions	Ability to codify transactions	Capabilities in the supply base	Degree of explicit coordination and power asymmetry
Market	Low	High	High	Low
Modular	High	High	High	Medium-low

Further down the chain, however, a modular structure becomes apparent (as defined in Table IV) since complex transactions occur that are relatively easy to codify. This translates to downstream products such as ferroalloys, EMD, and EMM, which are made to the customer's specifications and the suppliers spread investments across a wide customer base. Switching costs are still low even though buyer-supplier interactions can be very complex. Unlike in simple markets, the linkages or relationships between partners are more substantial due to the higher volume of information flowing between them.

The final step of Phase 3 deals with the key attributes specific to the manganese value chain. Such factors include technology usage, capital requirements, workforce characteristics, and operational technology. The investigation of these attributes often leads to the discovery of where the bottlenecks, process inefficiencies, and general opportunities for improvement lie in the value chain. The tools for this analysis entail a summary of the key aspects in the value chain, which are elaborated upon through a PESTLE factor analysis and SWOT analysis of the

manganese industry. A summary of the key aspects of the South African manganese constraints are provided in Table V.

Phase 4: Identifying and defining barriers in the MVC

Figure 9 presents an overview of the activities of Phase 4. Interviews were conducted with experts representing individuals from different sectors of the chain within the manganese mineral industry to identify its barriers. The barriers were then defined, and a survey conducted to determine the impact that each barrier has on each sector.

Semi-structured interviews were conducted with the aim of gaining comparable views of the most pressing issues in the industry faced by various role-players in different sectors of the manganese value chain. Representatives of the mining, alloy, EMD, and EMM sectors were approached. These included representatives from two of the largest manganese mining companies in the world, two of the four South African manganese alloy producers, representing both ferromanganese and silicomanganese operations, and the world's only non-China

Identifying barriers to growth in mineral value chains

Table V

Summary of key aspects in the manganese value chain

	Mineral production	Alloy production	EMD production	EMM production
Primary input required	Capital, labour, equipment	Electricity, labour, ore, reductants, fluxes	Electricity, labour, ore, process chemicals	Electricity, labour, ore, process chemicals
Type of product outputs	Low (< 30% Mn), medium (≥ 30% and < 44%) and high grade ore (≥44%)	HCFEMn, Ref. FeMn, SiMn	EMD	EMM
Capital requirements	High since these are large mining operations	Medium to high. Capital requirements are similar to other mineral processing facilities	High	High
Return to scale effects	Must be big mining operation to be profitable	Since it is directly linked with the mining sector, the scaling effects are similar	Scaling effects are important since high volumes of Mn ore is required for production	Scaling effects are important since high volumes of Mn ore is required for production
Nature of technologic requirements	Widely available	Widely available	Sophisticated, production is restricted to a few countries. The only Africa-based producer's processes were discontinued in 2015	Very sophisticated (only producer outside of China and only producer globally which produces it selenium-free, which is a superior product)
Labour requirements	High labour intensity consisting of low-skilled workers and a few highly skilled employees in planning and managerial positions	Workforce consisting of a large group semi-skilled workers and few very skilled workers	Small to medium sized workforce, typically consisting of larger group semi-skilled workers and smaller group of very skilled workers	Small to medium sized workforce, typically consisting of larger group semi-skilled workers and smaller group of very skilled workers
Transport cost of inputs	Very little	Very high	Very high	Very high
Transport cost of outputs	Very high (seen as highest operational cost)	Very high	High	High
Role of local transport infrastructure	Very high, it is controlled by state-owned Transnet. Rail capacity is allocated between different companies that want to make use of the railways. Transnet controls the allocation that each company receives.	Very high, it is controlled by state-owned Transnet. Rail capacity is allocated between different companies that want to make use of the railways. Transnet controls the allocation that each company receives.	High	High
Size of local supply	SA is the largest global producer of manganese (China is a close second)	SA is one of the largest global producers of HCFEMn and ref. FeMn alloys, but is much smaller than to China. SA is however in the top 2 largest exporters of these alloys	Local production discontinued in 2015	SA only producer outside of China
Primary competitors	Primarily China, Australia, Gabon, Brazil, India	China, India, Japan, South Korea, Ukraine (SiMn)	China, USA, Australia, Greece, Ireland, Japan, Belgium	China
Destinations of exports	Primarily China and India, but also includes Russia and other countries in Asia	Primarily the USA, but also includes India, countries in Europe, South America, and Asia	Europe, USA, Africa, Japan, Asia	Primarily the USA, Japan and countries in Europe, but also includes Taiwan, South America, Canada and Africa
Largest operational expenditures	Logistics, equipment, labour	Ore / raw materials, electricity, labour	Ore, labour, electricity	Electricity, labour

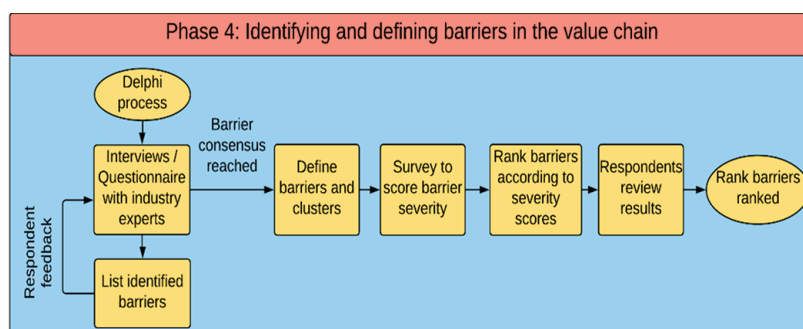


Figure 9—Overview of Phase 4 of the proposed framework

based producer of EMM and Africa's only producer of premium-quality EMD. Table VI summarizes the sampling of data.

The barriers identified from the literature were added to those identified directly by the respondents to form a list of 31 barriers and 9 barrier clusters, as indicated in Table VII. Questionnaires

were completed by the participants (from the mining, alloy production, EMD, and EMM sectors) in which they gave a score out of 10 for each of the 31 identified barriers (where zero represented no impact and 10 a very high impact). Table VII outlines the identified barriers.

Identifying barriers to growth in mineral value chains

Table VI

Sampling and sourcing of data

Role-player type	Interview	Questionnaire	Public records	Survey	Could not reach	Identified producers in sector
Mining	2	2	6	3	9	16
Alloy production	2	2	4	3	0	4
EMD production	1	1	1	1	0	1
EMM production	1	1	1	1	0	1
Total sources	6	6	12	8	10	

Table VII

List of identified barriers in the South African manganese industry

Sustained development	Insufficient physical infrastructure	Labour	Regulations / policies	Market conditions	Resource management	Electricity concerns	Social issues	Management-related
Restricted access to capital	Underdeveloped infrastructure and facilities	Rising cost of labour	Resource nationalism	Market volatility	Access to water	Unreliable supply	Social license to operate	Lack of policy implementation
Technology	Lack of railway capacity	Unrest / volatility in workforce	Mining Charter concerns	Fluctuations in exchange rate	Competing demands for land use	Rising tariffs		Poor corporate project execution and mismanagement
Lack of research and development and innovation	Lack of port facilities	Low productivity of workforce	Obtaining mining license	Competition / global oversupply	Scarcity of resources			Low efficiency
	Increasing transport costs	Skills shortage	Disposal of slag	Sizeable domestic market / proximity to market	Environmental concerns			
				Anti-dumping duty				
				Geopolitical uncertainty				

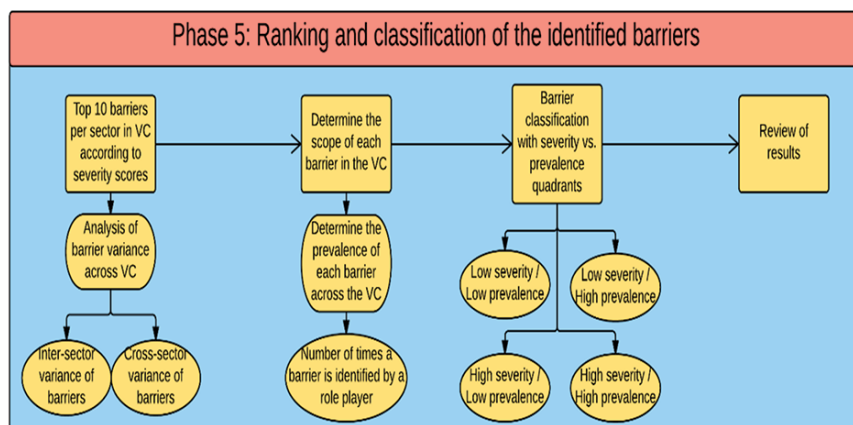


Figure 10—Overview of Phase 5 of the proposed framework

Phase 5: Ranking and classification of the identified barriers

During this phase, all of the data gathered from the industry experts was analysed to determine the impact that each barrier has on specific sectors within the value chain and how widespread the impact of the barrier is throughout the industry. The phase is outlined in Figure 10.

The severity of the barriers was based on the scale of the impact on the value chain and suppression of growth. The top ten most severe barriers in each sector of the value chain were then identified based on the expert rankings as shown in Table VIII.

The prevalence of the barriers was determined by evaluating how widespread the various barriers were as identified by the experts in the different segments of the value chain. This was

calculated by determining the number of respondents that identified the barrier in their list of top ten barriers. To ensure that all of the sectors were represented fairly, these numbers were normalized by using the sector's average prevalence, so that each sector was weighted equally. This prevented the number of respondents per sector from influencing the prevalence. In other words, sectors with few representatives, such as EMD and EMM, are represented equally with respect to the other sectors. The weighted prevalence and average severity scores for each of the identified barriers (out of a score of five) are shown in Table IX.

After the severity and prevalence of the identified barriers in the manganese industry had been investigated, the barriers could be classified in one of four groups. By grouping these barriers together, it was possible to assign a level of priority to each one,

Identifying barriers to growth in mineral value chains

Table VIII

Top ten barriers in each of the investigated sectors of the SA manganese value chain

Mining sector			Alloy manufacturing sector		
Rank	Barrier	Severity score	Rank	Barrier	Severity score
1	High transport costs	9.33	1	Unrest / volatility in workforce	9.00
2	Competition / global oversupply	9.00	1	Rising electricity tariffs	9.00
3	Underdeveloped infrastructure and facilities	7.67	3	Rising cost of labour	8.67
3	Poor governmental execution	7.67	3	Low productivity of workforce	8.67
5	Low productivity of workforce	7.00	3	Environmental concerns	8.67
5	Market volatility	7.00	6	Skills shortage	8.33
7	Lack of railway capacity	6.67	6	Disposal of slag	8.33
8	Skills shortage	6.33	6	Competition / global oversupply	8.33
9	Restricted access to capital	6.00	9	High transport costs	8.00
9	Resource nationalism	6.00	9	Obtaining mining license	8.00
EMD production sector			EMM production sector		
Rank	Barrier	Severity score	Rank	Barrier	Severity score
1	Fluctuations in exchange rate	10	1	Rising electricity tariffs	10
2	High transport costs	9	1	Competition / global oversupply	10
2	Rising cost of labour	9	3	Rising cost of labour	9
2	Unreliable electricity supply	9	3	Market volatility	9
2	Rising electricity tariffs	9	5	Restricted access to capital	8
2	Competition / global oversupply	9	5	Underdeveloped technology	8
2	Sizeable domestic market / Proximity to market	9	5	Lack of research & development and innovation	8
2	Anti-dumping duty	9	5	Skills shortage	8
9	Restricted access to capital	8	5	Environmental concerns	8
9	Lack of research and development and innovation	8	5	Disposal of slag	8
			5	Unreliable electricity supply	8
			5	Fluctuations in exchange rate	8

Table IX

Prevalence and severity scores of the identified barriers

Barrier	Prevalence	Severity	Barrier	Prevalence	Severity
Competition / global oversupply	4.58	4.54	Underdeveloped infrastructure	1.67	2.88
Rising electricity tariffs	3.75	4.17	Poor governmental execution	1.67	2.79
Rising cost of labour	3.75	4.00	Size of domestic market / proximity to market	2.50	2.79
High transport costs	3.33	3.92	Social license to operate	0.83	2.60
Market volatility	2.50	3.75	Lack of port facilities	0.83	2.58
Fluctuations in exchange rate	3.33	3.71	Geopolitical uncertainty	0.42	2.58
Environmental concerns	2.92	3.63	Disposal of slag	2.08	2.38
Low productivity of workforce	2.08	3.58	Poor project execution	0.42	2.29
Restricted access to capital	3.75	3.54	Low efficiency	0.00	2.17
Unrest / volatility in workforce	1.25	3.46	Competing demands for land use	0.83	2.13
Skills shortage	2.92	3.46	Access to water	0.42	2.08
Lack of railway capacity	0.83	3.421	Anti-dumping duty	1.67	2.04
Unreliable electricity supply	3.33	3.416667	Scarcity of resources	0.42	2.04
Lack of research and development	2.92	3.33	Obtaining mining license	0.83	1.71
Resource nationalism	1.25	3.25	Mining Charter concerns	0.42	1.52
Underdeveloped technology	1.25	3.04			

which in turn could provide policy-makers, government, or other industry stakeholders a guide as to which barriers to approach first when considering interventions. The barriers are categorized according to their respective severity (y-axis) and prevalence (x-axis) scores into four quadrants as indicated in Figure 11.

Framework validation

The framework was validated through application to a case study and expert analysis to determine the usefulness and value of such a framework. The validation was done in two parts:

1. *Using the South African manganese industry as a case study*—The full capacity of the barrier identification framework was used to analyse the industry and identify the barriers to growth faced by role-players from the

different sectors comprising the manganese value chain. Each tool of the framework phases was applied during the case study to illustrate the implementation of the framework and its capabilities.

2. *Framework validation through expert analysis*—The validation analysis was performed through questionnaires and interviews, with five experts from diverse fields. These experts comprised an individual in academia, an individual involved in research related to beneficiation at a research council, a senior expert that has worked throughout the mineral beneficiation industry in various research capacities and advised various policy-making processes related to the minerals industry, one senior analyst with a strategy background working in a company

Identifying barriers to growth in mineral value chains

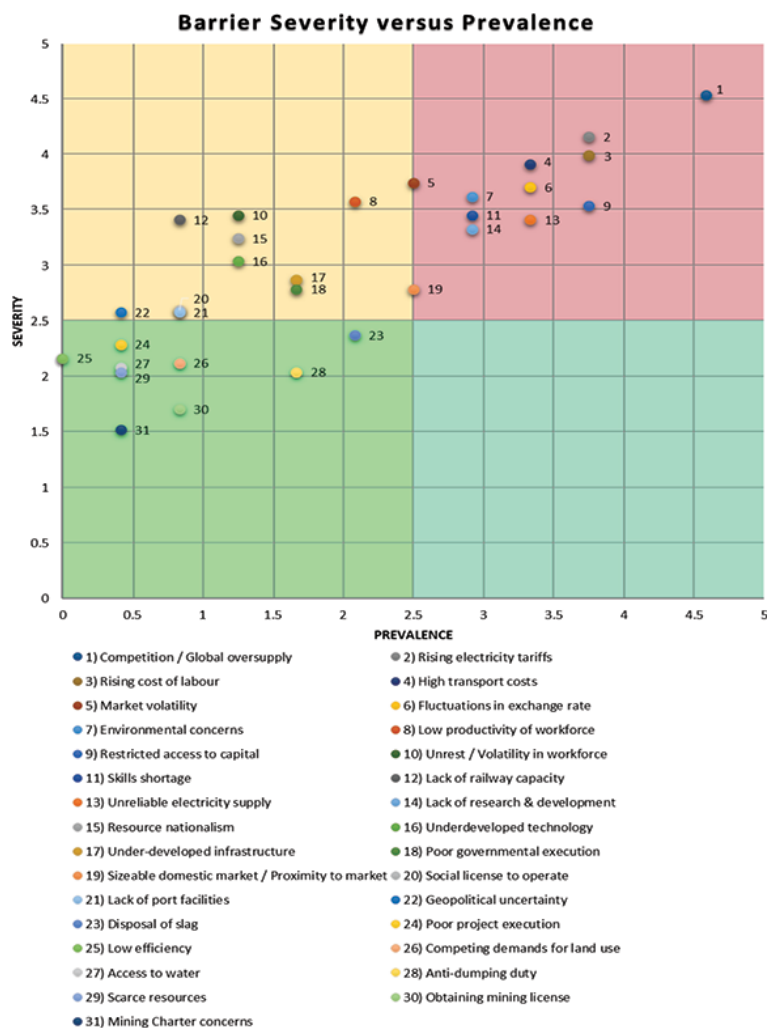


Figure 11 – Barriers classified according to their severity and prevalence in the manganese industry

active in the mineral value chain, and one senior manager from the mining industry. Each of these experts added input from a different perspective and made distinctive contributions from their respective areas of knowledge and expertise. This allowed the validity of the different aspects of the framework to be evaluated and refined.

The validation strategy that was followed for this study is shown in Figure 12.

Each of the five experts was given a 23-page validation document that summarized the outline of the framework structure, as well as the theories and methodologies used to develop the framework. The document provided a description of each phase with an explanation of how it should be applied and some of the key outputs of each phase to illustrate its usefulness. The document consisted of a short introduction providing information on the background to the study, followed by an outline of each of the five research phases and concluding with the validation questions. Six validation questions were included in the validation questionnaire. These focused on: the need for the framework, its usefulness, competing frameworks, the strengths of the framework, the shortcomings of the framework, and an open question for any other comments.

All the respondents that took part in the validation process agreed in their answers to the questionnaire that there is a need to identify barriers to economic growth for specific MVCs

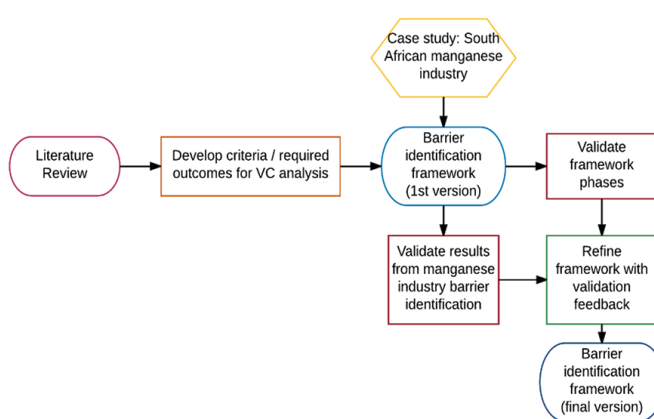


Figure 12 – Research validation strategy

and to determine their severity and prevalence. Due to the socio-economic imperative that exists to develop South Africa's economy and since the country's mineral resources play a key role in the economy, it can be concluded that any contributions that can add to the growth of specific value chains are relevant. It was also stated that proper understanding of the barriers to growth in order to support action to address them would be of significant value and is required by policy-makers and stakeholders within the industry.

Identifying barriers to growth in mineral value chains

Many of the respondents emphasised the complex challenges that relate to specific aspects in the mineral industries, as well as common challenges that affect industry in general. Investigating the industry from a value chain perspective provides an advantage of understanding holistically where the constraining factors lie. The respondents concurred that the approach would support a more effective analysis and provide a useful methodology and practical approach with tools that the relevant stakeholders could use individually and collectively.

The framework was noted for its differentiation approach between the various sectors by analysing barriers for each of the sectors along the value chain, as well as the effort to incorporate the value chain in a holistic manner, which included considerations of issues that are not apparent from typical market studies. Another unique contribution is the fact that the barriers are derived directly from the industry and from individuals who work in and understand the mining and commodity industry. The framework was overall described as a very logical and systematic approach to a multi-faceted and complex subject. The framework results were deemed to capture the essence of the challenges involved. Furthermore, the ranking of the barriers in the different sectors was deemed credible and a good basis to build on if this type of effort can be continued further with support from all the relevant stakeholders.

Despite the generally positive feedback, experts from different fields within the mineral industry identified various aspects of the framework that could be improved in future research. Firstly, it was noted that by quantifying the impact of specific barriers, more informed policy decisions could be made. Secondly, a sense of the main cost drivers in the different sectors of the value chain could provide a more nuanced understanding of the sensitivity of different sectors to changes in the prices of key inputs. Thirdly, some of the tools included in the analysis duplicate results. Tools can be better integrated to ensure that the same insights can be attained in less time. Finally, the effects of proprietary technology in different processing steps were not considered.

Conclusions

A framework was designed to identify and describe the mineral value chain (MVC) environment, identify barriers in the MVC, and rank the barriers in severity. The goal is to improve the efficiency by which, researchers, policy-makers, and other stakeholders can evaluate the binding constraints on an MVC in order to formulate effective responses to address these constraints. Different approaches for describing and investigating value chains were reviewed in order to identify the current research gap and limitations of similar frameworks for the identification of barriers. These limitations were addressed through the inclusion of tools to fulfil each of the framework requirements. The tools were partitioned into five framework phases, with each phase focusing on a specific element of analysis.

In order to convey the utility of the framework, it was applied to a case study of the South African manganese industry. Four different production sectors were identified in the chain within the scope of the study, namely the mining, alloy manufacturing, EMD, and EMM production sectors. Through an iterative process of interviews and surveys, 31 barriers to growth were identified across these four sectors, with global oversupply being the most significant impediment at the time (due to the end of the resource boom causing a general reduction of demand and the subsequent reduction of prices for most of the mineral-related industries),

followed closely by the rising costs of electricity, labour, and transport.

Through expert analysis based on the results from the case study, it was concluded that the framework successfully facilitates the identification of barriers within an MVC. The validators concurred that the proposed framework addresses a specific need within the industry and is a useful tool for its stakeholders. The holistic and systematic approach to a multi-faceted and complex subject was identified as the primary strength of the framework.

During the execution of the study, various aspects were identified that require further investigation. Firstly, the research relied on a narrow definition of the value chain, now taking into account side-stream linkages. This could be explored in further investigations. Secondly, the study sought to triangulate information in order to reduce bias. This included making use of interviews, questionnaires, and secondary data. However, the choice of secondary data, interviewees, and perceptions scales necessarily influenced the results of the study. In particular, the inputs from industry stakeholders allow for a detailed and prospective view of the industry and its challenges; however, this does provide an opportunity for manipulation. Triangulation was also hampered by the fact that certain sectors of the value chain had only a single company operating in South Africa, thus severely limiting the potential sample size. Further studies that investigate the potential bias that these choices could introduce in a study such as the one presented here, and how it might be further reduced, could be warranted. Thirdly, certain barriers were somewhat broad in definition, e.g. social license to operate. These might then be difficult to address as the definitions are imprecise. It is recommended that this should be explicitly avoided in future work.

References

- ALBA, E.M. 2009. Extractive Industries Value Chain - A Comprehensive Integrated Approach to Developing Extractive Industries. *Extractive Industries for Development Series*, no. 3 (March). World Bank, Washington, DC. <https://openknowledge.worldbank.org/handle/10986/18400>
- BAM, W. and DE BRUYNE, K. 2017. Location policy and downstream mineral processing: A research agenda. *Extractive Industries and Society*, vol. 4, no. 3. pp. 443–447. <https://doi.org/10.1016/j.exis.2017.06.009>
- BAM, W. and DE BRUYNE, K. 2019. Improving industrial policy intervention: The case of steel in South Africa. *Journal of Development Studies*, vol. 55, no. 11. pp. 2460–2475. <https://doi.org/10.1080/00220388.2018.1528354>
- CALLAGHAN, C. 2013. Mineral resource based growth pole industrialisation - Growth poles and value chains. https://www.researchgate.net/profile/Christopher_Callaghan2/publication/263129235_Mineral_Resource_Based_Growth_Pole_Industrialisation_-_Ferrous_Metals_Report/links/00b49539ff588e4212000000/Mineral-Resource-Based-Growth-Pole-Industrialisation-Ferrous-Metals-Report.pdf
- COE, N.M., DICKEN, P., and HESS, M. 2008. Global production networks: Realizing the potential. *Journal of Economic Geography*, vol. 8, no. 3. pp. 271–295. <https://doi.org/10.1093/jeg/lbn002>
- D'HARAMBURE, A. 2015. Overview of the Global Manganese Industry. *Proceedings of the 16th Asial Ferro-Alloys Conference*, Singapore, 31 March -2 April. <https://www.metalbulletin.com/events/download.ashx/document/speaker/7742/a0ID00000X0kCwMAJ/Presentation>
- DEPARTMENT OF MINERAL RESOURCES. 2011. A beneficiation strategy for the minerals industry of South Africa. Pretoria. pp. 1–23.
- EDINGER, H. 2014. Outlook of South Africa's Manganese Sector, May. *Frontier Advisory*.

Identifying barriers to growth in mineral value chains

- EY. 2013. Business risks facing mining and metals 2013–2014. http://www.ceecthefuture.org/wp-content/uploads/2013/12/Business_risks_facing_mining_and_metals_2013-2014_ER0069-1.pdf
- EY. 2019. Top 10 business risks facing mining and metals in 2019–20. https://assets.ey.com/content/dam/ey-sites/ey-com/en_gl/topics/mining-metals/mining-metals-pdfs/ey-top-10-business-risks-facing-mining-and-metals-in-2019-20.pdf
- FICCI (Federation of Indian Chambers of Commerce and Industry). 2014. Using steel slag in infrastructure development. <http://blog.ficci.com/archives/5291/5291>
- FORD, K., HOBBS, D., and URQUHART, R. 2007. CIS ferro alloys industry: Commercial opportunities, technical challenges and strategic implications. *Proceedings of Infacon XI: Innovation in Ferroalloy Industry*, New Delhi, India, 18–21 February 2007. <https://www.pyrometallurgy.co.za/InfaconXI/038-Ford.pdf>
- GAJIGO, O., MUTAMBATSERE, E., and ADJEI, E. 2011. Manganese industry analysis: Implications for project finance. *Working Paper* no. 132. African Development Bank. <https://www.afdb.org/en/documents/document/working-paper-132-manganese-industry-analysis-implications-for-project-finance-24162>
- GEREFFI, G. 1994. The organization of buyer-driven global commodity chains: How US retailers shape overseas production networks. *Commodity Chains and Global Capitalism*, January 1994. pp. 95–122. <https://doi.org/10.1177/0730888405277964>
- GEREFFI, G. 2011. Global Value Chain Analysis and Its Implications for Measuring Global Trade. <https://unstats.un.org/unsd/trade/presentations/wed-am/gary-gereffi>
- GEREFFI, G. 2019. Global value chains and international development policy: Bringing firms, networks and policy-engaged scholarship back in. *Journal of International Business Policy*, vol. 2, no. 3. pp. 195–210. <https://doi.org/10.1057/s42214-019-00028-7>
- GEREFFI, G. and FERNANDEZ-STARK, K. 2011. Global value chain analysis: a primer. Center on Globalization, Governance & Competitiveness. Durham, NC.
- GEREFFI, G., HUMPHREY, J., and STURGEON, T. 2005. The governance of global value chains. *Review of International Political Economy*, vol. 12, no. 1. pp. 78–104. <https://doi.org/10.1080/09692290500049805>
- GEREFFI, G. and LEE, J. 2012. Why the world suddenly cares about global supply chains. *Journal of Supply Chain Management*, vol. 48, no. 3. pp. 24–32. <https://doi.org/10.1111/j.1745-493X.2012.03271.x>
- GILBERTHORPE, E. and PAPYRAKIS, E. 2015. The extractive industries and development: The resource curse at the micro, meso and macro levels. *The Extractive Industries and Society*, vol. 2, no. 2. pp. 381–390. <https://doi.org/10.1016/j.exis.2015.02.008>
- GLOBAL SLAG. 2015. Korea develops cement from reduced metal slag. <https://www.globallslag.com/news/item/16-korea-develops-cement-from-reduced-metal-slag>
- HAUSMANN, R., KLINGER, B., and LAWRENCE, R. 2008. Examining beneficiation. *CID Working Paper Series*, no. 162. pp. 1–25. <http://www.cid.harvard.edu/southafrica>
- HIRSCHMAN, A.O. 1981. *Essays in Trespassing: Economics to Politics and Beyond*. Cambridge University Press.
- HUMPHREY, J. and SCHMITZ, H. 2001. Governance in global value chains. *IDS Bulletin*. <https://www.ids.ac.uk/files/dmfile/humphreyschmitz32.3.pdf>
- HUMPHREYS, D. 2013. New mercantilism: A perspective on how politics is shaping world metal supply. *Resources Policy*, vol. 38, no. 3. pp. 341–349. <https://doi.org/10.1016/j.resourpol.2013.05.003>
- INTERNATIONAL MANGANESE INSTITUTE. 2014a. 2013 Annual Report. Paris, France.
- INTERNATIONAL MANGANESE INSTITUTE. 2014b. Essential manganese. *Annual Review 2014*. Paris, France.
- INTERNATIONAL MANGANESE INSTITUTE AND RPA. 2015. Manganese: The global picture - A socio economic assessment. *Report for the International Manganese Institute*. Paris, France.
- KAHN, M. 2013. Natural resources, nationalism, and nationalization. *Journal of the Southern African Institute of Mining and Metallurgy*, vol. 113, no. 1. pp. 3–9. http://www.scielo.org.za/scielo.php?script=sci_arttext&pid=S2225-62532013000100004
- KAPLINSKY, R. and MORRIS, M. 2001. A Handbook for Value Chain Research. IDRC. <http://www.prism.uct.ac.za/Papers/VchNov01.pdf>
- KAPLINSKY, R., MORRIS, A., and KAPLAN, D. 2011. Commodities and Linkages : Industrialisation in Sub-Saharan Africa. Centre for Social Science Research (CSSR), University of Cape Town. <http://hdl.handle.net/11427/19295>
- MMC. 2016. Manganese Metal Company. Nelspruit, South Africa.
- NEILSON, J., PRITCHARD, B., FOLD, N., and DWIARTAMA, A. 2018. Lead firms in the cocoa-chocolate global production network: An assessment of the deductive capabilities of GPN 2.0. *Economic Geography*, vol. 94, no. 4. pp. 400–424. <https://doi.org/10.1080/00130095.2018.1426989>
- OECD, WTO, AND WORLD BANK GROUP. 2014. Global Value Chains: Challenges, Opportunities, and Implications for Policy. Report prepared for submission to the G20 Trade Ministers Meeting, Sydney, Australia, 19 July 2014. <https://pdfs.semanticscholar.org/f482/08032b3e6f9c981497dcf88a2d57d1f7cc75.pdf>
- OLSEN, S.E., TANGSTAD, M., and LINDSTAD, T. 2007. Production of Manganese Ferroalloys. Tapir Academic Press, Trondheim, Norway.
- POOE, R.I.D. and MHELEMBE, K. 2014. Exploring the challenges associated with the greening of supply chains in the South African manganese and phosphate mining industry. *Journal of Transport and Supply Chain Management*, vol. 8, no. 1. pp. 1–9. <https://doi.org/10.4102/jtscm.v8i1.139>
- PORTER, M.E. 1985. *The Competitive Advantage: Creating and Sustaining Superior Performance*. Free Press, New York.
- RATSHOMO, K. 2013. South Africa's Manganese Industry Developments 2004–2011. Directorate: Mineral Economics, Pretoria.
- SACHS, J.D. and WARNER, A.M. 1995. Natural Resource Abundance and Economic Growth. *Nber Working Paper Series*, no. 5398. <https://doi.org/10.3386/w5398>
- SCHMITZ, H. 2005. Value Chain Analysis for Policy-Makers and Practitioners. International Labour Organization, Geneva, Switzerland.
- STIJNS, J.-P.C. 2005. Natural resource abundance and economic growth revisited. *Resources Policy*, vol. 30, no. 2. pp. 107–130. <https://doi.org/10.1016/j.resourpol.2005.05.001>
- STURGEON, T.J. and GEREFFI, G. 2009. Measuring success in the global economy: international trade, industrial upgrading, and business function outsourcing in global value chains. United Nations Conference on Trade and Development, Geneva. https://unctad.org/en/docs/diaeia200910a1_en.pdf
- UNCTAD. 2013. World Investment Report 2013: Global Value Chain: Investment and Trade for Development. United Nations, New York and Geneva.
- US International Trade Commission. 2003. Electrolytic manganese dioxide from Australia, China, Greece, Ireland, Japan and South Africa. https://www.usitc.gov/publications/701_731/pub3633.pdf
- VAN ZYL, H., BAM, W.G., and STEENKAMP, J. 2016. Identifying barriers faced by key role players in the South African manganese industry. *Proceedings of the 27th SAIIE Annual Conference*. pp. 1–15. Southern African Institute of Industrial Engineering
- VON BELOW, M.A. 1992. Planning for future ferroalloy production in South Africa. *INFACON 6: Proceedings of the 6th International Ferroalloys Congress*, Cape Town. Volume 1. Southern African Institute of Mining and Metallurgy, Johannesburg. pp. 261–268. <https://www.pyrometallurgy.co.za/InfaconVI/1261-VonBelow.pdf>
- WORLD STEEL ASSOCIATION. 2014. World Steel in Figures 2014.. Brussels, Belgium: <https://www.worldsteel.org/en/dam/jcr:17354f46-9851-45c2-a1b6-a896c2e68f37/World+Steel+in+Figures+2014+Final.pdf> ◆

Identifying barriers to growth in mineral value chains

Appendix A: Framework phases

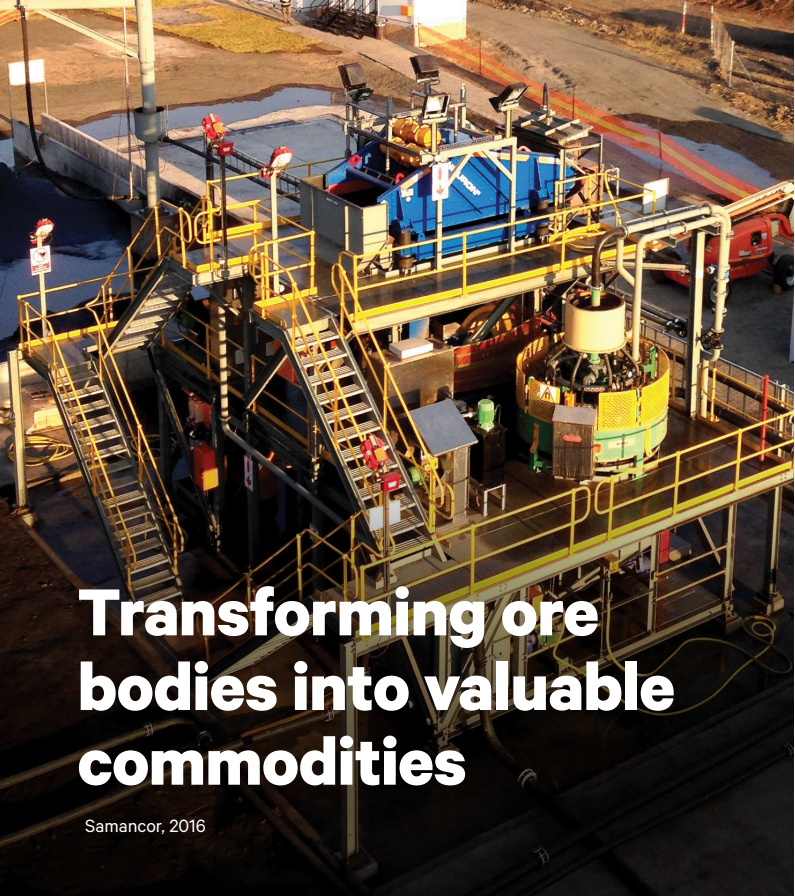
Table X provides an overview of the various framework phases. This includes the aim description and outcome of each phase.

Phase	Aim	Description	Outcome
1	Review literature regarding the specific mineral value chain.	The first step entails gathering and investigating various sources of literature regarding significant aspects of the mineral value chain in question. The literature review will provide a better understanding of the specific industry and explore key aspects in the value chain and the current problems it faces. It should contain updated information from previous publications and conclude with a comprehensive analysis of the literature.	Comprehensive literature review on key aspects relevant to the specific value mineral chain.
2	Identify the main activities/sectors in the value chain.	Once an overview of the mineral industry has been established, different sectors of the chain can be distinguished by the value they add to each output in the process. A general representation of the various sectors/segments comprising the value chain is provided in this framework phase. This provides an understanding of the structure of the chain, the inputs and outputs in each activity, and lastly, the different role-players involved in each process.	A general representation of the various sectors/segments comprising the value chain.
3	Expanding the mineral value chain to include a global context.	This phase focuses on integrating the complexities of a mineral value chain to analyse the characteristics which are unique to the chain in question. During this phase the chain's geographic scope of activities, role-player relationships and positions within the chain, as well as its institutional context are investigated. This would provide insight on the key attributes that have a significant impact on the specific mineral value chain.	Complete representation of the mineral value chain with the analysis of its geographic scope, governance structure, and institutional context.
4	Identifying barriers faced by role-players in different sectors of the value chain.	After sufficient knowledge of the industry has been collected and investigated, the barriers in the value chain are identified. During this phase interviews are conducted with industry experts who represent specific sectors of the value chain. A survey questionnaire will be provided afterwards that allows the experts to rank the major barriers they face in terms of severity. After the feedback from the industry experts has been reviewed, all the identified barriers will be listed and defined.	A list of all identified barriers to economic growth faced by role-players per sector in the value chain.
5	Determining the major barriers in each sector of the value chain and prioritizing them per severity and prevalence.	After the barriers are identified, they are ranked according to their severity and prevalence in the industry. The barriers are categorized in groups that have a specific priority assigned to each which relates to the size of its impact on the industry. The extent of the barrier impact on specific role-players, and the industry as a whole, are determined.	Top barriers per sector in the value chain which are ranked and categorized according to severity and prevalence in the industry.

Appendix B: Delphi process

Table XI provides a summary of the Delphi process used to identify and rank the barriers in the research.

Round	Step	Description
Round 1: Generation of initial barriers	Step 1	Determine questions for interview guide.
	Step 2: Interview	Conduct interviews with respondents
	Step 3: Interview (continued)	Respondents discuss different aspect of the company's operations that might encounter constraining factors
	Step 4	Researcher distils all the responses and creates initial list of barriers
Round 2: Review and finalize barriers	Step 5: List of barriers #1	Researcher mails first list of barriers to respondents. Questionnaire items are obtained from the generative round
	Step 6: Feedback #1	Respondents review initial list of the barriers
	Step 7	Respondents are encouraged to add to the list of barriers as well
	Step 8	Respondents rank the barriers according to severity
	Step 9	Finalize barrier list from respondents' input
	Step 10	Complete list by adding barriers identified prior to interviews to the list
	Step 11	Define each barrier to avoid definition overlap.
	Step 12: List of barriers #2	Group similar barriers in clusters
Round 3: Barrier severity survey	Step 13	Set up the survey with all of the barriers and a corresponding scale to score the severity for each
	Step 14: Survey	Respondents score each barrier with a score between 1 and 10 (or n/a) regarding severity
	Step 15	Researcher accumulates all the scores per sector
	Step 16: Ranking of barriers	Researcher ranks the top 10 barriers per sector from the respondents' input
Round 4: Finalize survey results	Step 17: List of barriers #3	The rankings of the barriers are sent to the respondents
	Step 18	The respondents review the final results
	Step 19	Analyse feedback
	Step 20	Determine if consensus is reached
	Step 21	Finalize rankings
Process complete		



Transforming ore bodies into valuable commodities

Samancor, 2016



Metallurgical Services



Industry Leading Equipment



Process Plant Design

MEET YOUR LOCAL TEAM



Edwin Phiri
Regional Manager



James Agenbag
Sales Manager



Schalk Vermeulen
Business Development



Blake van Steenburg
Customer Service



Jacques Barkley
Technical BD

Your go to partner for extracting maximum value from precious, base, battery and industrial minerals across the project lifecycle

MT Africa +27 35 797 3230
info@mineraltechnologies.com
www.mineraltechnologies.com



Mineral Technologies
A Downer Company

Downer
Relationships creating success

SAIMM MEMBERSHIP OR UPGRADE



SAIMM
THE SOUTHERN AFRICAN INSTITUTE
OF MINING AND METALLURGY



Website: <http://www.saimm.co.za>

Reasons to join the SAIMM

- ❖ To make a **contribution** to the Mining and Metallurgy industries
- ❖ The **opportunity to network** with a wide cross-section of professional people in the mining and metallurgy industry
- ❖ The opportunity to contribute to the development of **young talent** through mentoring and participating in schools
- ❖ **Fees for conferences are discounted for members** and annual subscriptions may be recovered by savings made from attending at least two conferences in a cycle
- ❖ Members receive **free membership** for the rest of the financial year if applying to join the SAIMM at one of its conferences
- ❖ Receive the **SAIMM Journal** which communicates a high standard of technical knowledge
- ❖ SAIMM members have **free access** to over 100 000 papers from around the world via OneMine.org
- ❖ **Engagement and involvement in SAIMM structures** and networking opportunities allow for additional Continuing Professional Development (CPD) point collection
- ❖ SAIMM provides its members with free access to some services of the **Technical Library** that combines the previous holdings of the Minerals Council and Anglo American
- ❖ Members of the Institute who are registered with the Engineering Council of SA (ECSA) qualify for a **rebate** on their ECSA fees.

Fifth Floor, Minerals Council South Africa
5 Hollard Street, Johannesburg, 2001
P.O. Box 61127, Marshalltown, 2107, South Africa
Tel: 27-11- 834-1273/7 · Fax: 27-11- 838-5923 or 833-8156
E-mail: membership@saimm.co.za



FOLLOW US ON...



www.facebook.com/TheSAIMM/



<https://twitter.com/SAIMM1>

<https://www.linkedin.com/company/saimm-->

-the-southern-african-institute-of-mining-and-metallurgy



Kinetics of advanced oxidative leaching of pyrite in a potassium peroxydisulphate solution

J. Ma¹, Y. Tang¹, D.Q. Yang¹, and P. Pei¹

Affiliation:

¹Mining College, Guizhou University, Guiyang, China

Correspondence to:

Y. Tang

Email:

caseyty@163.com

Dates:

Received: 9 Apr. 2019

Revised: 1 Jul. 2019

Accepted: 28 Nov. 2019

Published: February 2020

How to cite:

Ma, J., Tang, Y., Yang, D.Q., and Pei, P.

Kinetics of advanced oxidative leaching of pyrite in a potassium peroxydisulphate solution.

The Southern African Institute of Mining and Metallurgy

DOI ID:

<http://dx.doi.org/10.17159/2411-9717/710/2020>

ORCID ID:

J. Ma
<https://orcid.org/0000-0003-0999-5940>

Synopsis

This study investigates the leaching kinetics of gold-bearing pyrite in the potassium peroxydisulphate system and the potassium peroxydisulphate-ferrous sulphate combined system, using potassium peroxydisulphate as an oxidizing agent. Experimental results indicate that the pyrite leaching rate is roughly proportional to the potassium sulphate concentration. The pyrite leaching rate also increases with temperature, and is 48.19% faster at 70°C than at 30°C. Additionally, the pyrite leaching rate is inversely proportional to the particle size; the leaching rate of < 0.038 mm particles is 44.31% greater than that of 0.180–0.120 mm particles. At 70°C, the concentration of ferrous sulphate has no effect. However, at the more typical leaching temperature of 30°C, the addition of ferrous sulphate and hydrogen peroxide can increase the rate of leaching. Therefore, the kinetics of pyrite leaching in the potassium peroxydisulphate system at 70°C and in the potassium peroxydisulphate-ferrous sulphate combined system at normal temperatures were investigated in detail. Pyrite leaching kinetics follows the formula $kt = 1 - 2/3x - (1 - x)^{2/3}$ where solid film diffusion is the limiting process. The effective activation energy of pyrite leaching in the temperature range 30–70°C was 65.30 kJ/mol. Pyrite had a regular crystal habit prior to leaching, but exhibited faviform holes after leaching. These results provide a basis for effective leaching of gold from gold-bearing pyrite ores using the advanced oxidative leaching system.

Keywords

gold-bearing pyrite, high-grade oxidation, leaching dynamics, activation energy.

Introduction

Pyrite is one of the most common sulphide ores, and is an important carrier of gold, silver, and platinum (Gu *et al.*, 2010). In concert with China's rapid economic progress, the demand for gold continues to increase every year, such that difficult-to-process micro-disseminated gold deposits constitute a major category of gold resources. Gold contained in micro-disseminated gold deposits is typically encased in pyrite, such that the gold is physically shielded and thereby difficult to react with the leaching agent. This condition leads to relatively low leaching rates, typically less than 80%. Therefore, pretreatment is necessary prior to leaching of a micro-disseminated gold ore. Common pretreatment methods include oxidizing roast, microbial oxidation, and chemical hydrometallurgical oxidation (Hu *et al.*, 2017). The method of chemical hydrometallurgical oxidation has recently gained attention because of its advantages, including less pollution and a shorter treatment period (Gozmen *et al.*, 2009).

Chemical hydrometallurgical oxidation utilizes strong oxidants in solution to destroy the pyrite structure and expose the contained gold to subsequent chemical processes. The mostly frequently reported chemical hydrometallurgical oxidation systems for pyrite include $\text{Fe}_2(\text{SO}_4)_3$, HNO_3 , H_2SO_4 , and HClO_4 (Zhao *et al.*, 2016). The high-grade oxidation method, which has been used in wastewater treatment, has yet to be widely used in mineral processing (Hillea *et al.*, 2016). However, experimental pretreatments performed on micro-disseminated gold ores have yielded promising results, with leaching rates of up to 86.09% (Tang *et al.*, 2015). Peroxysulphate oxidizes pyrite by generating sulphate radical anions. To better understand the leaching characteristics and kinetics of high-grade oxidation of pyrite based on sulphate radical anion oxidation, controlled experiments were performed in the $\text{K}_2\text{S}_2\text{O}_8$ - FeSO_4 system. The leaching kinetics were investigated based on the experimental results, and SEM analyses were performed on the oxidation products. This study provides theoretical support and practical guidance for the high-grade chemical hydrometallurgical oxidation of micro-disseminated gold ores.

Kinetics of advanced oxidative leaching of pyrite in a potassium peroxydisulphate solution

Experimental

Sample preparation

Pyrite samples collected from an active mine contained few impurities and exhibited a high degree of crystallization. High-grade ore was selected by hand and coarsely crushed to < 2 mm. The sample was then sorted on shaking tables and the concentrate was dried at low temperatures. The sample was further pulverized and split into five size fractions: < 0.038 mm, 0.045–0.038 mm, 0.075–0.045 mm, 0.120–0.075 mm, and 0.180–0.120 mm, and sealed in jars. The theoretical mass fractions of sulphur and iron in stoichiometric pyrite (FeS₂) are 46.55% and 53.45%, respectively. For the pyrite sample used in this study, the sulphur and iron contents are 42.18% and 50.26%, respectively, and sample purity was determined to be 92.44% (Figure 1).

Experimental methods

The leaching experiments were performed on a magnetic stirrer. Leaching agent at a predetermined concentration was added to the beaker and stirring was initiated. A predetermined amount of pyrite was added when the temperature of the leaching agent reached target. Following addition of the pyrite, a 3 mL sample of the solution was taken every 30 minutes for the first 2 hours, and every hour for each subsequent hour of the experiment. To stop further reaction within the sample, samples were immediately filtered and diluted following collection. To keep the total volume of the solution unchanged, 3 mL of fresh leaching agent of the same concentration as the initial reagent was added to the beaker after each sample was taken. The leaching progress is indicated by the leaching rate of iron from the pyrite. The concentration of iron ions in the solution was analysed using a UV-visible spectrophotometer. Following completion of the leaching experiment, the leach residue was filtered, dried at low temperature, and then saved for examination by scanning electron microscopy (SEM).

Results and discussion

Effects of K₂S₂O₈ concentrations on pyrite leaching

Figure 2 displays the effect of K₂S₂O₈ concentration on pyrite

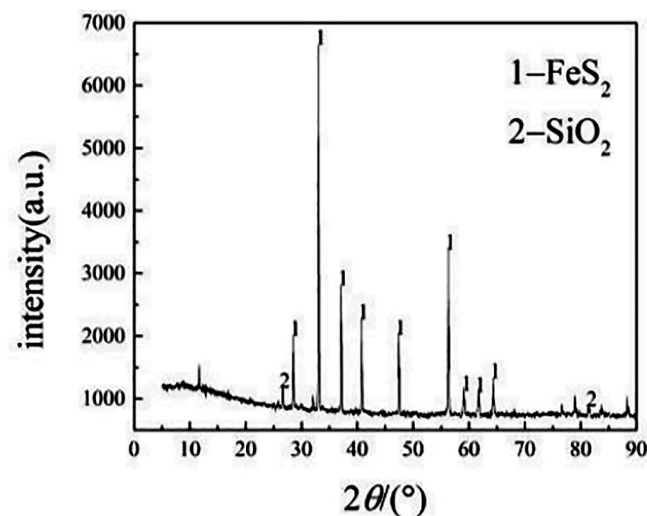


Figure 1—XRD spectrum of the pyrite sample

leaching at a pyrite concentration of 10 g/L, temperature of 70°C, stirring rate of 500 r/min, and a pyrite particle size of 0.075–0.045 mm.

From the data presented in Figure 2, it can be concluded that at K₂S₂O₈ concentrations between 0.111 mol/L and 0.555 mol/L, the leaching rate of iron from pyrite first increase with increasing K₂S₂O₈ concentration, then decrease, and then increases again. At K₂S₂O₈ concentrations less than 0.407 mol/L, the leaching rate and speed of the reaction both increase with increasing K₂S₂O₈ concentration. This is because there is less sulphate radical anion (SO₄⁻) in the low-concentration reagent, and the probability of reaction between pyrite and peroxydisulphate can be improved by increasing the concentration of the solution. At K₂S₂O₈ concentrations between 0.407 and 0.418 mol/L, the leaching rate of iron from pyrite decreases with increasing K₂S₂O₈ concentration according to Equation [1].



Based on this equation, it is expected that excess peroxydisulphate would function as a quenching agent to the SO₄⁻, and the S₂O₈²⁻ generated in Equation [1] is less utilized than SO₄⁻, which has the effect of decreasing the pyrite leaching rate (Xu and Li, 2010). When the concentration of K₂S₂O₈ is more than 0.481 mol/L, the leaching rate of pyrite increases again with increasing K₂S₂O₈ concentration, presumably because the total concentration of SO₄⁻ and S₂O₈²⁻ increases and the total oxidative capacity of the solution is greater. Based on the relationship between K₂S₂O₈ concentration and leaching rate and the desire to maximize the leaching rate while minimizing reagent consumption, the K₂S₂O₈ concentration was set at 0.407 mol/L for the following experiments.

Effects of temperature on pyrite leaching

Figure 3 displays the effect of leaching temperature on pyrite leaching at a pyrite concentration of 10 g/L, K₂S₂O₈ concentration of 0.407 mol/L, a stirring rate of 500 r/min, and a pyrite particle size of 0.075–0.045 mm.

It can be seen that the temperature has a significant effect on the pyrite leaching rate. The leaching rate and speed of the reaction both increase as a function of temperature. At 7 hours,

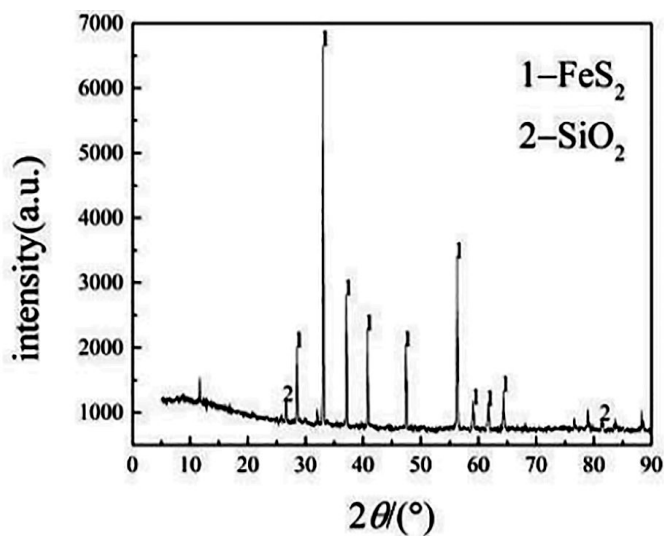


Figure 2—Effect of K₂S₂O₈ concentration on pyrite leaching

Kinetics of advanced oxidative leaching of pyrite in a potassium peroxydisulphate solution

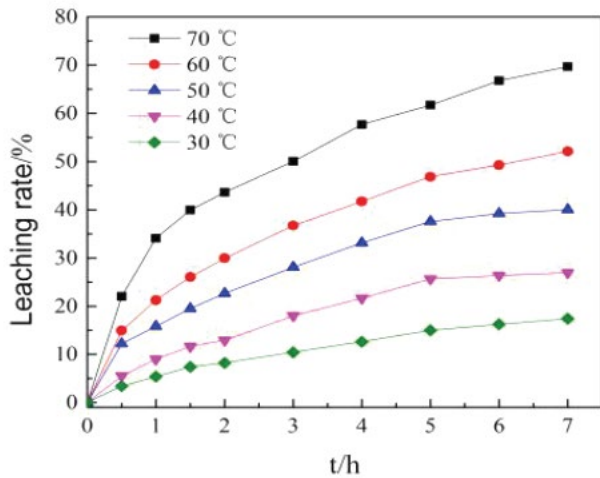


Figure 3—Effect of temperature on pyrite leaching

the leaching rate is 17.42%; at 30°C and 65.61%. at 70°C. The relationship between leaching rate and temperature over the course of 7 hours can be expressed using the regression equation $Y = 15.38 (e^{0.0247T} - 1)$, $R_2 = 0.9980$. Thus, the leaching rate improves exponentially with temperature. This is because as the temperature increases, effective collisions between molecules during the oxidation reaction increase, and the dissolution rate of pyrite likewise increases. Based on the relationship between leaching rate and temperature and the desire to maximize reaction rates and the speed of the reaction, the temperature of the following experiments was set to 70°C.

Effects of particle size on pyrite leaching

Figure 4 displays the effect of particle size on pyrite leaching at a pyrite concentration of 10 g/L, $K_2S_2O_8$ concentration of 0.407 mol/L, stirring rate of 500 r/min, and a leaching temperature of 70°C.

It can be seen that, for a given period of time, the leaching rate and reaction speed increase with decreasing pyrite particle size. After leaching for 7 hours, the leaching rate was 33.46% for a particle size of 0.180–0.120 mm, and 80.02% for a particle size of < 0.038 mm, a relative difference of 46.56%. The reason is that the specific surface area of a particle is inversely proportional to its size (Cho *et al.*, 2017). With smaller particle sizes and a larger specific area, more FeS_2 is exposed to the $-SO_4^-$ in the solution, which improves the pyrite leaching rate. Based on the relationship between leaching rate and particle size and the desire to maximize reaction rates, the particle size was set to 0.075–0.045 mm for the following experiments.

Effects of ferrous sulphate concentration on pyrite leaching at 70°C

Figure 5 shows the effects of the ferrous sulphate concentration on pyrite leaching at 70°C, with a pyrite concentration of 10 g/L, $K_2S_2O_8$ concentration of 0.407 mol/L, stirring rate of 500 r/min, and a pyrite particle size of 0.075–0.045 mm.

From the data in Figure 5, it can be concluded that in the high-grade $K_2S_2O_8$ oxidation solution at 70°C, the ferrous sulphate concentration has a relatively minor effect on the pyrite leaching rate. There are two activation mechanisms to convert $K_2S_2O_8$ to $-SO_4^-$ – thermal activation and chemical activation (Li *et al.*, 2014). Thermal activation is the predominant mechanism at 70°C, hence the concentration of ferrous ion has little effect on

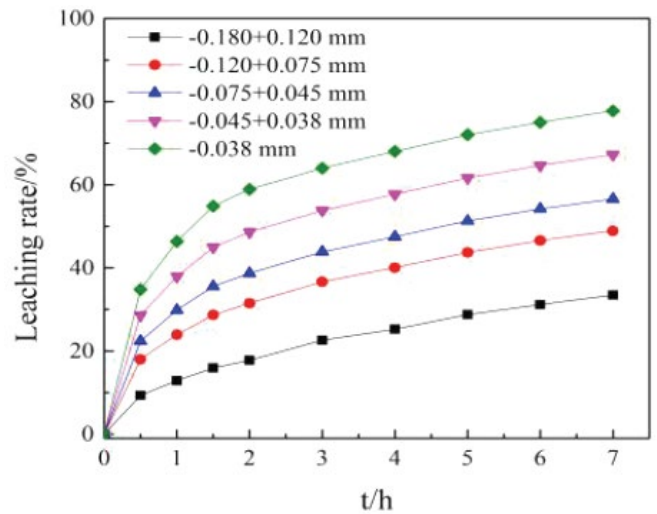


Figure 4—Effect of particle size on pyrite leaching

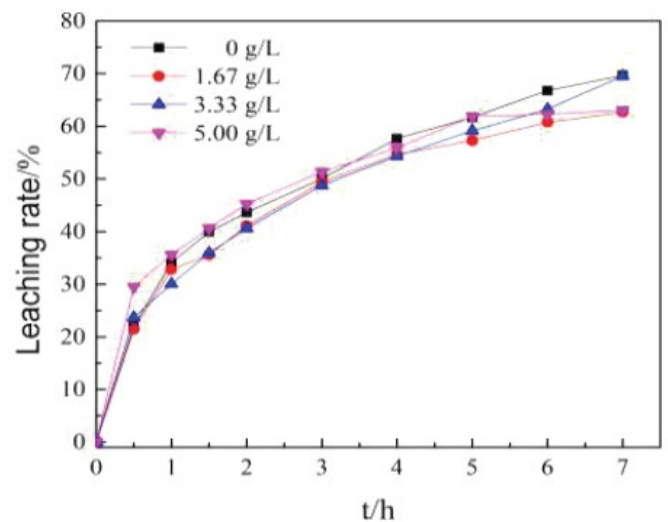


Figure 5—Effect of the ferrous sulphate concentration on pyrite leaching

the generation of $-SO_4^-$. Therefore, at 70°C, the ferrous sulphate concentration has little effect on the leaching of pyrite.

Effects of ferrous sulphate concentration on pyrite leaching at normal temperature (30°C)

Figure 6 displays the effect of the ferrous sulphate concentration on pyrite leaching at the normal leaching temperature of 30°C, a pyrite concentration of 10 g/L, $K_2S_2O_8$ concentration of 0.407 mol/L, a stirring rate of 500 r/min, and a pyrite particle size of 0.075–0.045 mm.

From the data in Figure 6, it can be concluded that when the ferrous sulphate concentration is zero, the leaching ratio of iron from pyrite increases slowly over time, achieving a rate of 16.59% over 12 hours. The leaching rate and reaction speed can be effectively improved by increasing the concentration of ferrous sulphate. This is because the Fe^{2+} in ferrous sulphate can catalyse the generation of $-SO_4^-$ from peroxydisulphate. As the concentration of ferrous sulphate is increased from 1.67 g/L to 5.00 g/L, the leaching rate of pyrite is improved. However, further increases in ferrous sulphate concentration have little effect on the leaching rate. This suggests that a low concentration of Fe^{2+} is sufficient to catalyse the generation of $-SO_4^-$ from $K_2S_2O_8$.

Kinetics of advanced oxidative leaching of pyrite in a potassium peroxydisulphate solution

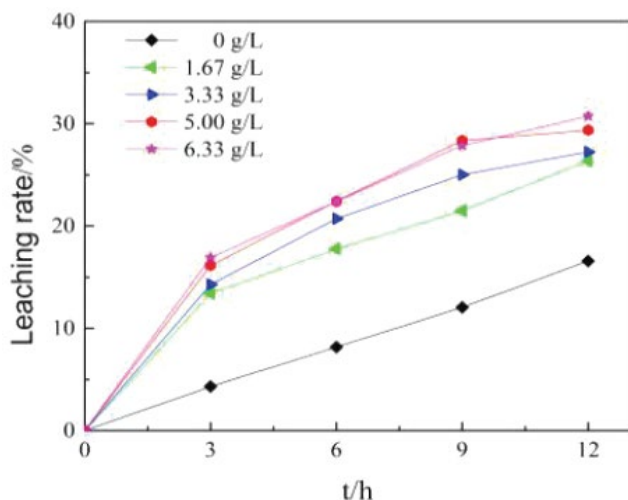


Figure 6—Effect of ferrous sulphate concentrations on pyrite leaching at 30°C

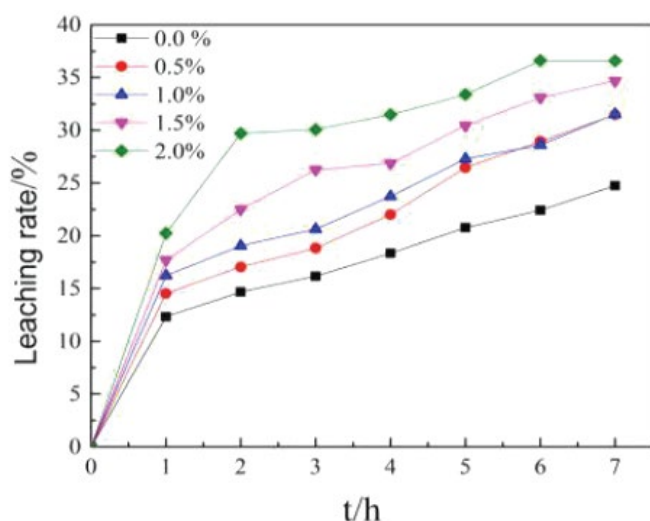


Figure 7—Effect of volumetric H₂O₂ concentration on pyrite leaching at 30°C

Effects of volumetric H₂O₂ concentration on pyrite leaching at normal leaching temperatures

Figure 7 displays the effect of volumetric concentration of H₂O₂ on pyrite leaching at 30°C at a pyrite concentration of 10 g/L, a K₂S₂O₈ concentration of 0.407 mol/L, a ferrous sulphate concentration of 5.00 g/L, a stirring rate of 500 r/min, and a pyrite particle size of 0.075–0.045 mm.

Increasing the H₂O₂ concentration can increase the leaching rate of iron from pyrite, and both the pyrite leaching rate and the speed of iron release are proportional to the H₂O₂ concentration. At 7 hours, the leaching rate at an H₂O₂ concentration of 2% was 36.60%, which is 11.85% higher than the leaching rate of 24.75% with no H₂O₂ added. During the initial stage of the experiment, bubbles generated in the solution were observed, and the formation of bubbles increased with increasing H₂O₂ concentration. The reason is that hydrogen peroxide can quickly generate hydroxyl radicals (OH·) through the catalysis of Fe²⁺, and the combined effect of ·OH and ·SO₄⁻ can increase the speed of the leaching reaction. Additionally, the total oxidation capacity is enhanced by the input of H₂O₂ (Fischbacher, von Sonntag, and

Schmidt, 2017), thus improving the leaching rate of iron from pyrite.

Kinetics of oxidative pyrite leaching

Pyrite leaching is a fluid-solid two-phase reaction, and the leaching rate might be controlled by liquid film diffusion, solid film diffusion (the slowest process in surface oxidation), or a combination of these mechanisms (Zhong *et al.*, 2013). Assuming that the pyrite particles in the fluid-solid two-phase reaction may be approximated as spheres of the same size, that the concentration of the leaching agent is maintained constant, and that the leaching process is controlled by chemical reaction, the kinetic equation of a shrinking core model can be expressed as:

$$kt = 1 - (1 - x)^{1/3} \quad [2]$$

Liu (2012) and Zhong *et al.* (2013) used Equation [2] to investigate the oxidation kinetics of pyrite in sulphuric acid media, and concluded that the apparent activation energy of pyrite leaching is 37 kJ/mol with a Fe³⁺ concentration of 30 g/L and at temperatures between 45°C and 90°C. When the concentration of the leaching agent is altered during the course of the reaction, leaching is controlled by solid film diffusion in the remaining solid, and the kinetic equation for the shrinking core model can be expressed as:

$$kt = 1 - 2/3x - (1 - x)^{2/3} \quad [3]$$

Bingöl, Canbazoglu, and Aydoğan (2005) proposed a kinetic model based on the interface mass transfer and solid film diffusion, which can be expressed as:

$$kt = \ln(1 - x)^{1/3} - 1 + (1 - x)^{-1/3} \quad [4]$$

Ekmekyapar (2003) proposed a kinetic equation controlled by combined dynamics:

$$kt = 1 - 2(1 - x)^{1/3} + (1 - x)^{2/3} \quad [5]$$

According to Equation [2], if the leaching process is controlled by chemical reaction, the linear relationship $1 - (1 - x)^{1/3}$ vs. t can be plotted as in Figure 8a. Similarly, Equations [3], [4], and [5] can be used to approximate the leaching process of pyrite, as displayed in Figure 8b, 8c, and 8d. Table I lists the correlation coefficients (R²) of the four models, which can be used to indicate the applicability of these models.

From the results presented in Table I, it can be determined that the R² of the dynamics model controlled by single solid film diffusion is closest to unity, suggesting that the oxidative leaching of pyrite is primarily controlled by solid film diffusion in the remaining solid.

To determine effects of additional variables, including K₂S₂O₈ concentration and particle size at 70°C and FeSO₄ and H₂O₂ concentrations at 30°C on the pyrite leaching rate, a semi-empirical model (Equation [6]) is applied to model the effects of K₂S₂O₈ concentration and particle size at 70°C. An additional semi-empirical model (Equation [7]) is applied to calculate the effects of FeSO₄ and H₂O₂ concentrations at 30°C.

$$1 - 2x/3 - (1 - x)^{2/3} = k_0 \times c_{K_2S_2O_8}^a \times (d_p)^b \times e^{-\frac{E_a}{RT}} \times t \quad [6]$$

Kinetics of advanced oxidative leaching of pyrite in a potassium peroxydisulphate solution

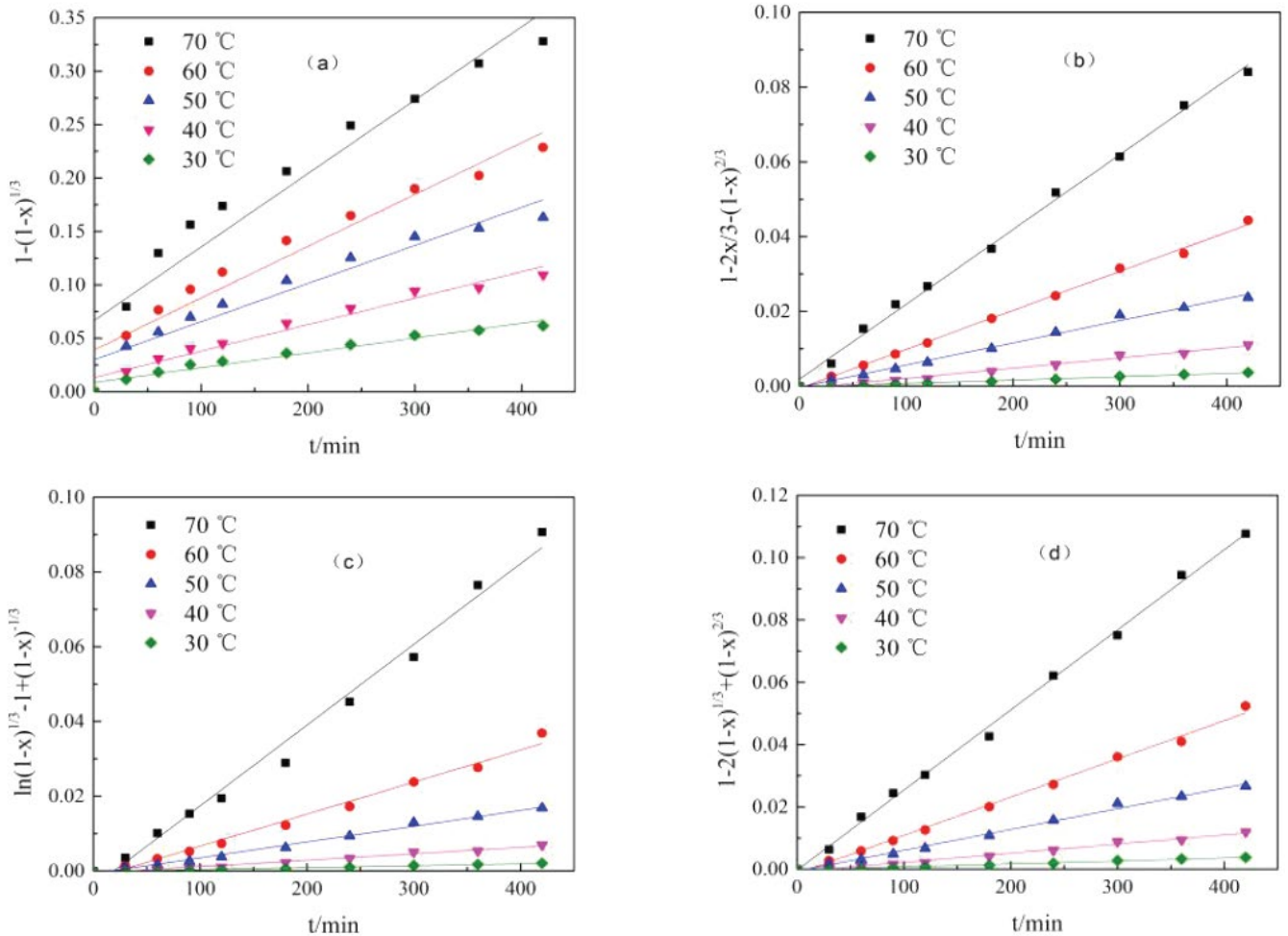


Figure 8—Kinetic model curves at four different temperatures (a) $1 - (1-x)^{1/3} \sim t$; (b) $1-2x/3 - (1-x)^{2/3} \sim t$; (c) $1/3 \ln(1-x) - 1 + (1-4x)^{-1/3} \sim t$; (d) $1 - 2(1-x)^{1/3} + (1-x)^{2/3} \sim t$

T(°C)	(R ²)			
	$1-(1-x)^{1/3}$	$1-2x/3-(1-x)^{2/3}$	$\ln(1-x)^{1/3}-1+(1-x)^{-1/3}$	$1-2(1-x)^{1/3}+(1-x)^{2/3}$
30	0.9558	0.9960	0.9880	0.9901
40	0.9607	0.9855	0.9797	0.9838
50	0.9284	0.9931	0.9911	0.9930
60	0.9368	0.9973	0.9849	0.9949
70	0.9105	0.9965	0.9872	0.9976

$$1 - 2x/3 - (1-x)^{2/3} = k_1 \times c_{K_2S_2O_8}^a \times (d_p)^b \times c_{FeSO_4}^c \times c_{H_2O_2}^d \times e^{-\frac{E_a}{RT}} \times t \quad [7]$$

where x is the leaching rate; k_0 , k_1 are the constants representing the reaction rate, $c_{K_2S_2O_8}$ is the concentration of $K_2S_2O_8$ in mol/L; c_{FeSO_4} is the concentration of $FeSO_4$ in mol/L; $c_{H_2O_2}$ is the concentration of H_2O_2 in mol/L; d_p is the particle size in mm; t is the reaction time in minutes; and T is the temperature in kelvin.

If the concentration of $K_2S_2O_8$ is modified while other conditions are kept the same, Equation [6] can be expressed as:

$$1 - 2x/3 - (1-x)^{2/3} = k_2 \times c_{K_2S_2O_8}^a \times t \quad [8]$$

$$\frac{d[1 - 2x/3 - (1-x)^{2/3}]}{dt} = k_2 \times c_{K_2S_2O_8}^a \quad [9]$$

Figure 9 displays curves representing the relationships between $K_2S_2O_8$ concentration and time according to Equation [9]. The slopes represent the values of $d[1 - 2x/3 - (1-x)^{2/3}]/dt$ corresponding to different $K_2S_2O_8$ concentrations. Similarly, Figures 9b and 9c display curves representing the relationships

Kinetics of advanced oxidative leaching of pyrite in a potassium peroxydisulphate solution

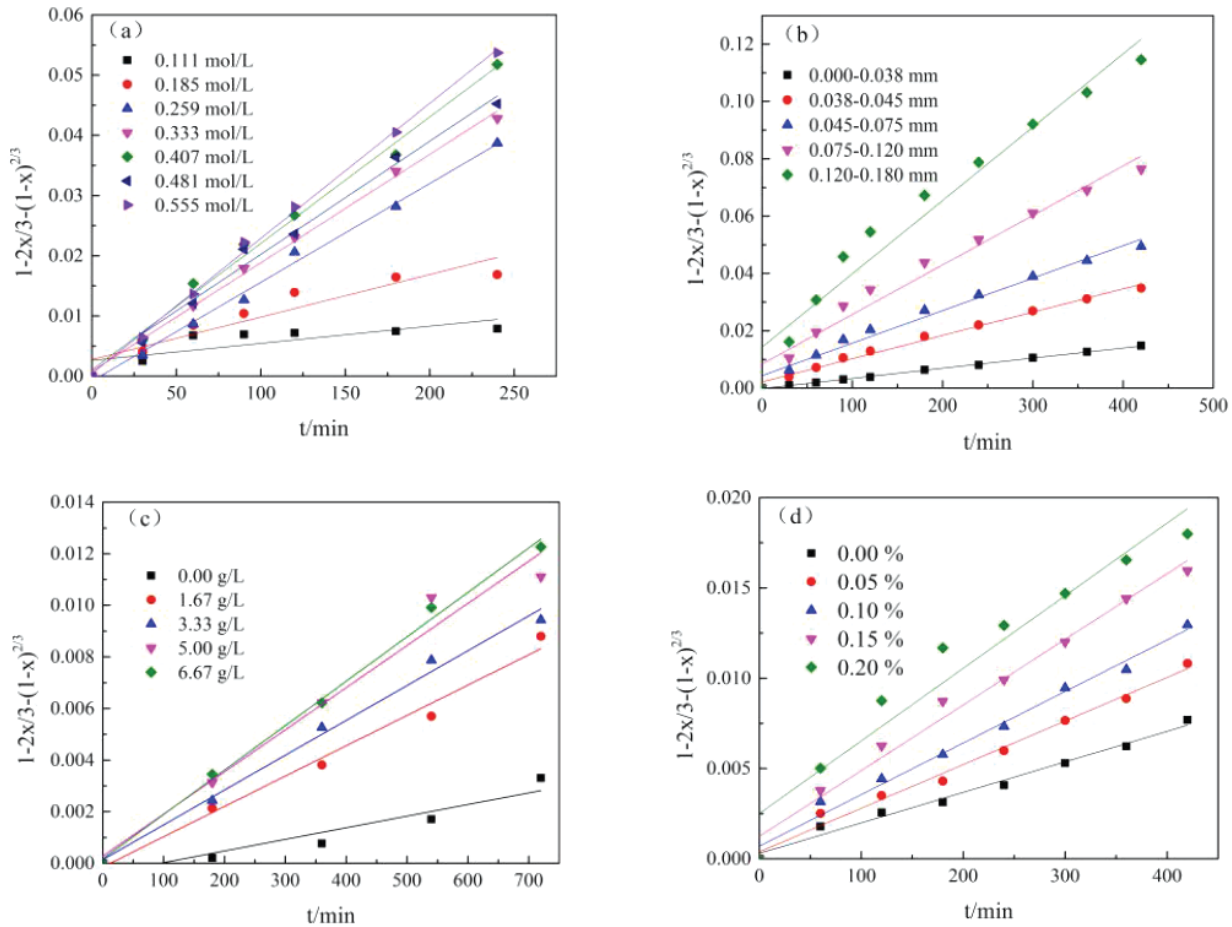


Figure 9—Plots of $1 - 2x/3 - (1-x)^{2/3}$ vs. t as a function of: (a) $K_2S_2O_8$ concentration; (b) particle size; (c) $FeSO_4$ concentration; (d) H_2O_2 concentration

between $K_2S_2O_8$ concentrations and time at different particle sizes, $FeSO_4$ concentrations, and H_2O_2 concentrations. The slope of $\ln[d[1 - 2x/3 - (1-x)^{2/3}]/dt]$ vs $\ln c_{K_2S_2O_8}$ is 0.431 as shown in Figure 9a; that of $\ln[d[1 - 2x/3 - (1-x)^{2/3}]/dt]$ vs $\ln d_p$ is -0.920 ; that of $\ln[d[1 - 2x/3 - (1-x)^{2/3}]/dt]$ vs $\ln c_{FeSO_4}$ is -0.295 ; and that of $\ln[d[1 - 2x/3 - (1-x)^{2/3}]/dt]$ vs $\ln c_{H_2O_2}$ is 0.378, as shown in Figure 10.

If the temperature is changed but other conditions remain constant, the slopes of the lines in Figure 8 represent the reaction rate constants at different temperatures, which can be expressed as Equation [10].

$$k = A \cdot e^{-\frac{E_a}{RT}} \quad [10]$$

where k is the reaction rate constant; A is the frequency factor, a constant; E_a is the apparent activation energy; R is the ideal gas constant; and T is the temperature in kelvin.

Taking the logarithm on both sides of Equation [10] yields Equation [11]:

$$\ln k = \ln A - \frac{E_a}{RT} \quad [11]$$

Figure 11 shows the Arrhenius curve for oxidative pyrite leaching, where $1/T$ is plotted on the x-axis and $\ln k$ on the y-axis. From the approximate slope of the curve, the apparent activation energy of pyrite leaching over the temperature range

30–70°C is 65.30 kJ/mol, within the previously reported range of 46–98 kJ/mol (Zhong, 2015).

By inputting the values for a , b , c , d , and E_a into Equations [6] and [7], the statistical average values of k_0 and k_1 are shown to be $k_0 = 2.3 \times 10^5 \text{ min}^{-1}$, $k_1 = 5.2 \times 10^5 \text{ min}^{-1}$. The resulting kinetic equation for oxidative pyrite leaching at 70°C is:

$$1 - 2x/3 - (1-x)^{2/3} = 2.35 \times 10^5 \times c_{K_2S_2O_8}^{0.431} \times (d_p)^{-0.920} \times e^{\frac{7853.5}{T}} \times t \quad [12]$$

When ferrous sulphate and hydrogen peroxide are added to the potassium peroxydisulphate single system at the normal leaching temperature of 30°C, the kinetic equation for the leaching reaction that expresses the effects of their concentrations is:

$$1 - 2x/3 - (1-x)^{2/3} = 2.28 \times 10^5 \times c_{K_2S_2O_8}^{0.431} \times (d_p)^{-0.920} \times c_{FeSO_4}^{0.295} \times c_{H_2O_2}^{0.378} \times e^{\frac{7853.5}{T}} \times t \quad [13]$$

Scanning electron microscopy

SEM images of pyrite before and after oxidative leaching are shown in Figure 12.

Prior to leaching, pyrite samples exhibited a compact structure and regular morphology with no fracture or pores. Pyrite samples examined after 3 hours of leaching exhibited some

Kinetics of advanced oxidative leaching of pyrite in a potassium peroxydisulphate solution

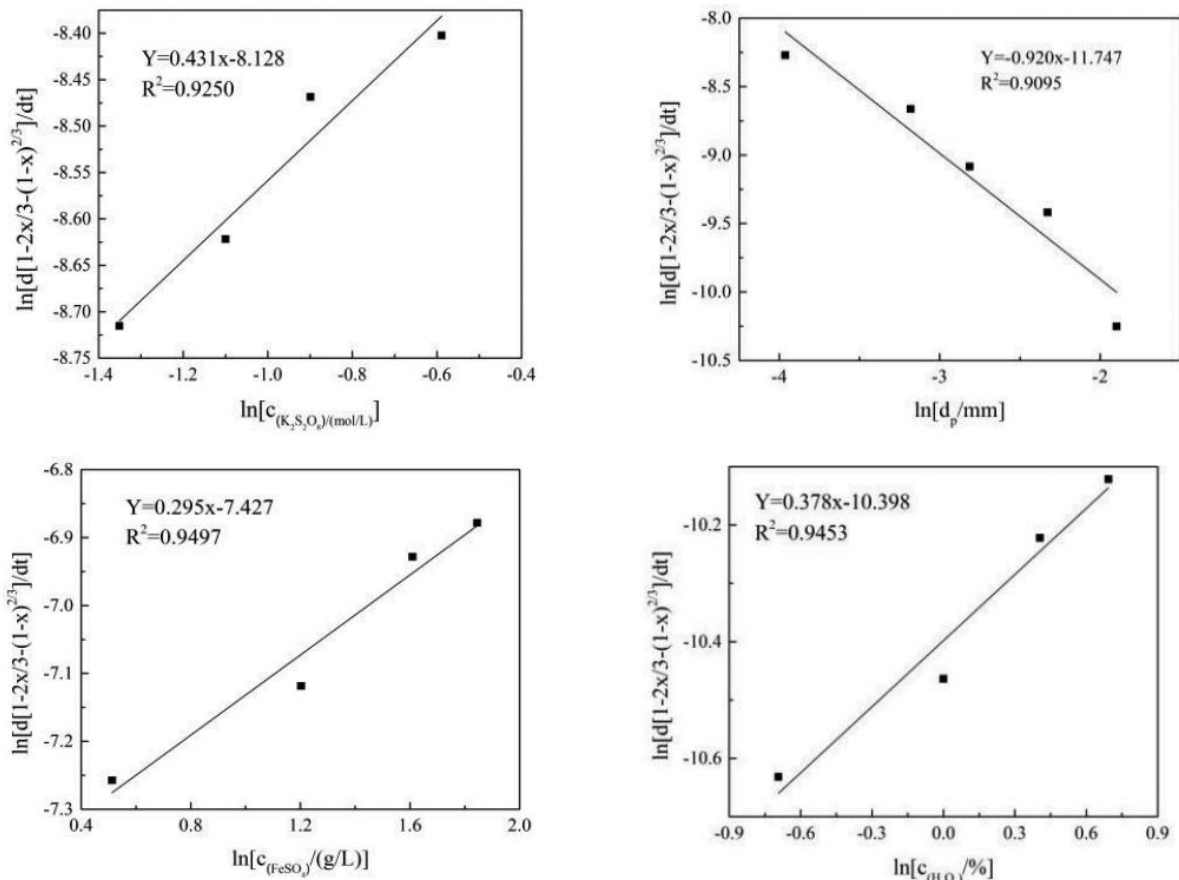


Figure 10—Plots of $\ln[d(1 - 2x/3 - (1 - x)^{2/3})/dt]$ and $\ln[c_{(K_2S_2O_8)}(\text{mol/L})]$, $\ln[d_p/\text{mm}]$, $\ln[c_{(FeSO_4)}(\text{g/L})]$, $\ln[c_{(H_2O_2)}\%]$

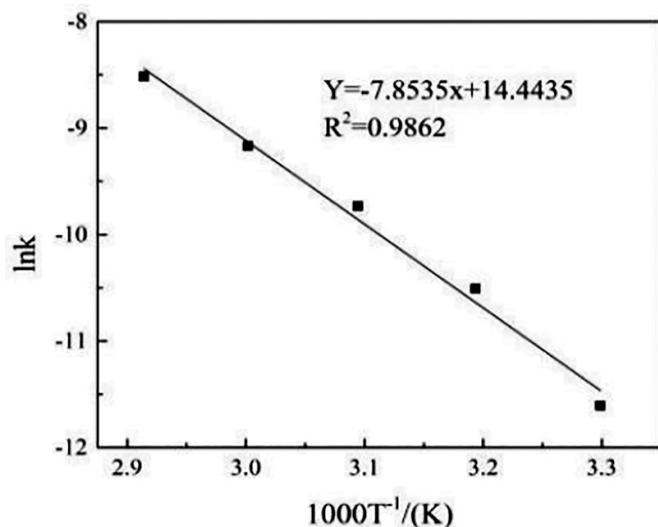


Figure 11—Arrhenius curve for oxidative pyrite leaching

cracks and hollows. After leaching for 7 hours, pyrite exhibited severely eroded surfaces and many faviform holes.

Conclusion

This study investigated the impacts of potassium persulphate concentration, leaching temperature, pyrite particle size, and the presence of ferrous sulphate and hydrogen peroxide on pyrite

leaching using potassium persulphate as the oxidizing agent in a single system of potassium persulphate and a combined system of potassium persulphate plus ferrous sulphate. The following conclusions are derived.

- At a $K_2S_2O_8$ concentration of 0.111–0.555 mol/L, the leaching rate of iron from pyrite first increases with increasing $K_2S_2O_8$ concentration, and then falls. The leaching rate reaches a peak value of 73.69% at a $K_2S_2O_8$ concentration of 0.407 mol/L. The leaching rate is also positively correlated with temperature, as it increases by 48.19% when the temperature is raised from 30°C to 70°C. An exponential relationship can be derived between the leaching rate and temperature, which can be approximated by the formula: $Y = 15.38(e^{0.0247} - 1)$, $R^2 = 0.9980$.
- The leaching rate and speed are both inversely proportional to the pyrite particle size. After leaching for 7 hours, the leaching rate of the sample with particle size 0.180–0.120 mm reaches to 33.46%, and that of the sample with particle size < 0.038 mm is 80.02%. The difference between these two values is 46.56%. Adding ferrous sulphate and hydrogen peroxide at the normal leaching temperature of 30°C can also enhance the leaching of pyrite. However, the ferrous sulphate concentration has no impact on the pyrite leaching reaction.
- Pyrite leaching follows the kinetic equation $1 - 2/3x - (1 - x)^{2/3} = kt$, which is controlled by solid film diffusion in the remaining solid. A kinetic equation for oxidative pyrite

Kinetics of advanced oxidative leaching of pyrite in a potassium peroxydisulphate solution

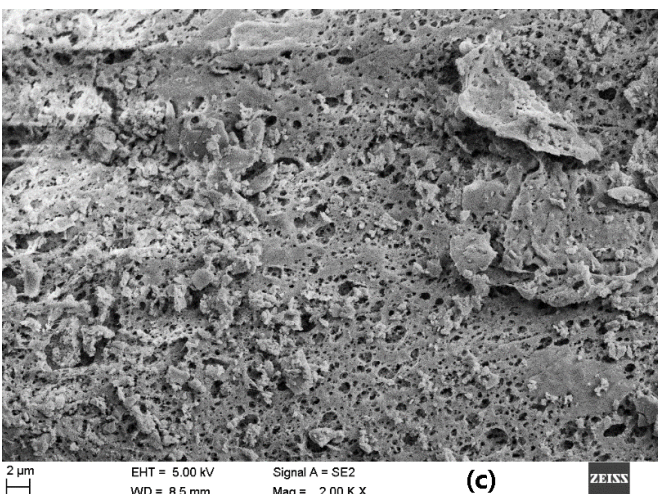
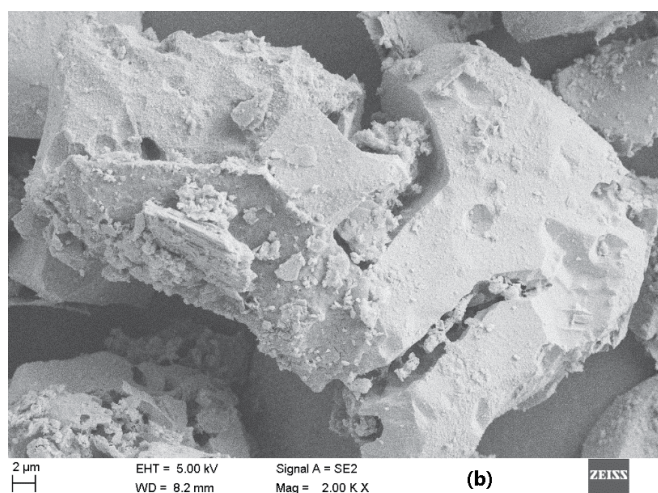
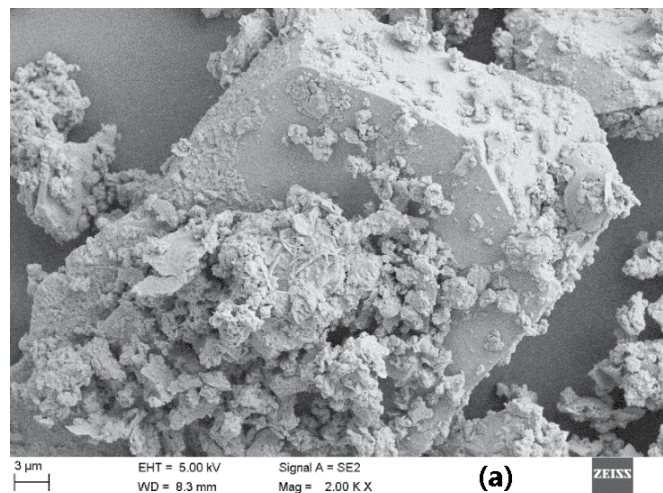


Figure 12—SEM images of pyrite (a) before leaching, (b) after leaching 3 hours, and (c) after leaching for 7 hours

leaching at 70°C is derived by approximating the leaching processes as two different systems:

$$1 - 2x/3 - (1-x)^{2/3} = 2.35 \times 10^5 \times c_{M_2S_5O_8}^{0.431} \times (d_p)^{-0.920} \times e^{-\frac{7853.5}{T}} \times t$$

The kinetic equation for leaching that considers concentrations of ferrous sulphate and hydrogen peroxide at normal temperatures of 30°C is:

$$1 - 2x/3 - (1-x)^{2/3} = 2.28 \times 10^5 \times c_{M_2S_5O_8}^{0.431} \times (d_p)^{-0.920} \times c_{FeSO_4}^{0.295} \times c_{H_2O_2}^{0.378} \times e^{-\frac{7853.5}{T}} \times t$$

Pyrite samples exhibit a regular morphology before leaching, but faviform holes on the surface after leaching.

Acknowledgements

This work was supported by National Natural Science Foundation of China (51864010), the Plan Project of Science and Technology of Guizhou Province of China (Qiankehe Foundation [2017]1404 and Qiankehe Platform Talents [2018]5781) and the Postgraduate Scientific Research Foundation of Guizhou Province of China (Qianjiaohu YJSCXJH (2018)082). We thank Dr Guy Evans from Liwen Bianji, Edanz, Editing China (www.liwenbianji.cn/ac), for editing the English text of a draft of this manuscript.

References

- BINGOL, D., CANBAZOGLU, M., and AYDOGAN, S. 2005. Dissolution kinetics of malachite in ammonia/ammonium carbonate leaching. *Hydrometallurgy*, vol. 76, no. 1-2. pp. 55-62.
- CHO, T.Y., YOON, J.H., YOON, S.H., JOO, Y.K., CHOI, W.H., and SON, Y.B. 2017. The effects of particle size on the surface properties of an HVOF coating of WC-Co. *Korean Journal of Metals and Materials*, vol. 55, no. 4. pp. 227-231.
- EKMEKYAPAR, A.O.R.K.A. 2003. Dissolution kinetics of an oxidized copper ore in ammonium chloride solution. *Chemical and Biochemical Engineering Quarterly*, vol. 4, no. 17. pp. 261-266.
- FISCHBACHER, A., VON SONNTAG, C., and SCHMIDT, T.C. 2017. Hydroxyl radical yields in the Fenton process under various pH, ligand concentrations and hydrogen peroxide/Fe(II) ratios. *Chemosphere*, vol. 182. pp. 738-744.
- GOZMEN, B., KAYAN, B., GIZIR, A.M., and HESENOV, A. 2009. Oxidative degradations of reactive blue 4 dye by different advanced oxidation methods. *Journal of Hazardous Materials*, vol. 168, no. 1. pp. 129-136.
- GU, G.H., SU, L.J., CHEN, M.I., SUN, X.J., and ZHOU, H.B. 2010. Bio-leaching effects of *Leptospirillum ferriphilum* on the surface chemical properties of pyrite. *Mining Science and Technology*, vol. 20, no. 2. pp. 286-291 [In Chinese].
- HILLESIA, A.H., ABU AMRB, S.S., HUSSEINA, R.A., EL-SEBAIEA, O.D., and ARAFA, A.I. 2016. Performance of combined sodium persulfate/H₂O₂ based advanced oxidation process in stabilized landfill leachate treatment. *Journal of Environmental Management*, vol. 166. pp. 493-498.
- HU, J., HUANG, H., XIE, H., GAN, L., LIU, J., and LONG, M. 2017. A scaled-up continuous process for biooxidation as pre-treatment of refractory pyrite-arsenopyrite gold-bearing concentrates. *Biochemical Engineering Journal*, vol. 128. pp. 228-234.
- LIU, Z.X. 2012. Leaching kinetics of copper bearing minerals and leaching process of copper oxide / zinc ore in ammonia solution. PhD thesis, Central South University, China. [In Chinese].
- LI, H.X., WAN, J.Q., MA, Y.W., HUANG, M.Z., WANG, Y., and CHEN, Y.M. 2014. New insights into the role of zero-valent iron surface oxidation layers in persulfate oxidation of dibutyl phthalate solutions. *Chemical Engineering Journal*, vol. 250, no. 250. pp. 137-147.
- TANG, L.J., TANG, Y., WANG, Y.N., and YANG D.Q. 2015. Study on alkaline pretreatment and non cyanide leaching of fine disseminated gold ore. *Gold Science and Technology*, vol. 23, no. 5. pp. 94-98 [In Chinese].
- XU, X.R. and LI, X.Z. 2010. Degradation of azo dye Orange G in aqueous solutions by persulfate with ferrous ion. *Separation and Purification Technology*, vol. 72, no. 1. pp. 105-111.
- ZHONG, L., WU, Z., HUANG, Z., and GUO, Z. 2013. Oxidation kinetics of gold bearing pyrite in sulfuric acid medium. *Rare Metals*, vol. 37, no. 2. pp. 295-301.
- ZHONG, S.P. 2015. Leaching kinetics of gold bearing pyrite in H₂SO₄-Fe₂(SO₄)₃ system. *Transactions of Nonferrous Metals Society of China*, vol. 25, no. 10. pp. 3461-3466.
- ZHAO, H., WANG, J., GAN, X., HU, M., TAO, L., QIN, W., and QIU, G. 2016. Role of pyrite in sulfuric acid leaching of chalcopyrite: An elimination of polysulfide by controlling redox potential. *Hydrometallurgy*, vol. 164. pp. 159-165. ◆

NATIONAL & INTERNATIONAL ACTIVITIES

2020

1–4 March 2020 — PDAC 2020 Convention

Metro Toronto Convention Centre, Toronto, Canada
Contact: info@pdac.ca / convention@pdac.ca
Website: <https://www.pdac.ca/convention>

8 March 2020 — International Womens Day Luncheon Series 2020

Sydney Australia
Website: <https://www.internationalwomensday.com>

10–14 March 2020 — CONEXPO 2020

Las Vegas, NV
Website: <https://www.conexpoconagg.com>

17–18 March 2020 — 5th Young Professionals Conference 2020

The Canvas, Riversands, Fourways
Contact: Camielah Jardine
Tel: +27 11 834-1273/7, Fax: +27 11 838-5923/833-8156
E-mail: camielah@saimm.co.za, Website: <http://www.saimm.co.za>

25–26 March 2020 — GMG Forum

Glenhove Events Hub, Melrose Estate
Contact: Gugu Charlie
Tel: +27 11 834-1273/7, Fax: +27 11 838-5923/833-8156
E-mail: gugu@saimm.co.za, Website: <http://www.saimm.co.za>

25–27 March 2020 — Underground Operations 2020

Perth Convention and Exhibition Centre, Perth Western Australia
Website: <https://undergroundoperators.ausimm.com>

1–2 April 2020 — Mines and Money Asia 2020

Hong Kong Convention & Exhibition Centre, Hong Kong
E-mail: asia@minesandmoney.com
Website: <https://asia.minesandmoney.com>

22 April 2020 — Reconnecting with the Future Workshop

The Equinox Leadership and Innovation Centre, Sandhurst
Contact: Camielah Jardine
Tel: +27 11 834-1273/7, Fax: +27 11 838-5923/833-8156
E-mail: camielah@saimm.co.za, Website: <http://www.saimm.co.za>

21–23 April 2020 — MiningWorld Russia 24th International exhibition of machines and equipment for mining, processing and transportation of minerals

Crocus Expo, Moscow, Russia
Website: <https://www.miningworld.ru/en-GB/>

3–6 May 2020 — CIM Convention and Expo

Vancouver, Canada
Website: <https://convention.cim.org>

10–13 May 2020 — Uranium 2020

Saskatoon, Canada
Website: <https://u2020.metsoc.org>

10–13 May 2020 — 8th Annual Current Trends in Mining Finance (CTMF) Conference 2020

New York
Website: <https://community.smenet.org>

12–13 May 2020 — Digitalization in Mining Conference 2020

The Canvas, Riversands, Fourways
Contact: Gugu Charlie
Tel: +27 11 834-1273/7, Fax: +27 11 838-5923/833-8156
E-mail: gugu@saimm.co.za, Website: <http://www.saimm.co.za>

23–30 May 2020 — ALTA 2020 Nickel-Cobalt-Copper, Uranium-REE, Gold-PM, In Situ Recovery, Lithium & Battery Technology Conference & Exhibition

Perth, Australia
Contact: Allison Taylor
Tel: +61 411 692 442, E-mail: allisontaylor@altamet.com.au
Website: <https://www.altamet.com.au/conferences/alta-2020/>

25–29 May 2020 — The 11th International Conference on Molten Slags, Fluxes and Salts 2020

The Westin Chosun Seoul Hotel, Seoul, Korea
Website: <http://www.molten2020.org>

27–28 May 2020 — Revitalising Exploration Activity in Southern Africa 2020

Glenhove Events Hub, Melrose Estate
Contact: Camielah Jardine
Tel: +27 11 834-1273/7, Fax: +27 11 838-5923/833-8156
E-mail: camielah@saimm.co.za, Website: <http://www.saimm.co.za>

3–5 June 2020 — ROLLS6 2020

London, UK, Website: <http://www.rolls6.org/home>

7–11 June 2020 — NAT2020 North American Tunneling Conference

Nashville, Tennessee
Website: <http://www.natconference.com>

9–11 June 2020 — Diamonds – Source to Use — 2020 Conference

The Birchwood Hotel & OR Tambo Conference Centre
Contact: Camielah Jardine
Tel: +27 11 834-1273/7, Fax: +27 11 838-5923/833-8156
E-mail: camielah@saimm.co.za, Website: <http://www.saimm.co.za>

14–17 June 2020 — 2nd European Mineral Processing and Recycling Congress – EMPRC 2020

Aachen, Germany
Contact: Jürgen Zuchowski, Email: gdmb@gdmb.de
Website: <https://emprc.gdmb.de>

22–23 June 2020 — Renewable Solutions for an Energy Intensive Industry Colloquium

Kathu, Northern Cape
Contact: Camielah Jardine
Tel: +27 11 834-1273/7, Fax: +27 11 838-5923/833-8156
E-mail: camielah@saimm.co.za, Website: <http://www.saimm.co.za>

24–25 June 2020 — 3rd School on Manganese Ferroalloy Production 2020

Kathu, Northern Cape
Contact: Gugu Charlie
Tel: +27 11 834-1273/7, Fax: +27 11 838-5923/833-8156
E-mail: gugu@saimm.co.za, Website: <http://www.saimm.co.za>

22–23 July 2020 — 5th Mineral Project Valuation Colloquium

Glenhove Events Hub, Melrose Estate
Contact: Gugu Charlie
Tel: +27 11 834-1273/7, Fax: +27 11 838-5923/833-8156
E-mail: gugu@saimm.co.za, Website: <http://www.saimm.co.za>

18–19 August 2020 — SAMCODES Conference

The Birchwood Hotel & OR Tambo Conference Centre
Contact: Camielah Jardine
Tel: +27 11 834-1273/7, Fax: +27 11 838-5923/833-8156
E-mail: camielah@saimm.co.za, Website: <http://www.saimm.co.za>

Company affiliates

The following organizations have been admitted to the Institute as Company Affiliates

3M South Africa (Pty) Limited	Expectra 2004 (Pty) Ltd	MSA Group (Pty) Ltd
AECOM SA (Pty) Ltd	Exxaro Coal (Pty) Ltd	Multotec (Pty) Ltd
AEL Mining Services Limited	Exxaro Resources Limited	Murray and Roberts Cementation
Air Liquide (PTY) Ltd	Filtaquip (Pty) Ltd	Nalco Africa (Pty) Ltd
Alexander Proudfoot Africa (Pty) Ltd	FLSmith Minerals (Pty) Ltd	Namakwa Sands(Pty) Ltd
AMEC Foster Wheeler	Fluor Daniel SA (Pty) Ltd	Ncamiso Trading (Pty) Ltd
AMIRA International Africa (Pty) Ltd	Franki Africa (Pty) Ltd-JHB	New Concept Mining (Pty) Limited
ANDRITZ Delkor (Pty) Ltd	Fraser Alexander (Pty) Ltd	Northam Platinum Ltd - Zondereinde
Anglo Operations Proprietary Limited	G H H Mining Machines (Pty) Ltd	Opermin Operational Excellence
Anglogold Ashanti Ltd	Geobrug Southern Africa (Pty) Ltd	Optron (Pty) Ltd
Arcus Gibb (Pty) Ltd	Glencore	Paterson & Cooke Consulting Engineers (Pty) Ltd
ASPASA	Hall Core Drilling (Pty) Ltd	Perkinelmer
Atlas Copco Holdings South Africa (Pty) Limited	Hatch (Pty) Ltd	Polysius a Division of Thyssenkrupp Industrial Sol
Aurecon South Africa (Pty) Ltd	Herrenknecht AG	Precious Metals Refiners
Aveng Engineering	HPE Hydro Power Equipment (Pty) Ltd	Ramika Projects (Pty) Ltd
Aveng Mining Shafts and Underground	Immersive Technologies	Rand Refinery Limited
Axiom Chemlab Supplies (Pty) Ltd	IMS Engineering (Pty) Ltd	Redpath Mining (South Africa) (Pty) Ltd
Axis House Pty Ltd	Ingwenya Mineral Processing (Pty) Ltd	Rocbolt Technologies
Bafokeng Rasimone Platinum Mine	Ivanhoe Mines SA	Rosond (Pty) Ltd
Barloworld Equipment -Mining	Joy Global Inc. (Africa)	Royal Bafokeng Platinum
BASF Holdings SA (Pty) Ltd	Kudumane Manganese Resources	Roytec Global (Pty) Ltd
BCL Limited	Leco Africa (Pty) Limited	RungePincockMinarco Limited
Becker Mining (Pty) Ltd	Leica Geosystems (Pty) Ltd	Rustenburg Platinum Mines Limited
BedRock Mining Support Pty Ltd	Longyear South Africa (Pty) Ltd	Salene Mining (Pty) Ltd
BHP Billiton Energy Coal SA Ltd	Lull Storm Trading (Pty) Ltd	Sandvik Mining and Construction Delmas (Pty) Ltd
Blue Cube Systems (Pty) Ltd	Maccaferri SA (Pty) Ltd	Sandvik Mining and Construction RSA (Pty) Ltd
Bluhm Burton Engineering Pty Ltd	Magnetech (Pty) Ltd	SANIRE
Bond Equipment (Pty) Ltd	Magotteaux (Pty) Ltd	Schauenburg (Pty) Ltd
Bouygues Travaux Publics	Malvern Panalytical (Pty) Ltd	Sebilo Resources (Pty) Ltd
CDM Group	Maptek (Pty) Ltd	SENET (Pty) Ltd
CGG Services SA	Maxam Dantex (Pty) Ltd	Senmin International (Pty) Ltd
Coalmin Process Technologies CC	MBE Minerals SA Pty Ltd	Smec South Africa
Concor Opencast Mining	MCC Contracts (Pty) Ltd	Sound Mining Solution (Pty) Ltd
Concor Technicrete	MD Mineral Technologies SA (Pty) Ltd	SRK Consulting SA (Pty) Ltd
Council for Geoscience Library	MDM Technical Africa (Pty) Ltd	Time Mining and Processing (Pty) Ltd
CRONIMET Mining Processing SA Pty Ltd	Metalock Engineering RSA (Pty)Ltd	Timrite Pty Ltd
CSIR Natural Resources and the Environment (NRE)	Metorex Limited	Tomra (Pty) Ltd
Data Mine SA	Metso Minerals (South Africa) Pty Ltd	Ukwazi Mining Solutions (Pty) Ltd
Digby Wells and Associates	Micromine Africa (Pty) Ltd	Umgeni Water
DRA Mineral Projects (Pty) Ltd	MineARC South Africa (Pty) Ltd	Verni Speciality Construction Products (Pty) Ltd
DTP Mining - Bouygues Construction	Minerals Council of South Africa	Webber Wentzel
Duraset	Minerals Operations Executive (Pty) Ltd	Weir Minerals Africa
Elbroc Mining Products (Pty) Ltd	MineRP Holding (Pty) Ltd	Welding Alloys South Africa
eThekwini Municipality	Mintek	Worley
Ex Mente Technologies (Pty) Ltd	MIP Process Technologies (Pty) Limited	
	MLB Investment CC	
	Modular Mining Systems Africa (Pty)Ltd	



SAIMM
THE SOUTHERN AFRICAN INSTITUTE
OF MINING AND METALLURGY



REVITALISING EXPLORATION ACTIVITY IN SOUTHERN AFRICA

POTENTIAL FOR EXPLORATION

Date: 27-28 May 2020

**Venue: Glenhove Events Hub, Melrose Estate
Johannesburg**



TARGET AUDIENCE

Mining Companies, Exploration companies,
industry funders, government, academics,
geologists, mining executives, consultants,
students



OBJECTIVE

The objective of this conference is to understand the barriers that exist in terms of establishing exploration activity, and to develop solutions in terms of opportunities, funding, skills, technology and policy.

ABOUT THE EVENT:

Exploration is a critical component of the development and sustainability of the minerals industry, in any resource endowed country.

Southern Africa still has vast untapped mineral resources, yet the level of exploration is at an all-time low.

TOPICS:

- Policies and Legal Issues
- Brownfields/Greenfields Exploration
- What are the potential successes
- Strategic/Local Success
- Technology
- Data Modelling
- Financing and Funding

SPONSORSHIP

Sponsorship opportunities are available. Companies wishing to sponsor or exhibit should contact the Conference Coordinator.

Conference Coordinator:

Camielah Jardine, Head of Conferencing

E-mail: camielah@saimm.co.za

Tel: +27 11 834-1273/7

Resilient futures for mineral processing

We would like to invite you to attend the
XXX International Mineral Processing Congress in Cape
Town, South Africa from 18 to 22 October 2020.

IMPC 2020 will be hosted by the Southern African
Institute of Mining and Metallurgy (SAIMM).



IMPC2020

XXX INTERNATIONAL MINERAL PROCESSING CONGRESS

18 - 22 OCTOBER CAPE TOWN SOUTH AFRICA

www.impc2020.com



THE SAIMM

IMPC 2020 will be hosted by the Southern African Institute of Mining and Metallurgy (SAIMM). The SAIMM has been in existence for 125 years, having been established in 1894 as a 'learned society' to support mining and metallurgical professionals during the emergence and growth of the early South African minerals industry.

Mining is of great importance to Africa in general, and particularly to Southern Africa. Africa accounts for a major portion of the world's mineral reserves and more than half of gold, platinum group metals, cobalt and diamonds. Southern Africa produces over two-thirds of Africa's mineral exports by value.

Photo courtesy CTICC



CAPE TOWN INTERNATIONAL CONVENTION SQUARE
1 LOWER LONG STREET, CAPE TOWN 8001

CAPE TOWN INTERNATIONAL CONVENTION CENTRE

IMPC 2020 will be hosted at Cape Town International Convention Centre (CTICC). Since the inception of the CTICC in 2003, Cape Town has been proudly the number one destination for conferences in Africa, according to the latest International Congress and Convention Association (ICCA) statistics.

Cape Town, the "Mother City", is the oldest city in South Africa and has a cultural heritage spanning more than 300 years. Cape Town is a modern, cosmopolitan city and is often rated as one of the premier world holiday destinations. The city has a large range of hotels & guest houses and modern transport infrastructure. The city has numerous activities & attractions, including Table Mountain, Robben Island, Cape Point, the Castle, V&A Waterfront, world class beaches, wine farms, nature reserves, scenic drives, hiking, whale watching, shark cage diving and fine dining.

EVENT SPONSORS



Outotec



INSTITUTE
TOMS
www.tomsmineral.ru



MEDIA SPONSOR

